ABSTRACT

Title of dissertation: EARLY AFTERGLOW EVOLUTION OF X-RAY FLASHES OBSERVED BY SWIFT

Derek Hullinger, Doctor of Philosophy, 2006

Dissertation directed by: Dr. Ann Parsons
NASA Goddard Space Flight Center

Gamma-ray bursts (GRBs) are bright flashes of gamma-ray energy that originate in distant galaxies and last only a matter of seconds before fading away, never to appear again. They are accompanied by longer-wavelength "afterglows" that fade away much more gradually and can be detected for up to several days or even weeks after the gamma-ray burst has vanished.

In recent years, another phenomenon has been discovered that resembles gamma-ray bursts in almost every way, except that the radiated energy comes mostly from x-rays instead of gamma-rays. This new class of bursts has been dubbed "x-ray flashes" (XRFs). There is strong evidence to suggest that GRBs and XRFs are closely-related phenomena.

The Swift mission, launched in November of 2004, is designed to answer many questions about GRBs and their cousins, XRFs—where they come from, what causes them, and why gamma-ray bursts and x-ray flashes differ. The key to the Swift mission is its ability to detect and determine the location of a burst in the sky and then autonomously point x-ray and optical telescopes at the burst position within seconds of the detection. This allows the measurement of the afterglow within 1 – 2 minutes after the burst, rather than several hours later, as was necessary with past missions. This early afterglow measurement is an important key to distinguishing between different theories that seek to explain the differences between XRFs and GRBs.

This dissertation describes the calibration of the Burst Alert Telescope, which measures the spectral and temporal properties of GRBs and XRFs. It also presents a study of XRFs and GRBs detected by Swift, including the first analysis and comparison of the early afterglow properties of

these phenomena. This study reveals interesting differences between the temporal properties of GRB and XRF afterglows and sets strong constraints on some theories that seek to explain XRF origins.

EARLY AFTERGLOW EVOLUTION OF X-RAY FLASHES OBSERVED BY SWIFT

by

Derek Hullinger

Dissertation submitted to the Faculty of the Graduate School of the
University of Maryland, College Park in partial fulfillment
of the requirements for the degree of
Doctor of Philosophy
2006

Advisory Committee:

Professor Greg Sullivan, Chair
Dr. Ann Parsons
Dr. Elihu Boldt
Professor Kara Hoffman
Professor Christopher Reynolds

ACKNOWLEDGMENTS

Where to begin! There are so many people to whom I owe so much!

First, I am very grateful to my advisor, Ann Parsons, who has always, at every stage of my work, been anxious for me to have a good experience, and who has ever been ready and eager to help me. I also owe an immense debt of gratitude to Taka Sakamoto, who suggested this study and made it possible, and who shepherded me through every stage of the analysis and interpretation. I want to thank Cathy Dicks, who helped me edit my dissertation and even took a couple of chapters home with her over Thanksgiving because I was so eager for them. I'm grateful to the entire BAT science team—Scott Barthelmy, Louis Barbier, Jay Cummings, Ed Fenimore, Hans Krimm, Craig Markwardt, David Palmer, Ann Parsons, Taka Sakamoto, and Jack Tueller—for their individual help and tutelage over the last six years, and for making this a memorable experience for me. I am very grateful to Goro Sato, who worked alongside me throughout my time at Goddard. His wisdom and ingenuity made the calibration work possible, and he was a delight to work with.

I appreciate very much my dissertation committee for their patience with me and for reading and giving insightful help on a dissertation that ended up being rather long. I want to thank Valentin Pal'shin of the Konus science team, who provided me with the spectra and response files for the bursts detected by Konus, and who tutored me on how to adjust for time delay differences between the Swift and Wind spacecrafts. I'm grateful to the HETE-2 science team for the collaboration and assistance they gave me in doing joint studies of those bursts observed by the FREGATE and by BAT. I appreciate the help of Kevin Hurley in providing me with timing information that allowed me to check and verify the results of my own time delay calculations. I'm grateful to David Morris of the XRT science team for providing me with the *plot_lc* source code and for his kind and readily available support for it.

To Donald Knuth, Leslie Lamport, and the other creators of LaTeX—I will forever praise

their names! When I think of the work this dissertation would have taken without the assistance of LaTeX, I shudder!

I am especially full of gratitude to my dear wife, Christina, who has supported me and has been completely understanding as I worked from dawn to dusk on my dissertation for months, and who let me tell her all about gamma-ray bursts and even acted interested.

Finally, I would be unthinking and foolish if I didn't thank my heavenly Father, who has supported me and sustained me throughout this endeavor.

TABLE OF CONTENTS

LIST OF TABLES

LIST OF FIGURES

Chapter 1

Introduction

Every day, a few brief but very bright bursts of gamma rays appear in the sky. They are brighter than any other gamma-ray emitting object in the heavens, but they last only a short time—from as little as a few milliseconds to as long as a few hundred seconds. During those few seconds, they may vary in brightness quite a bit (growing brighter, then dimmer, then brighter again) or there may be just a single flash. The spectra (that is, the number of photons as a function of energy) of these bursts tend to show a gradual increase up to a certain "peak" energy, followed by a gradual decrease. They originate from distant galaxies that are billions of light years away, and they never repeat in the same place twice. These "gamma-ray bursts" have intrigued and baffled the astrophysics community ever since their discovery over 30 years ago.

1.1 The Discovery

In 1963, the first of a group of observatories called the Vela satellites were launched into high Earth orbit. Equipped with instruments that could detect x-rays (photons carrying between about 0.1 keV and about 10 keV of energy each, though this definition is somewhat fuzzy), gamma rays (photons carrying more than about 10 keV of energy each) and neutrons (uncharged particles often emitted in nuclear explosions), these satellites were designed to monitor the Earth and the nearby solar system for signs of violations of the 1963 nuclear test ban treaty between the United States and the Soviet Union. In 1967, these satellites detected an intense, brief emission of gamma-rays from outside the solar system. Between 1967 and 1972, the satellites detected sixteen such gamma-ray bursts (GRBs). The data was classified until 1973, when Ray Klebesadel, Ian Strong, and Roy Olsen of Los Alamos Scientific Laboratory (now LANL) were finally permitted to publish the discovery [51]. Prior to this announcement, no one had proposed a mechanism for such a phenomenon, but soon thereafter, hundreds of theories were advanced seeking to explain

the origins of these bursts.

1.2 The Extra-Galactic Origin of Gamma-Ray Bursts

One of the hottest debates in the early days of discovery was whether gamma-ray bursts came from within or near our own galaxy or whether they originated much farther away. If their origins were local, the total gamma-ray energy generated at their source would be quite a bit smaller than if they originated from far beyond our own galaxy. If the bursts came from distant galaxies, the amount of gamma-ray energy given off in a few seconds' time would have to be about the same as the total mass of our sun converted into energy. It was hard to imagine anything that could do that. So the predominant theories hypothesized that gamma-ray bursts resulted from explosions or interactions on the surfaces of neutron stars within our own galaxy.

An interesting breakthrough came with the launch of the Compton Gamma-Ray Observatory in 1991. Aboard this orbiting spacecraft was an instrument called the Burst and Transient Source Experiment (BATSE). BATSE's primary purpose was to measure the distribution of gamma-ray bursts in the sky by determining the locations of a large number of bursts to within a few degrees. It also measured the number of photons coming from these bursts as a function of time ("light curves") and as a function of energy ("spectra"). BATSE consisted of 8 detector modules–one on each corner of the satellite. Each module housed detectors that could measure gamma-ray photons with energies ranging from 15-2000 keV [24]. Since it was able to monitor the entire sky at once (except for the portion that was blocked by the earth), BATSE was able to detect thousands of gamma-ray bursts and measure their spatial distribution. During the course of its nine-year mission, BATSE made measurements and found positions of over 2700 gamma-ray bursts [62].

One of the greatest discoveries was that, contrary to all expectations, gamma-ray bursts did **not** cluster around the plane of our galaxy (which would be expected if they came from neutron stars or other objects within our galaxy). Instead, they were distributed very evenly all over the sky (that is, "isotropically") (see figure 1.1).

An isotropic distribution of bursts could mean one of three things:

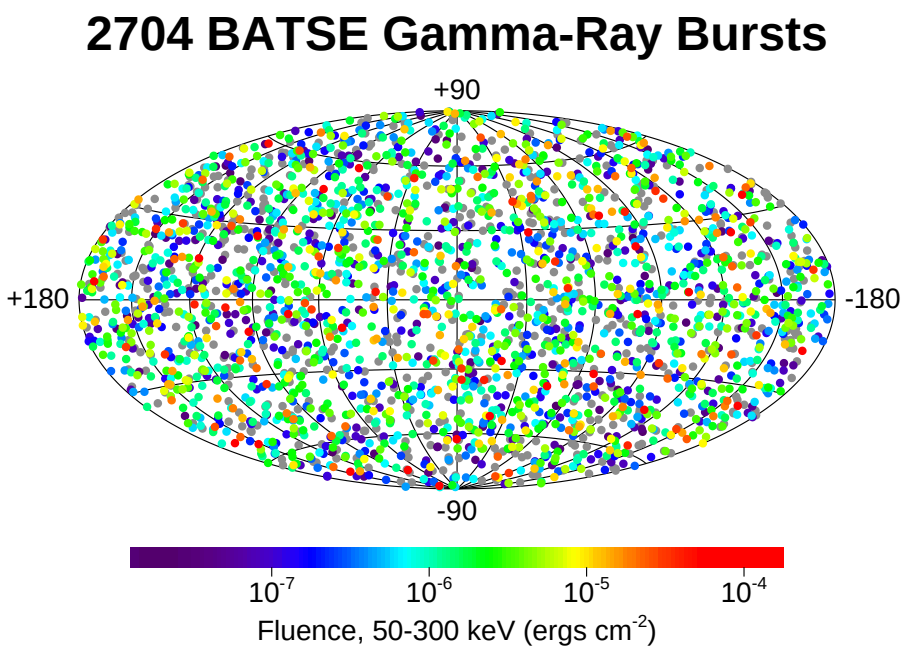

Figure 1.1: The distribution of BATSE burst positions in galactic coordinates. If GRBs originated from within our own galaxy, we would expect the bursts to cluster mostly along the galactic plane (the line joining the 180° and the -180° marks). (from http://www.batse.msfc.nasa.gov/batse/grb/skymap/)

1. Gamma-ray bursts might still originate from within our own galaxy, but only if BATSE were detecting bursts only from our own local vicinity within the galaxy (at a distance smaller than the distance to the edge of the galaxy in any direction).

2. Gamma-ray bursts might originate from a large spherical halo surrounding our galaxy.

3. Gamma-ray bursts might be "cosmological" in origin. That is, they may originate from distances far beyond our galaxy or even our own local cluster of galaxies. On such distance scales, the distribution of matter in the universe is homogeneous, so that an isotropic distribution would be expected.

Another piece of information that can provide a clue about burst origins is a plot of the number of bursts N with a peak "flux" (that is, a peak number of photons passing through a cm^2 of area in 1 second) greater than a certain value vs. the value of that limiting flux P. If the bursts that BATSE detected all originated fairly close to us within our own galaxy, then we would expect the number of bursts to be pretty evenly distributed within the volume in which BATSE was detecting them. This would lead to a relationship between N and P of

$$N \propto P^{-\frac{3}{2}}. \tag{1.1}$$

If this equation were plotted with both axes of the plot having a logarithmic scale, it would look like a straight line with a slope of -3/2.

It turns out that the plot of N vs. P for BATSE bursts has a slope of -3/2 for brighter bursts, but then it becomes less steep for fainter bursts (see figure 1.2). This, together with the isotropic nature of the distribution of bursts in the sky, gave an indication that gamma-ray bursts weren't a local phenomenon, but it still left open the question of whether they originated in a halo around our galaxy or at cosmological distances.

1.3 The Discovery of Afterglows

The brief duration of gamma-ray bursts made measurements rather difficult. Gamma-ray telescopes tend to have poor imaging capabilities, and with only a few seconds of gamma-ray

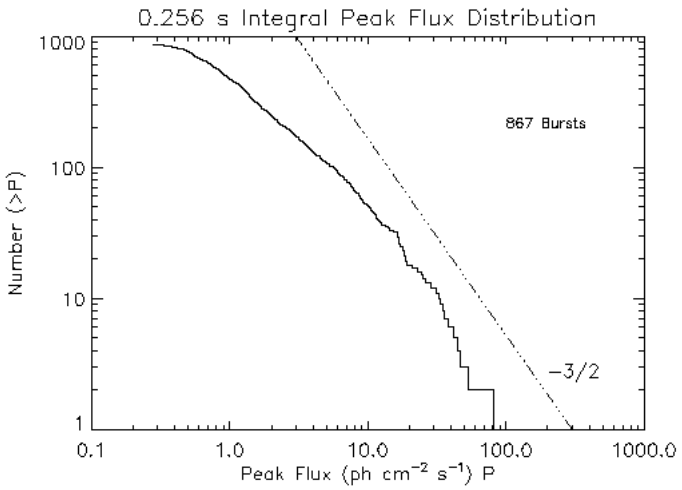

Figure 1.2: A plot of the number of bursts N with a peak flux greater than some value P. If GRBs came from our own local part of the galaxy, the curve would have a slope of -3/2 throughout the entire range. A straight line with a slope of -3/2 is shown for comparison. (from http://science.nasa.gov/newhome/headlines/ast06may98_1.htm)

emission to work with, it wasn't possible to determine with high precision the position of a gamma-ray burst, and only a limited amount of information could be extracted. If a counterpart could be identified at longer wavelengths, it would provide a wealth of additional information. Some models predicted a longer-lived "afterglow" at longer wavelengths [56], and an intense search began which sought to identify such a counterpart [40]. A breakthrough came with an Italian-Dutch satellite named BeppoSAX. BeppoSAX bore a complement of instruments that covered a wide energy range, from 0.1 to 600 keV. These included two instruments sensitive to gamma-rays and "hard" (that is, high energy) x-rays, and that had a wide "field of view" (that is, they could monitor a large portion of the sky at once) along with a set of telescopes that were sensitive to photons with lower energies and which observed a relatively narrow field of view. With this combination, BeppoSAX was able to monitor the sky for gamma-ray bursts, and when it detected one, the narrow-field instruments could be pointed at the location of the burst to search for a lower-energy counterpart. On 28 February 1997, the first measurement of such an event took place with the detection of a gamma-ray burst by the wide-field instruments. Data processing on the ground revealed a point source with an error circle 3 arcminutes in radius. This enabled a series of follow-ups with the

narrow field instruments that resulted in the detection of x-ray emission that gradually faded over the course of a few weeks [18].

Since this discovery, afterglows have been seen from dozens of gamma-ray bursts. They remain visible for hours and even days, gradually growing dimmer. They've been observed not only in the x-ray band, but also in optical, infrared, and radio bands. X-ray and optical telescopes can obtain a much more precise position of a source, down to the arcsecond level and smaller– precisely enough to determine what distant galaxy the burst is associated with. Furthermore, with x-ray and optical radiation, the presence of emission or absorption features from either the afterglow itself or from its associated galaxy allow observers to obtain a measure of the redshift (z) of the burst, which is a surrogate measure for its distance from us (see section 2.3). In the case of this first afterglow discovered with BeppoSAX, the redshift was found to be 0.695 [11], placing it far beyond our own galaxy in the outer reaches of the universe. This and subsequent afterglow measurements have definitively established the distant (or "cosmological") origin of at least most gamma-ray bursts.

1.4 The Discovery and Observations of X-Ray Flashes

During the early days of discovery, x-ray emission was sometimes observed from gamma-ray bursts while the bursts were taking place. Some of the bursts observed with the Vela satellites and contemporaneous instruments saw simultaneous x-ray emission [80, 58, 78]. This emission showed temporal structure that was similar to that of the gamma-ray emission.

Gotthelf et al. searched for transient (i.e., not steady-state) x-ray sources in data collected by the Einstein Observatory [36]. They found 18 with emission in the 0.2 - 3.5 keV band that had temporal and spectral properties similar to those of gamma-ray bursts. They called these sources "x-ray flashes" (XRFs). (The term "x-ray burst" was already taken, being used to describe x-ray emission from thermonuclear explosions on the surface of neutron stars within our galaxy.)

Strohmayer et al. studied the gamma-ray bursts detected by the Ginga satellite, which was sensitive to 2-400 keV photons. They found that the spectra of these bursts were consistent with

BATSE GRBs, but that the peak energy distribution extended to below 10 keV (much lower than the peak energies of bursts detected by BATSE), hinting that XRFs were simply a continuation of GRBs down into x-ray energies [75]. Results from the BeppoSAX and HETE-2 missions, which both include instruments sensitive to both x-rays and gamma-rays, have also indicated that XRFs and GRBs form a single continuum and are not distinct phenomena, with XRFs tending to have lower peak energies than GRBs [50].

With the evidence that GRBs and XRFs are simply two extremes of a single population, there is great potential for understanding the nature and origins of the phenomenon by studying the differences between the two types of events and investigating the reasons for those differences. Several models have been proposed that seek to explain why some bursts emit mostly gamma-rays and others mostly x-rays. An important key to distinguishing between these models lies in the early afterglow emission of the burst. Swift is the first mission capable of observing afterglows within seconds to minutes of the prompt emission. Previous missions required response times on the order of hours. Swift's prompt multi-wavelength capability allows us to gain a clearer understanding of the origin and nature of GRBs.

1.5 Overview of This Thesis

In this thesis, I explore the properties of prompt and afterglow emission of x-ray flashes detected by Swift, comparing them with x-ray flashes observed with other missions and with gamma-ray bursts detected by Swift. Chapter 2 reviews the observational characteristics of the prompt and afterglow emission of x-ray flashes and gamma-ray bursts. Chapter 3 describes the notable observations and contributions made by past missions. An overview of the current standard theoretical models for prompt and afterglow emission is presented in chapter 4, along with a review of different x-ray flash models. In chapter 5, I describe the Swift mission and its component instruments: the BAT, the XRT, and the UVOT. The methods and procedures involved in calibrating the Swift Burst Alert Telescope are described in chapter 6. The analysis and data reduction procedures used are discussed in chapter 7. Chapter 8 gives detailed analysis results

of each x-ray flash and gamma-ray burst included in the study. A comprehensive overview of the global characteristics of Swift x-ray flashes and gamma-ray bursts is presented in chapter 9. In chapter 10, I conclude by comparing these results to predictions made by various x-ray flash models. In the appendices, I describe the derivation of a technique known as "mask-weighting". I also provide a glossary of some of the acronyms and concepts discussed in this dissertation.

Chapter 2

Observational Characteristics of Gamma-Ray Bursts and X-Ray Flashes

At a conference a few years ago, I attended a series of lectures and presentations describing many aspects of gamma-ray burst astronomy. I found that in the case of some GRB theories or ideas, most people seemed to agree. With others, everyone seemed to disagree. Even when there was a general consensus (for example, on the cosmological nature of gamma-ray bursts), there was always someone with an opposing opinion. Sometimes I would listen to one speaker describe evidence that supported one view, and then another speaker would stand and present evidence for an opposing view, and I would wonder to myself which of them would end up being right. I commented on this to one of the other participants at lunch one day. With a wry smile he replied, "What makes you think anybody's right?" That's the nature of observational astronomy. There are many theories and many views, but over time and with more observations, a general understanding eventually emerges. Here I present a brief list of some of the observations that have led to the current understanding of gamma-ray bursts.

2.1 Nomenclature

Before describing the characteristics of gamma-ray bursts, we should say something about the naming convention that has been adopted. A gamma-ray burst is designated by the date on which its emission was detected, as measured in Universal Time (UT).[1] This designation is composed of the last two digits of the year, followed by the month, followed by the day of the month. Hence, GRB 990510 was detected on 10 May 1999. In cases where more than one burst was detected on a given day, a letter is added to distinguish them. GRB 050502a, for example, was the first burst detected on 2 May 2005, and GRB 050502b was the second. Sometimes bursts that have been designated as x-ray flashes are labelled with the prefix "XRF" instead of "GRB".

[1] Univeral Time is the time of day as measured from a longitude of zero (for example, in Grenwich, England).

So one might see the burst detected on 3 September 2002 labelled as either GRB 020903 or as XRF 020903. An intermediate class of bursts, referred to as "x-ray rich gamma-ray bursts" are sometimes designated with the prefix "XRR" or "XRGRB".

2.2 Frequency

Over the course of its lifetime, BATSE observed about 305 gamma-ray bursts each year (nearly one per day) [62]. With BATSE's field of view, this leads to an extrapolation of around three bursts per day. BATSE was able to detect bursts that had a total fluence[2] above about 10^{-8} ergs/cm^2 for photons ranging from 50 and 300 keV. Near the edge of BATSE's sensitivity limit, bursts continued to be more numerous, indicating that an instrument able to detect bursts with a smaller fluence in this energy range would probably detect many more bursts.

BATSE's energy range did not extend below 30 keV. However, the energy range of HETE-2's Wide-field X-ray Monitor (WXM) extended down to 2 keV, making it well-suited for detecting x-ray flashes. In its first 1.1 years of "on-time" (time during which it was actually enabled and able to detect bursts), HETE-2 detected 15 XRFs, 20 XRRs and 10 GRBs [70]. Thus, about 1/3 of all bursts detected by HETE-2 were XRFs. Considering the WXM's $60^\circ \times 60^\circ$ field of view, this means about 160 XRFs, 220 XRRs, and 110 GRBs take place each year that have a fluence in the WXM's energy range large enough for the WXM to be able to detect them. Based on BeppoSAX data, Heise et al. estimated a rate of ~ 100 XRFs per year [43].

2.3 Redshift

When two observers are in relative motion, light propagating between them will have a different wavelength when measured in each observer's own reference frame. Light originating from a star that is moving toward us has a shorter wavelength when it is measured here on earth

[2]Fluence is the total amount of energy per cm^2 that passes through the region of space where the instrument is located in a given amount of time. For GRBs, it's the average intensity of the burst multiplied by the duration of the burst. Fluence is often given for a specific range of photon energies.

than it had in the star's own reference frame. This is referred to as a "blueshift". On the other hand, Light originating from a star that is moving away from us has a longer wavelength when measured on Earth than it had in the star's own reference frame. This is known as a "redshift". The redshift (z) of an object is defined as

$$z = \frac{\Delta\lambda}{\lambda} \tag{2.1}$$

where λ is the wavelength of light measured at the source, and $\Delta\lambda$ is the difference between the wavelength measured on earth and the wavelength measured at the source. By this definition, $z = 0$ would correspond to a source that is neither moving away from nor toward the earth.

In 1929, Edwin Hubble noticed that galaxies farther from us tend to emit light that has been "redshifted" more than galaxies closer to us. This redshift can be understood to mean that galaxies farther from us are moving away from us at a faster rate than those nearby, which led to the modern understanding of the expansion of the universe. At the same time, "Hubble's law" provided a way to directly measure the distance to distant objects. In modern astronomy, we usually cite the "redshift" of a distant object when we want to specify how far away it is (much the same way we often say that another city is "an hour away"). Redshift is a surrogate measure for distance.

When we know the distance to a gamma-ray burst, we can calculate the energy emitted by the burst at its source. We can then test and constrain different models of energy production. A knowledge of GRB distances also allows us to track the evolution of GRBs in cosmic time (GRBs originating at greater distances took place longer ago). As such, redshifts are a valuable piece of information, and obtaining them has been a high priority in GRB studies.

Each element radiates at characteristic wavelengths when it absorbs energy. This radiation is like a fingerprint that can be used to identify the element. Afterglow emission at the source of a gamma-ray burst often interacts with atoms in the vicinity, causing them to radiate. These characteristic photons travel through space along with the smoother spectrum of photons from the afterglow and arrive at telescopes here on earth redshifted. These characteristic photons can be picked out of the spectrum and, by noting how many of these photons there are what their

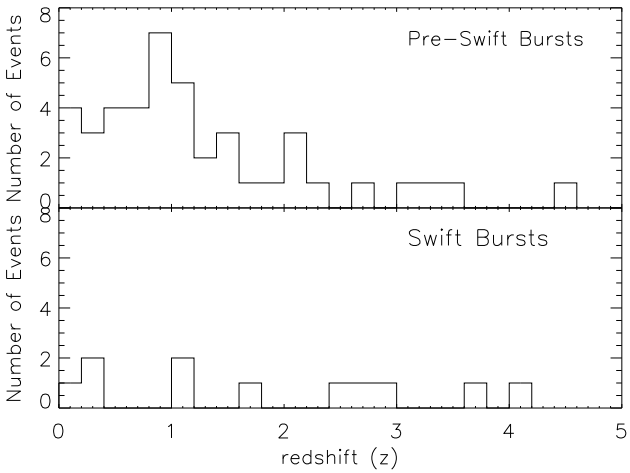

Figure 2.1: Redshifts of bursts detected by Swift as of 31 July 2005 and of bursts detected before the launch of Swift

energies are, they can be identified and their redshift determined. On the other hand, sometimes light from the host galaxy provides a measure of the redshift of the burst. The host galaxy can only be determined if an afterglow is detected, so in either case, the detection of an afterglow is essential. In the 7 years between the first afterglow detection and Swift's launch, redshifts for 45 GRBs were measured or constrained. These redshifts range from 0.0085 all the way up to 4.5. Since Swift's launch, at least one burst with an even higher redshift has been measured.

One of Swift's primary goals is to provide precise positions very early after the detection of the gamma-ray burst, at a time when many more afterglows will be bright enough to detect, so that many more gamma-ray burst redshifts can be measured. Between it's launch in November of 2004 and 31 July 2005, Swift detected 11 GRBs for which redshifts were subsequently measured. During that same period, The HETE-2 and Integral missions each detected one GRB for which the redshift was successfully measured. Although this isn't a very large data set, it appears that the redshift distribution of Swift bursts is consistent with the redshift distributions of bursts detected in the pre-Swift era. (see Figure 2.1).

An analysis of GRBs and XRFs detected by HETE-2 and by BeppoSAX show that the distributions of redshifts for the two populations appear to overlap [70]. The sample isn't large

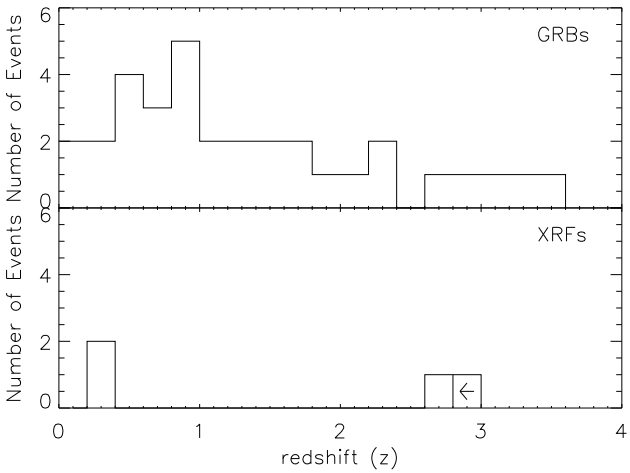

Figure 2.2: Redshifts of GRBs and XRFs detected by HETE-2 and BeppoSAX

enough, though, to firmly state whether XRFs tend to appear at lower or higher redshifts on average than GRBs (see Figure 2.2).

2.4 Prompt Emission

Most GRB characteristics can be categorized as either pertaining to the prompt burst emission itself or to the longer-lived afterglow. Here we examine a few of these characteristics.

2.4.1 Duration

Each gamma-ray burst lasts anywhere from a few milliseconds all the way up to ten minutes or more. Several authors have noted that a plot of the number of bursts vs. the duration of those bursts reveals two distinct groups (i.e., there is a "bimodal distribution") [55, 52], (see Figure 2.3). This indicates the likelihood of at least two distinct classes of gamma-ray bursts that arise from different mechanisms. It has been noted that the long class of bursts tend to be spectrally "softer" than the short class of bursts (meaning that they tend to have more low-energy photons and fewer high-energy photons). A good way to characterize burst "hardness" is with a fluence ratio, dividing the energy detected in some high-energy band with the energy detected in some low-energy band. Figure 2.4 shows a plot of a fluence ratio vs. duration for bursts detected by

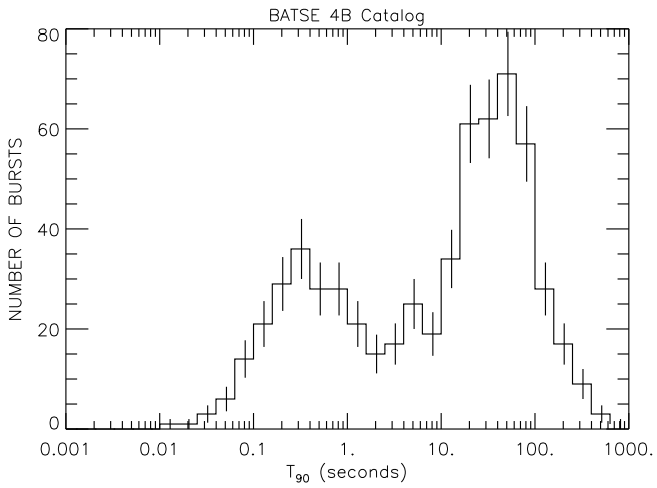

Figure 2.3: Durations of GRBs Measured by BATSE. In this case, the duration is defined as the time in which the burst emits between 5% and 95% of its energy, often labelled "T90". (From http://www.batse.msfc.nasa.gov/batse/grb/duration/)

BATSE. Studies have been shown that these two populations differ from each other in other ways, too, lending support to the argument that they arise from distinctly different phenomena [60]. XRFs discovered to date appear to be a sub-class of the long, soft GRB population and show little resemblance to the short, hard population.

2.4.2 Variability

Some Gamma-ray bursts show a great deal of variability within their temporal profiles, with many peaks appearing within a given burst (see Figure 2.5). Other bursts have very simple profiles with only a single peak. When multiple peaks are present, those peaks sometimes have very complicated structures, varying in individual durations and intensities. Studies have shown that the variability of bursts is correlated with intrinsic luminosity (or total energy emitted in all directions per second by the burst): bursts with more variability tend, on average, to be brighter than bursts with less variability (see, for example, [74]). This variability also places strong constraints on the size of the emission region, as we shall discuss in section 4.1.

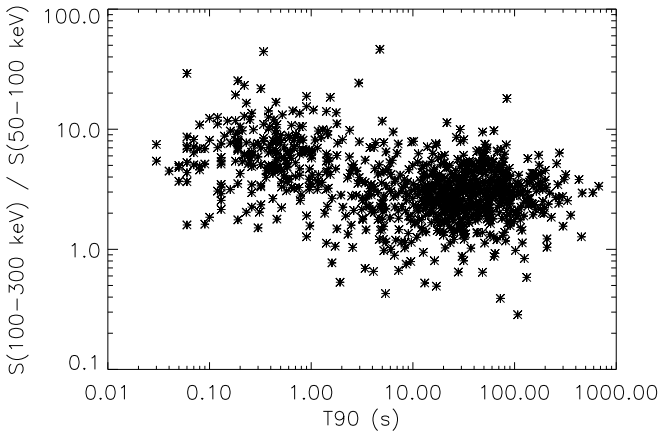

Figure 2.4: Durations vs. fluence ratios of GRBs detected by BATSE. The fluence ratio, in this case, is the ratio of total fluence from 100 – 300 keV photons to total fluence from 50 – 100 keV photons.

2.4.3 Intensity

At gamma-ray wavelengths, GRBs are the brightest objects in the universe, outshining all other sources. BATSE's results indicate that their fluences in the 50 – 300 keV energy band can be anywhere from 10^{-8} to 10^{-4} ergs/cm^2. It's likely that bursts with fluences below the detection threshold of current and past missions also exist. X-ray flashes tend to have lower gamma-ray fluences simply because most of their energy falls in the x-ray band.

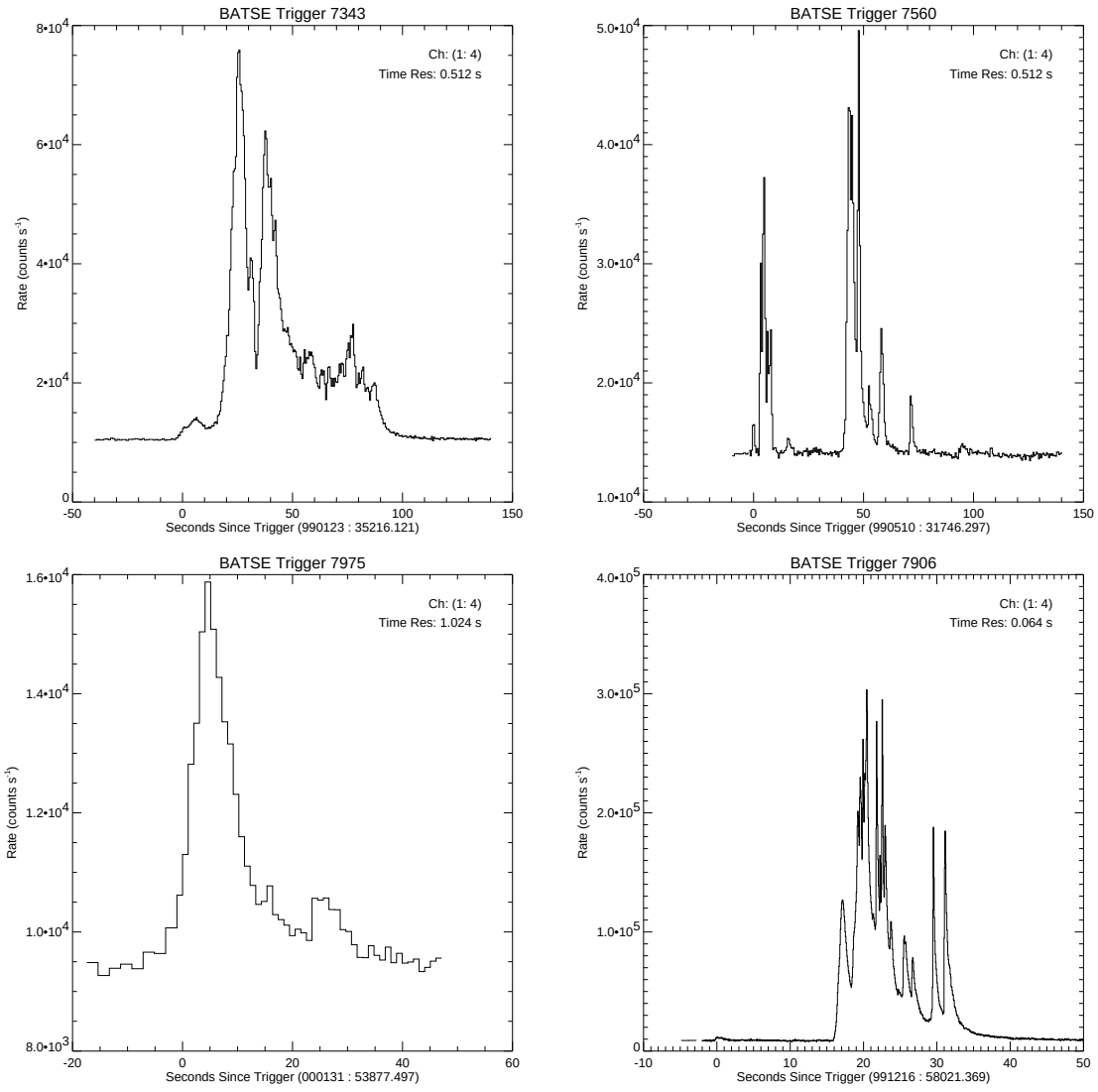

Figure 2.5: Light curves for some gamma-ray bursts detected by BATSE [33]. A light curve is the number of photons detected by an instrument per second, so it measures the brightness of the burst as a function of time. Clockwise, from top left: GRB 990123, GRB 990510, GRB 991216, and GRB 000131.

2.4.4 Spectral Characteristics

It was first noted by Band et al. [5] that GRB spectra are well fit in general by a power law (that is, a function of the form $y = ax^k$, where k is called the "power law index") at low energies and another power law at high energies, joined smoothly by an exponential expression:

$$\begin{aligned} N(E) &= A\left(\frac{E}{100\text{ keV}}\right)^{\alpha}\exp\left(\frac{-E(2+\alpha)}{E^{\text{obs}}_{\text{peak}}}\right) && E < \left(\frac{(\alpha-\beta)E^{\text{obs}}_{\text{peak}}}{2+\alpha}\right) \\ &= A\left[\frac{(\alpha-\beta)E^{\text{obs}}_{\text{peak}}}{(100\text{ keV})(2+\alpha)}\right]^{\alpha-\beta}\exp(\beta-\alpha)\left(\frac{E}{100\text{ keV}}\right)^{\beta} && E > \left(\frac{(\alpha-\beta)E^{\text{obs}}_{\text{peak}}}{2+\alpha}\right) \end{aligned} \tag{2.2}$$

where

$N(E)$ is the number of photons/cm^2/s/keV,

α is the spectral index of the low-photon-energy portion of the spectrum,

β is the spectral index of the high-photon-energy portion of the spectrum,

$E^{\text{obs}}_{\text{peak}}$ is the photon energy at which the greatest amount of energy is radiated, and

A is a normalization constant with units of photons/cm^2/s/keV.

Figure 2.6 shows the shape of this curve for some typical parameters. The values of these parameters vary over a wide range from one burst to the next, with α varying from -2 to +1, β from -4 to -1.5, and $E^{\text{obs}}_{\text{peak}}$ from 30 keV to 1.5 MeV in the BATSE data set, with the greatest number of bursts having an $E^{\text{obs}}_{\text{peak}}$ value at around 250 keV. Spectra from bursts detected by BeppoSAX and HETE-2 have the same overall shape, but with different distributions of α, β, and $E^{\text{obs}}_{\text{peak}}$. In particular, while the $E^{\text{obs}}_{\text{peak}}$ values for the bursts in the BATSE data set tend to cluster around 250 keV, the $E^{\text{obs}}_{\text{peak}}$ values of bursts detected by BeppoSAX and HETE-2 are distributed prominently to lower energies. This also appears to be the primary spectral difference between GRBs and XRFs: x-ray flashes tend to have the same spectral characteristics as gamma-ray bursts except that $E^{\text{obs}}_{\text{peak}}$ tends to fall at lower energies.

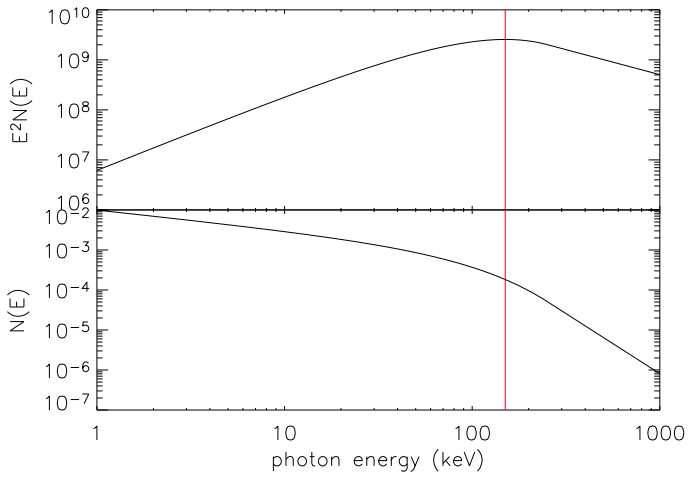

Figure 2.6: A plot of the Band spectral model $N(E)$, in units of photons/s/cm^2/keV, with with $\alpha = -0.5$, $\beta = -3.0$, $E^{\rm obs}_{\rm peak} = 150$ keV, and $A = 10^{-3}$ photon/cm^2/s/keV. Above the plot of N(E) is a plot of E^{2}N(E) (in units of ergs/cm^2/s), which is proportional to the radiated energy as a function of photon energy. Note that the peak of this spectrum is at $E^{\rm obs}_{\rm peak}$, indicated by the vertical line.

2.4.5 Amati Relation

We noted earlier that $E^{\rm obs}_{\rm peak}$ is defined as the photon energy at which a plot of radiated power (as measured by the observer) vs. photon energy reaches its peak. When we correct $E^{\rm obs}_{\rm peak}$ for redshift, the result is the energy of peak power in the reference frame of the source. We refer to this value as $E^{\rm src}_{\rm peak}$. When the redshift is known, finding $E^{\rm src}_{\rm peak}$ is simply a matter of multiplying $E^{\rm obs}_{\rm peak}$ by $(1+z)$. A number of correlations between $E^{\rm src}_{\rm peak}$ and various other quantities have been discovered, and we shall examine several of these.

Amati et al. [1] first noted a correlation between $E^{\rm src}_{\rm peak}$ and the isotropic equivalent energy $E_{\rm iso}$ (the total amount of gamma-ray energy emitted by the burst if it emitted equally in all directions). A good way to tell how well "correlated" (or related) two quantities are is to calculate their "correlation coefficient". Correlation coefficients range from -1 to 1. A coefficient close to 1 indicates that when one quantity is large, the other quantity will likely be large, too. A coefficient close to -1 indicates that when one quantity is large, the other quantity is likely to be small. A coefficient near 0 indicates that if one quantity is large, there's no telling what the other quantity will be. A coefficient identically equal to 1 or -1 means that the two quantities lie exactly on a

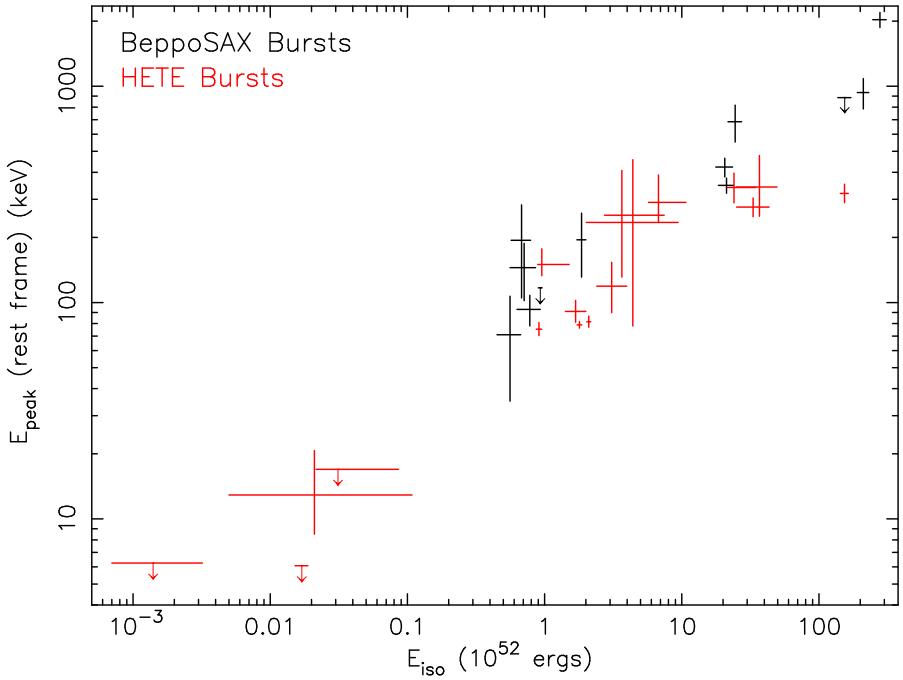

Figure 2.7: Correlation between $E^{\rm src}_{\rm peak}$ and $E_{\rm iso}$. The correlation coefficient between the two quantities is 0.902 ± 0.078.

straight line, so that you can predict one precisely if you know the other.

In this case, the correlation coefficient for $\log(E^{\rm src}_{\rm peak})$ and $\log(E_{\rm iso})$ was found to be 0.902 ± 0.078, indicating quite a strong correlation. The authors found that

$$E^{\rm src}_{\rm peak} \propto E^{p}_{\rm iso}, \tag{2.3}$$

where $p = 0.52 \pm 0.06$. Calculating both $E^{\rm src}_{\rm peak}$ and $E_{\rm iso}$ requires a knowledge of the redshift of the bursts, so it has only been possible to test this relation on the limited sample of bursts with known redshifts. Recent measurements have confirmed that XRFs, when combined with GRBs, follow the same correlation, extending the relation to lower peak energies. (see Figure 2.7) [4, 53, 69].

2.4.6 Yonetoku Relation

There is also a correlation between $E^{\rm src}_{\rm peak}$ and the peak isotropic equivalent luminosity $L_{\rm iso}$ (the energy per second that is emitted by the source if it emits equally in all directions) (see Figure 2.8). This correlation was discovered by Yonetoku et al. [83], who found a correlation

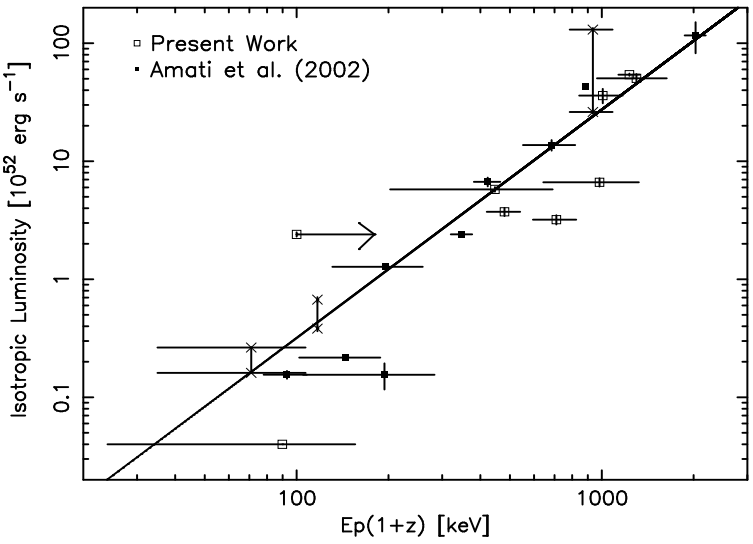

Figure 2.8: Correlation between $E^{\rm src}_{\rm peak}$ and $L_{\rm iso}$. The diagonal line is a plot of equation 2.4.

coefficient for $\log(E^{\rm src}_{\rm peak})$ and $\log(L_{\rm iso})$ of 0.957, indicating that it is a tighter correlation than the Amati relation. The authors found that $E^{\rm src}_{\rm peak}$ and peak $L_{\rm iso}$ obey

$$\frac{L_{\rm iso}}{10^{52}\ {\rm ergs}/2} = (4.29 \pm 0.15) \times 10^{-5} \left(\frac{E^{\rm src}_{\rm peak}}{1\ {\rm keV}} \right)^{1.94 \pm 0.19}, \tag{2.4}$$

if the peak $L_{\rm iso}$ includes photons with energies ranging from 30 keV – 10 MeV in the source frame. The uncertainties shown reflect a 68% probability.

In part because this correlation is quite strong, it can be used to estimate gamma-ray burst redshifts when the redshifts cannot be measured directly. This procedure is described in section 7.3.

2.5 Afterglow Emission

2.5.1 Spectral Characteristics

Nearly every GRB for which x-ray observations have been promptly conducted has exhibited an x-ray afterglow. Usually the number of photons per given photon energy follows a power law modulated by some absorption from intervening hydrogen atoms:

$$\frac{dN}{dE} \propto E^{-I} \cdot \exp[n_H \cdot \sigma(E)], \tag{2.5}$$

where I is called the photon index, n_H is the number of hydrogen atoms per cm^2 between the detector and the source, and $\sigma(E)$ is the photo-electric cross-section of hydrogen (which is just a known function of photon energy).

The measured photon indices lie in an approximately Gaussian distribution with a mean value of 1.95 ± 0.03 and a standard deviation σ_I of ~ 0.4. Hydrogen column densities (n_H) usually tend to be consistent with the measured values of our own galaxy in the direction of the burst but in some cases have been significantly higher [27].

There are indications that the spectral properties of XRFs are similar to those of GRBs. Piro found that the fluxes of XRFs 12 hours after the bursts are consistent with those of GRBs 12 hours after the bursts [64]. XRR041006 exhibited a photon index of 2.1 and XRF030723 a photon index of $1.9^{+0.3}_{-0.2}$, both near the center of the distribution described by Frontera [38].

2.5.2 Temporal Characteristics

Prior to the early observations made possible by Swift, Gamma-ray burst afterglow fluxes were observed to usually follow a power law in time ($N_{photon} \propto t^{\beta}$). The power law indices β for the various bursts that have been observed are distributed in a roughly Gaussian distribution with a mean value of -1.30 ± 0.02 and a standard deviation σ_β of about 0.35 [27].

Some afterglow light curves have exhibited "breaks" (or changes in shape from one power law index to another) after about 8 hours or so. Examples of these include GRB 010214, which gave signs of a power law index β of about 1 early on and of 2.1 later, and also GRB 010222 which actually showed signs of increasing in intensity with a power law index β of -0.8 before beginning to diminish [27].

XRF afterglow light curves seem to lie firmly within this distribution. Granot cites a decay index of 1.0 ± 0.1 for XRF 030723 between 3.2 and 13.2 days after the burst [38]. Amati found a decay index of $1.33^{+0.02}_{-0.03}$ for XRF 020427 [2].

2.5.3 Jet Breaks

Many gamma-ray burst afterglow light curves have been found to exhibit a "break" where the power law index changes abruptly. Sometimes this break is "achromatic", occurring at all wavelengths simultaneously, as opposed to "chromatic" breaks that would result from the evolution of the afterglow spectrum with time [71]. These breaks often appear on the order of a day following the burst. The afterglow is believed to originate in a relativistic outflow of material that forms a narrow "jet" emanating from the burst site. This material emits radiation in a narrow cone due to relativistic beaming. As the material decelerates, the emission cone grows wider. When the cone width reaches an angle comparable to the width of the jet, the observer begins to observe the edge of the jet, which causes the light curve to steepen. The relationship between the time of this steepening (the so-called "jet break") and the jet angle was derived by Sari et al. [72, 34]:

$$\Delta\theta = 0.161\Big(\frac{t_{jet,d}}{1+z}\Big)^{3/8}\Big(\frac{n\eta_\gamma}{E_{\mathrm{iso},52}}\Big)^{1/8}, \tag{2.6}$$

where $t_{jet,d}$ is the jet break time (measured in days), z is the burst redshift, n is the particle density in the region surrounding the burst, η_γ is the fraction of the burst's kinetic energy that is emitted in gamma-rays, and $E_{\mathrm{iso},52}$ is the isotropic-equivalent energy of the burst, in units of 10^{52} ergs. Frail et al. first noted these jet breaks and derived jet angles for several bursts [26]. They found a correlation between the isotropic-equivalent energies E_{iso} and the jet angles $\Delta\theta$, leading to the relationship

$$E_{\mathrm{iso}} \propto \Delta\theta^2. \tag{2.7}$$

Since the isotropic-equivalent energy E_{iso} is related to the actual total energy E_γ by

$$E_\gamma = E_{\mathrm{iso}}(1-\cos(\Delta\theta)), \tag{2.8}$$

(assuming a uniform flux distribution within the jet), where $\Delta\theta$ is the half opening angle of the jet, Frail et al. found that the total gamma-ray energy emitted by the bursts E_γ fit within a relatively narrow distribution (see Figure 2.9). Bloom et al. expanded on this data set and found that the peak of the E_γ distribution is 1.33×10^{51} ergs with a width of 0.07×10^{51} ergs [12]. Lamb et

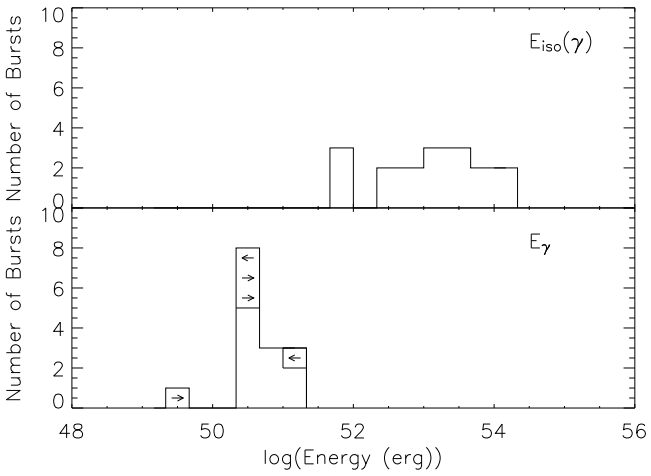

Figure 2.9: $E_{\rm iso}$ and E_γ for bursts studied by Frail et al. They found that when $E_{\rm iso}$ was corrected for jet angle (resulting in E_γ), they were much more tightly distributed. Boxes with arrows in them indicate that those bursts either have an upper limit (left-pointing arrow) or a lower limit (right-pointing arrow) for E_γ.

al. noted that the isotropic energies of x-ray flashes are so small that even an isotropic outflow wouldn't be sufficient to enable their values of E_γ to be $(1.33 \pm 0.07) \times 10^{51}$ ergs [54].

2.5.4 Ghirlanda Relation

Ghirlanda et al. [34] discovered a correlation between the total gamma-ray energy E_γ and $E^{\rm src}_{\rm peak}$ (see Figure 2.10):

$$E^{\rm src}_{\rm peak} \propto E^p_\gamma, \tag{2.9}$$

where $p = 0.706 \pm 0.047$. They found that the correlation coefficient between $\log(E^{\rm src}_{\rm peak})$ and $\log(E_\gamma)$ was 0.94, so that this correlation is stronger than the correlation found by Amati between $\log(E^{\rm src}_{\rm peak})$ and $\log(E_{\rm iso})$.

2.5.5 Dark Bursts

As noted earlier, it appears that for nearly every GRB, there is a corresponding x-ray afterglow. On the other hand, it appears that only a fraction of bursts have corresponding optical afterglows (about 50% of the well-localized bursts detected by BeppoSAX). Those without detected optical afterglows have been dubbed "dark bursts". A few possible explanations have been

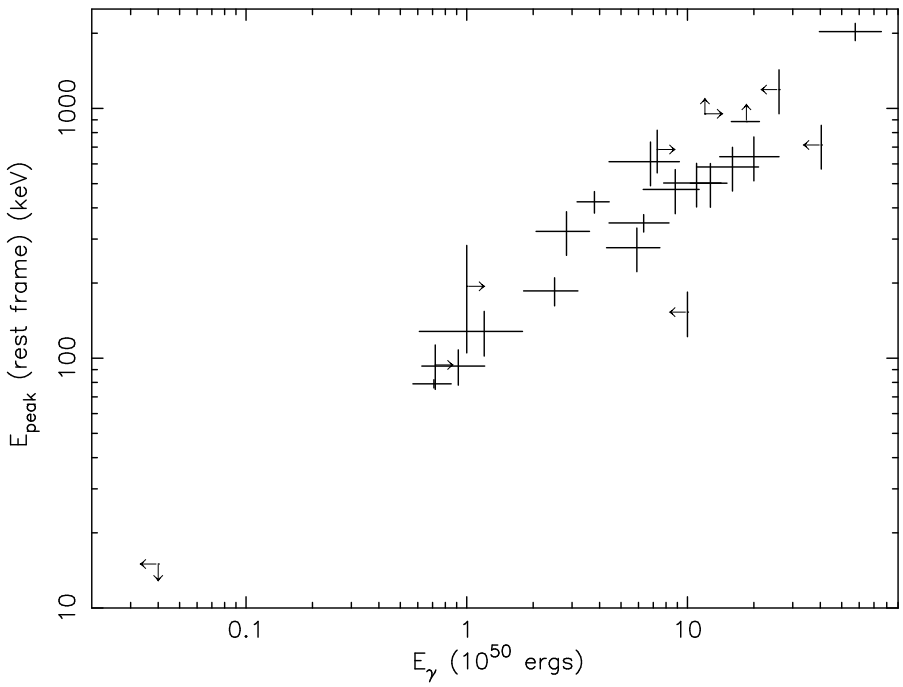

Figure 2.10: Correlation between $E^{\rm src}_{\rm peak}$ and E_γ. The correlation coefficient for these two quantities is 0.94, indicating a stronger correlation than that of $E^{\rm src}_{\rm peak}$ and $E_{\rm iso}$ (see Figure 2.7).

proposed for them:

- There may be a significant amount of dust between the source and the observer, obscuring the optical emission but allowing the x-ray emission to pass through.
- They may lie at high redshifts ($z > 7$), so that their optical emission is redshifted down to a wavelength at which it is susceptible to absorption by intervening hydrogen atoms (so called "Lyman-α" absorption).
- They may come from regions with less material surrounding the burst.

It has been found that dark bursts also tend to have relatively dim x-ray afterglows (about a factor of 5 times less flux on average than those with optical afterglows). This argues against the dust absorption hypothesis, since dust has little effect on x-ray photons. Furthermore, those dark bursts for which redshifts have been measured do not lie at significantly high redshifts [20]. HETE-2 was able to begin prompt optical follow-up of XRF 021211 within 90 seconds of the burst,

and it detected a faint optical afterglow that would have been below the detection threshold if it had been observed any later. This burst would have been characterized as a dark burst if not for the prompt follow-up [19].

Chapter 3

Previous XRF Observations

Over the past 25 years, a number of different missions have observed X-Ray Flashes. In this chapter, we review the results of these observations.

3.1 Einstein

The Einstein observatory, which was launched into orbit in November of 1978, had the distinction of being the first imaging x-ray telescope in space. Among the instruments aboard the observatory was a Wolter Type I grazing incidence telescope sensitive to photons with energies ranging from 0.1 – 4 keV. This instrument included four different detectors, each of which could be rotated into the focal plane: an Imaging Proportional Counter, a High Resolution Imager, a Solid State Spectrometer, and a Focal Plane Crystal Spectrometer. A non-imaging instrument called the Monitor Proportional Counter was co-aligned with the x-ray telescope and was sensitive to photons with energies ranging from 1.5 – 20 keV. An Object Grating Spectrometer, used in conjunction with the High Resolution Imager, rounded out the complement of instruments. The mission ended in April of 1981.

In 1996, Gotthelf et al. conducted a search of the data acquired by the Imaging Proportional Counter to identify fast x-ray transient sources [36]. They were able to detect transients that varied on time scales on the order of 10s of seconds down to a limiting sensitivity of 10^{-11} ergs/cm^2. Their search resulted in 18 candidates (which they named "X-Ray Flashes") that had spectra consistent with the x-ray counterparts of GRBs previously reported. They noted that while these XRFs were not coincident with known GRBs, the instrument was never coincidentally pointed at a known GRB during the lifetime of the mission.

The X-ray flashes identified by this search were distributed isotropically on the sky, consistent with BATSE's results, and in particular, were not preferentially found in the direction of

nearby galaxies. The logarithmic plot of fluence vs. the number of bursts with a fluence greater than that fluence showed a differential slope of -2.5, which the authors speculated could be consistent with either a local or an extragalactic population. The XRFs tended to exhibit rise times shorter than their decay times and lasted anywhere from a few seconds to a few tens of seconds. As such, they were shorter than the prompt x-ray counterparts of GRBs previously reported. The number of events detected in this search implied a rate of about 2×10^6 per year.

3.2 Ginga

Ginga was a Japanese x-ray astronomy mission launched in February of 1987 and lasting until November of 1991. It included three instruments: the Large Area Proportional Counter (LAC), which was sensitive to photons with energies ranging from 1.5 – 37 keV, the All Sky Monitor (ASM) sensitive in the 1 – 20 keV range, and the Gamma-ray Burst Detector (GBD). The primary purpose of the GBD was to investigate the spectra of gamma-ray bursts in the x-ray regime. It consisted of two parts: a proportional counter which was sensitive to 2 – 25 keV photons, and a scintillation counter which was sensitive to 15 – 400 keV photons. The GDB had a field of view of π steradians, or about 1/4 of the sky.

Strohmayer et al. [75] identified 22 bursts that occurred between March of 1987 and October of 1991 for which the instrument measured spectra that could be reliably analyzed. They noted that these bursts resembled BATSE bursts in duration and overall spectral shape (that is, the Band function provided a good fit to the data), but the peak energies $E_{\rm peak}^{\rm obs}$ extended to lower values than those of the BATSE bursts. In the BATSE data set, the $E_{\rm peak}^{\rm obs}$ distribution peaks at about 300 keV and extends down to about 30 keV. Also, $\alpha > 0$ for 15% of the bursts. In the Ginga data set, the $E_{\rm peak}^{\rm obs}$ distribution peaks somewhere below 20 keV and extends down to 2.5 keV (see Figure 3.1), and $\alpha > 0$ for 40% of the bursts. The authors pointed out that the BATSE data set and the Ginga data set both display a correlation between $E_{\rm peak}^{\rm obs}$ and α. They also noted that the low energy emission of the Ginga bursts lasts longer than the high energy emission, suggesting overall spectral softening, as was also seen in BATSE bursts. They suggest

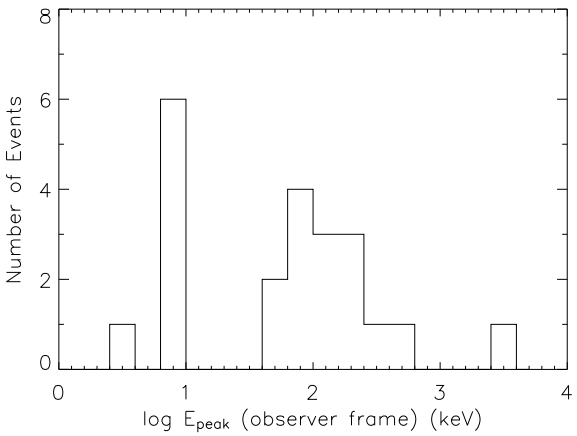

Figure 3.1: $E_{\rm peak}^{\rm obs}$ for Ginga GRBs

that perhaps the differences between the BATSE and Ginga $E_{\rm peak}^{\rm obs}$ and α distributions are simply a selection effect—each mission saw the portion of the burst population to which they were most sensitive.

Although they didn't make a distinction between gamma-ray bursts and x-ray flashes, Strohmayer et al. did define a quantity that they used to characterize the hardness of each burst: the ratio of burst energy in the x-ray band (defined as 2 – 10 keV) to burst energy in BATSE's energy range (50 – 300 keV). Most of the bursts have ratios below about 0.1 (indicating spectrally hard GRBs like those detected by BATSE), but the distribution also extends to higher ratios, even above 1.0 for one burst (see Figure 3.2).

3.3 BeppoSAX

In April of 1996, an Italian-Dutch x-ray observatory called BeppoSAX was launched into orbit. Its complement of instruments covered more than three decades of energy from 0.1 – 300 keV and enabled it to provide arcminute localizations of gamma-ray bursts, permitting follow-up observations at longer wavelengths. The spacecraft carried a set of narrow-field instruments that included 4 x-ray telescopes, each with a Low or Medium Energy Concentrator Spectrometer

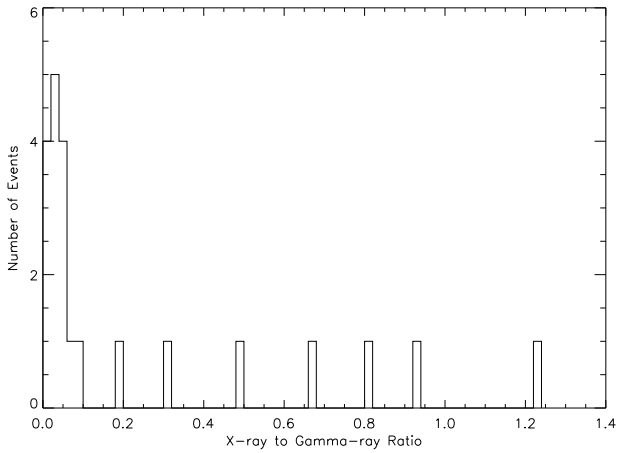

Figure 3.2: Ratio of 2 – 10 keV x-ray energy to 50 – 300 keV gamma-ray energy for Ginga GRBs

(LECS or MECS) sensitive to photons up to 10 keV, a High Pressure Gas Scintillator Proportional Counter (HPGSPC) sensitive to 4 – 120 keV photons, and a Phoswich Detection System (PDS) which covered a range of 15 – 300 keV. In addition, the observatory carried two Wide Field Cameras (WFCs) sensitive to 2 – 30 keV photons. These cameras used a coded aperture imaging system and were mounted perpendicular to the axis of the narrow field instruments and pointed in opposite directions to each other. Each camera had a field-of-view of $20^\circ \times 20^\circ$. These cameras made it possible for scientists on the ground to determine the position of a gamma-ray burst to 2 – 3 arcmin within 4 – 5 hours. Finally, the lateral shields of the PDS served a dual role as the Gamma-Ray Burst Monitor (GRBM) and could detect photons with energies ranging from 60 – 600 keV. The observatory re-entered the Earth's atmosphere in April of 2003.

Heise et al. reported that among the sources imaged by the WFCs was a class of fast x-ray transients with durations less than 1000 s that were not "triggered" (that is, detected) by the GRBM [43]. This became their working definition of x-ray flashes. Seventeen such sources were identified by the authors, who estimated a rate of about 100 per year for such events. Their peak fluxes tended to fall in the range of 10^{-8} – 10^{-7} ergs/cm^2/s and they tended to last anywhere from about 10 seconds to about 200 seconds, similar to the durations of gamma-ray bursts. The spectra of x-ray flashes were generally consistent with a single power law with photon indices

ranging from 3 to 1.2, attenuated by galactic hydrogen absorption. Two of the flashes observed by the BeppoSAX WFCs showed indications of spectral breaks between 30 and 50 keV. Kippen et al. noted that the temporal structure, spectra, and spectral evolution of these flashes were similar to the x-ray properties of gamma-ray bursts.

In some instances, these XRFs were observed simultaneously with BATSE. In these cases, a comparison of the x-ray (2 – 10 keV) fluence (from the WFCs) and the gamma-ray (50 – 300 keV) fluence (from BATSE) revealed that the XRFs tended to exhibit an x-ray/gamma-ray ratio of between 0.2 to 10, with an average value of about 2, whereas gamma-ray bursts had ratios of between 0.004 to about 1, with an average value of about 0.1. Joint spectral analysis with BATSE and BeppoSAX data showed that while these XRFs had significantly lower $E_{\rm peak}^{\rm obs}$ values than GRBs, the distribution of their low-energy photon indices (α) was similar to that of GRBs [50].

3.4 HETE-2

HETE-2 was launched in October 2000 and is still in operation. It has the distinction of being the first satellite dedicated to observing GRBs and is able to localize bursts to anywhere from 10s of arcmin to 10s of arcsec with delay times between about 10 seconds to a few hours. Instruments aboard the observatory give an energy coverage of 2 – 400 keV. These include the French Gamma Telescope (FREGATE), which is a cleaved NaI crystal read out by a photomultiplier tube and guarded by a graded-z shield. The FREGATE has a field of view of 3 steradians and is sensitive to photons with energies between 6 and 400 keV. It triggers on gamma-ray bursts, alerting the community to their detection. HETE-2 also carries a Wide-field X-ray Monitor (WXM) that consists of two units, each with a 1-dimensional position sensitive proportional counter and coded aperture mask. The two units are oriented perpendicular to each other, are sensitive to 2 – 25 keV photons, and provide burst positions to 10 arcmin. The final instrument aboard HETE-2 is the Soft X-ray Camera (SXC), which consists of X-ray CCDs and a fine coded aperture mask. SXC has an energy range of 2 – 14 keV and a field of view of 0.9 sr.

Sakamoto et al. [70] studied the properties of x-ray flashes detected and measured by HETE-

2. For their analysis, they distinguished between gamma-ray bursts (GRBs), x-ray rich gamma-ray bursts (XRRs) and x-ray flashes (XRFs) using the fluence ratio $S_X(2-30\text{ keV})/S_\gamma(30-400\text{ keV})$:

$$\begin{aligned} \log[S_X(2-30\text{ keV})/S_\gamma(30-400\text{ keV})] &\leq -0.5 && \text{GRB} \\ -0.5 < \log[S_X(2-30\text{ keV})/S_\gamma(30-400\text{ keV})] &\leq 0 && \text{XRR} \\ \log[S_X(2-30\text{ keV})/S_\gamma(30-400\text{ keV})] &> 0 && \text{XRF} \end{aligned} \tag{3.1}$$

They selected bursts that were recorded between January 2001 and September 2003 by both the WXM and FREGATE which were sufficiently bright to provide adequate statistics for spectral analysis. Forty-five events met these criteria.

33% of the bursts they identified qualified as XRFs. All of the events (GRBs, XRRs, and XRFs) showed a positive correlation between S(2-30 keV) and S(30-400 keV), indicating that when x-rays were prominent, so were γ-rays. The distribution of low-energy photon indices α for XRFs did not differ significantly from that of GRBs, but $E_{\text{peak}}^{\text{obs}}$ tended to be lower for XRFs than for GRBs (~ 25 keV or smaller for XRFs and 150 keV on average for GRBs). No correlation between α and $E_{\text{peak}}^{\text{obs}}$ was seen. The overall distribution of $E_{\text{peak}}^{\text{obs}}$ values was consistent with that of BATSE, with an excess at low energies and a deficit at high energies, resulting from the different sensitivities of the instruments. A plot of the number of XRFs detected vs. XRF brightness was consistent with a homogenous distribution in space, indicating that XRFs may tend to lie at lower redshifts ($z \leq 0.2$) than GRBs. The number of XRFs detected was consistent with a rate of about 160 per year.

3.5 XRF Afterglow Observations

Until the launch of Swift, only a handful of afterglows associated with x-ray flashes were reported. Here we review those events for which relatively good measurements were made.

3.5.1 XRF 011030

The first x-ray flash for which an afterglow was reported was XRF 011030. It was detected and observed by BeppoSAX [31, 44], and its afterglow was identified with the Chandra x-ray

observatory [41].

The prompt emission lasted 1400 s (longer than most GRBs) and had a spectrum characterized by a photon index of 1.9 ± 0.1. $E_{\rm peak}^{\rm obs}$ was constrained to less than 40 keV. The measured 2 – 28 keV fluence was 9×10^{-7} ergs/cm^2, and the measured peak flux was 8.3×10^{-9} ergs/cm^2/s in the same energy range [44]. These spectral parameters fit nicely within the usual range for GRBs.

The x-ray afterglow was first detected by Chandra 29 days after the burst. Its spectrum was found to be consistent with a power law with a photon index of about 1.45 (which is within the norm for GRBs), attenuated by a hydrogen column density consistent with galactic values. Its intensity was measured to be 2.4×10^{-13} ergs/cm^2/s in the 2 – 10 keV band 29 days after the burst [41]. Its flux was found to be decreasing over time at a rate consistent with a power law decay index of about -2.00 [28]. Extrapolating this decay back in time to the time of the burst yields an intensity consistent with that of the prompt emission. This index is a bit steeper than most GRB decay indices. The redshift of this burst was constrained to be < 3 based on the probable host galaxy, which was faint and blue, similar to most GRB host galaxies [28].

3.5.2 XRF 020427

XRF 020427 was detected and observed by BeppoSAX, which also identified and measured its afterglow. Chandra provided additional follow-up observations of the afterglow, making possible the measurement of the decay rate [2].

The prompt emission consisted of two peaks with a total duration of about 60 s. The spectrum was consistent with a power law photon index of $2.09^{+0.23}_{-0.21}$ with an attenuating hydrogen column density consistent with galactic values. By fixing α at 1, $E_{\rm peak}^{\rm obs}$ was constrained to be less than 5.5 keV. The 2 – 28 keV fluence and peak flux were $(5.8 \pm 0.4) \times 10^{-7}$ ergs/cm^2 and $(3.0 \pm 0.4) \times 10^{-8}$ ergs/cm^2/s, respectively, both of which are similar to those of BeppoSAX GRBs.

The first measurement of the afterglow from XRF 020427 was made by BeppoSAX approximately 8 hours after the burst. Assuming a galactic column density, the afterglow photon index was found to be $2.0^{+2.2}_{-1.1}$. Chandra measured a photon index of $1.5^{+0.5}_{-0.5}$ about 9 days later. Both

measurements are consistent with the spectrum of the second pulse of the prompt emission, which exhibited a photon index of $2.22^{+0.31}_{-0.25}$. The time decay index was found to be $-1.30^{+0.09}_{+0.10}$, which extrapolates back to the second pulse of the prompt emission. The intensity, spectrum, and decay are all consistent with normal GRBs [27].

Bloom et al. [13] were able to constrain the redshift of this burst to $z < 2.3$ based on the spectrum of the host galaxy. If the redshift is less than 0.1 or 0.2, then the $E_{\rm iso}$ and $E^{\rm src}_{\rm peak}$ of the burst satisfy the Amati relation quite nicely.

3.5.3 XRF 020903

XRF 020903 was detected and observed by HETE-2. It was the first x-ray flash for which a definitive redshift was measured. The duration of the prompt emission was about 10 seconds. Its spectrum was consistent with a photon index of $-2.4^{+0.5}_{-0.6}$ with a galactic hydrogen column density. $E^{\rm obs}_{\rm peak}$ was constrained to $2.4^{+1.2}_{-0.7}$ keV. The 2 – 10 keV fluence and peak flux were $(5.9 \pm 1.4) \times 10^{-8}$ ergs/cm^2 and $(14.7 \pm 5.3) \times 10^{-9}$ ergs/cm^2/s, respectively [69]. An x-ray afterglow was not found, but an optical afterglow was detected during measurements that began about 21 hours after the burst [73]. The afterglow was found to have a decay index of about 1. A redshift of 0.236 was measured for the host galaxy. At this redshift, the calculated $E^{\rm src}_{\rm peak}$ and $E_{\rm iso}$ are consistent with the Amati relation.

3.5.4 XRR 030723

XRR 030723 was detected and observed by HETE-2 on 23 July 2003, with x-ray afterglow measurements made two days later using Chandra observations. Although some observers classified it as an x-ray flash, by the working definition used by the HETE-2 team, it technically qualified as an x-ray rich gamma ray burst with $\log[S_X(2 - 30 \text{ keV})/S_\gamma(30 - 400 \text{ keV})] = 0.9$. It was the first XRF (or borderline XRF) for which a joint study of prompt and x-ray afterglow emission was presented [16].

The duration of the prompt emission was approximately 23 s [65]. The spectrum was consistent with a power law with photon index of $1.93^{+0.17}_{-0.15}$. It was not possible to constrain the

value of $E_{\rm peak}^{\rm obs}$. The total fluence of the burst (2 – 30 keV) was 2.4×10^{-7} ergs/cm^2 [70], and the peak flux (7 – 30 keV) was $> 3 \times 10^{-8}$ ergs/cm^2/s [65].

The afterglow was first detected in the optical wavelengths 24 hours after the burst, followed by an x-ray detection 51 hours after the burst. The x-ray afterglow spectrum was well fit by a power law with a photon index of 1.9 ± 0.3 and a hydrogen absorption column density consistent with galactic values [70]. Between 51.4 and 59 hours after the burst, the average x-ray flux was $(2.2 \pm 0.3) \times 10^{-14}$ ergs/cm^2/s in the 0.5 – 0.8 keV band. The afterglow decayed with a power law index of 1.0 ± 0.1. At optical frequencies, the afterglow decayed with an index of about 0.9 until about 30 – 50 hours after the burst, after which time, its decay steepened to an index of about 2 [16]. The optical afterglow showed signs of rebrightening at 7 days after the burst [29]. Fynbo et al. were able constrain the redshift to < 2.3 [30].

3.5.5 XRF 040701

Another HETE-detected x-ray flash for which an afterglow was measured was XRF 040701. Follow-up observations with Chandra detected the x-ray afterglow 8 days later [25]. The prompt emission lasted roughly 60 s, with a spectrum consistent with a power law of photon index 2.394 ± 0.3. The total fluence was reported to be $(4.5 \pm 0.8) \times 10^{-7}$ ergs/cm^2 [6]. The afterglow was found to decay with a power law index of ~ 1 [25]. A redshift of 0.2146 was found from the host galaxy [49].

Table 3.1: Prompt emission properties of XRFs detected prior to Swift's launch

	Prompt Emission			
	Duration	Photon Index	$E_{\rm peak}^{\rm obs}$	Fluence (ergs/cm^2)
XRF 011030	1400 s	1.9 ± 0.1	< 40 keV	9×10^{-7} (2 – 28 keV)
XRF 020427	60 s	$2.09^{+0.23}_{-0.21}$	< 5.5 keV	$(5.8 \pm 0.4) \times 10^{-7}$ (2 – 28 keV)
XRF 020903	10 s	$2.4^{+0.6}_{-0.5}$	$2.4^{+1.2}_{-0.7}$ keV	$(5.9 \pm 1.4) \times 10^{-8}$ (2 – 10 keV)
XRF 030723	23 s	$1.93^{+0.17}_{-0.15}$	unconstrained	2.4×10^{-7} (2 – 30 keV)
XRF 040701	60 s	2.395 ± 0.3	unconstrained	$(4.5 \pm 0.8) \times 10^{-7}$ (2 – 25 keV)
Mean GRB values	50^{+550}_{-48} s	1.5 to 4 (β)	30 keV to 1.5 MeV	10^{-4} to 10^{-8} (50 – 300 keV)

Table 3.2: Afterglow emission properties and redshifts of XRFs detected prior to Swift's launch

	Afterglow Emission			Redshift
	First Observation	Photon Index	Decay Index	
XRF 011030	T + 29 days	~ 1.45	2	< 3
XRF 020427	T + 8 hours	1.5 ± 0.5	$1.30^{+0.10}_{-.09}$	< 2.3
XRF 020903	T + 21 hours	unknown	~ 1	0.236
XRF 030723	T + 24 hours	1.9 ± 0.3	1.0 ± 0.1	< 2.3
XRF 040701	T + 8 days	unknown	~ 1	0.2146
Mean GRB values		1.95 ± 0.4	1.30 ± 0.35	0.0085 to 4.5

Chapter 4

Gamma-Ray Burst Theory

4.1 The Prompt Emission

Those who study gamma-ray bursts often refer to the gamma-ray burst itself as the "prompt emission" (as opposed to the "afterglow emission" that starts later and lasts longer). The characteristics of the GRB prompt emission place some stringent constraints on GRB models. As already noted, whatever produces these bursts must be capable of generating an enormous output of gamma-ray energy ($\sim 10^{51}$ ergs or so) in a matter of seconds. Another important condition is "compactness". The duration of the individual peaks in the gamma-ray emission place an upper limit on the size of the emission region. This size must be equal to or smaller than the distance that a photon could travel in the duration of the burst peak, $c \cdot \delta t$. For a peak with a duration of 1 ms (as is sometimes observed), the emitting region must be no larger than 300 km in size.

A third requirement from observation has to do with "optical thickness" (also sometimes called "optical depth") τ. The optical thickness of a region is a measurement of how likely it is that a photon might be able to pass through that region without being absorbed or scattered. A region's optical width is defined as the thickness of the region divided by the average distance a photon can travel within that region before it gets absorbed or scattered. Thus the optical thickness of a region could be described as its thickness in units of "average photon distances". If $\tau = 3$ for a particular region, then the region is three times as wide as the average distance a photon would be able to travel before being absorbed or scattered. So usually a good dividing point between a region that is "optically thick" and one that is "optically thin" is about $\tau = 1$. Since photons of different energy have different probabilities of being absorbed or scattered, the optical thickness of a region will depend on the energy of the photons.

As we've seen, the emission region of a gamma-ray burst must be very compact. As a

result, the gamma-ray photon density must be very high (considering the number of photons that are emitted). At such a density, we would expect many photons to annihilate each other, creating electron-positron pairs in their place. This would radically reduce the number of photons above 511 keV (source frame energy). This reduction isn't observed, though. The best explanation is that the emitting material is moving at relativistic speeds. At such speeds, "relativistic beaming" would take place (that is, all of the photons would be emitted in the direction of motion within a narrow beam), so that the angle between emitted photons (in the observer reference frame) would be much smaller and the probability of pair production much lower. In order for the pair production to be suppressed to the extent that measurements demand (the pair production optical depth $\tau_{\pm}$ must be $\lesssim 1$ for photons of energy ~ 100 MeV), the Lorentz factor Γ (pronounced "Gamma") of the emitting material must be > 100. The Lorentz factor Γ is given by

$$\Gamma = \frac{1}{\sqrt{1 - v^2/c^2}}, \tag{4.1}$$

where v is the speed of the material and c is the speed of light. As v gets closer and closer to c, Γ gets larger and larger. A Γ greater than 100 means that the material must be traveling in excess of 0.99995 times the speed of light.

4.1.1 The Fireball Model

One model that satisfies most of these requirements is the so-called "fireball" model. The fireball model has become the "standard" model for gamma-ray burst emission. The treatment presented here follows the review given by Piran [63].

In the fireball model, a compact, hidden "inner engine" of some kind produces a relativistic "fireball"—a plasma of electrons, photons, and a small concentration of baryons (such as protons and neutrons)—that propagates outward. This fireball is believed to be made up of a series of "shells", each having its own well-defined thickness. The number of shells may vary from burst to burst. In some variations of the model, a Poynting flux is also involved. These shells undergo two distinct phases: an initial energy-dominated phase and a later matter-dominated phase. During the energy-dominated phase, the photon concentration in the shells is extremely high, resulting

in a pair-production optical thickness $\tau_{\pm}$ that is much greater than 1, so that radiation cannot escape. Under these conditions, the plasma can be termed a "photosphere". Unable to release any of their internal energy in the form of radiation, the plasma shells cool adiabatically as they expand, causing them to accelerate to ultrarelativistic speeds. During this phase, the Temperature (T) and Lorentz factor Γ of the shells change as the radius(R) increases according to the following relationships:

$$T \propto R^{-1}, \qquad \Gamma \propto R. \tag{4.2}$$

Throughout this phase, the thickness of the shells remains constant (in the observer frame).

Throughout this expansion and acceleration, the internal energy of the plasma (mostly in the form of photons that are continually being converted into and from electron-positron pairs) is converted into bulk kinetic energy, mostly carried by the more massive (though relatively few) baryons. At some point, the majority of the energy of the fireball is kinetic, and Γ becomes constant with time, settling at a value of approximately E/mc^2 (where E is the energy of the fireball and m is the mass of the baryons within the fireball, which make up most of its mass), so that the fireball begins to coast along at a constant speed. This marks the beginning of the matter-dominated phase. This transition typically occurs at a radius of about 10^9cm, or about one and a half times the radius of the earth. As the fireball shells coast along, variations in Γ cause them to expand, and the thicknesses of the shells begin to grow linearly with their radii.

At some point, the fireball cools sufficiently that the plasma becomes optically thin. The radius at which this takes place is known as the "photospheric radius". The presence of the small concentration of baryons delays this transition until after the fireball has become matter-dominated. This radiation phase begins at a radius $R_{\text{rad phase}}$ of about

$$R_{\text{rad phase}} = 6 \cdot 10^{13}\text{cm}\sqrt{\frac{E}{10^{52}\text{ergs}}}\left(\frac{\eta}{100}\right)^{-1}, \tag{4.3}$$

where E is the energy of the fireball, and η is the ratio of energy to baryon mass (E/mc^2). After this point, any radiation that exists or is generated inside the fireball freely escapes.

The presence of baryons serves a crucial role in the fireball model. Without them, the plasma would become optically thin much earlier (at a radius of typically 10^{10}cm instead of 10^{14}cm). The

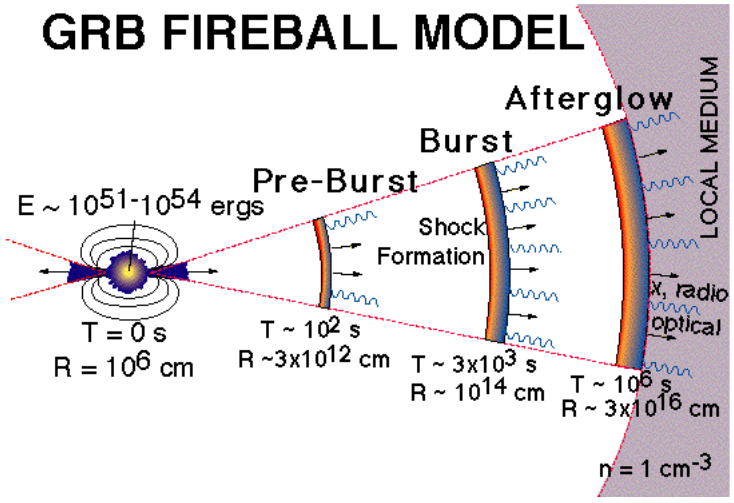

Figure 4.1: The fireball and the internal/external shock scenario [33]. At a time T=0, the "internal engine" emits a series of plasma shells which begin to expand outward. When the shells reach a radius of about 10^{14}cm, they begin colliding with one another, resulting in the prompt emission of the gamma-ray burst. At a radius of about 3×10^{16}cm, they begin to slow down as they interact with material in space. As they slow down, they radiate at x-ray and other wavelengths, giving rise to the afterglow.

plasma would not become matter-dominated, and the radiation emitted would have a "thermal" spectrum, which looks different from the actual spectrum we observe from gamma-ray bursts. If, on the other hand, the concentration of baryons were too large, the plasma would not be able to achieve the ultrarelativistic speeds that we have shown are a necessary condition for generating gamma-ray bursts. This is because when the fireball becomes matter-dominated, with its internal energy entirely converted into kinetic energy, this kinetic is proportional to both the baryon mass m and the Lorentz factor Γ. For a fixed kinetic energy, a greater mass m results in a smaller Lorentz factor Γ. So the model requires that some baryons be present, but not too many.

4.1.2 Internal Shocks

For reasons that are not well understood, the internal engines of some bursts apparently emit many shells while others emit few. If there are multiple shells, each with a slightly different Lorentz factor Γ, faster shells will overtake slower shells and collide with them, producing "internal shocks" that propagate forward into the slower shell and backward into the faster shell. These shocks

facilitate the conversion of some of the kinetic energy into radiation. They are designated "internal" because they result from interactions between different shells within the fireball, as opposed to "external shocks" which result from interactions between these shells and the local environment and give rise to the afterglow emission, as we will discuss in the next section. Each collision results in an observed peak in the gamma-ray burst light curve with a duration t determined by the thickness w of the shells involved. The duration of the entire burst is determined by the width of the entire complex of shells, W. The variability of the "inner engine" determines the number of shells and their widths, and hence the number and widths of the burst peaks. In every other way, the inner engine is completely hidden from direct observation. The radius at which the GRB emission occurs is

$$R_{\rm prompt} \approx 10^{14}{\rm cm} \left(\frac{\Delta R}{10^{10}{\rm cm}}\right) \left(\frac{\Gamma}{100}\right), \tag{4.4}$$

where ΔR is the initial separation between the shells in the observer's reference frame, and Γ is the Lorentz factor of the inner shell (assumed to be slightly larger but on the same order as that of the outer shell). The typical radius of 10^{14} cm is a littler larger than the radius of the orbit of Jupiter. In order to explain gamma-ray bursts, the Lorentz factors of these shells must be large enough to limit the optical depth due to pair production, yet small enough to produce the short durations and short timescale variability that we observe:

$$570 \left(\frac{\zeta}{0.01}\right)^{-\frac{1}{4}} \left(\frac{T}{10{\rm s}}\right)^{-\frac{1}{4}} \leq \Gamma \leq 2800 \left(\frac{\zeta}{0.01}\right)^{-\frac{1}{2}} \left(\frac{T}{10{\rm s}}\right)^{-\frac{3}{8}} \left(\frac{l}{10^{18}{\rm cm}^2}\right)^{\frac{3}{8}}, \tag{4.5}$$

where $\zeta = T/\Delta T$, T is the total duration of the burst, ΔT is the typical duration of the individual peaks in the burst, and l is a constant known as the Sedov length which depends on the energy of the burst and the density of the interstellar medium. These constraints on Γ in turn constrain the radius at which the GRB can be produced by an internal shock:

$$10^{15}{\rm cm} \left(\frac{\zeta}{0.01}\right)^{\frac{1}{2}} \left(\frac{T}{10{\rm s}}\right)^{\frac{1}{2}} \leq R_{\rm prompt} \leq 2.5 \cdot 10^{16}{\rm cm} \left(\frac{T}{10{\rm s}}\right)^{\frac{1}{4}} \left(\frac{l}{10^{18}{\rm cm}^2}\right)^{\frac{3}{4}}. \tag{4.6}$$

The amount of energy converted to radiation by the forward shock and the reverse shock are comparable to each other. The most likely conversion process is synchrotron emission, whereby a relativistic electron interacts with a magnetic field and emits radiation of a characteristic frequency.

The photon energy of typical synchrotron photons resulting from an internal shock $E_{\rm internal}$ (in the observer's reference frame) is

$$E_{\rm internal} = \frac{\hbar q_e B}{m_e c}\Gamma_e^2\Gamma, \tag{4.7}$$

where q_e is the charge of an electron, B is the strength of the magnetic field, m_e is the mass of an electron, Γ_e is the Lorentz factor of the shocked electron, Γ is the Lorentz factor of the shell through which the shock is propagating, $\hbar$ is Dirac's constant, and c is the speed of light. For typical values of these variables, Einternal is about 200 keV, which is consistent with the magnitude of $E_{\rm peak}^{\rm obs}$ values observed in gamma-ray burst spectra. This internal shock process is capable of converting about $2-20\%$ of the kinetic energy of the fireball into radiation.

4.2 The Afterglow Emission and External Shocks

As we mentioned in the last section, "external" shocks result when the relativistic outflow of the fireball interacts with surrounding material (either a solar wind generated by the burst progenitor or interstellar material). These shocks form later than the internal shocks and are the most likely cause of the afterglow emission. They generate emission with very little variability on short timescales. In this section, I follow the derivation described by Sari et al. [71].

As with internal shocks, the most likely radiation mechanism is synchrotron emission. As given in Equation 4.7, the frequency at which a relativistic electron interacting with a magnetic field emits energy is given by

$$\nu(\Gamma_e) = \Gamma\Gamma_e^2\frac{q_e B}{2\pi m_e c}. \tag{4.8}$$

The individual Lorentz factors of the electrons in the plasma (Γ_e) are assumed to follow a power law distribution, down to some minimum Lorentz factor Γ_m:

$$n(\Gamma_e) \propto \Gamma_e^{-p}, \qquad \Gamma_e \geq \Gamma_m, \tag{4.9}$$

where $n(\Gamma_e)$ is the number of electrons with a Lorentz factor of Γ_e and p is a constant known as the "electron power law index". In addition to Γ_m, there is another value of Γ_e that is significant: a

critical value below which the electron begins to lose a significant fraction of its energy to radiation:

$$\Gamma_c = \frac{6\pi m_e c}{\sigma_T \Gamma B^2 t}, \tag{4.10}$$

where σ_T is the Thompson cross-section and t is the time in the observer's reference frame. There are two possible scenarios, each with its own predicted spectrum:

1. $\Gamma_m > \Gamma_c$. In this situation, all of the electrons cool down to Γ_c. This is known as the "fast-cooling" regime. The flux in this regime at different frequencies ν is given by

$$F_\nu = \begin{cases} (\nu/\nu_m)^{1/3} F_{\nu,\max}, & \nu_c > \nu, \\ (\nu/\nu_m)^{-1/2} F_{\nu,\max}, & \nu_m > \nu > \nu_c, \\ (\nu_m/\nu_c)^{-1/2} (\nu/\nu_m)^{-p/2} F_{\nu,\max}, & \nu > \nu_m, \end{cases} \tag{4.11}$$

   where $\nu_c \equiv \nu(\Gamma_c)$ and $\nu_m \equiv \nu(\Gamma_m)$ (see Figure 4.2. ν_c and ν_m are spectral break frequencies, at which the power law index of the spectrum suddenly changes. This spectrum is expected at early times, during the first few days following the burst.

2. $\Gamma_m < \Gamma_c$. In this case, only those electrons with $\Gamma > \Gamma_c$ can cool. This is known as the "slow-cooling" regime. The flux in this regime is given by

$$F_\nu = \begin{cases} (\nu/\nu_m)^{1/3} F_{\nu,\max}, & \nu_m > \nu, \\ (\nu/\nu_m)^{-(p-1)/2} F_{\nu,\max}, & \nu_c > \nu > \nu_m, \\ (\nu_m/\nu_c)^{-(p-1)/2} (\nu/\nu_c)^{-p/2} F_{\nu,\max}, & \nu > \nu_c. \end{cases} \tag{4.12}$$

   (see Figure 4.2. This condition is expected at late times—weeks or months after the burst.

The time-dependence of the flux depends on how these break frequencies (ν_m and ν_c) evolve with time. There are two limiting cases:

1. fully radiative evolution, in which all of the internal energy of the fireball is radiated away (this is the case if the fraction of internal energy going to electrons is very large, and if fast cooling is taking place),

2. fully adiabatic evolution, in which the internal energy of the fireball remains constant.

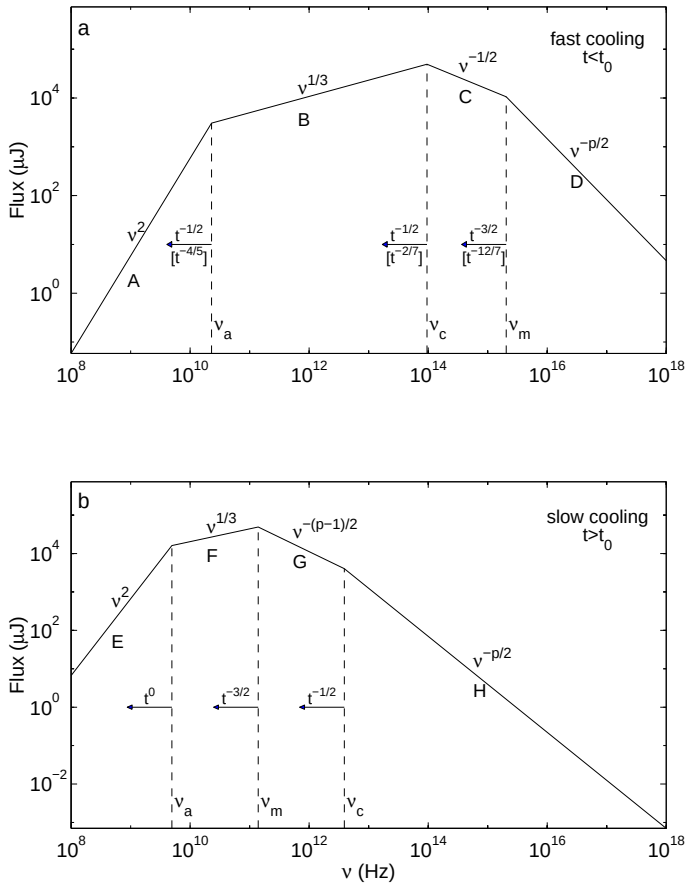

Figure 4.2: Synchrotron spectrum from a relativistic shock with a power law distribution of electrons. (a) The case of fast cooling, which is expected at early times ($t < t_0$) in a γ-ray burst afterglow. t_0 is the transition time between fast and slow cooling and occurs when $\nu_c = \nu_m$. The spectrum consists of four segments, identified as A, B, C, D. Self-absorption is important below ν_a. The frequencies, ν_m, ν_c, ν_a, decrease with time as indicated; the scalings above the arrows correspond to an adiabatic evolution, and the scalings below, in square brackets, to a fully radiative evolution. (b) The case of slow cooling, which is expected at late times ($t > t_0$). The evolution is always adiabatic. The four segments are identified as E, F, G, H. [71]

In the fully radiative case, the break frequencies and peak flux evolve according to

$$\begin{aligned}
\nu_c &= 1.3 \times 10^{13}\, \epsilon_B^{-3/2} E_{52}^{-4/7} \Gamma_2^{4/7} n_1^{-13/14} t_d^{-2/7} \text{ Hz}, \\
\nu_m &= 1.2 \times 10^{14}\, \epsilon_B^{1/2} \epsilon_e^2 E_{52}^{4/7} \Gamma_2^{-4/7} n_1^{-1/14} t_d^{-12/7} \text{ Hz}, \\
F_{\nu,\max} &= 4.5 \times 10^3 \epsilon_B^{1/2} E_{52}^{8/7} \Gamma_2^{-8/7} n_1^{5/14} D_{28}^{-2} t_d^{-3/7}\, \mu\text{Jy}.
\end{aligned} \tag{4.13}$$

where ϵ_B is the fraction of the shock energy density that is in the form of magnetic energy, ϵ_e is the fraction of internal energy which is carried by the electrons, $n_1 \equiv n/(1\text{cm}^{-3})$ is the density of electrons in the interstellar medium, $t_d \equiv r/(1\text{day})$ is the number of days since the burst, and $D_{28} \equiv D/(10^{28} cm)$ is the luminosity distance between the burst and us. In the fully adiabatic case, the break frequencies and peak flux evolve according to

$$\begin{aligned}
\nu_c &= 2.7 \times 10^{12} \epsilon_B^{-3/2} E_{52}^{-1/2} \Gamma_2^{4/7} n_1^{-1} t_d^{-1/2} \text{ Hz}, \\
\nu_m &= 5.7 \times 10^{14} \epsilon_B^{1/2} \epsilon_e^2 E_{52}^{1/2} t_d^{-3/2} \text{ Hz}, \\
F_{\nu,\max} &= 1.1 \times 10^5 \epsilon_B^{1/2} E_{52} n_1^{1/2} D_{28}^{-2}\, \mu\text{Jy}.
\end{aligned} \tag{4.14}$$

The flux at a given frequency decreases with time according to a simple power law, with two frequency-dependent breaks at which the index of the power law changes (see Figure 4.3):

$$t_c = \begin{cases} 7.3 \times 10^{-6}\, \epsilon_B^{-3} E_{52}^{-1} n_1^{-2} \nu_{15}^{-2} \text{ days}, & \text{adiabatic}, \\ 2.7 \times 10^{-7}\, \epsilon_B^{-21/4} E_{52}^{-2} \Gamma_2^2 n_1^{-13/4} \nu_{15}^{-2/3} \text{ days}, & \text{radiative}, \end{cases} \tag{4.15}$$

$$t_m = \begin{cases} 0.69\, \epsilon_B^{1/3} \epsilon_e^{4/3} E_{52}^{1/3} \nu_{15}^{-2/3} \text{ days}, & \text{adiabatic}, \\ 0.29\, \epsilon_B^{7/24} \epsilon_e^{7/6} E_{52}^{1/3} \Gamma_2^{-1/3} n_1^{-1/24} \nu_{15}^{-7/12} \text{ days}, & \text{radiative}. \end{cases} \tag{4.16}$$

At sufficiently late times and at all frequencies, the light curve decreases as $t^{(2-3p)/4}$, which, for a typical value of $p = 2.5$, becomes $t^{-1.4}$.

4.3 Models for the "Inner Engine"

So far, we've described the physics and dynamics of the relativistic fireball emanating from the hypothetical "inner engine". Here we address the question of what the inner engine might be. Observations give us a few clues:

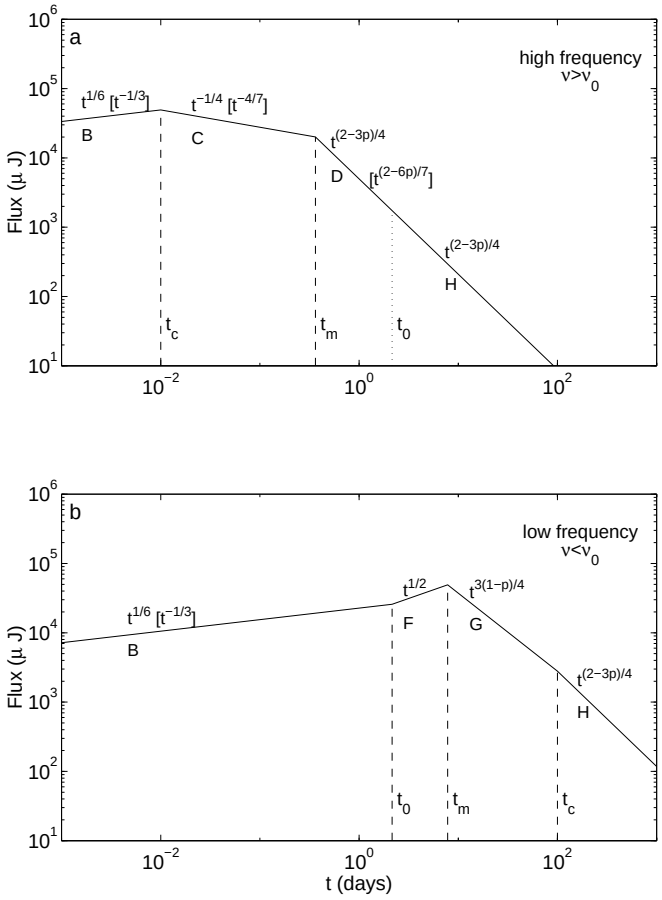

Figure 4.3: Light curve due to synchrotron radiation from a spherical relativistic shock. (a) The high frequency case ($\nu > \nu_0$). The light curve has four segments, separated by the critical times, t_c, t_m, t_0. The labels, B, C, D, H, indicate the correspondence with spectral segments in Fig. 1. The observed flux varies with time as indicated; the scalings within square brackets are for radiative evolution (which is restricted to $t < t_0$) and the other scalings are for adiabatic evolution. (b) The low frequency case ($\nu < \nu_0$). [71]

- The inner engine must be a compact source in order to produce the observed variability.
- Long gamma-ray bursts (at least) typically seem to occur in regions rich in star formation.
- The rate of gamma-ray bursts is consistent with about 1 burst per 10^6 years per galaxy, if the energy is emitted isotropically. We know that the energy is actually collimated into narrow beams, increasing this rate by a factor of $(4\pi/\theta^2)$.
- The amount of energy produced is around 10^{51} ergs.
- If we assume that the fireball model is indeed correct, it requires that $\approx 10^{-5}$ solar masses of material be accelerated to relativistic energies.
- The internal shock model further requires a variable energy flow from the engine.

Models that satisfy these requirements all involve the formation of a compact object (like a black hole) and the release of its binding energy. Here we discuss the two most prominent candidates.

4.3.1 Collapsars

A "Collapsar" is a rotating massive star whose center collapses into a black hole surrounded by an accretion disk. In order for the collapsar to meet the compactness requirement discussed in section 4.1, it must lose its hydrogen envelope prior to its collapse. Material accreting from the disk onto the black hole would produce the relativistic outflow along the axis of rotation. This outflow would then pass through the rotating stellar mantle (which would further collimate it) and then give rise to the GRB. The observed variability could arise from instabilities that result during the interaction between the outflow and the stellar envelope.

This particular inner engine model has a number of advantages:

1. It is expected to produce a strongly collimated beam, which we indeed observe.
2. It would naturally occur in star-forming regions.
3. A good mechanism exists for the high variability we see in gamma-ray bursts.

4. Numerical simulations indicate that the time scale of the collapse is on the order of tens of seconds. This would be consistent with the durations of the long class of GRBs, but it is hard to reconcile with the durations of short GRBs.

4.3.2 Compact Mergers

Another prominent model for the inner engine involves two compact objects (for example, two neutron stars, or a neutron star and a black hole) in a binary orbit. Over time (10^8 years or so) the objects gradually lose energy to gravitational radiation causing their orbits to decay until they eventually spiral in and merge, resulting in a rotating black hole. Models predict that this merging event would release about 5×10^{53} ergs of energy, mostly in the form of gravitational energy and neutrinos. Enough energy would be left over, though, to power a gamma-ray burst.

A neutron star binary system would have a long enough lifetime to allow it to wander far from the environment of the supernova that created its constituents, even far enough that it could end up outside of its host galaxy. A burst created by a merger would likely not be well-collimated. Simulations indicate that the time scales of the event would be smaller than those of long-duration gamma-ray bursts, but it may be a viable model for short GRBs [48].

4.4 X-Ray Flash Models

Several models have been proposed to explain what circumstances give rise to x-ray flashes as opposed to gamma-ray bursts. We may classify these models broadly into two categories: geometric and intrinsic. Those that suggest that GRBs and XRFs arise from different physical processes we shall call "intrinsic" models. Those that propose that GRBs and XRFs appear different to us only because of our particular location or orientation in relation to them we shall call "geometric" models. We'll begin by describing the most prominent geometric models.

4.4.1 Models Based on Geometric Effects

Off-Jet Model

Yamazaki et al. have proposed that x-ray flashes are gamma-ray bursts viewed from an angle outside the emission jet [81] (see Figure 4.4). Thus, an x-ray flash is an "off-jet" gamma-ray burst. According to their predictions, the peak energy in the co-moving frame of the ejected material E_0 is reduced by a factor of δ when viewed from an angle θ_v with respect to the jet axis by an observer in the frame of the burst progenitor:

$$E_{\rm peak}^{\rm src} = \frac{E_0}{\Gamma(1-\beta\cos(\theta_v - \Delta\theta))}, \tag{4.17}$$

where Γ is the Lorentz factor of the ultrarelativistic outflow, β is the speed of the outflow divided by the speed of light (v/c), and $\Delta\theta$ is the jet opening half-angle. The denominator in Equation 4.17 is a quantity known as the "relativistic Doppler factor" δ. In this model, an observer within the jet would see a peak energy $E_{\rm peak}^{\rm obs}$ of:

$$E_{\rm peak}^{\rm src} = \frac{E_0}{\Gamma(1-\beta)}, \tag{4.18}$$

so that the relationship between $E_{\rm peak}^{\rm src}$ as seen from off the jet and $E_{\rm peak,in\ jet}^{\rm src}$ as seen from within the jet is

$$\begin{aligned} E_{\rm peak}^{\rm src} &= E_{\rm peak,in\ jet}^{\rm src}\frac{1-\beta}{1-\beta\cos(\theta_v - \Delta\theta)} \\ &\approx \frac{E_{\rm peak,in\ jet}^{\rm src}}{1+\Gamma^2(\theta_v - \Delta\theta)^2}. \end{aligned} \tag{4.19}$$

Thus, a gamma-ray burst with an $E_{\rm peak}^{\rm src}$ of 300 keV, a typical Γ of ~ 300 would appear as an x-ray flash with an $E_{\rm peak}^{\rm obs}$ of 20 keV if viewed from just slightly outside the jet at $\theta_v - \Delta\theta = 0.7^\circ$.

Also according to this model, the peak fluence S is reduced by a factor of δ^3 (see Figure 4.5):

$$S = \frac{S_0}{\delta^3}. \tag{4.20}$$

With the off-jet model, it is possible to calculate a number of different measurable quantities and compare them to observation. The model predicts peak XRF fluxes that range from about

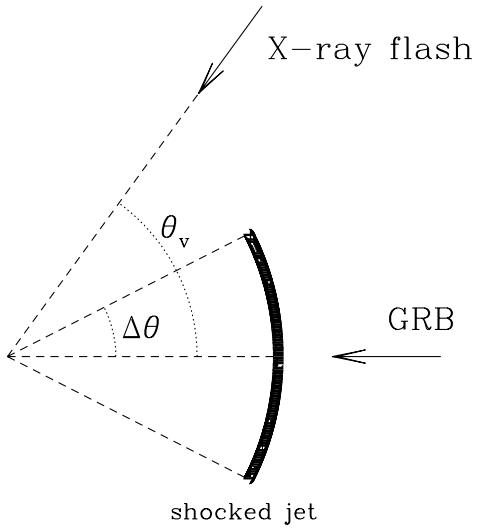

Figure 4.4: A drawing illustrating the off-jet model for x-ray flashes. In this model, it is proposed that x-ray flashes are typical GRBs observed from outside the jet [81].

10^{-8} to 10^{-7} ergs/s/cm^2. The x-ray to gamma ray fluence ratio S(2 – 10 keV)/S(50 – 300 keV) predicted by the model extends up to 20 and the peak flux ratio corresponding to the same energy bands extends up to 100. The 2 – 25 keV spectrum is consistent with a power law with a photon index ranging from 1.2 to 3, with a mean of ≈ 2. The duration of XRFs is predicted to be roughly the same as for GRBs: between about 10 s and about 200 s. The predicted event rate is ~ 100/yr, and the sky distribution is expected to be isotropic. All of these predictions agree with observation.

Because the fluence of the emission from outside the jet is many orders of magnitude lower than the emission from inside the jet, XRFs as a population would be dimmer than GRBs and therefore would not be visible at such high redshifts. We would therefore expect those XRFs we detect to lie at smaller redshifts than GRBs. The sample of XRF redshifts measured to date is not large enough to be able to determine if this is the case.

A crucial prediction made by this model which we may test directly, thanks to Swift's rapid response capabilities, pertains to the characteristics of the early afterglow. If a gamma-ray burst is observed from anywhere within the jet opening angle, the afterglow flux would decrease

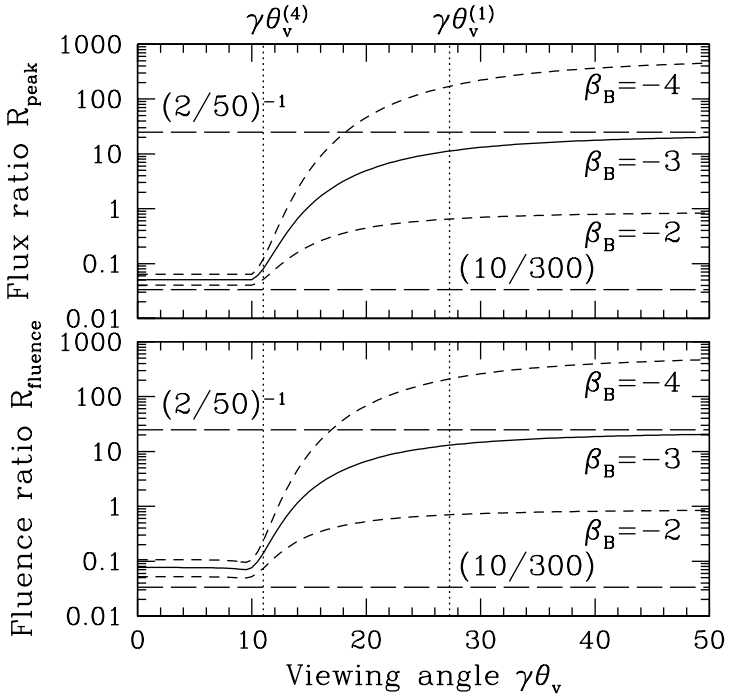

Figure 4.5: The peak flux ratio (upper panel) and fluence ratio (lower panel) of 2 – 10 keV to 50 – 300 keV photons as a function of viewing angle [81]

monotonically with time. But if the afterglow is viewed from outside the jet, the flux rises until it reaches a peak, and then it begins to diminish again at a rate consistent with that of an afterglow observed on axis [37, 77]. If $\theta_v \gtrsim \Delta\theta$, the peak t_p of the light curve would be observed at a time:

$$t_p = \left(5 + 2\ln\left(\frac{\theta_v}{\Delta\theta} - 1\right)\right)\left(\frac{\theta_v}{\Delta\theta} - 1\right)^2 t_{j,0} \text{ [37]}, \tag{4.21}$$

where $t_{j,0}$ is the time at which the jet break would be observed if the afterglow were viewed from within the jet. Equation 4.21 is valid when the Lorentz factor Γ is relatively large ($\Gamma \gtrsim 300$) or when $\theta_v \gtrsim \Delta\theta$ is relatively large ($\theta_v \gtrsim \Delta\theta \gtrsim 5°$). Under these conditions, the peak would come some time after the jet break, which has typically been on the order of a day after the burst.

Another model with similar predictions was proposed by Toma et al. [76] in which multiple sub-jets explain the differences between XRFs, XRRs, and GRBs. The multiple sub-jet model explains the correlation between $E_{\rm iso}$ and $E^{\rm obs}_{\rm peak}$ discovered by Amati et al. [1] and, like the off-jet model, it predicts that XRFs arise when the viewing angle is outside all of the sub-jets.

Structured Jet Model

Another model that seeks to explain x-ray flashes on the basis of viewing geometry is the so-called "structured jet model". Instead of assuming that the collimated relativistic outflow is uniform within the jet, this model assumes that the Lorentz factor Γ and the energy per unit solid angle ϵ are functions of angle. Rossi et al. [68] consider a case in which these parameters decrease with angle according to a power law:

$$\Gamma = \begin{cases} \Gamma_c & 0 \le \theta \le \theta_c \\ \Gamma_c \left(\frac{\theta}{\theta_c}\right)^{-\alpha_\Gamma}, \alpha_\Gamma > 0 & \theta_c \le \theta \le \theta_j, \end{cases} \tag{4.22}$$

$$\epsilon = \begin{cases} \epsilon_c & 0 \le \theta \le \theta_c \\ \epsilon_c \left(\frac{\theta}{\theta_c}\right)^{-\alpha_\epsilon}, \alpha_\epsilon > 0 & \theta_c \le \theta \le \theta_j, \end{cases} \tag{4.23}$$

where θ_c is introduced simply to avoid Γ or ϵ becoming infinite at $\theta = 0$. Like the off-jet model, this model postulates that x-ray flashes are the result of a larger viewing angle θ than gamma-ray bursts.

This model is able to explain the correlation between $E_{\rm iso}$ and jet break time t_b that is alluded to in section 2.5.3. Furthermore, it predicts a rising afterglow light curve with the same general shape as that predicted by the off-jet model. In this model, the time of the peak of the light curve depends only on the observing angle $t_p \propto \theta^2$.

A further prediction of this model is that since the average viewing angle would be very large (because as θ increases, the solid angle encompassed by a given increment $\Delta\theta$ also increases), the number of x-ray flashes we observe should exceed the number of gamma-ray bursts by several orders of magnitude [54]. Observations thus far do not support this prediction: XRFs and GRBs are observed by HETE-2 in roughly the same numbers [70].

Another type of structured jet—a two-component jet—has been suggested to account for sharp rebrightening features in the afterglows of XRF 030723 [46] and GRB 030329 [10]. It was suggested that if the inner jet had a much larger Lorentz factor than the outer jet, and if our line of sight were outside the jet structure, the beaming angle from the inner jet would reach our line of sight much later than the outer jet, causing a rebrightening. Granot investigated the light curve arising from such a jet and concluded that the rebrightening bump it would produce is much too smooth to explain the features seen in those two bursts [39].

Other types of structured jets that have been proposed include ring-shaped and fan-shaped jets. A ring-shaped jet can be described by a jet profile of

$$\epsilon = \frac{dE}{d\Omega} = \begin{cases} \epsilon_0 & \theta_c < \overline{\theta} < \theta_c + \Delta\theta \\ 0 & otherwise \end{cases}, \tag{4.24}$$

where $\overline{\theta}$ is the angle from the symmetry axis of the jet, θ_c is the inner half-opening angle, and $\Delta\theta$ is the angular width. Granot calculated the light curve arising from this model (see Figure 4.6) [39]. In the case of a thin jet ($\Delta\theta \ll \theta_c$), observing angles θ_{obs} within the jet itself (that is, $\theta_c < \theta_{obs} < \theta_c + \Delta\theta$) result in a light curve that peaks very early (on the order of 1 s) and then decreases monotonically. For angles outside the jet (either $\theta_{obs} < \theta_c$ or $\theta_{obs} > \theta_c + \Delta\theta$), the light curve peaks relatively late, on the order of a day after the burst (see Figure 4.6). It was noted that this model predicts two shallow but distinct steepening epochs and cannot produce the large single-epoch

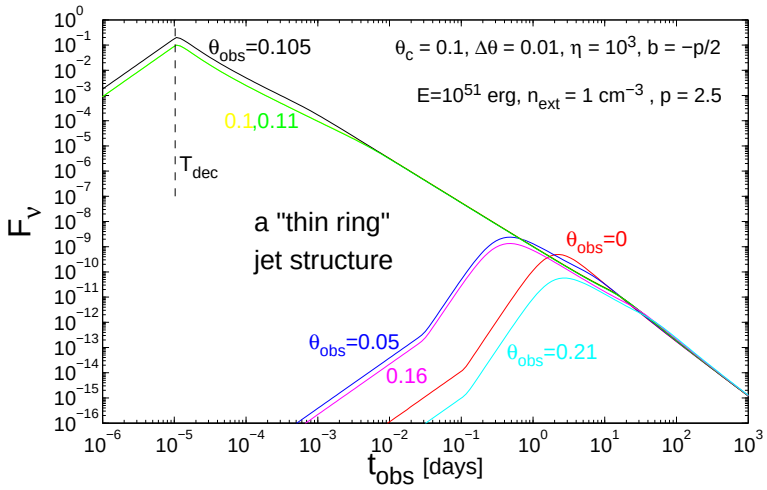

Figure 4.6: Light curves from a jet a thin uniform ring structure [39]

steepening that is typically seen in GRB afterglows. If the ring is thick ($\Delta\theta \gtrsim \theta_c$), the light curve is practically indistinguishable from that of a uniform jet.

Granot also calculated the light curves arising from a thin, fan-shaped jet [39]. He found that the steepening is about half what would be observed from a uniform jet and much smaller than is typically observed in GRB afterglows. Depending on the viewing angle, the light curve would peak a few hours to a few days after the burst (see Figure 4.7).

High Redshift Model

It has also been suggested that x-ray flashes may be gamma-ray bursts originating at high redshifts [43]. For instance, if a gamma-ray burst with a peak energy at the source $E^{\rm src}_{\rm peak}$ of 100 keV were detected at a redshift of 5, its peak energy would be shifted down to 20 keV. As we have seen, there are reasons to suspect that gamma-ray bursts follow star-formation rates, and if this is the case, we would expect GRBs to be present out to redshifts of ~ 10 or even higher.

If most XRFs were actually high-redshift GRBs, we would also expect other properties to be affected by their high redshift. For instance, XRF durations would tend to be longer than GRB durations due to time dilation. Observations to date, however, show that the duration distribution of XRFs is similar to that of GRBs [43]. Furthermore, those XRF redshifts which have been

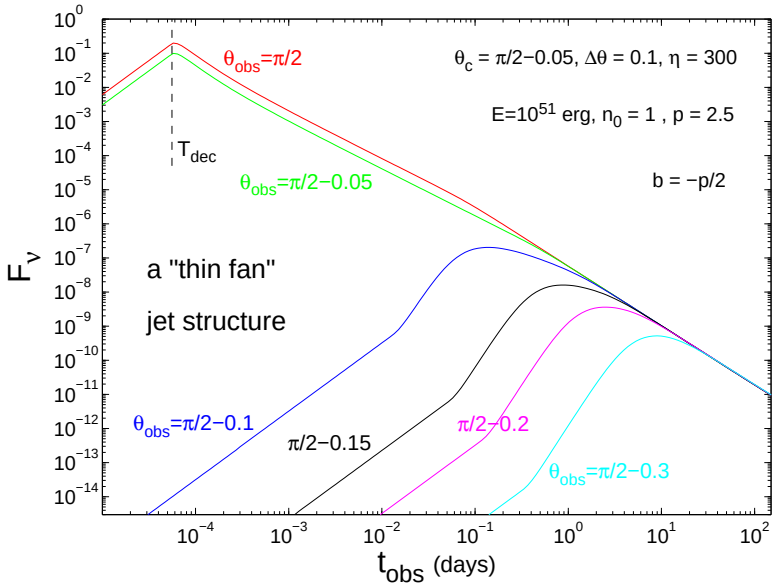

Figure 4.7: Light curves for a jet with an angular structure of a thin fan, with an opening angle of $\Delta\theta = 0.1$ centered on $\theta = \pi/2$ [39]

measured have been not been drastically different from GRB redshifts.

4.4.2 Models Based on Intrinsic Properties

There are also several models that propose that XRFs are intrinsically different from GRBs. Here we review four such models.

Photosphere-Dominated Fireball Model

In section 4.1.1, we described the fireball model, which predicts a radius called the "photospheric radius" r_{ph}, beyond which the ultrarelativistic outflow becomes optically thin. Mészáros et al. have proposed that if the plasma becomes optically thin before it reaches the matter-dominated phase, internal shocks may produce enough photons to create a second photosphere [57]. There exists a radius, called the "pair-shock" radius ($r_{\pm}$), beyond which this second photosphere cannot form. If the internal shocks form at a radius $r > r_{\pm}$, a regular gamma-ray burst is generated. Shocks that form at $r_{ph} < r < r_{\pm}$ could produce x-ray flashes. These x-ray flashes would, in general, be less variable than GRBs, their variability being somewhat damped by the pair-shock

photosphere. Internal shocks that are generated at a radius $r < r_{ph}$ would be x-ray rich.

This photosphere-dominated fireball model, together with the observed anti-correlation between the isotropic-equivalent luminosity L_{iso} and θ, provides a geometric interpretation for the correlation between variability and isotropic-equivalent luminosity L_{iso} that has been observed [66]. It also makes the testable prediction that x-ray flashes are less variable than gamma-ray bursts.

Low Γ ("Dirty") Fireball Model

As we described in section 4.1.1, one of the requirements of the standard fireball model is a small density of baryons which would enable the internal energy to be efficiently converted into kinetic energy and carry the plasma beyond the photospheric radius before internal shocks began. A fireball with a low baryon density is sometimes referred to as a "clean" fireball. A "dirty" fireball, on the other hand, would have a somewhat larger baryon density and, hence, would achieve a smaller Lorentz factor Γ by the time it reached the matter-dominated phase. In the fireball model, $E_{\rm peak}^{\rm obs} \propto \Gamma^4$, so even a slightly smaller Γ could result in a significantly softer spectrum [45, 21]. A fireball with $1 \ll \Gamma \ll 100$ would emit mostly in x-rays instead of gamma-rays.

The afterglow of the burst should depend very little on the baryon load, so the afterglow of an XRF in this model would be just as prominent as that of a GRB. Calculations indicate that at very early times (up until about $\sim 1000s$ or so), the light curve of an XRF afterglow would be quite flat, whereas the afterglow of a GRB would increase slightly with time. At these early times, XRF afterglows would tend to be slightly weaker ($\sim 5\times$) than those of GRBs. At later times (after about a day or so), the afterglows would be indistinguishable (see Figure 4.8).

Small Contrast in Γ Fireball Model

Barraud et al. [7] set out to determine under what conditions a set of internal shocks might produce an x-ray flash. To do this, they investigated the behavior of a toy model in which two ultrarelativistic shells of the same mass m but slightly different values of Γ collide, producing synchrotron emission. The parameters of the model were Γ_1 (the Lorentz factor of the first, slower shell), Γ_2 (the Lorentz factor of the second, faster shell), and τ (the delay between the generation

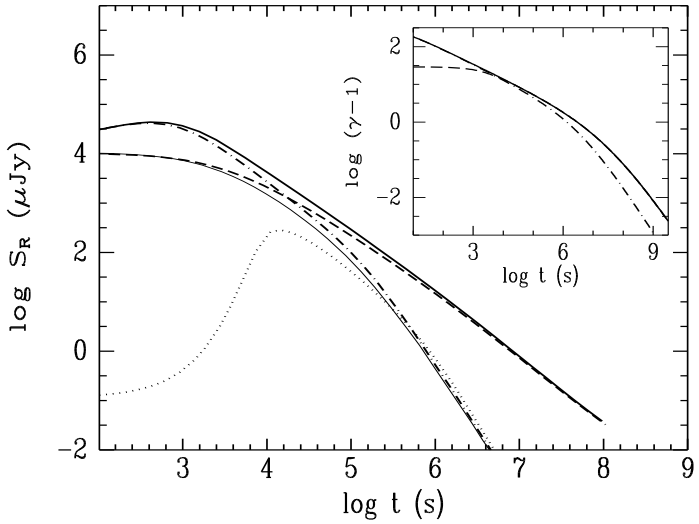

Figure 4.8: A light curve calculation for typical GRB afterglows in the "dirty fireball" model. The thick solid line is plotted for a usual isotropic GRB with $\Gamma_0 = 300$. The dashed line represents an isotropic GRB with $\Gamma_0 = 30$. The dash-dotted line corresponds to a jetted GRB viewed from within the jet with $\Gamma_0 = 300$, and the dotted line is for a jetted GRB viewed from outside the jet. The thin solid line is for a beamed GRB with $\Gamma_0 = 30$, $\theta_{obs} = 0$. The Inset shows the evolution of the Lorentz factor correspondingly. See [45] for details of the model parameters.

of the first shell and the second shell). The model predicts that

$$E_{\rm peak}^{\rm obs} \propto \frac{\dot{E}\psi_{xy}(\kappa)}{\tau^{2x}\overline{\Gamma}^{6x-1}}, \tag{4.25}$$

where $\dot{E} = (mc^2/\tau)(\Gamma_1 + \Gamma_2)$ is the energy loss rate of the inner engine, $\overline{\Gamma} = (\Gamma_1 + \Gamma_2)/2$ is the average Lorentz factor, $\kappa = \Gamma_2/\Gamma_1$, x and y are variables that depend on how the initial energy of the shells is distributed between the magnetic field and the electrons, and $\psi_{xy}(\kappa)$ is an increasing function of κ for all reasonable values of x and y. From this equation, we note that since κ is larger when there is a larger contrast between Γ_1 and Γ_2, $E_{\rm peak}^{\rm obs}$ is also larger in those circumstances. We also note that as long as $x > 1/6$, $E_{\rm peak}^{\rm obs}$ decreases as $\overline{\Gamma}$ increases. Statistical simulations with this model verify that XRFs are created when $\overline{\Gamma}$ is large and/or when κ is small. On a physical basis, the production of XRFs in clean fireballs may be explained by a reduction in shock efficiency. In the case of dirty fireballs (with a greater contrast in Γ), internal shocks take place closer to the source, where the density is higher. The injected power $\dot{E}$ has very little bearing on whether a gamma-ray burst or an x-ray flash is created.

This "small contrast in Γ" model reproduces the observed correlation between duration and hardness as well as the correlation between hardness and intensity [52, 35]. It also predicts similar duration distributions for XRFs and GRBs, as has been observed. Furthermore, it predicts that the redshift distribution for XRFs should be nearly the same as that of GRBs.

Amati et al. describe a procedure by which they were able to constrain Γ using the afterglow energy, the circumburst density, and the duration of the emission [2]. They found that in the case of XRF 020427, $\Gamma > 195$, which is consistent with this model.

Uniform jet model

The final model we shall examine was proposed by Lamb et al. [54]. Based on the results that XRFs tend to have low isotropic-equivalent energies and using the observed anti-correlation between $E_{\rm iso}$ and jet opening angle θ, they proposed that gamma-ray bursts tend to have very narrow jets and x-ray flashes tend to have much wider jets. Unlike the other models we have considered, this model is based entirely on observation and offers no particular physical explanation

or basis. It therefore may well turn out to be consistent with one of the other intrinsic models described in this section.

Chapter 5

The Swift Observatory

5.1 Description of the Swift Mission

One of the greatest difficulties that confront gamma-ray burst studies is the transient nature of the phenomenon. The bursts themselves only last for a few seconds, and although the afterglows last much longer, they also fade very quickly, typically at a rate proportional to around t^{-1} or t^{-2}. Swift is the first observatory with the ability to begin multi-wavelength observations within ~ 1 minute of the burst, at a time when the afterglow is orders of magnitude brighter than it is even an hour later. This early follow-up permits us to detect many more afterglows than has been possible in the past. It also provides the key to constraining afterglow models and evaluating x-ray flash models.

Launched in November of 2004, the Swift observatory (see Figure 5.1) is a medium-sized explorer (MIDEX) mission whose primary scientific objectives are to determine the origin of GRBs and to pioneer their use as probes of the early universe. Unlike most space missions, which are either acronyms or are named after famous scientists, Swift was named after a bird. These birds have the ability to scan the sky for insects and quickly change direction in mid-flight to catch them. In a similar way, Swift scans the sky for gamma-ray bursts and quickly slews to the position of a burst when one is detected. The Swift spacecraft, which was built by Spectrum Astro, houses a trio of instruments: the Burst Alert Telescope (BAT), the X-Ray Telescope (XRT), and the UltraViolet and Optical Telescope (UVOT). The Burst Alert Telescope searches the sky for new GRBs and, upon discovery, triggers an autonomous spacecraft slew to bring the burst into the XRT and UVOT fields of view. Such autonomy allows Swift to perform X-ray and UV/optical observations of ≈ 100 bursts per year within 20 - 70 seconds of a burst detection. Once the burst is within the fields of view of the XRT and UVOT, the pointing stability is better than 0.1 arcsec.

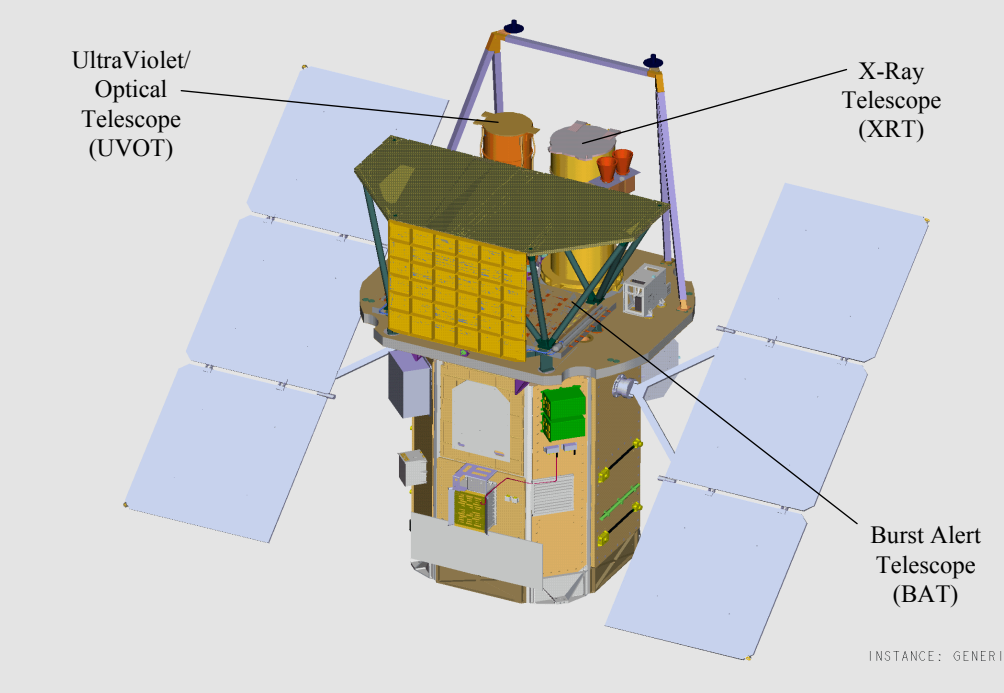

Figure 5.1: The Swift Observatory. The BAT, consisting of the coded aperture mask above and the detector array below, is shown in the forefront. A fringe shield that surrounds the BAT is not pictured. The XRT and UVOT are shown behind the BAT.

Table 5.1 summarizes the basic mission profile parameters. The orbital radius of 600 km was selected so that the instrument would be in a low enough orbit that the Van Allen radiation belts not interfere very much, yet the orbit would still be high enough to guarantee a longer than 2-year orbit lifetime. The worst-case solar activity scenarios predict a minimum orbit lifetime of 5 years. The Delta 7320 launch vehicle had a 280 kg mass margin beyond what was required by the observatory, which made possible a maneuver during launch to decrease the orbit inclination from the 28.5° to 22°. The lower inclination minimizes the amount of time the spacecraft spends in the South Atlantic Anomaly (SAA), which is a region over the south Atlantic Ocean and South America with a large number of high energy protons that bombard spacecraft passing through it. When Swift passes through the SAA, the BAT is swamped with counts due to these protons, so BAT effectively "shuts down" during that time. Less time in the SAA means more time

Table 5.1: Swift Mission Characteristics

Mission Parameter	Value
Slew Rate	50° in < 75 sec
Orbit	Low Earth, 600 km altitude
Inclination	22°
Launch Vehicle	Delta 7320-10 with 3 meter fairing
Total Mass	1270 kg
Total Power	1640 W
Launch Date	November 2004
Mission Life	2 yr
Orbital Life	> 5 yr

watching for bursts—about 10% more than would be possible at a 28.5° inclination. It also means a slower increase in background due to activation of the spacecraft materials. The high energy protons of the SAA interact with the materials of the spacecraft and cause some of them to become radioactive, emitting hard x-rays that increase the background level detected by BAT. Over time, this background level increases and interferes with the ability of BAT to detect and distinguish counts due to gamma-ray bursts. The high energy proton bombardment can also degrade the electronic components of the spacecraft over time. Less time spent in the SAA slows this degradation. The observatory was launched from Cape Canaveral and has a nominal lifetime of 2 years with a goal of 5 years and an orbital lifetime of greater than 8 years.

5.2 The Burst Alert Telescope

5.2.1 Purpose

As its name suggests, the Burst Alert Telescope (BAT) provides the initial detection of the gamma-ray burst. It then calculates the position of the burst and sends the position to the spacecraft attitude control system. Swift does all this within 12 seconds of the initial detection of the burst. In order to monitor as much of the sky at possible at once, BAT has a large FOV—about 2 sr, or roughly 1/6 of the sky. This is approximately the same field of view that a human being has staring straight ahead. One of the few ways to produce hard x-ray images with such a large FOV is to use the coded-aperture technique, which is described in section 5.2.3. For each detected burst,

event data is accumulated during an adjustable time window surrounding the time of the initial burst trigger. This event data consists of the time that each photon was detected (to an accuracy of $\sim 200\mu$s), the detector in which it was detected, and the size of the electrical signal induced by the detector (the "pulse height"). From these event files, spectra (the number of photons detected as a function of energy) and light curves (plots of the number of photons detected as a function of time) can be created. A more detailed description of the BAT instrument and its pre-launch performance is given by Barthelmy et al. [9].

5.2.2 Physical Description

The basic parameters of the BAT instrument are listed in table 5.2. It can detect photons in the energy range of 15-150 keV and contains 32,768 pieces of $4mm \times 4mm \times 2$ mm CdZnTe (CZT) room temperature semiconductor material which form a 1.2×0.6 m sensitive area in the detector plane. Groups of 128 detector elements are assembled into 8×16 sub arrays, with the detectors connected to a 128-channel readout XA 1.23 Application Specific Integrated Circuits ASIC; which is designed and produced by Integrated Detector and Electronics (IDE AS) of Norway. Detector modules, each containing two such sub-arrays, are further grouped by eights into 2048-detector blocks. This hierarchical structure, along with the forgiving nature of the coded-aperture technique, means that the BAT can tolerate the loss of individual pixels, individual detector modules, and even whole blocks without losing the ability to detect bursts and determine locations. The CZT array has a nominal operating temperature of 20°C, and its thermal gradients (temporal and spatial) are kept to within ± 1°C. The typical bias voltage applied to the detectors is 200 V, with a maximum of 300 V. The detectors are calibrated in flight with an electronic pulser which periodically sends an electronic signal of a known voltage into the electronics, and two ^{241}Am tagged sources that are located just inside the mask and constantly illuminate the array with photons of specific energies. The tagged sources are small pieces of scintillator doped with 241Am. The scintillators detect the light flash accompanying each 241Am decay so that any photon detected at the same time as the scintillator signal is identified as coming from the tagged source.

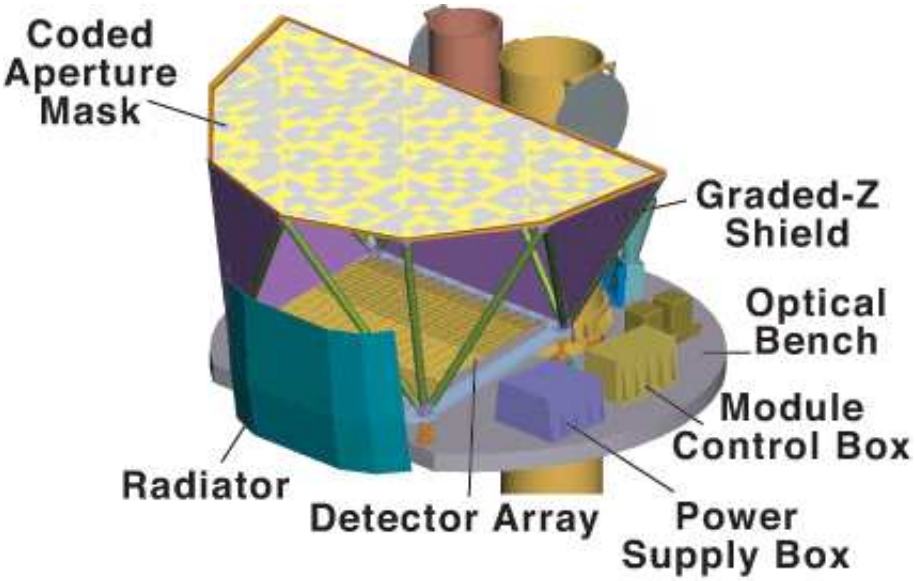

Figure 5.2: A drawing of the Burst Alert Telescope and other components of the Swift observatory [32]

The BAT has a D-shaped coded mask made of 54,000 lead tiles ($5mm \times 5mm \times 1$ mm) mounted on a 5-cm-thick composite honeycomb panel, that is supported by composite fiber struts at 1 meter above the detector plane. The BAT coded mask has a completely random, but known 50% open-50% closed pattern tile. The mask area is 2.7 m^2, resulting in a half-coded FOV (that is, a field of view in which every point in the sky illuminates at least half the area of the array through the mask) of $100° \times 60°$, or 1.4 steradians.

A "graded-Z" fringe shield, located both under the detector plane and surrounding the mask and detector plane, reduces the number of photons from sources outside the field of view and others from background radiation by $\sim 95\%$. The shield is composed of layers of Pb, Ta, Sn, and Cu, which are thicker toward the bottom nearest the detector plane and thinner near the mask.

A "Figure of Merit" (FoM) algorithm decides if a burst detected by the BAT is worth requesting a slew maneuver by the spacecraft. If the new burst has more "merit" than the pre-programmed observations, a slew request is sent to the spacecraft. The ground control team can also upload target positions, which are processed exactly the same as targets discovered by the BAT.

Table 5.2: Burst Alert Telescope Characteristics

BAT Parameter	Value
Energy Range	15-150 keV
Energy Resolution	~ 7 keV
Aperture	Coded mask, random pattern, 50% open
Detection Area	5240 cm^2
Detection Material	CdZnTe (CZT)
Detection Operation	Photon counting
Field of View (FOV)	1.4 sr (half-coded)
Detector Elements	128 Detector Modules with 256 detectors each
Detector Element Size	$4 \times 4 \times 2$ mm^3
Coded-Mask Cell Size	$5 \times 5 \times 1$ mm^3 Pb tiles
Telescope PSF	17 arcmin
Source Position Accuracy	$1 - 3$ arcmin (depending on source position)
Sensitivity	$\sim 10^{-8}$ ergs/cm^2/s
Number of Bursts Detected	~ 100/yr

5.2.3 Coded Aperture Imaging

As we described in section 5.2.1, BAT is required to generate a gamma-ray image of a large area of the sky on a short time scale. Focusing optics are very difficult above about 10 keV, because the techniques that are typically applied at x-ray energies, in which x-rays graze the surface of mirrors, require grazing angles that are too small to be practical, although these angles can be increased using multi-layer mirrors like those used by the InFocus mission [61]. Another difficulty is that most imaging techniques are not feasible for large fields of view. Coded aperture imaging solves both of these problems [17, 22].

As photons coming from a particular direction in the sky pass through the mask, they cast a shadow across the detector array. Those detectors that are illuminated through the mask will detect a high number of photons, whereas those that are in shadow will detect very few. The result is a pattern of detected photons (or "counts") in the detector array. By comparing the pattern of these counts with the known pattern of the mask, it is possible to determine from which direction the photons originated. This process is automated and is conducted for every point in the sky using a Fourier transform algorithm. The result is an image of the sky, with bright points where gamma-ray sources are present and dark background everywhere else.

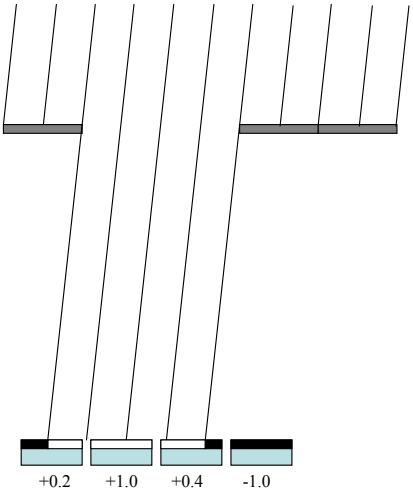

Figure 5.3: The mask weight values assigned to various detectors. Detectors that are fully-illuminated are assigned a value of +1 and detectors that are fully-masked are assigned a value of -1.

We can use a similar technique to produce a count rate for a particular source in the sky. We do this by assigning a weight to each detector, according to the degree to which it is illuminated through the mask. Detectors that are fully-illuminated would receive a mask weight of +1 and detectors that are fully-masked would receive a mask weight of -1. All other detectors would receive a mask weight somewhere between -1 and +1 (see Figure 5.3). If the count rates from each individual detector are all added together, weighted by these mask weight values, the result is a value that is proportional to the number of counts received in a single fully-illuminated detector as a result of photons arriving directly from the source in question, with all other counts removed. See Appendix A for a complete derivation of the mask-weighted count rate.

5.2.4 Effective Area

The "effective area" of an x-ray or gamma-ray instrument is typically defined as the ratio of the count rate due to photons of a given energy and the actual incident flux of those photons. Thus, effective area has units of area (as the name suggests) and depends upon the energy and

direction of the incident photons.

For a typical x-ray or gamma-ray instrument, the effective area is defined in terms of every count recorded by the instrument that results from the incident photon flux coming from the direction of the source of interest. As such, it includes counts from photons that arrive directly from the source as well as those that enter the detectors after first scattering off of some passive material. The mask-weighted count rate differs from the full count rate typically considered in several ways:

- Counts resulting from scattered photons are removed as background.
- Counts resulting from photons that pass through the various passive materials, including the lead tiles, are removed as background.
- Counts that arrive at detectors that are half-illuminated are removed, because such detectors receive a weight of 0. Likewise, counts that arrive at detectors that are less than half-illuminated actually contribute negatively to the total rate. The overall result is that many counts that really do result from photons coming directly from the source are cancelled out.

When we define the effective area in terms of the mask-weighted count rate, it is likewise reduced for these reasons. Figure 5.4 shows the mask-weighted effective area as a function of incident photon energy at two different incident angles. Figure 5.5 shows the traditionally-defined effective area for the BAT instrument. The latter curve was generated by Monte Carlo GEANT simulations of incident photons interacting with the materials comprising the entire Swift observatory. The simulations use a model called SwiMM (short for "Swift Mass Model") which was developed by David Willis, formerly of the University of Southampton, and is currently maintained by collaborators at JAXA/ISAS in Japan.

5.2.5 The Trigger Algorithm

The Burst Alert Telescope constantly watches for new gamma-ray bursts. Since burst durations can range from a few milliseconds to a number of minutes, BAT has many different

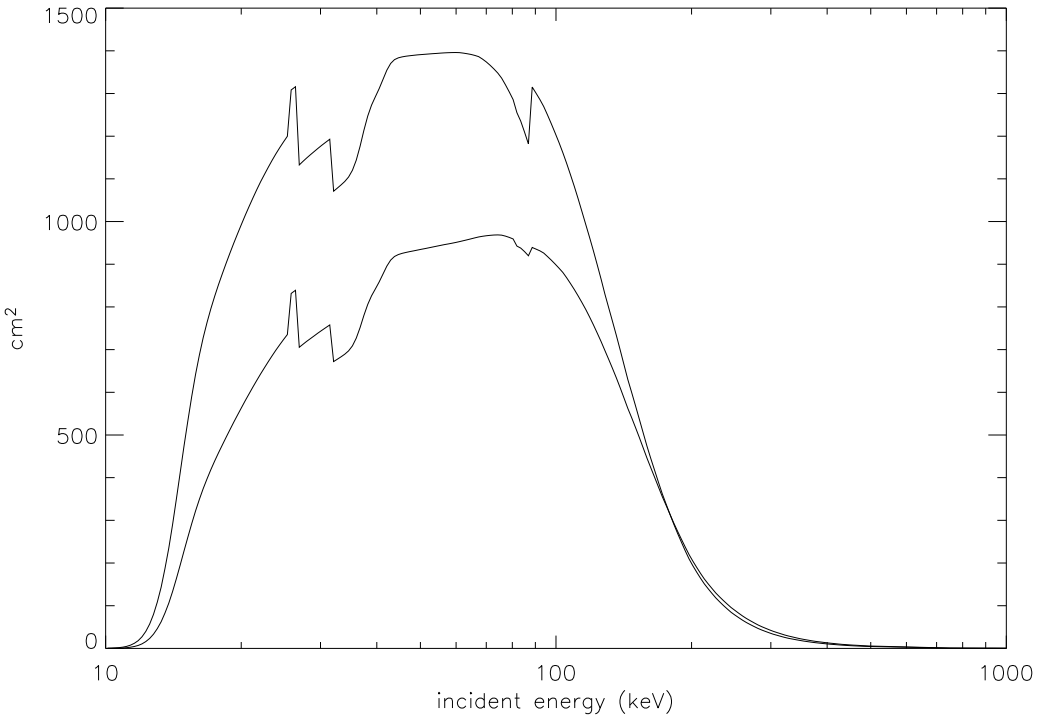

Figure 5.4: The "mask-weighted" effective area curve for the Burst Alert Telescope. This effective area curve is defined as the ratio of the mask-weighted count rate to incident photon flux. The top curve is the effective area for photons that hit the array from directly above. The bottom curve is the effective area for photons incident on the array at a 45° angle.

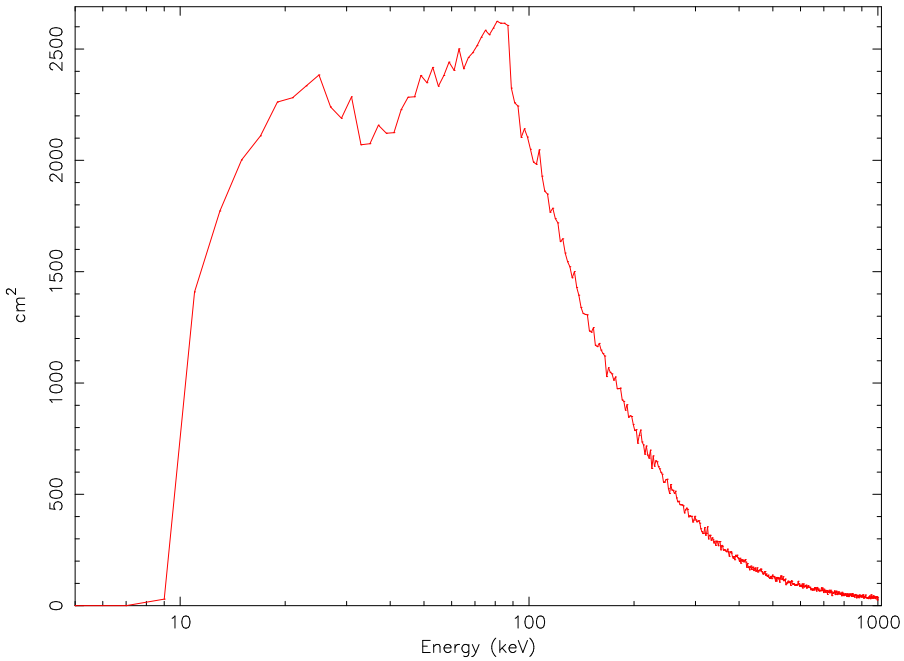

Figure 5.5: The "traditional" effective area curve for the Burst Alert Telescope for photons incident from directly above the array. This effective area curve is defined as the ratio of the total count rate to incident photon flux. This particular plot was generated using a Monte Carlo simulation, so there are small statistical fluctuations that give it a jagged appearance in places.

search criteria that it uses to identify a burst. When a potential burst is identified by a combination of these criteria, We call that detection a "trigger", because it sets in motion a set of automated actions, including possibly slewing to the position of the burst. There are two different ways in which a potential burst may be identified: either as a result of an increase in the count rate in the array (which we call a "rate trigger") or as a result of the detection of a new source in an image generated by the onboard software (an "image trigger") [23]. The rate triggers can further be classified as "short rate triggers", in which BAT searches for rate increases on time scales of less than 64 ms, or as "long rate triggers", in which BAT searches for rate increases on time scales longer than 64 ms.

Short Rate Triggers

BAT continuously watches for statistically significant increases in the count rate during 4 ms, 8 ms, 16 ms, 32 ms, and 64 ms intervals. A burst is more likely to be detected in a time interval that is similar to its duration. During each of these time intervals, the BAT software monitors the count rates in 9 different regions of the array: the 4 quadrants, the top half, the bottom half, the left half, the right half, and the entire array. A burst in a part of the sky that is shielded from all but one quadrant of the array would result in a rate increase mostly confined to that quadrant. Furthermore, 4 different energy ranges are continuously monitored: for counts that are likely to originate from photons with energies between 15 and 25 keV, between 25 and 50 keV, between 50 and 100 keV, and between 100 and 350 keV (although these limit values range are commandable). A "hard" burst (that is, one with many high-energy photons and fewer low-energy photons) would more likely be detected in a higher energy range. Considering all combinations of these criteria, there are 26,496 samples that must be checked every 1.024 seconds. The on-board software compares the maximum count rate in each sample to the average count rate in a 1.024 second interval and calculates a detection "score". If the score is greater than some commandable value, the on-board software searches backward in time until it finds the moment when the rate increase began. Using data from that time interval, it generates an image and compares it to the

most recent 8-second image (which the software is constantly producing) to see if there are any new sources. This step permits BAT to eliminate false triggers from rate increases due to known gamma-ray sources and due to showers of charged particles that illuminate the array from time to time. If a new source exists (to a certain commandable level of significance), the trigger is announced to the world via the Gamma-ray burst Coordinates Network (GCN).

Long Rate Triggers

Long triggers are significant rate increases in time intervals longer than 64 ms. BAT monitors the same energy ranges and regions of the array for long triggers as for short triggers. However, on these longer time scales, the background count rate may be changing, so it isn't possible to simply compare the maximum rates to an average rate in some longer time interval, as is done with short triggers. Instead, a linear or quadratic function is fit to a set of background regions to remove any trends in the overall background rates. Then the count rate in some specified "foreground" interval is calculated, with the background rate subtracted off. Up to 3 background time intervals can be specified. Commandable parameters also specify the degrees of the polynomials that should be used to fit the background and the threshold for how high the trigger "score" must be before it is considered real (or likely to be real). As with the short triggers, an image is formed and searched for new sources before the trigger is announced.

Image Triggers

We have already mentioned that the on-board software creates an image of the sky every 8 seconds. These 8-second images can be combined into images comprising larger durations. Three such durations are possible at a time, and those durations are adjustable. These durations must be multiples of 8 seconds, and examples might be 64 seconds, 10 minutes, and 45 minutes (half an orbit). The on-board software searches these combined images for new sources, ignoring those that are in positions where known gamma-ray sources exist. If the source detection score exceeds some commandable value, the trigger is announced.

The TDRSS and GCN Systems

Triggers are relayed to the ground by the Tracking and Data Relay Satellite System (TDRSS). Once on the ground, they are transferred to the Gamma-ray burst Coordinates Network (GCN) system, which distributes the information to any instrument, person, or institution wishing the information (to make follow-up observations or for general awareness about the current state of GRB activity) [8]. GCN circulars are also distributed by the Swift instrument teams and by follow-up instrument teams, providing additional information about the burst. Throughout this work, sources that are cited as "GCN" followed by a number refer to these circulars, and can be found at http://gcn.gsfc.nasa.gov/gcn3_archive.html. The position of the burst is available on the ground within about 20 seconds of the initial detection. Light curve information on the burst follows about 110 seconds later.

5.2.6 GRB Data Products

The key aspect of the BAT instrument is to produce burst information quickly and have it distributed to other spacecraft and to ground-based observatories as soon as possible. Table 5.3 lists the burst-related data products, and how soon they become available. The burst trigger starts the time-available delay clock listed in the table. The Trigger Alert message alerts ground-based personnel that the BAT trigger algorithm has been satisfied. It contains the time of the trigger and which particular time, energy, and geometry trigger was satisfied. This alert message is sent to the ground through TDRSS and distributed to the world through the GCN. Meanwhile the BAT continues to process the event data to determine the location of the burst, which is also transmitted to the ground through TDRSS. BAT produces burst location error circles with a 4 arcmin diameter, that are made available on the ground within 20 sec of the start of the burst. The results of the decision made by the spacecraft as to whether or not to slew to the burst is also transmitted. After 130 sec, 30 sec of pre-trigger and 120 sec of post-trigger light curve information in 4 energy ranges is transmitted. Once the XRT and UVOT instruments are slewed into position, they also produce position, spectra, and images of the burst afterglow, which also

Table 5.3: BAT burst-related data products and their time delays after the burst trigger

Data Product	Time Available
Trigger Alert	5 sec
Burst Position	12 sec
FOM Will/Won't Observe	14 sec
Spacecraft Will/Won't Slew	14 sec
Burst Light Curve	130 sec
Burst Afterglow Light Curve	$\sim$ 20 min
Burst Event-By-Event Data	2-4 hrs

go through TDRSS to the ground and through GCN. More detailed event-by-event information is transmitted to the ground some time later when the Swift spacecraft passes over the Malindi ground station in Kenya.

5.3 The X-Ray Telescope

5.3.1 Purposes

Swift's X-Ray Telescope (XRT) is designed to measure the 0.2 to 10 keV X ray fluxes, spectra, and light curves of GRBs and afterglows over a wide dynamic range covering more than 7 orders of magnitude in flux. The XRT pinpoints GRBs to 5 arcsec accuracy within 10 seconds of target acquisition for a typical GRB and studies the X-ray counterparts of GRBs beginning at the time the XRT has stabilized on-target (20 - 70 seconds after burst discovery) and continuing for days to weeks. Figure 5.6 shows a schematic of the XRT, and Table 5.4 summarizes XRT parameters. Further information on the XRT is given by Burrows et al. [15].

5.3.2 Physical Description and Performance

The XRT is a focusing X-ray telescope with a 110 cm^2 effective area at 1.5 keV, 23 arcmin FOV, 18 arcsec resolution (half-power diameter), and 0.2 - 10 keV energy range. The XRT uses a grazing incidence Wolter 1 telescope to focus X-rays onto a CCD. The complete mirror module for the XRT consists of the X-ray mirrors, thermal baffle, a mirror collar, and an electron deflector. To prevent on-orbit degradation of the mirror module's performance, the mirror is maintained at

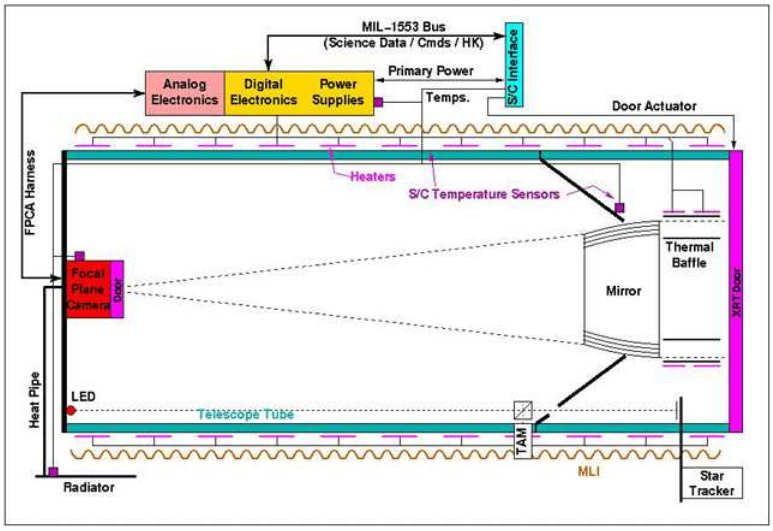

Figure 5.6: Block diagram of the X-Ray Telescope [32]

$20 \pm 5°$C with gradients of $< 1°$C by an actively controlled thermal baffle. A composite telescope tube holds the focal plane camera, containing a single CCD detector. The CCD consists of an image area with 600×602 pixels (40×40 mm) and a storage region of 600×602 pixels (39×12 mm). The FWHM energy resolution of the CCD decreases from $\sim$ 190 eV at 10 keV to $\sim$ 50 eV at 0.1 keV, where below $\sim$ 0.5 keV the effects of charge trapping and loss to surface states become significant. The detectors operate at $\approx -50°$C to ensure low dark current and to reduce the CCD's sensitivity to irradiation by protons (which can create electron traps that ultimately affect the detector's spectroscopy).

5.3.3 GRB Data Products

The XRT supports three readout modes to enable it to cover the large range of intensities expected from GRB afterglows and autonomously determines which read-out mode to use. In order of bright flux capability (and the order that would normally be used following a GRB), the modes are:

1. **Imaging Mode**, which produces an integrated image measuring the total energy deposited in each pixel and does not provide any spectroscopic information and only coarse timing

Table 5.4: X-Ray Telescope Characteristics

XRT Parameter	Value
Energy Range	0.2-10 keV
Telescope	Wolter 1 (3.5 m focal length)
Detector	e2v CCD-22
Detection Elements	600×600 pixels
Pixel Size	40 μm $\times$ 40 μm
Pixel Scale	2.36 arcsec/pixel
Effective Area	~ 125 cm^2 at 1.5 keV
	~ 20 cm^2 at 8.1 keV
Readout Modes	Imaging (IM) mode, Photodiode (PD) mode,
	Windowed Timing (WT) mode, Photon-Counting (PC) mode
Field of View (FOV)	23.6×23.6 arcmin
Point Spread Function (PSF)	18 arcsec (HPD) at 1.5 keV
	22 arcsec (HPD) at 8.1 keV
Position Accuracy	3 arcsec
Sensitivity	2×10^{-14} ergs/cm^2/s in 10^4 s

information. Depending on the brightness of the source, the images are accumulated for either 0.1 or 2.5 seconds. Images provide a position for the source and an estimate of the flux. They are useful for fluxes up to 7×10^{-7} ergs/cm^2/s.

2. **Photodiode Mode**, which is useful for obtaining timing information for very bright sources (up to about 4×10^{-6} ergs/cm^2/s). Photodiode Mode enables the XRT to produce a set of time-resolved images on a time scale of about 0.14 ms. Unless the flux is too high (above about 10^{-7} ergs/cm^2/s), the energy and "grade" (or pattern of detected photons in nearby pixels) of each recorded photon can be extracted from these images. The grade provides information that can be used to screen valid events from those that most likely result from charged particles or piled-up events.

3. **Windowed Timing Mode** uses a 200 column window covering the central 8 arcminutes of the XRT FOV. It provides position information in one dimension, and each image column provides a measured flux at a different moment in time. The time resolution is about 1.8 ms in this mode. Useful fluxes can be measured up to about 3×10^{-7} ergs/cm^2/s, and spectroscopic information can be obtained for fluxes up to about 6×10^{-8} ergs/cm^2/s allowing bright source

Table 5.5: Summary of the XRT mode characteristics. 1 Crab is the flux emitted by the Crab nebula in the energy range of interest. In XRT's energy range, 1 Crab $\approx 6 \times 10^{-8}$ ergs/cm^2/s.

Mode	Image Capability	Spectral Capability	Time Resolution	On-Board Event Reconstruction	Flux Level Mode Switch
PU & LR	No	Yes	0.14 ms	No, Done on ground	0.6-60 Crab
WT	1D	Yes	1.7 ms	No, Done on ground	1-600 mCrab
PC	2D	Yes	2.5 s	Yes	$<$ 1 mCrab
IM	2D	No	0.1 s (short) 2.5 s (long)	Not Applicable	$>$ 140 mCrab (short) $<$ 5.6 mCrab (long)

spectroscopy through rapid CCD readouts. For each photon, the arrival time, 1-D position, energy, and grade are provided in this mode.

4. **Photon-Counting Mode** permits full spectral and spatial information to be obtained for source fluxes ranging from 2×10^{-14} to 2×10^{-11} ergs/cm^2/s. However, the CCD is only read out every 2.5 seconds, so for fluxes larger than $\sim 2 \times 10^{-11}$ ergs/cm^2/s, pile-up is a problem. For each photon, this mode provides the 2-D position, arrival time, energy, 3×3 pixel neighborhood centered on the event, and the grade of the event.

With the exception of Imaging Mode, all data is collected and transmitted to the ground in the form of an event list. Each event list file consists of a time-ordered list of photon attributes (for example, time, position and pulse-height information). Images, spectra, and light curves can be created from these event lists.

5.4 The UltraViolet and Optical Telescope

5.4.1 Purposes

The UltraViolet and Optical Telescope (UVOT) generates spectra, images, and light curves in several different ultra-violet and optical wavebands. It is co-aligned with the XRT and carries an 11-position filter wheel which allows low-resolution grism spectra of bright GRBs and broad-band UV/visible photometry. Photons register on the microchannel plate intensified CCD (MIC). Figure 5.7 shows a schematic of the UVOT, and Table 5.6 summarizes the UVOT parameters. Further information on the UVOT is given by Roming et al. [67].

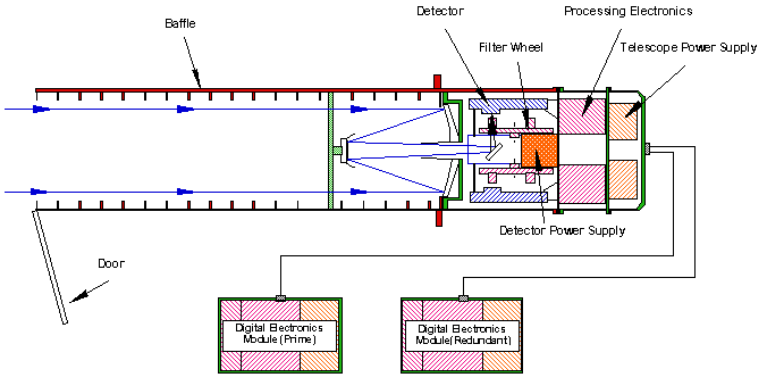

Figure 5.7: Block diagram of the UltraViolet and Optical Telescope [32]

5.4.2 Physical Description and Performance

The UVOT's optical train consists of a 30 cm Ritchey-Chrétien telescope with a primary f-ratio of f/2.0 increasing to f/12.72 after the secondary. An INVAR structure that is intrinsically thermally stable is used between the mirrors and maintains the focus. Fine adjustment to the focus is achieved by activating heaters on the secondary mirror support structure and on the INVAR metering rods that separate the primary and secondary mirrors. The UVOT carries two redundant photon-counting detectors that are selected by a steerable mirror mechanism. Each detector has a filter wheel mounted in front of it carrying the following elements: a blocked position for detector safety; a white light filter; a field expander; two grisms; U, B, and V filters; and three broadband UV filters centered on 190, 220 and 260 nm. One grism on each wheel is optimized for the UV, the other for optical light, and both offer a spectral resolution of ~ 1 nm/pixel. The UVOT operates as a photon-counting instrument. The two detectors are MICs incorporating CCDs with 384×288 pixels, 256×256 of which are usable for science observations. Each pixel corresponds to 4×4 arcsec on the sky, providing a 17×17 arcmin FOV. Photon detection is performed by reading out the CCD at a high frame rate and determining the photon splash's position using a centroiding algorithm. The frame rate for the UVOT detectors is 10.8 ms.

Table 5.6: UltraViolet and Optical Telescope Characteristics

UVOT Parameter	Value
Wavelength Range	170-600 nm
Telescope	Modified Ritchey-Chrétien
Aperture	30 cm diameter
F-number	12.7
Detector	Intensified CCD
Detector Operation	Photon counting
Field of View (FOV)	17×17 arcmin
Detection Elements	2048×2048 pixels
Telescope PSF	0.9 arcsec FWHM at 350 nm
Colors	6
Sensitivity	B = 24 in white light in 1000 s
Pixel Scale	0.5 arcsec

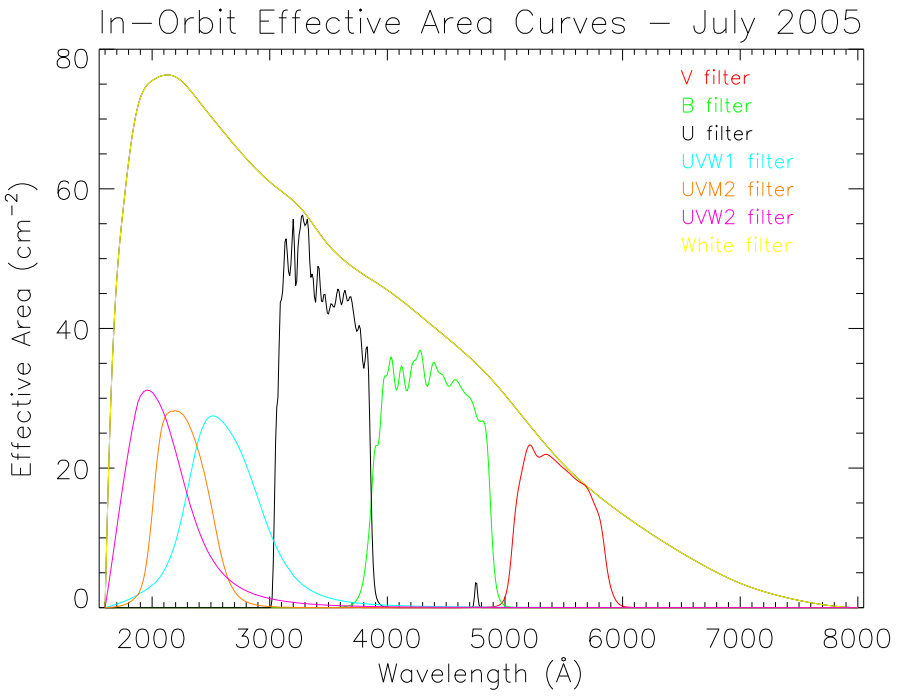

Figure 5.8: The Effective Area of the UltraViolet and Optical Telescope with Different Color Filters in Place [14]

5.4.3 GRB Data Products

When the spacecraft slews to a gamma-ray burst, the UVOT records a 100-second image using its V filter. This image is called a "finding chart" and contains an image of the burst afterglow and any stars that are in the field of view. This finding chart is to aid ground-based observers in localizing the afterglow. The positional accuracy of the finding chart is approximately 0.3 arcsec relative to the background stars in the FOV. After recording this finding chart, the UVOT begins producing a set of exposures using an automated sequence of filters.

There are two data collection modes for the UVOT: Event and Imaging, which can be run at the same time if desired. In Event Mode, the UVOT stores time-tagged photon events in memory as they arrive. The timing resolution is $\sim$ 11 ms. In Imaging Mode, photon events are summed into an image for a time period known as the tracking frame time ($\leq$ 20 s). The advantage of Imaging Mode is that it minimizes the telemetry requirements when the photon rate is high, but at the expense of timing information.

Chapter 6

Calibration of the Burst Alert Telescope

6.1 The Physics of Gamma Ray Detection

6.1.1 Processes of Photon Interaction

When a photon enters a detector (or any other material), it may interact with the detector (and in the process transfer a portion of its energy to the detector) by one of three main processes: photoelectric absorption, Compton (or incoherent) scattering, or pair production. Any of these processes might take place when the photon comes in contact with an atom, but depending on the energy of the photon and the type of atom, some processes are more likely than others.

Photoelectric Absorption

When a photon interacts with an atom by photoelectric absorption, its energy is absorbed by the atom, freeing one of the electrons in the atom (usually one of the innermost "K shell" electrons), and leaving a vacancy in the electron structure (see Figure 6.1). The remaining electrons rearrange themselves, filling the vacancy and emitting a series of photons with characteristic energies in the process. These characteristic photons may then be absorbed themselves by other atoms, or they may manage to escape from the detector altogether.

The likelihood of photoelectric absorption taking place is much greater for atoms with a large number of electrons. For neutral atoms, the number of electrons is the same as the number of protons in the nucleus (the "atomic number" Z). The probability of absorption is also much greater for photons with a small amount of energy E:

$$P \propto \frac{Z^5}{E^{3.5}}. \tag{6.1}$$

Photoelectric absorption is the dominant interaction process for photon energies less than about 200 keV. Hence, this is the dominant interaction mechanism for the BAT detectors.

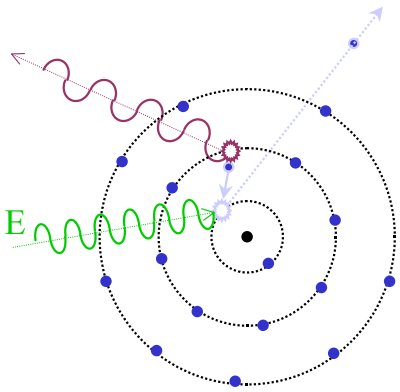

Figure 6.1: Photoelectric absorption is the process whereby a photon of energy E imparts its energy to an electron, allowing it to escape from the atom. In the process, one or more fluorescence photons (and sometimes an Auger electron) are emitted. Adapted from www.indyrad.iupui.edu/public/ radsci/R250/Assignment%20Chapter%2013.pdf

Compton Scattering

Compton scattering occurs when an electron absorbs only a portion of the photon's initial energy, resulting in the creation of a new, low energy photon that takes off in a new direction. The energy of the new photon is given by

$$E' = \frac{E}{1 + \frac{E}{m_0 c^2}(1 - \cos\theta)}, \tag{6.2}$$

where E is the energy of the initial incident photon, E' is the energy of the final photon, and $\cos\theta$ is the angle between the direction of the initial photon and the direction of the final photon. The greater the scattering angle θ, the more energy is absorbed by the electron. Incident photons with greater energies tend to result in smaller scattering angles. The probability that a photon will Compton-scatter is proportional to the electron density of the material and inversely proportional to the energy of the photon:

$$P \propto \frac{\rho_e}{E}. \tag{6.3}$$

This is the dominant process for gamma-rays with energies between about 200 keV and about 5 MeV.

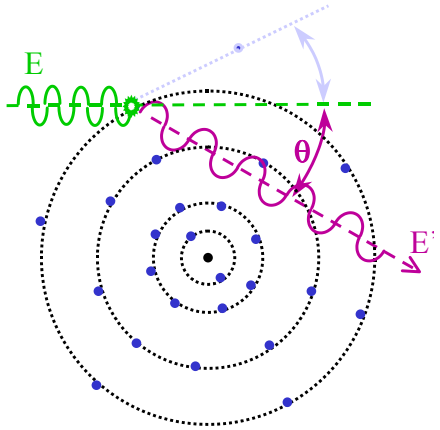

Figure 6.2: Compton scattering, whereby a photon imparts a portion of its energy E to an electron, allowing it to escape from the atom. In the process, a new photon is created with energy E'. Adapted from www.indyrad.iupui.edu/public/ radsci/R250/Assignment%20Chapter%2013.pdf

Pair Production

During pair production, a photon interacts with the strong nuclear force of an atom and creates an electron and positron in its place. Since electrons and positrons have masses equivalent to 511 keV, the photon must have at least twice that energy (or 1.022 MeV) for this process to be possible. Any energy the photon has above and beyond 1.022 MeV becomes kinetic energy for both the electron and positron. The positron doesn't last very long and annihilates fairly quickly with another electron, producing two "annihilation photons", each with an energy of 511 keV. The probability of pair production increases as the number of protons in the nucleus (Z) increases, because such atoms have a greater nuclear "strong force" which facilitates the process. Pair production is only significant for photons with energies greater than about 5 MeV.

6.1.2 What Takes Place Inside a Semiconductor Detector

When a gamma-ray photon transfers a portion of its energy to an electron in a semiconductor detector by one of the processes we've described, the electron usually carries with it a significant

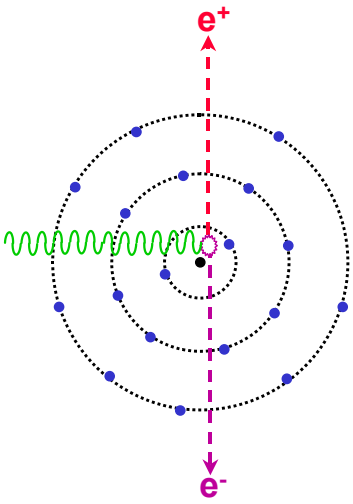

Figure 6.3: Pair production, whereby a photon is converted into a positron and an electron. Adapted from www.indyrad.iupui.edu/public/ radsci/R250/Assignment%20Chapter%2013.pdf

amount of kinetic energy. As this energetic electron collides with nearby atoms, it transfers its kinetic energy to the electrons in those atoms, liberating them as well. Soon, there is a "cloud" of free electrons and a corresponding cloud of atoms with electron vacancies (or "holes"). During normal detector operation, a bias voltage is applied between the metallized top and bottom electrode surfaces of the detector, so that an electric field exists inside the detector and the cathode is the side facing the photon source. Under the influence of this electric field, the free electrons migrate toward the bottom surface of the detector. The "holes" behave very much like free particles themselves, migrating toward the cathode (the top surface of the detector — see Figure 6.4).

The migration of these electrons and holes results in a current that begins to flow through the detector and through the Application-Specific Integrated Circuit (ASIC) to which it is coupled. This current is integrated over time and converted into a voltage pulse with a pulse height amplitude (PHA) proportional to the time-integrated current (i.e., the total charge of the electrons and holes that were created as a result of the initial photon interaction). This PHA value is then transformed into a number between 0 and 4095, recorded in the instrument's solid-state recorder, and eventually transmitted to the ground in a data stream. Usually when we refer to a PHA value, we mean the

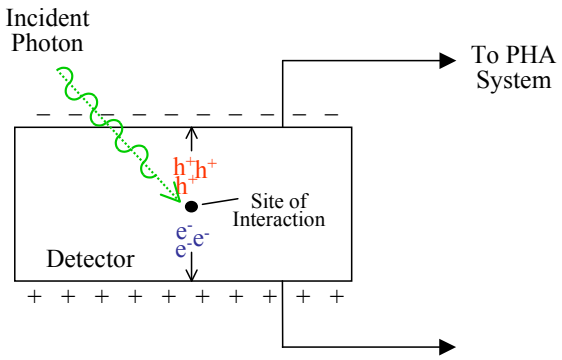

Figure 6.4: When a photon deposits energy within a detector, a cloud of electrons and of holes is generated that migrates toward the electrodes on the surface of the detector, due to the applied bias voltage.

number between 0 and 4095 that the voltage pulse height amplitude has been converted into. We often refer to each of these numbers as a "channel".

6.2 Properties of CZT Detectors

CdZnTe (or CZT) detectors are a relatively new technology that has only been around for the last 10-15 years. They have several advantages over other semiconductor materials that are commonly used for gamma-ray detection. For one thing, they have a relatively large band gap (the amount of energy required to excite a single electron-hole pair): 1.6 eV. The size of the band gap dictates the magnitude of the detector's "leakage" current simply due to thermally excited electron-hole pairs. If the band gap is low and the temperature is high, then there is enough thermal energy to excite electron-hole pairs, and it is difficult to distinguish detected photons from the counts generated by thermal energy. Silicon and germanium, which are also common semiconductor detector materials, have band gaps of only 1.1 and 0.7 eV, respectively. Thus, germanium must be cooled to cryogenic temperatures (for example, with liquid nitrogen) in order

to operate effectively as a detector. CZT, on the other hand, operates well at room temperatures ($20° - 25°$).

Another advantage of CZT is that its constituent elements (Cadmium, Zinc, and Tellurium) have large atomic numbers (48, 30, and 52, respectively). As we have seen in the last section, the probability of photon interaction is greater when the atoms involved have large atomic numbers. By comparison, silicon has an atomic number of only 14 and germanium of 32. Thus, CZT has a significantly greater detection efficiency. These two advantages—the ability of CZT to operate at room temperature and the high atomic numbers of its component atoms–are the primary reasons that CZT was selected as the material for the BAT detectors.

CZT detectors have a drawback, though—one that is common among "composite" semiconductor detectors (those made of more than one element). It relates to a phenomenon known as charge trapping. Defects within the semiconductor material result in sites at which charge carriers (electrons or holes) are trapped for a period of time that is long compared to the time over which the detector circuitry measures the induced current. As the charge carriers migrate through the detector, their numbers decrease exponentially as more and more carriers are trapped, reducing the overall current flowing through the detector. The overall reduction in integrated current depends on the depth at which the photon interaction takes place. The ability of a charge carrier (an electron or a hole) to migrate successfully through a detector depends on carrier's "mobility" μ and its "lifetime" τ. Mobility is a measure of how quickly a charge is able to move through the material when a given electric field is applied:

$$\mu = \frac{v_d}{E}, \tag{6.4}$$

where v_d is the drift velocity of the charge carrier, and E is the electric field. The typical units of mobility are $\mathrm{cm}^2/(V \cdot s)$. The lifetime of a charge carrier is defined as the average amount of time between the liberation of the charge carrier (either as a free electron or as a hole) and the charge carrier's entrapment. A useful combination of these quantities gives the average distance that a charge carrier is able to travel before being trapped:

$$\lambda = \mu \, \tau \, E. \tag{6.5}$$

Charge trapping is a phenomenon that occurs, to some extent, in all semiconductor detectors. As long as the average distance the charge carrier can travel is significantly larger than the thickness of the detector, little charge is lost. In Ge and Si detectors, this is generally the case, and λ for electrons and for holes are comparable to each other. In CZT, however, λ for holes is often a factor of 10 or more smaller than λ for electrons. In the case of the BAT detectors, for which the applied bias voltage is nominally 200 V, the average path length of electrons in the BAT detectors is on the order of 2 cm. This is much longer than the distance between the top and bottom surfaces of the detectors (2 mm), so electrons have no trouble migrating through the detectors with little charge lost. The average path length for holes, on the other hand, is much smaller—on the order of 0.2 mm—so hole trapping is significant. The voltage is applied in such a way that holes migrate toward the top surface of the detectors, so that the deeper the photon interaction occurs, the more holes are trapped before arriving at the top surface, and the smaller the overall measured signal will be.

There is an equation, known as the "Hecht relation", which gives the "effective charge" measured by the detector electronics as a function of the depth of the photon interaction:

$$\frac{Q}{Q_0} = \left(\frac{\lambda_e}{D}\right)\left[1 - \exp\left(-\frac{D-z}{\lambda_e}\right)\right] + \left(\frac{\lambda_h}{D}\right)\left[1 - \exp\left(-\frac{z}{\lambda_h}\right)\right], \tag{6.6}$$

where Q is the "effective" charge that is measured by the detector electronics, Q_0 is the charge that would have been measured if all of the charge had been collected (that is, if there had been no charge trapping), D is the thickness of the detector (in our case, 2 mm), and z is the depth of the photon interaction, where the top surface of the detector is taken to be $z = 0$ and the bottom surface is at $z = 2$ mm [42]. A plot of the charge collection efficiency (Q/Q_0) as a function interaction depth is shown in Figure 6.5.

Figure 6.5 illustrates the shape of the Hecht relation for typical values of BAT CZT detectors. One can see that photons that interact deeper in the detector result in a smaller charge collection efficiency. In the case of photons with low energies ($E < 50$ keV or so), most of the photons do not penetrate very deeply into the detector, so most interactions occur near the top surface ($z = 0$) where the charge collection efficiency is high and is nearly the same for all interactions. If we plot

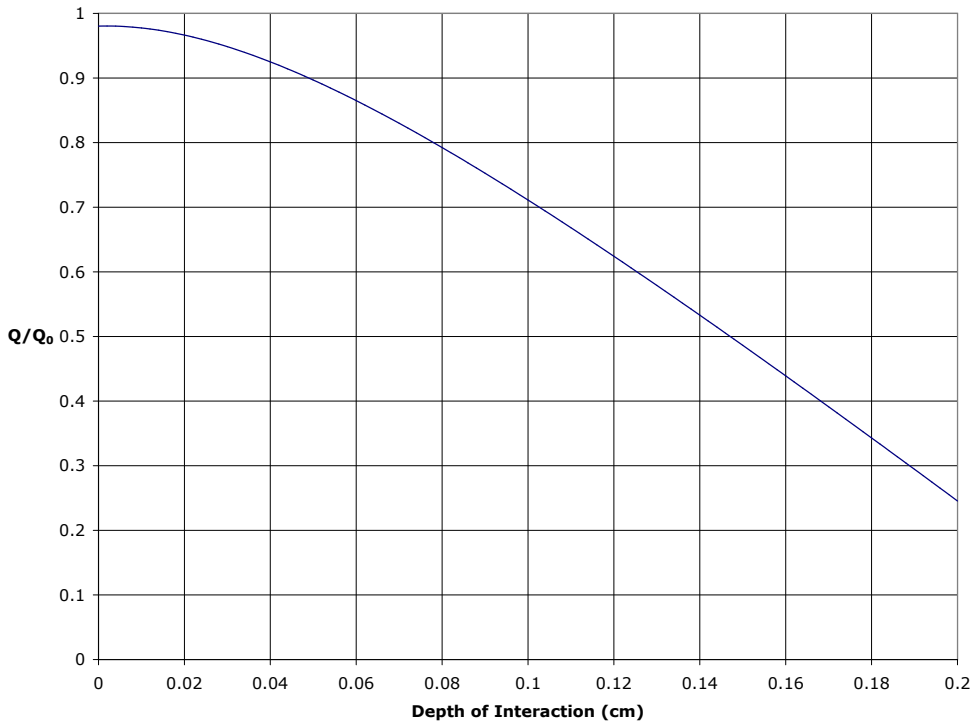

Figure 6.5: The charge collection efficiency (Q/Q_0), as given by the Hecht relation [42], as a function of photon interaction depth, for $\lambda_e = 2$ cm and $\lambda_h = 0.02$ cm. These are typical values for the BAT CZT detectors.

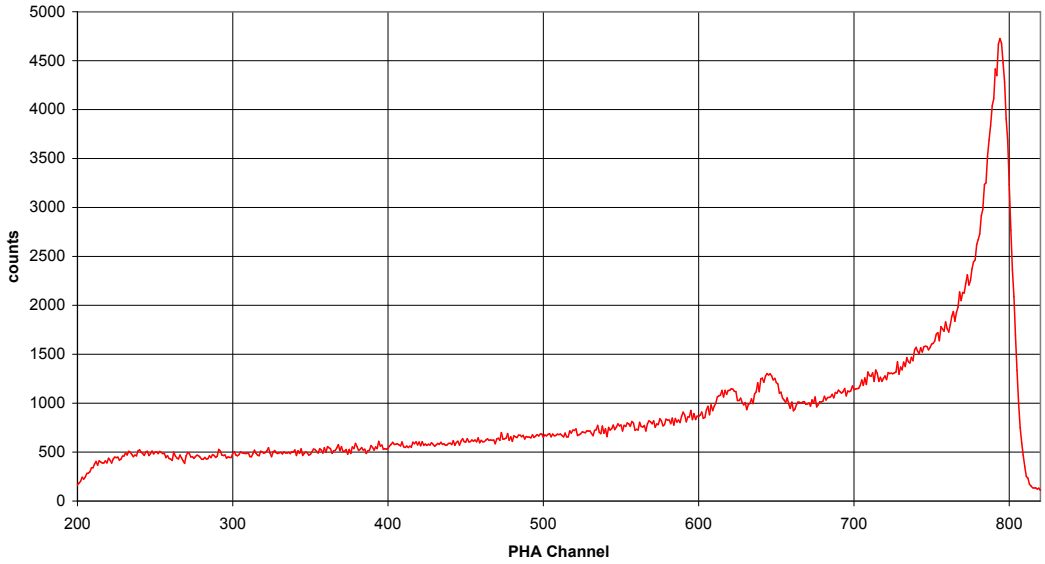

Figure 6.6: An example of a PHA spectrum from 122 keV photons interacting with a CZT detector. Peaks resulting from higher photon energies result in tails that are more pronounced. Note the two small "escape peaks" sitting on the tail of the main peak. These are discussed in section 6.3.1.

the number of events in each PHA channel as a function of PHA channel, we see a fairly narrow peak. Photons with high energies, however, are able to penetrate deeper into the detector and thus a significant number of photons produce voltage pulses that are much smaller than would have been the case if the interaction had occurred near the top surface. Instead of a narrow peak, a monoenergetic beam of these photons results in a peak with a long "tail" which extends to lower PHA values (see Figure 6.6). This "tailing effect" is the primary drawback of using CZT detectors.

6.3 Measuring the $\mu\tau$ Products

In the Hecht relation given by equation 6.6, there are two quantities that describe the charge-trapping characteristics of a detector: λ_e and λ_h. These values depend on the electric field inside

the detector (which is known) and on the product of the mobility and the lifetime of electrons and of holes ($\mu\tau_e$ and $\mu\tau_h$). In order to describe how charges are trapped within the detector, we need to know these values. Note that, for our purposes, it doesn't matter what the mobility μ or the lifetime τ of a charge carrier is—all that we need to know is their product ($\mu\tau$).

Every one of the 32,768 detectors that make up the BAT array has its own value for $\mu\tau_e$ and for $\mu\tau_h$. Our first task in calibrating the BAT instrument was to determine what those values are. This was done by measuring the PHA spectrum resulting from a beam of monoenergetic photons. The photon energy had to be sufficient so that the photons were able to penetrate all the way through the detector. From this measured spectrum, we were able to determine what $\mu\tau_e$ and $\mu\tau_h$ values were required to reproduce the shape of the spectrum. We developed a "single-detector" model that reproduces the shape of the spectrum, given a particular set of values for $\mu\tau_e$ and $\mu\tau_h$. The values of $\mu\tau_e$ and $\mu\tau_h$ were adjusted until the model spectrum matched the real one. In particular, we performed a least-squares fit of the single-detector spectral model to the measured spectrum, with the $\mu\tau_e$ and $\mu\tau_h$ values as free parameters. This process was repeated for each of the 32,768 detectors to find $\mu\tau$ values for each detector.

6.3.1 Energy Deposition Distributions

For a particular depth within the detector, the Hecht relation tells us the size (or "amplitude") of the voltage pulse generated when photons deposit their energy at that depth. But a spectrum tells us the number of voltage pulses that have a particular voltage amplitude. So in order to use the Hecht relation to create a single-detector model spectrum, we not only need a pair of $\mu\tau$ values, we also need to know how many photons deposit their energy at different depths in the detector. To determine the fraction of the incident monoenergetic photons that are absorbed at various depths in the detector, we ran a set of "Monte Carlo" simulations, in which we use a software tool called *grmcflight* to simulate a beam of monoenergetic photons interacting with a detector. This tool tracks the path of each photon as it enters the detector. As the photon travels through the detector, the program calculates the probability that it will deposit a

portion of its energy (either by photoelectric absorption or by Compton scattering) at any given position along its path. It then chooses a position (based on the calculated probabilities) at which a particular energy deposition takes place. It records the position and the amount of energy that was deposited and, if a new photon was generated in the process, it continues tracking the new photon. It continues to do this until the photon is either entirely absorbed or exits the geometry of the simulation. This simulation tool repeats this whole process for many photons, building up a long list of locations and deposited energies. After a predetermined number of photons have been tracked through the simulation, the detector is divided into 1000 "slices", and the number of photons that deposited energy in each slice is calculated and divided by the total number of photons/cm^2 that the simulation generated and by the thickness of the slice. The result is a list of 1000 numbers, each in units of cm, that represents the probability that a photon with the particular energy we simulated will deposit its energy at a given depth (see Figure 6.7). We call this list a "depth distribution" list. We repeat this whole process using 50 different photon energies, ranging from 10 keV all the way up to 9 MeV.

If a photon enters the detector directly from above, it will have a different probability of depositing its energy in a given slice than if it enters the detector at an angle (see Figure 6.8). Because of this angular dependence, we must repeat the simulations using many different incident angles. We chose 105 different incident photon angles and repeated all of the simulations described above using each of those angles. Because most of the detectors in the array are surrounded by neighboring detectors, we included a layer of CZT around the lone detector in the simulation, so that photons that are absorbed before they even reach the detector are properly accounted for (see Figure 6.9).

Another complication in the process is that a photon rarely deposits all of its energy at one location within the detector. Usually (especially at high incident photon energies where Compton scattering begins to dominate and pair production becomes energetically possible), a portion of its energy is deposited at one location and another portion at some other location. Because of this,

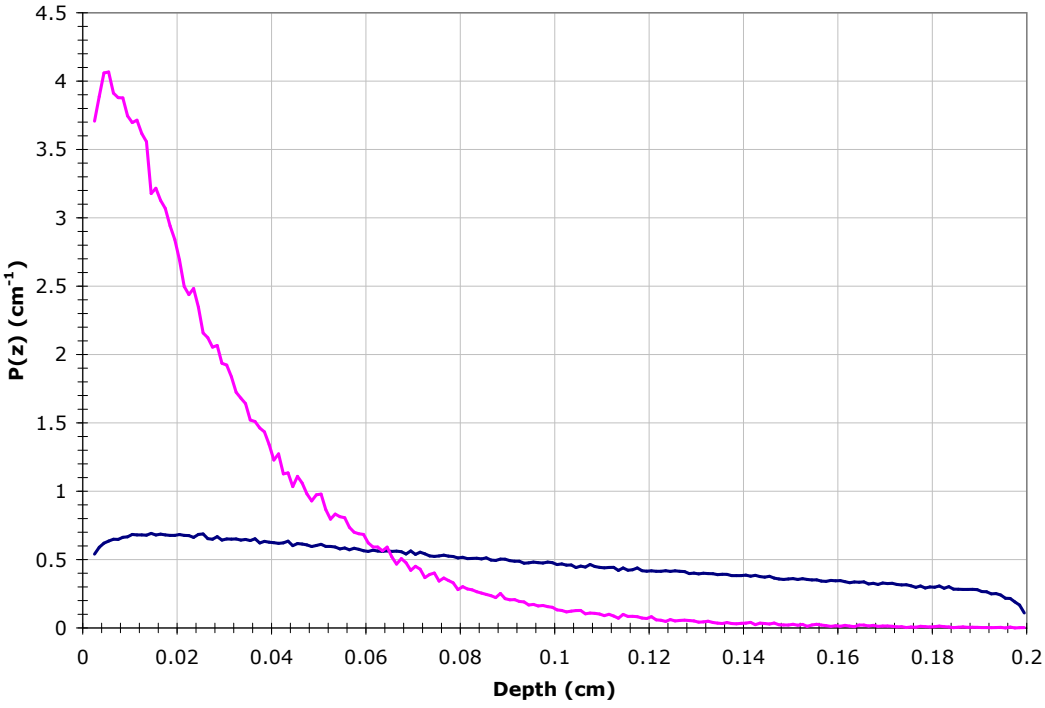

Figure 6.7: Two examples of depth distributions generated by the Monte Carlo simulations. The pink line gives the distribution for 60 keV photons and the blue line for 122 keV photons. The y-axis gives the number of photons that deposit their full energy in the detector at a given depth, divided by the slice thickness (in cm) and by the incident flux of photons (in photons/cm^2). The simulated photons all originate from above the detector in a downward-pointing, collimated beam, with a beam area sufficient to encompass the entire area of the detector.

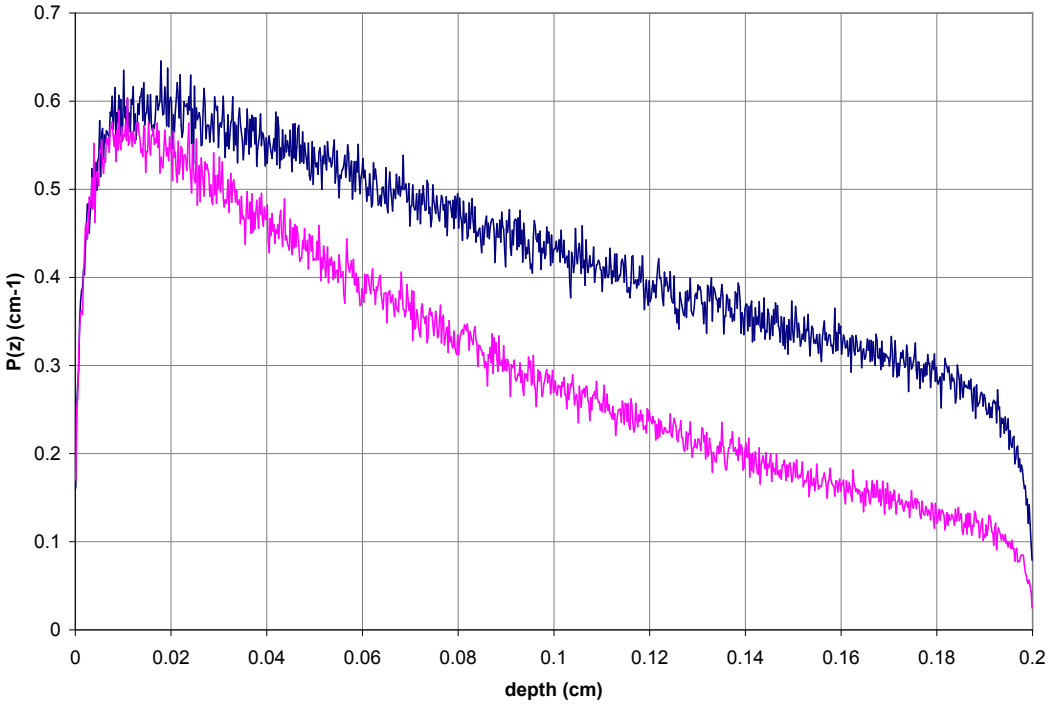

Figure 6.8: Depth distributions generated using 129 keV photons incident on a detector from two different incident angles: 0° (blue) and 61° (pink). The y-axis gives the number of photons that deposit their full energy in the detector at a given depth, divided by the slice thickness (in cm) and by the incident flux of photons (in photons/cm^2).

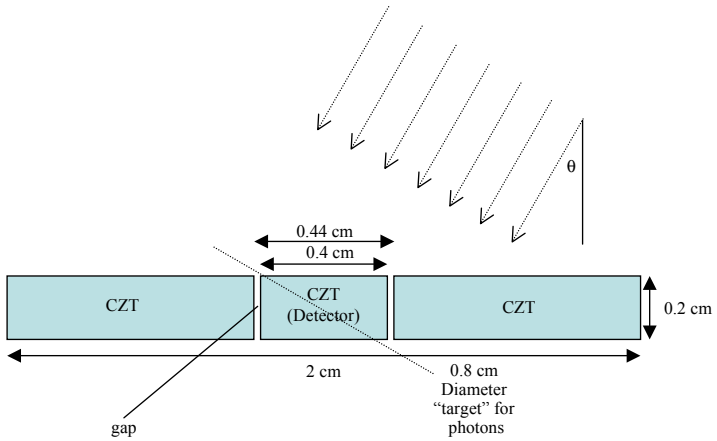

Figure 6.9: The geometry of the simulations used to generate the depth distribution lists. A stream of photons is incident from a given angle on a single CZT detector surrounded by neighboring detectors.

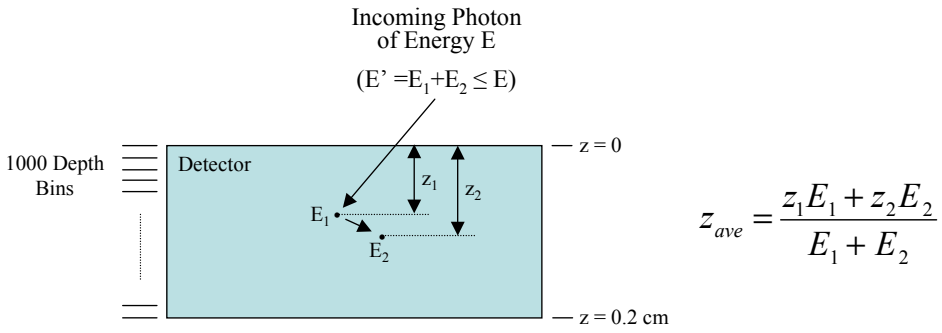

Figure 6.10: The weighted average depth at which a photon deposits its energy is calculated from the various depths at which portions of its energy are deposited.

we calculated the weighted average depth at which each photon deposited its energy:

$$z_{ave} = \frac{\sum z_i E_i}{\sum E_i}, \tag{6.7}$$

where z_i is the depth at which a particular amount E_i of the photon's energy is deposited. This average depth is the depth we counted as the one at which the photon's energy was deposited (see Figure 6.10).

Sometimes, one of the secondary photons leaves the detector entirely, so that not all of the energy of the incident photon is deposited in the detector. Compton scattering is less likely than photoelectric absorption at the energies at which the BAT array is most sensitive, so we neglect those photons that Compton scatter out of the detector. However, it is also possible for a secondary photon generated during a photoelectric absorption event to leave the detector without being reabsorbed. By far the most likely energies of these secondary photons are 27 keV and 31 keV, which result when the incident photon interacts with an electron in the innermost shell (the K shell) of either a Cd or a Te atom. We therefore keep track of all incident photons that deposit all of their energy **except** 27 or 31 keV. These interactions produce small so-called "escape peaks" in the measured spectrum that appear to have energies equal to 27 keV and 31 keV less than the incident photon energy (see Figure 6.6). We record the events associated with these escape peaks in separate depth distribution lists. In the end, we have a set of 15,750 depth distribution lists—a

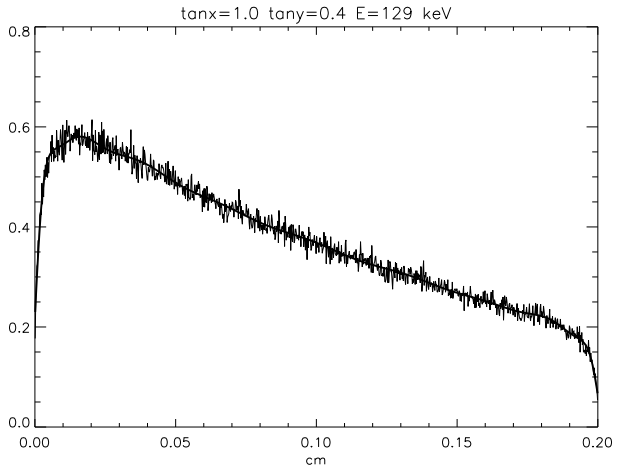

Figure 6.11: A full-energy depth distribution for 129 keV photon incident on a detector, fit to a 20th-order polynomial. The depth distributions corresponding to lower photon energies, especially at large incident angles, have fairly sharp features which are also well-fit by a 20th-order polynomial.

full-energy list, a Cd K-escape list, and a Te K-escape list for each energy and angle.

These depth distributions take up a fair amount of computer memory— 15,750 distributions $\times$ 1000 numbers per distribution $\times$ 8 bytes per number, which comes to about 120 MB. To reduce the size of the file that stores these numbers, we fit the distributions to a 20th-order polynomial. This enabled us to store 20 numbers (the coefficients of the polynomial) for each distribution instead of 1000 numbers, reducing the memory required by a factor of 50. A 20th-order polynomial is able to fit the shape of the distribution sufficiently well to reproduce the essential features of the distribution's shape (see, for example, Figure 6.11).

6.3.2 The Single-Detector Spectral Model

With a depth distribution and a set of $\mu\tau$ values, we have everything we need to generate a model spectrum for a given incident photon energy and a given detector. We begin by evaluating the Hecht relation at the center of each of the 1000 slices into which we have divided our detector. This tells us the charge collection efficiency resulting from photons that deposit their energy at those depths. For a given incident photon energy, the charge collection efficiency is proportional

to the voltage pulse height amplitude, or PHA channel:

$$PHA = K \cdot \left(\frac{Q}{Q_0} \right). \tag{6.8}$$

For our single-detector model spectrum, we are free to choose the scale of the PHA channels, so we can define the proportionality constant K any way we wish. For convenience, we chose K such that a full charge collection ($Q = Q_0$) would place a count in a PHA channel with a value equal to 4 times the energy that is deposited:

$$PHA = 4 \cdot E \cdot \left(\frac{Q}{Q_0} \right). \tag{6.9}$$

With this choice, a 122 keV photon that deposited all of its energy and for which the full charge was collected would result in a count in PHA channel 488. Since the charge trapping properties of our detectors never permit a full charge to be collected, the peak resulting from 122 keV photons would actually lie at a PHA channel that is somewhat smaller than 488. With our PHA channels defined in this way, we simply place the values from the depth distribution into the PHA channels corresponding to the charge collection efficiencies of those depths. Because of random fluctuations in the electronics, a range of voltage pulse amplitudes may result from a set of interactions, even if those interactions all occur at the same depth and all deposit the same amount of energy. This results in peaks that are somewhat "smeared out". This is known as energy resolution. We include, in our single-detector model, a parameter which dictates the width of the energy resolution. We generate a Gaussian-shaped peak with this width and convolve this peak with the spectrum. This produces the desired energy resolution effects.

6.3.3 Correcting for Electronics Nonlinearity

As we described in section 6.1.2, the voltage pulses that are produced when energy is deposited in a detector are transformed into PHA values that range from 0 to 4095. Because of the properties of the ASIC circuitry that measures these voltage pulses, the resulting PHA values are not directly proportional to the amplitudes of the voltage pulses (we can't simply say that the signal which was transformed into a PHA value of 2000 is twice as large as the signal which

was transformed into a PHA value of 1000). This is known as electronics nonlinearity. Before we can directly compare a single-detector model spectrum with a real spectrum, we need to apply a correction for this nonlinearity, so that the PHA values **are** directly proportional to the voltage pulses. This is done by measuring the positions of peaks resulting from a set of voltage pulses with known amplitudes that are sent through the ASIC circuitry. For instance, in a particular detector, we may find that a 0.5 V pulse results in a peak that is centered at a PHA channel of 1500. By repeating this for several voltage pulses, we can determine the relationship between PHA channel and voltage pulse, which turns out to be well approximated by an equation of the form V=a·(PHA)^3 + b·(PHA)^2 + c·(PHA) + d. We use this relationship to help define a new set of "corrected" PHA values that **are** directly proportional to the amplitude of the voltage pulses, and we "rebin" the spectra by redistributing the counts in the original PHA channels into the appropriate "corrected" PHA channels.

As illustrated in Figure 6.12, the position of the model peak is quite sensitive to the value of $\mu\tau_e$, while the value of $\mu\tau_h$ strongly affects the prominence of the tail. Since λ_e and λ_h in equation 6.6 are both proportional to the electric field E within the detector, a change in E affects both λ_e and λ_h. Therefore, a change in the bias voltage applied to the detector influences the spectral shape. As the bias voltage increases, the peak channel approaches some limit (which we label CH_{max}) which corresponds to the channel at which the efficiency given by the Hecht relation becomes unity. Also, at higher bias voltages, the tail structure is reduced. By fitting our single-detector spectral model to multiple spectra measured with different bias voltages, we can obtain values for $\mu\tau_e$ and $\mu\tau_h$.

For our measurements, we illuminated each detector with photons from a ^{57}Co source, which emits 14.4, 122.1 and 136.5 keV photons (the most prominent being 122.1 keV photons). For each detector, we made three measurements: one with a bias voltage of 100 V, another of 200 V, and a third of 300 V. To minimize counts resulting from photons that Compton scattered off of other materials in the vicinity before entering the detector, we restricted our fitting region to the portion of the spectrum above the escape peaks. The temperature for all three measurements was held at

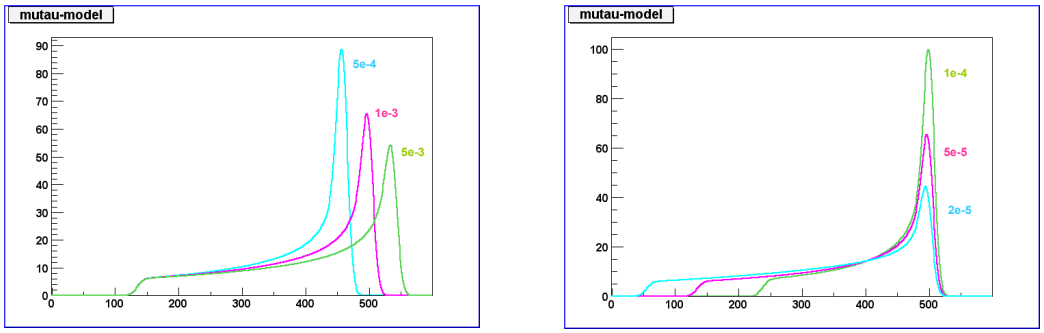

Figure 6.12: The dependence of the model peak shape on different values of $\mu\tau_e$ and $\mu\tau_h$ (given here in units of cm^2/V). Different values of $\mu\tau_e$ (left panel) strongly affect the position of the peak, while different values of $\mu\tau_h$ strongly affect the prominence of the tail.

20°C, the nominal operating temperature of the detectors in orbit.

The results of our measurements are shown in Figure 6.13. Note that the $\mu\tau_e$ values range from about 10^{-3} to 10^{-2} cm^2/V, whereas the $\mu\tau_h$ values are much smaller, ranging from about 10^{-5} to 10^{-4} cm^2/V. We discovered that detectors grown from the same crystal ingot tended to have similar values for $\mu\tau_e$, but that $\mu\tau_h$ varied widely from detector to detector even within the same ingot.

6.4 Determining the Energy Scale

Even after the rebinning process described in section 6.3.3, the PHA channels at which the peaks of each particular photon energy are centered differ significantly from one detector to another. In one detector, the 122 keV peak may lie at PHA channel number 500, whereas in another detector, the 122 keV peak may lie at PHA channel number 450. The primary cause of these energy scale differences is variations in $\mu\tau$ values (particularly $\mu\tau_e$) from one detector to the next, as illustrated in Figure 6.12. As we've seen from the Hecht equation in Section 6.2, different $\mu\tau$ values result in different maximum charge collection efficiencies.

In Section 5.2.3, we described how a mask-weighted count rate could be generated by combining the count rates from each individual detector in such a way that background counts are

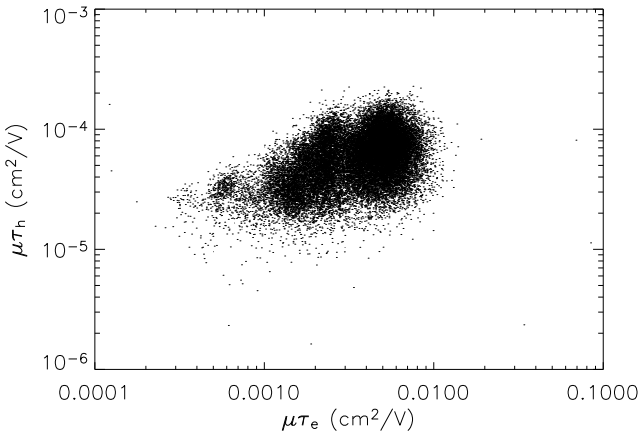

Figure 6.13: A plot of the $\mu\tau_e$ and $\mu\tau_h$ values measured for the 32,768 detectors that make up the BAT array

.

removed. It is possible to use the same process to combine individual detector spectra to build up a background-subtracted, mask-weighted spectrum. Before we can combine the spectra from each detector, however, we need to adjust each spectrum so that all of the peaks corresponding to a given incident photon energy appear at the same PHA channel. In section 6.3.3, we described a process in which we defined a new set of PHA channels that are proportional to the voltage amplitude of the signal generated in the ASIC. This time we use a similar process to define a set of PHA channels that are proportional to the peak energy, so that for every detector, a photon of a given energy always produces a peak centered at the same PHA channel. We do this by finding a relationship between peak energy and PHA channel:

$$E = f(PHA), \tag{6.10}$$

defining a new set of channels (which we shall label "PHA′") that are proportional to the peak energy:

$$PHA' \propto E, \tag{6.11}$$

and rebinning the spectra into these new PHA′ channels.

Finding the specific relationship described by equation 6.10 is done in several steps. First, we find the PHA channels at which several calibration source energy peaks are centered. We use

photons from an ^{241}Am source (which emits 59.5 keV photons, among others), a ^{133}Ba source (which emits 30.9 keV and 81 keV photons), a ^{109}Cd source (which emits 22.1 keV photons), and a ^{57}Co source (which emits 122.1 keV photons). We use these PHA channels along with the relationship between voltage amplitude and PHA channel found previously (as described in section 6.3.3) to find a relationship between voltage pulse amplitude and peak energy. This relationship is well-approximated by a linear function:

$$V = G \cdot E + O, \tag{6.12}$$

where G and O are constants, E is the photon energy, and V is the voltage pulse that is produced by that photon energy that results in a peak in the spectrum. This equation can be combined with the relationship between V and PHA described in section 6.3.3 to derive a relationship between E and PHA that has the form:

$$E = A \cdot (PHA)^3 + B \cdot (PHA)^2 + C \cdot (PHA) + D, \tag{6.13}$$

where A, B, C, and D are constants. This process is repeated for each of the 32,768 detectors.

We have described how some of the properties of the detectors (for example, the energy resolution) depend upon their temperature. The relationship between peak energy and PHA channel (equation 6.13) is also temperature-dependent. By measuring the 122 keV peak position at different temperatures, we have found that the constant G in equation 6.12 increases by between 1% and 4% (depending on the detector) when the temperature is reduced from 20°C to 4°C. This is one reason that the temperature of the detectors is carefully maintained at 20°C.

6.5 The Angular Dependence of the Peak Shape

In section 6.3.1, we described the need to find the depth distributions resulting from photons illuminating a detector from several different angles, and Figure 6.8 gives an example, illustrating the depth distributions for 129 keV photons when the photons are incident on the detector from directly above the detector and also from angle of 61°C. We expect fewer photons overall to interact in the detector when the photons are incident at an angle (because the area intersected by the

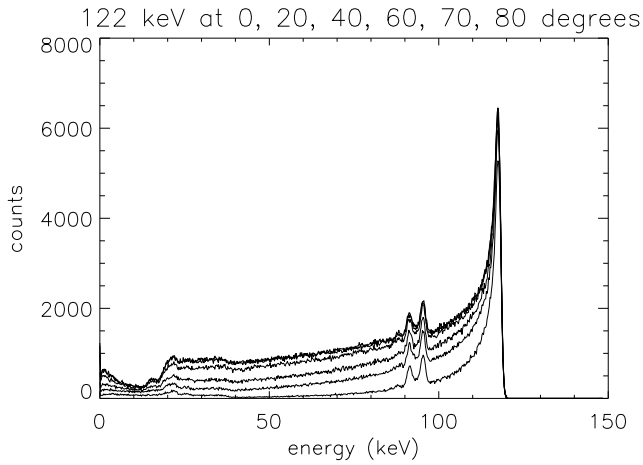

Figure 6.14: Simulated spectra from 122 keV photons incident on a detector from various angles. As the angle increases, the tail becomes smaller.

stream of photons is smaller). There are also good physical reasons to suspect that the overall shape of the peak will be different depending on the angle of the incident photons. A photon that is traveling through a detector at an angle is able to travel the same average distance before being absorbed as a photon that is incident on-axis, but because it travels at an angle, it does not penetrate as deeply into the detector. For this reason, when photons are incident at larger angles, a larger fraction deposit their energy near the top surface of the detector. As we note in Figure 6.5, photons that penetrate deeper into the detector result in a smaller charge collection efficiency. These are the photons that contribute to the tail of the peak. As a result, the tail is not as prominent when photons are incident at a larger angle. Figure 6.14 shows a set of simulated spectra resulting from 122 keV photons incident at various angles. As the angle increases, the tail becomes smaller. Note that for small angles (less than about 40° or so), the effect is quite small.

Most of the detectors in the array are surrounded on all sides by other CZT detectors, but due to engineering considerations, the detectors are clustered in groups of 128 detectors, with gaps separating each group from the others (see Figure 6.15). If photons are incident on the array at an angle, detectors on the "front" (or "leading") edges of these groups will have their sides illuminated more than those that are surrounded by photons. This means that more will interact at greater

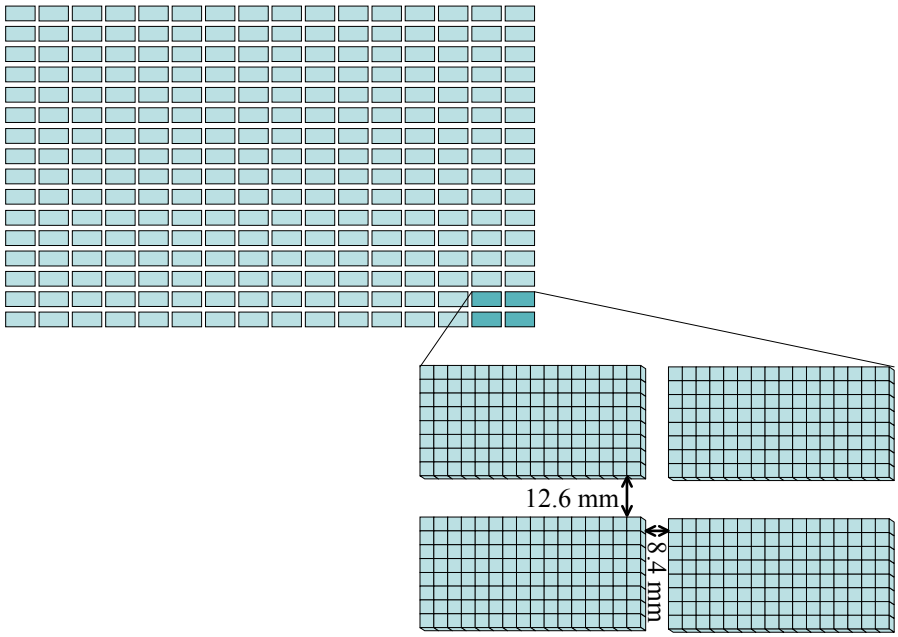

Figure 6.15: The array is divided into groups of 128 detectors that are separated from each other by gaps.

depths in those leading edge detectors, contributing more to the tail in their spectra. Differences in the spectra of these leading edge detectors and those of other detectors do not become significant until the incident angle reaches about 60° or so.

The spectra from all of the detectors are summed (weighting them by their mask weight factors) to produce a composite spectrum. Leading edge detectors only make up 18% of the total array, so when they are combined with the rest of the detectors, the overall affect these differences have on the shape of the composite spectrum is negligible.

6.6 Adjusting for Distance and Angle Variations

The spectral model we have discussed so far is a single-detector model, able to reproduce the shape of the spectrum from a single detector. Since the spectra from all of the detectors are

combined in a mask-weighted sum, we need a full-array spectral model that can reproduce the shape of the composite spectrum. To assist us in creating this full-array spectral model, we used BAT to measure the real gamma-ray spectra from radioactive sources that emit photons at specific energies. We placed these sources in different positions relative to the detector array and measured their spectra. Usually, the sources were placed at a distance of about 3 meters above the array.

When a source is placed 3 meters directly over the center of the array, detectors at the farthest corners of the array are slightly farther from the source (308 cm) than detectors at the center of the array (300 cm). This means that the number of photons/cm^2/s that fall on these detectors will be smaller than those at the center of the array by a factor of $300^2/308^2 = 0.95$. This isn't a large difference, but it is significant, and when the source is not directly above the center of the array, the difference is larger.

Furthermore, photons from the calibration source approach different detectors at different angles. When photons are incident on the top surface of a detector at an angle, the projection of the area perpendicular to the incident photons is smaller than when photons are incident from directly above, by an amount $\cos\theta$ (see Figure 6.16).

Both of these effects result in differences in the total number of photons that hit detectors at different positions on the array. In orbit, photons come from so far away that these differences are undetectable. We must correct for these differences before combining the spectra so that our ground measurements will give us an accurate idea of how the spectra from distant sources will look. We correct for differences in illumination angle and distance to the source done by multiplying the count rate observed in each detector by a correction factor:

$$\left(\frac{r_d^2}{C_{angle,d}}\right)\left(\frac{C_{angle,c}}{r_c^2}\right), \tag{6.14}$$

where the subscripts "d" and "c" refer to the detector to which the factor is being applied and to the center of the array, respectively, r is the distance from the source to the detector (or to the center of the array), and C_{angle} is a constant that is equal to the perpendicular area visible to the incident photons at the detector (or at the center of the array) divided by the full area of the top surface of the detector (0.16 cm^2). (C_{angle}) is approximately equal to $\cos\theta$, but since photons at

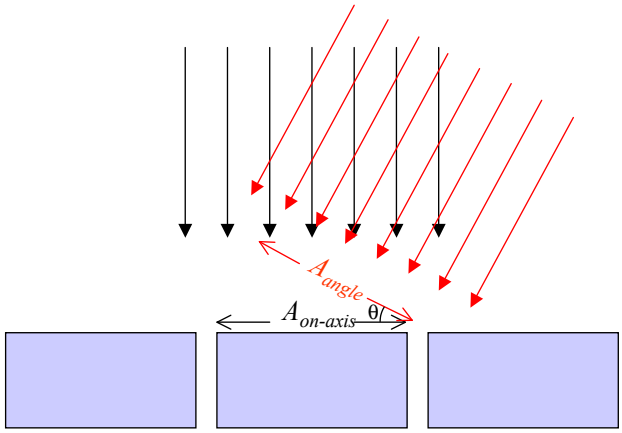

Figure 6.16: Photons that are incident from directly above a detector intersect an area of $A_{on-axis}$ (= 0.16 cm^2), whereas photons that are incident from an angle θ intersect an area of A_{angle}, where $A_{angle} = A_{on-axis} \cdot \cos\theta$ (plus a little bit, due to the edges of the detector being visible).

an angle will intersect the sides of the detectors to a certain extent, there are two terms that are included to account for this:

$$\begin{aligned} C_{angle} = & \cos\theta_z \\ & + \min\left[0.15, 0.05 \cdot \left|\frac{z_s}{x_s}\right|\right] \cdot \cos\theta_x \\ & + \min\left[0.15, 0.05 \cdot \left|\frac{z_s}{y_s}\right|\right] \cdot \cos\theta_y, \end{aligned} \tag{6.15}$$

The overall result of multiplying the spectrum from each detector by the factor given in equation 6.14 is that it adjusts the overall height of each detector spectrum to what it would have been if the detector were at the center of the array.

6.7 The Full-Array Spectral Model

In the beginning of the last section, we described the need for a full-array spectral model that can reproduce the shape of the mask-weighted summed spectrum. This is somewhat different from the single-detector spectral model we've discussed up to this point. The single-detector model reproduces the shape of a peak resulting from the photoelectric absorption of photons of a given

energy in a single detector, and it depends on the $\mu\tau_e$ and $\mu\tau_h$ values of the detector. As we saw in Figure 6.13, these values are very different from one detector to another.

The full-array spectral model must be a combination of the single-detector spectral models of all of the detectors in the array. One way to generate this full-array model spectrum would be to compute the single-detector model spectrum for every detector, and then take the average of these spectra, but generating so many computing so many spectra would be very computationally intensive. So instead, we divide Figure 6.13 into 35 regions and use the average $\mu\tau$ values in each region to calculate a model spectrum for that region. Then we combine the 35 spectra, weighting each one according to the number of detectors within the corresponding region. This produces a full-array model spectrum that matches the real data reasonably well.

Another matter we must consider for our full-array spectral model is the absorption due to passive material in the BAT FOV that might reduce the number of photons/cm^2/s hitting the detector array. There are several materials that lie between the photon source and the array. These include a Multi-Layer Insulation (MLI) needed for thermal control, a wire grid that maintains the bias voltage, epoxy dots that hold the grid in place, the mask structure to which the lead tiles are fastened, and layers of thin conducting materials intended to protect the array from stray electrical discharges. All of these materials absorb gamma-ray photons. Our full-array model therefore includes a calculation of the fraction of photons that will successfully arrive at the array. This fraction depends on what materials the photons pass through and how thick they are, and it is also a function of photon energy. When we are making measurements on the ground with radioactive calibration sources, the air between the source and the detectors also absorb photons, so we must also include this in our calculation. Rather than perform this calculation for each individual detector, we make the assumption that the absorption at different detector positions is about the same, and we simply calculate the absorption for the center of the array. More detailed calculations have shown that this assumption is reasonable.

There are 7 parameters required for our full-array spectral model:

- A parameter that specifies the energy resolution. This is defined as the standard deviation

(σ) of the best-fit Gaussian function that is convolved with the peaks to smear them out.

- Two parameters that enable the model peak positions to be slightly adjusted by a factor of $C \cdot E^I$, where we label C the "gain coefficient" and I the "gain index". If no adjustment were needed, C would be 1 and I would be 0. The best fit parameters were indeed found to be close to 1 and 0, respectively.

- Three parameters that add an extra "tail" component to the peaks at lower energies. It was found during the fitting process that our model was unable to provide a good fit to the ^{133}Ba 31 keV peak. The real data seemed to show a large tail that our model didn't predict. Consequently, we incorporated an empirical exponential tail into the model of the form

$$F(PHA) = A \cdot \exp\left(\frac{PHA - PHA_{peak}}{PHA_{peak} \cdot \lambda}\right), \tag{6.16}$$

$$\text{with } A = C \cdot \left(\frac{\max(E, E_0)}{E_0}\right)^I$$

  where PHA_{peak} is the PHA channel at which the photopeak generated by photons of energy E appears, $E_0 = 31$ keV, C is a constant which we label the "exponential tail coefficient", λ is a constant which determines how steeply the exponential tail falls off, and I is a constant which we label the "exponential tail index". The overall prominence of the exponential peak (as quantified by A) becomes smaller as the photon energy E increases, so the exponential tail is less pronounced at higher energies. A portion of the counts in the main photopeak (equal to A) is removed, and then $F(PHA)$ is added to the spectrum.

- A parameter that adjusts the overall normalization of the entire spectrum, which we label the "normalization adjustment". This is a value that is multiplied to the model spectrum, so that if no adjustment were necessary, it would be equal to 1.

A ^{133}Ba source was placed at 57 distinct positions, and measurements were taken with the BAT instrument (see Figure 6.17). ^{133}Ba emits photons with four energies that are within the range in which the BAT is particularly sensitive: 31 keV, 35 keV, 53 keV, and 81 keV. The two

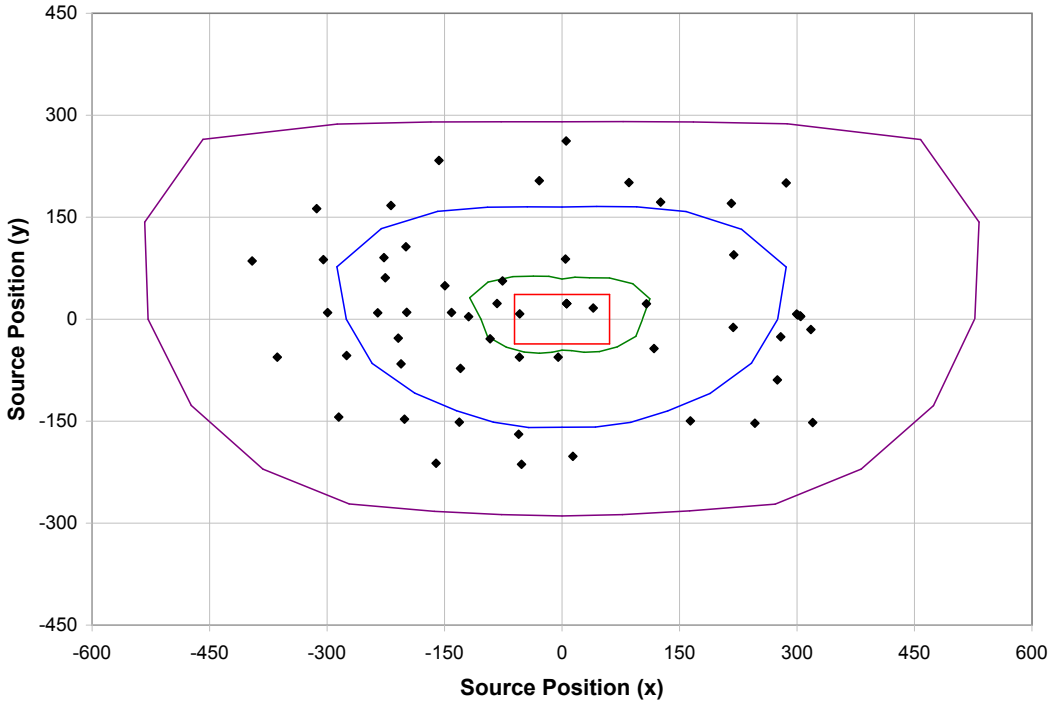

Figure 6.17: The positions of the 57 ^{133}Ba spectra measured with the BAT instrument for calibration purposes are shown here. The sources were placed at various distances from the detector array, but most were placed about 300 cm above the array. This plot shows the positions of these sources, in coordinates centered at the detector array. For reference, the position of the detector array is outlined in red. The UVOT and XRT are located in the +y direction from the detector array. Depending on the position of the source, a certain fraction of the detectors are illuminated through the mask. Those points inside the green contour illuminate the entire array. Such points are "100% coded". Points lying on the blue contour would illuminate exactly half of the array (that is, for half of the detectors, the graded-Z shield would lie between the source and the detector). These points would be "50% coded". For any points outside the purple contour, the shield would lie between the source and every detector in the array (that is, they would be "0% coded").

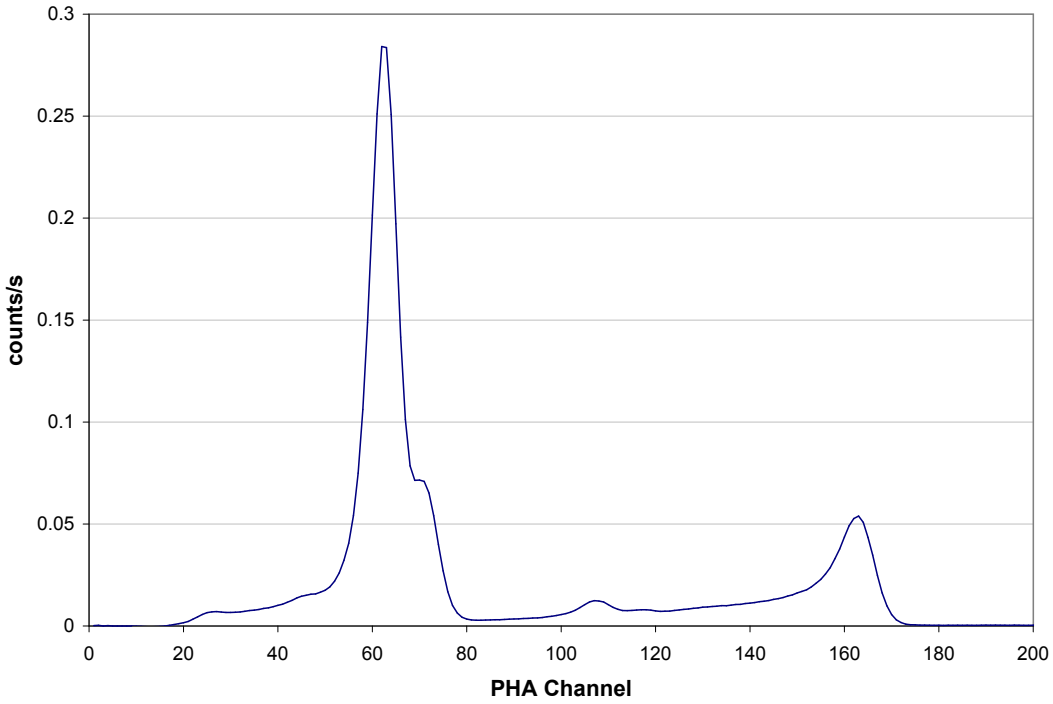

Figure 6.18: A typical composite spectrum obtained by measuring the photons incident on the BAT array from a ^{133}Ba source. ^{133}Ba emits photons at 4 energies to which BAT is particularly sensitive: 31 keV, 35 keV, 53 keV and 81 keV. the 31 keV and 81 keV peaks are the most prominent (peaking at PHA channels of 62 and 163, respectively). The 53 keV peak shows up as a very small peak at a PHA channel of 107, and the 35 keV peak shows up at a channel of 70, right next to the 31 keV peak and almost unresolvable from it.

most prominent lines are at 31 and 81 keV. Figure 6.18 shows a typical spectrum measured at one of these positions. The source emits about 6×10^7 photons/cm^2/s in all directions at these four energies, resulting in about 59 photons/cm^2/s at the center of the array when the source was placed 300 cm above it. A duration of about 600 s was required to accumulate spectra with sufficient counts to perform a good fit. Once the spectra were measured, they were adjusted using the procedures described in sections 6.4 and 6.6 so that they could be combined, and then they were added together, weighted by their mask-weighting factors. The full-array spectral model was calculated and compared to the real combined spectrum, and the 7 parameters described above were adjusted until the model spectrum matched the real one. This process involved a least squares fit of these 7 free parameters using the Levenberg-Marquardt algorithm. Of the 57 measurements

Table 6.1: The mean and standard deviations of the 7 full-array model fit parameters

Parameter	Mean	Standard Deviation	% Standard Deviation
sigma	1.345 keV	0.03550 keV	2.6%
gain coefficient	1.014	0.002842	0.28%
gain index	-0.002140	0.0005344	25%
exponential tail coefficient	0.2197	0.02975	14%
exponential tail index	1.957	0.7318	37%
exponential tail λ	0.2768	0.05422	20%
normalization adjustment	1.069	0.05546	5.2%

made, 39 resulted in good fits and 18 of the measurements were excluded from the sample for reasons such as improper measurement setups or unreasonable fit values. Table 6.1 gives the mean values and the standard deviations for the 7 fit parameters. As you can see, in some cases, there was a significant spread in the measured parameters. Our original expectation was that a smooth variation with source position would be present in these parameters. In fact, when the measurements were made, we found no clear correlation between the parameters and the positions of the source. This led us to conclude that either (1) the parameters vary with source position on a very small scale—much smaller than the distance between measured source positions, or (2) the variations seen in the fit parameters are smaller than the uncertainties in those fit parameters.

After we derived these parameters using our ^{133}Ba measurements, we checked the results against measurements with other calibration sources. We noticed that the model wasn't able to reproduce the position or width of the peak resulting from the 122 keV photons produced by ^{57}Co. This prompted us investigate whether we needed a better functional form for the factor used to adjust the peak positions than the power law function we had assumed (of which, the coefficient and index were among the 7 parameters in our fit). It also prompted us to investigate whether the energy resolution was a function of photon energy. We measured the required position adjustment factor and energy resolution width σ for several calibration peaks ranging from 14 keV all the way to 384 keV. We then found functions that reproduced these values (see Figures 6.19 and 6.20).

These functions were incorporated into our model, and we found that it was able to reproduce the measurements at photon energies above 80 keV much more accurately.

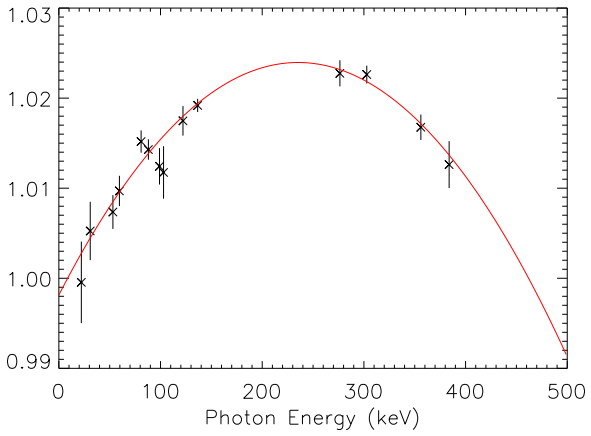

Figure 6.19: The peak position adjustment factor, as a function of photon energy. We found that a quadratic function of the form $(-4.66 \times 10^{-7})E^2 + (2.19 \times 10^{-4})E + 0.998$ adequately fit the data points.

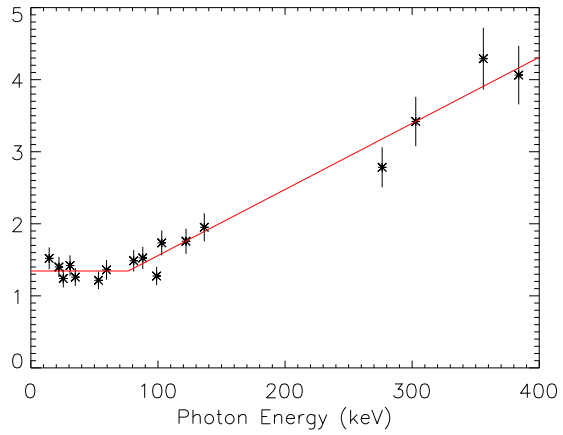

Figure 6.20: The energy resolution width "sigma", in units of keV, as a function of photon energy. We found that a constant value of 1.35 keV up to a photon energy E of 77 keV and a linear function of the form $0.00918E + 0.641$ beyond E=77 keV adequately fit the data points.

6.8 On-Orbit Calibration Results

After Swift was launched, we began making measurements of astrophysical sources. One source in particular with a well-known measured spectrum in the BAT energy range is the Crab Nebula. It emits a spectrum of photons in which the number of photons N varies with photon energy E according to

$$\frac{dN}{dE} = A \cdot \left(\frac{E}{1 \text{ keV}} \right)^{I}, \tag{6.17}$$

where $A = 10.17$ photons/cm^2/s/keV and $I = 2.15$. We made several measurements of the Crab spectrum by orienting the BAT instrument at 40 different angles relative to the position of the Crab Nebula. We then compared the spectrum we measured with the spectrum we expected to measure (the spectrum predicted by our model).

Figure 6.21 shows the measured spectrum vs. the model spectrum for one particular measurement. One thing we note right away is that the regions where the model is less accurate are also just outside the range of the ^{133}Ba photon energies where we primarily focused our calibration efforts.

To correct these problems, we developed an empirical correction model which consisted of three parts:

1. a parameter that makes it possible to include extra absorption that may be present but which we didn't originally account for,
2. a parameter that dictates to what degree edges of the lead tiles affect the absorption,
3. a six-degree polynomial function which, when multiplied to the model spectrum of the Crab Nebula, "forces" it to match the measured spectrum.

The first two components of this correction model are motivated by actual, physical processes that we expect may be at play. It is conceivable that extra absorptive material may be present, and we know that the edges of the lead tiles play some roll in reducing the number of photons arriving at the detector array. The last component is entirely empirical, without any attempt to explain it in terms of known physical processes (though this only reflects our ignorance of what

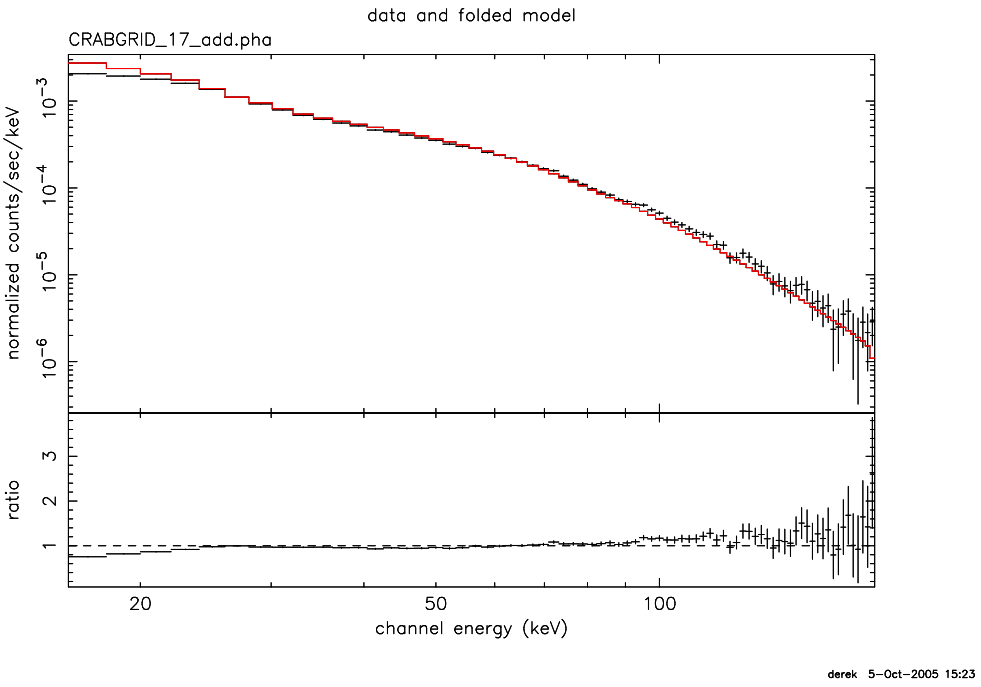

Figure 6.21: A measurement of the Crab Nebula spectrum (black), along with our model of the Crab Nebula spectrum (red). Our model is a bit high for PHA channels corresponding to photon peak energies below about 25 keV and a bit low for PHA channels corresponding to photon peak energies above about 90 keV. To adjust for these differences, an empirical correction model was applied.

processes are not being accounted for by our model). The empirical correction model involves 8 free parameters which are derived by comparing the Crab spectrum from our full-array spectral model to the actual Crab spectrum measured at five different positions relative to the BAT array. Although this correction model enables us to reproduce the measured Crab Nebula spectrum, it is imperfect for astrophysical sources with spectra that are much different from that of the Crab. Ongoing efforts seek to understand the physical reasons behind the need for this empirical correction model, so that they can be more properly accounted for.

Using this empirical correction, we compared the model spectrum to the measured spectrum for each of the different Crab measurements. By allowing the spectral index and the normalization to vary in the model, we fit the model to the measured data to determine whether the best-fit spectral index and flux from the Crab Nebula matched the known canonical spectral index and flux. The results are shown in Figures 6.22 and 6.23. There is some spread in the best-fit values, and in some cases the best-fit value is farther from the true value than the size of the error in the best-fit value would permit. There is also a slight systematic drift to higher photon indices at greater angles. In general, though, the measured values are fairly consistent with the best-fit values.

6.9 The Purpose of a Response Matrix

Up to this point, we have described in detail the single-detector and full-array spectral models that we have developed which reproduce the spectra generated by the BAT instrument. But so far, we have said nothing of their purpose. We shall now describe why we need such a spectral model.

If life were simple, photons of a given energy that come in contact with a detector would all deposit all of their energy in the detector, and the electrical signal generated by the detector would always have the same amplitude. Thus, photons of a given energy would all result in counts in a particular PHA channel. It would be very easy to interpret the measured PHA spectrum because it would exactly resemble the spectrum of incident photons. As we have seen, though, life is not

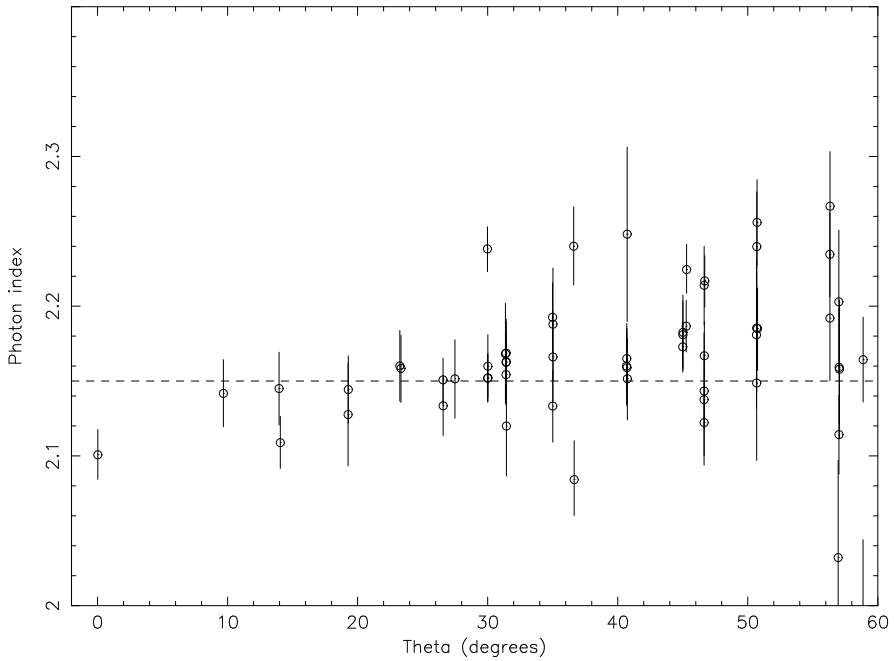

Figure 6.22: θ verses best-fit photon index for the Crab spectrum measurements. The horizontal dashed line indicates the known "canonical" value of the Crab spectrum photon index. Ideally, all of the measurements would fall right on that line.

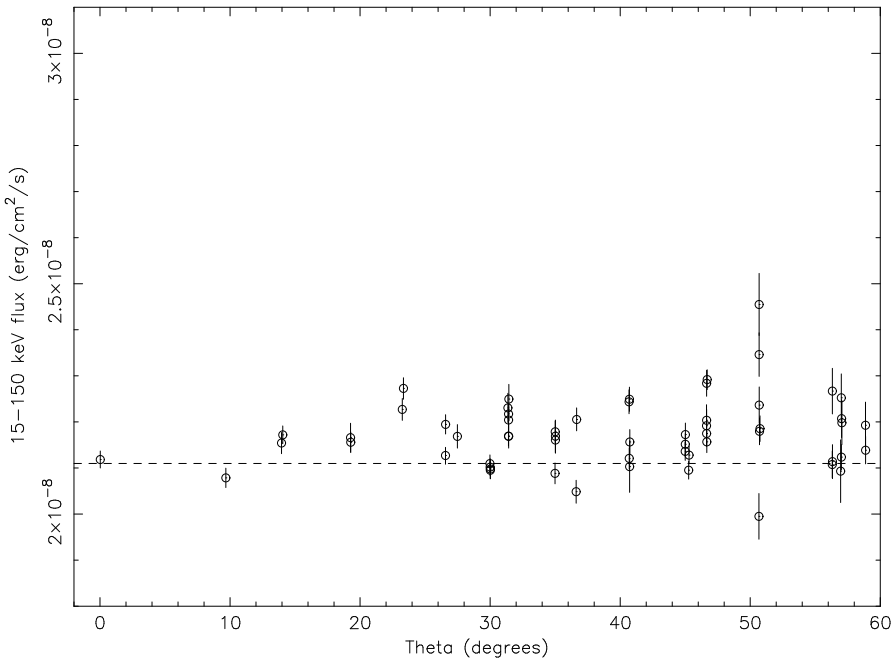

Figure 6.23: θ verses best-fit 15-150 keV flux for the Crab spectrum measurements. The horizontal dashed line indicates the known "canonical" 15-150 keV flux from the Crab Nebula. Ideally all of the measurements would fall right on that line.

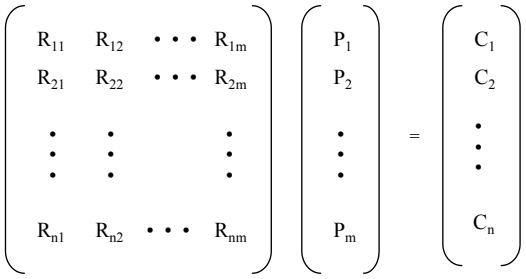

Figure 6.24: An m × n response matrix transforms an m-element photon spectrum into an n-element count spectrum.

so simple. A stream of monoenergetic photons results in a PHA spectrum with counts in many different PHA channels. Therefore, a stream of photons of many different energies will deposit counts in overlapping PHA channels, and the result is a rather convoluted PHA spectrum that is not obvious to interpret.

We can describe the way in which an instrument transforms a photon spectrum into a PHA (or "count") spectrum by describing it as a matrix (see Figure 6.24). We can describe the incident photon spectrum as a vector, in which each vector element represents the number of photons/cm^2/s that have energies within some energy range $E_1 - E_2$. For instance, perhaps there are 20 photons/cm^2/s incident on the instrument with energies ranging from 10-12 keV, 16 photons/cm^2/s with energies ranging from 12-14 keV, and so forth. We can describe the PHA spectrum in the same way: as a vector whose elements give the number of counts/s measured in a particular PHA channel. The "response matrix" is then a matrix that deterministically transforms any photon spectrum into a corresponding measured count spectrum. If we choose the photon spectrum to have N elements (or "bins") and the count spectrum to have M bins, then the response matrix will be an M × N matrix. Note that because the elements in the count spectrum have units of counts/s and the elements in the photon spectrum have units of photons/cm^2/s, the elements in the response matrix must have units of "counts/(photons/cm^2)", or (since "counts"

and "photons" are technically dimensionless numbers) just cm^2—the units of effective area, which we described in Section 5.2.4. In fact, if the matrix were "collapsed" by adding together all of the elements in each column, the result would be a vector containing the effective area of the instrument for each photon energy range.

If only a single element of the photon spectrum were non-zero —say, for example, the third element—then only the third column in the response matrix would contribute to the count spectrum. One can see, then, that each column of the matrix is simply the count spectrum that would result if 1 photon/cm^2/s in the corresponding photon energy range were incident on the instrument. So in order to build up and generate a response matrix, all we need to do is find each of the count spectra that would result from photons in each of the incident photon energy ranges. This, then, is the purpose of our spectral model. Because the depth distributions from which the response matrix is created depend on the direction of the incident photons, the response matrix is likewise a function of incident direction. In fact, for any given incident direction relative to the BAT instrument, there exists a unique response matrix.

How, then, do we use the response matrix? When the BAT measures a count spectrum, and the position of the source is determined (by the processes described in section 5.2.3), we would like to be able to insert this count spectrum into some mathematical tool and have it return the photon spectrum (which is, after all, what we are really interested in). This would require a matrix that transforms a count spectrum into a photon spectrum, which is the inverse of what the response matrix does. In fact, we would love to have the inverse of the response matrix, which would do just that. Unfortunately, deriving the inverse of the response matrix from first principles is not possible, and finding it by inverting the response matrix is not generally possible because such matrices tend to be singular (or nearly singular) and therefore do not have inverses. So we are stuck with finding a way to do the best we can with what we have: the response matrix, which transforms something we don't have (the photon spectrum) into something we do (the count spectrum). A common method is to choose a model of some kind for the photon spectrum—a model that can be described in terms of a few parameters. A good example is the Band function we described

in section 2.4.4, which is characterized by four parameters: a low-energy index α, a high-energy index β, a peak energy $E_{\rm peak}^{\rm obs}$, and a normalization constant A. We begin with our best guesses as to what four values would generate a photon spectrum that would result in the count spectrum we have measured. Then, we iteratively make small changes to these parameters (usually using some automated fitting software tool) until they result in a count spectrum that matches the one we have measured. We can even assign a confidence to each parameter, stating for example, a "90% confidence interval", which, roughly speaking, gives us a range of values that the "true" value has a 90% probability of falling within.

The size and number of photon bins are entirely at our discretion, and since we rebin the PHA spectra prior to using the response matrix, we can also assign PHA bins that cover any range and have whatever widths we desire. Because we are not trying to invert the matrix, we don't need to worry about making sure that it is square (with the number of photon bins equaling the number of count bins). In order to not lose any resolution in the PHA spectrum, it is wise to make the PHA bins narrower than the widths of the peaks. The standard choice for BAT spectra is to have 80 count bins, with widths such that 200 keV photons would produce peaks centered in the 79th bin. In order to guarantee the optimum conditions for fitting parameters, it is wise to choose the photon bin widths to be somewhat finer than the count bin widths, by at least a factor of two. The standard choice for defining such photon bins for BAT spectra is to choose about 200 bins that range from 10 keV up to 500 keV, with exponentially increasing bin widths such that the first bin has a range from 10 to 10.1975 keV and the 200th bin has a range from 490.314 keV to 500 keV. Photons with energies less than 10 keV are not detected by BAT, and BAT has very little sensitivity to photons with energies greater than about 300 keV (let alone 500 keV), as demonstrated by the effective area curve in Figure 5.4.

With this response matrix, we now have the tool we need for investigating the spectral properties of gamma-ray bursts and x-ray flashes detected by BAT.

Chapter 7

Analysis Procedures

7.1 Data Reduction

7.1.1 BAT Data

All data that comes from the Swift spacecraft and from its three instruments is available through the High Energy Astrophysics Science Archive Research Center (HEASARC) which is located at Goddard Space Flight Center. The HEASARC provides:

- "raw" data files—these are files that have not yet been processed (at least, very much) by data analysis tools. One example is event files, which give the time, PHA channel, and detector of each count recorded by the BAT. Other raw data files give descriptions of which detectors are enabled at a given time, what the bias voltage is, where the spacecraft is located and where it is pointing at any given moment, etc.

- data analysis tools—these are software tools that can be used to create (for example) light curves, spectra, and response matrices from the raw data files.

- some processed files—some files that are generated automatically by the HEASARC, using the data analysis tools. These include light curves and spectra. Often, scientists want to obtain files that are processed in a specific way and will therefore run the data analysis tools themselves. Some files (like response matrices) are not provided by the HEASARC and must be generated by the user.

The data files are provided in FITS format, which is a standard form for many astrophysical data files supported by the HEASARC. Likewise, the analysis tools are designed to process FITS files. All of these tools and data files can be obtained from the 'Archive' or 'Quicklook Data' pages accessible from the main Swift web page at http://swift.gsfc.nasa.gov.

The process by which one generates a spectrum and a response matrix from BAT event data is as follows:

1. Assign an energy to each PHA channel for each detector. This is done using the relationship between peak energy and PHA channel described in section 6.4. The tool that assigns this energy is *bateconvert*.

2. Create a "detector plane image" from the event file. This is just a map showing the number of counts recorded in each detector. The tool that generates this is called *batbinevt*.

3. Determine which detectors are "noisy". For reasons not well understood, some detectors sometimes begin recording a large flow of counts that aren't the result of detected photons. These detectors can be singled out so that they can be excluded when an image of the sky, a light curve, or a spectrum is generated. The tool that finds these noisy detectors is called *bathotpix*.

4. Mask out noisy detectors, then convolve the detector plane image with the pattern of the mask to create an image of the sky. The tool that does this is *batfftimage*.

5. Determine the position of the gamma-ray burst. For bright bursts, this is the most prominent object in the sky image. For weaker bursts, sometimes there are other gamma-ray sources with known positions that can be ignored. The tool that determines the positions of sources in the image is *batcelldetect*.

6. Calculate the mask weight for each detector. This requires a knowledge of the position of the burst, which we found using *batcelldetect*. The tool that calculates these mask weights is *batmaskwtevt*.

7. With the energy scale and the mask weights, we can now combine the individual spectra into a single composite mask-weighted spectrum. This is done by *batbinevt*.

8. Finally, generate a response matrix appropriate for the spectrum we have just produced. This is done with *batdrmgen*.

For my analysis, I have used the following versions of these tools:

Tool	Version
batbinevt	1.23
bathotpix	1.7
batfftimage	1.15
batcelldetect	1.28
bateconvert	4.1
batmaskwtevt	1.11
batdrmgen	3.1

Because we introduced a set of empirical corrections to the batdrmgen model, we recognized that there are still, at this point, some limitations in our understanding of the response. We evaluated the size of the empirical corrections at each channel and derived a set of "systematic errors". The overall magnitudes of these errors were adjusted until the errors in the best-fit parameters from the various Crab measurements were consistent with each other. This systematic error vector is found in a calibration file distributed with the BAT tools and was applied to each BAT spectrum before fitting it with the response matrix. Channels corresponding to photon energies of 14 to 200 keV were included in each fit.

7.1.2 Wind Konus Data

The Wind satellite was launched on 1 November 1994 and currently resides in a halo orbit about the L1 Lagrangian point between the Earth and the sun. The L1 Lagrangian point is one of 5 points at which a spacecraft can be positioned where it will remain "fixed" with respect to the sun and the Earth. The L1 point lies directly between the Earth and the sun at a distance of about 900,000 miles from the Earth (which is about 1/100th of the distance between the Earth and the sun). One of Wind's primary missions is to measure the solar wind, but there are also gamma-ray burst instruments aboard such as Konus.

Konus consists of two identical detectors with nearly omnidirectional sensitivity that are

placed on opposite sides of the spacecraft so that together they can observe almost the entire sky at once [3]. Each detector consists of a NaI(Tl) scintillator crystal that is 5 inches in diameter and 3 inches high that is housed in an aluminum container with a beryllium entrance window. When a gamma-ray photon interacts with the crystal, it produces visible light that is detected and converted into an electrical signal by a photomultiplier tube.

The Konus detectors can measure incident photons with energies ranging from 10 keV to 10 MeV. Konus has no independent imaging ability and can only determine the origin of a photon by which detector is hit. Konus records 64 individual spectra each time it detects a gamma-ray burst. The first four are accumulated for 64 ms each. The accumulation times of the next 52 spectra are determined by an adaptation system and depend on the time structure of the burst. They range from 0.256 s to 8.192 s. The last 8 spectra are accumulated for 8.192 s each.

Because the mask-weighting technique removes most counts resulting from photons above 200 keV or so, it is difficult to measure $E_{\rm peak}^{\rm obs}$ if $E_{\rm peak}^{\rm obs}$ happens to be above 200 keV. Konus, on the other hand, can measure photons with energies up to 10 MeV. For this reason, it is very helpful to fit the spectrum measured by BAT and the one measured by Konus simultaneously. Of course, each spectrum requires its own response matrix.

One difficulty in doing this simultaneous fit arises from the delay time between the two spacecraft. Because Konus is so far from the Earth (and hence, from Swift), there can be a significant delay between when the photons of a given gamma-ray burst are first measured by one spacecraft and when they are measured by the other. In the most extreme cases, this delay time can be as large as 5 seconds. A short burst could be over and finished in the Konus detectors before BAT even begins to detect it, or vice versa.

In order to simultaneously fit spectra from both instruments, it is important that the two spectra include the same time intervals, relative to when the burst photons arrived at the two instruments. This requires us to know the time delay, for a given incident direction, between when a plane wave would intersect Swift and when it would intersect the Wind satellite. In order to determine this delay time, we need 3 pieces of information:

1. The position of the Swift spacecraft at the time it detected the burst. This information is available in an "attitude" file made available through HEASARC.

2. The position of the Konus spacecraft at the time the burst triggered it. This information is contained in the Konus spectral files that are provided to us by the Konus team.

3. The direction from which photons came for the burst in question. Typically this direction is measured in celestial coordinates of Right Ascension (RA) and Declination (Dec). This information comes through the TDRSS message but can also be found independently using the steps listed in Section 7.1.1.

Once we have these 3 pieces of information, the delay time between when Konus would have observed the burst and when Swift would have observed the burst is given by

$$\frac{(k_x - s_x)e_x + (k_y - s_y)e_y + (k_z - s_z)e_z}{c}, \tag{7.1}$$

where (k_x, k_y, k_z) are the x, y, and z coordinates of the position of the Konus spacecraft in geocentric inertial coordinates (coordinates in which the center of the Earth is the origin, the +z-axis extends through the north pole, and the +x-axis points in the direction of the Vernal Equinox), and (s_x, s_y, s_z) are the x, y, and z coordinates of the position of the Swift spacecraft in geocentric inertial coordinates, and e is the unit vector in the direction of the burst, which is given in terms of RA and Dec:

$$\begin{aligned} e_x &= \cos(\text{Dec})\cos(\text{RA}) \\ e_y &= \cos(\text{Dec})\sin(\text{RA}) \\ e_z &= \sin(\text{Dec}) \end{aligned} \tag{7.2}$$

With this delay time, it is a simple matter to specify time intervals that are the same for both instruments. Since the time intervals of the Konus spectra are rigidly set by the instrument, it is necessary to find the corresponding times for Swift and specify them when producing the BAT spectra.

7.1.3 HETE-2 FREGATE Data

In the case of XRF 050219B, the HETE-2 French Gamma-Ray Telescope (FREGATE) observed the burst and obtained spectral measurements. The energy range of the FREGATE extends from 6 – 400 keV, which is significantly larger than BAT's nominal range of 14 – 200 keV. The HETE-2 science team provided me with spectral and response matrix FITS files, so that I was able to fit the FREGATE data jointly with the BAT data and better constrain the spectral parameters of this burst. For more information on the HETE-2 mission, see Section 3.4.

7.1.4 XRT Data

As with the BAT data files and software, the XRT files and software are also distributed through the HEASARC. An *xrtpipeline* script is available that simplifies the data analysis process considerably, automating the basic data reduction tasks and producing (among other files) a set of event files that is "clean"—that is, in which counts that have been deemed unreliable or invalid are removed. Examples of such counts would be those that occur in bad pixels, those that are judged invalid according to their "grade" (or the pattern of counts in surrounding pixels), or those that are due to photons coming from a calibration source. The XRT can sometimes overheat due to the failure of the Thermal Electric Cooler (TEC) early in the mission, and this invalidates the data taken during such time periods, so the event files also must be screened to include only those time intervals during which the CCD temperature was below $-40°$. *xrtpipeline* was run for each data set to produce clean event files, and then each event file was screened for temperature.

Extracting a spectrum from a cleaned event file can be done using a tool developed by HEASARC called "xselect", which allows the user to select a portion of the CCD array from which to extract the spectrum. Since each position on the CCD array corresponds to a point in the sky, this makes it possible to extract a "foreground" spectrum (one that includes the position of the afterglow) as well as a "background" spectrum (one that does not include the afterglow). By subtracting these two from each other, we obtain a spectrum due entirely to the afterglow. Xselect allows the user to specify the radius of the region within the image (in pixel coordinates)

to use for extracting each spectrum. For the analysis described herein, a radius of 20 pixels was used for foreground spectra and a radius of 70 pixels was used for background spectra. Xselect version 2.3 was used for this analysis. When performing the spectral fits, channels corresponding to photon energies of 0.3 to 10 keV were included.

It is also possible to find the number of counts/s as a function of time from the cleaned event file using xselect, but it is a rather cumbersome and time-consuming process, especially for GRB afterglow data in which the count rate diminishes with time (as opposed to the count rates from many astrophysical phenomenon, which remains constant or varies much more slowly). For most of the analysis described in this work, I have used a tool called *plot_lc*, which was developed by a member of the XRT instrument team named David Morris. This tool produces a light curve for which each data point contains a specified number of counts each. In this way, the relative error for each data point can be precisely controlled. Including many counts in a data point results in a small measurement error but fewer overall data points, while including fewer counts results in a larger error but more data points.

plot_lc also corrects for an effect known as "pile-up". Pile-up refers those counts that arrive at the instrument nearly simultaneously and are recorded as a single event rather than as multiple events. This reduces the number of counts recorded, the flux inferred from the measured count rate is lower than the true flux. By observing the shape of the point spread function, a "flattening" can be detected near the center of the point spread function when the count rate exceeds a certain level. To correct for pile-up, one must exclude all counts from pixels near the center of the point spread function and multiply the remaining counts by a correction factor. If the count rate exceeds 1 count/s, *plot_lc* excludes all counts recorded in pixels that are within a radius of 4 pixels of the center. These are known to be the pixels affected by pile-up and high count rates. The remaining counts within the region of interest are multiplied by a factor of 2.08, which corrects for the loss of the pixels that were excluded. If the count rate exceeds 10 counts/s (which occurred in the case of XRR 050315), the radius is expanded to 8 pixels and a correction factor of 4.01 is used.

7.2 Spectral Models

We have count spectra and response matrices available to us for both the prompt gamma-ray emission and the longer-lasting afterglow emission. In order to find photon spectra, we must select some suitable models that we suspect may (with the proper parameters) match those photon spectra.

7.2.1 Prompt Emission

Band Model

As we described in section 2.4.4, the photon spectrum of the prompt gamma-ray emission is, in general, well-fit by what has come to be known as the Band function:

$$\begin{aligned} N(E) &= A\left(\frac{E}{50\text{ keV}}\right)^{\alpha}\exp\left(\frac{-E(2+\alpha)}{E^{\text{obs}}_{\text{peak}}}\right) && E < \left(\frac{(\alpha-\beta)E^{\text{obs}}_{\text{peak}}}{2+\alpha}\right) \\ &= A\left[\frac{(\alpha-\beta)E^{\text{obs}}_{\text{peak}}}{(50\text{ keV})(2+\alpha)}\right]^{\alpha-\beta}\exp\left(\beta-\alpha\right)\left(\frac{E}{50\text{ keV}}\right)^{\beta} && E > \left(\frac{(\alpha-\beta)E^{\text{obs}}_{\text{peak}}}{2+\alpha}\right) \end{aligned} \tag{7.3}$$

where

$N(E)$ is the number of photons/cm^2/s/keV,

α is the spectral index of the low-photon-energy portion of the spectrum,

β is the spectral index of the high-photon-energy portion of the spectrum,

$E^{\text{obs}}_{\text{peak}}$ is the photon energy at which the greatest amount of total energy is detected, and

A is a normalization constant with units of photons/cm^2/s/keV.

The form of the Band function presented here is slightly different from the form given in Equation 2.2. We have substituted a value of 50 keV in place of 100 keV as the denominator in several of the fractions. BAT is most sensitive to photons with energies near 50 keV, so this choice enables us to find normalization constants A that are better constrained. The Band function will be the primary model of choice for studying the prompt emission.

For some bursts, we expect that $E^{\text{obs}}_{\text{peak}}$ will be above the energy range of the instruments from which we have data (BAT, Konus, and FREGATE). In these instances, we will only detect

the low-energy portion of the Band model spectrum, and the data will be well fit by either the simpler power law model or the so-called "cut-off" power law model (which is a power law function multiplied by an exponential "cut-off" term).

Constrained Band Model

We also recognize that for some bursts, $E_{\rm peak}^{\rm obs}$ will fall below the energy range of our instruments. For these bursts, a simple power law model is often sufficient to fit the spectrum. However, since we are often interested in obtaining a value for $E_{\rm peak}^{\rm obs}$, we may be tempted to use the Band function as our model in all cases and see what constraints it provides for $E_{\rm peak}^{\rm obs}$. Unfortunately, the constraints it provides may be inaccurate, since the high energy AND the low energy portions of the Band function can be made to fit the data equally well, giving us, in one instance, a value of $E_{\rm peak}^{\rm obs}$ below our energy range and in the other, a value above our energy range.

An alternative approach is to use a spectral model called the "constrained" Band function, which was developed by Sakamoto et al. [69] This model has three spectral parameters instead of four: β, $E_{\rm peak}^{\rm obs}$, and a normalization constant A, along with a fixed parameter $E_{\rm pivot}$. If the data is well fit by a power law with some small curvature at the lower energy end, this model is able to fit that data well. If, on the other hand, the data is well fit by a power law alone, this model forces that power law to coincide with the high-energy portion of the Band function, so that $E_{\rm peak}^{\rm obs}$ will be constrained to some value lower than the energy range of our instrument.

The results of the constrained Band function are only meaningful if $\beta < -2$. For higher values of β, the constrained Band function may produce a value of $E_{\rm peak}^{\rm obs}$ that is higher than the true value. For a more detailed explanation of this model, see the description given by Sakamoto et al. [69].

7.2.2 Afterglow Emission

In section 2.5, we described the photon spectra of x-ray afterglow emission as typically a power law function with some absorption by intervening hydrogen atoms:

$$N(E) = A \cdot E^{-I} \cdot \exp[n_H \cdot \sigma(E)], \tag{7.4}$$

where I is the photon index, n_H is the number of hydrogen atoms per cm^2 between the detector and the source, $\sigma(E)$ is the photoelectric cross-section of hydrogen (which is just a known function of photon energy), and A is a normalization constant. This will be our model of choice for the x-ray afterglow emission.

We note that in some cases, n_H will be consistent with values measured for our own galaxy, indicating that hydrogen concentrations within our own galaxy are sufficient to explain what we see. In other cases n_H will be higher than can be explained by absorption due to hydrogen in our own galaxy, indicating the presence of absorbing material beyond our galaxy. Galactic hydrogen concentrations are obtained using the HEASARC galactic hydrogen column density calculator (http://heasarc.gsfc.nasa.gov/cgi-bin/Tools/w3nh/w3nh.pl).

7.2.3 Error Bars

The errors cited throughout the following chapter are, for the most part, for the 90% confidence interval (meaning, loosely speaking, that there is a 90% probability that the true value lies within the interval specified by the error values). The exceptions are the light curve temporal decay indices and break times. In those instances, the errors cited are for the 68% confidence interval.

7.3 Estimating Redshifts

Many times, despite the best efforts of observers, it isn't possible to measure the redshift of a gamma-ray burst. A redshift measurement typically requires the observation of an optical afterglow, and sometimes the optical afterglow either isn't observed or is too faint to provide a

redshift measurement. Fortunately, there are ways to estimate the redshift. One of these is to use the correlation between peak $L_{\rm iso}$ and $E^{\rm src}_{\rm peak}$ that was discussed in section 2.4.6.

For a given redshift, the peak isotropic luminosity resulting from photons with energies between 30 keV and 10 MeV in the source frame is given by

$$L_{\rm iso}(30\ {\rm keV}, 10\ {\rm MeV} = 4\pi d_L^2 F\Big(\frac{30\ {\rm keV}}{1+z}, \frac{10\ {\rm MeV}}{1+z}\Big), \tag{7.5}$$

where $F(\frac{30\ {\rm keV}}{1+z}, \frac{10\ {\rm MeV}}{1+z})$ is the measured peak flux that results from photons with energies ranging from (30 keV)/(1 + z) to (10 MeV)/(1 + z), and the "luminosity distance" d_L is a function of redshift z. Likewise, $E^{\rm src}_{\rm peak}$ is given by

$$E^{\rm src}_{\rm peak} = E^{\rm obs}_{\rm peak} \cdot (1+z). \tag{7.6}$$

Both quantities are functions of redshift z.

If we fit an appropriate model (in our case the Band function) to the peak 1 second of the prompt emission count spectrum, we can derive spectral parameters that allow us to calculate $F(\frac{30\ {\rm keV}}{1+z}, \frac{10\ {\rm MeV}}{1+z})$ for some value of z. We can then see if this z leads to values of $L_{\rm iso}$ and $E^{\rm src}_{\rm peak}$ that agree with equation 2.8. Since there is a range of possible values for the coefficient and the power law index in equation 2.8, there will also be a range of redshifts that result in values that match the correlation. We can find this range of values by repeating this process for multiple redshift values. Because the spectral parameters are poorly constrained when only one second of data is used, we use α, β, and $E^{\rm obs}_{\rm peak}$ from a fit to the full time interval and the normalization parameter A from a fit to the peak 1 second of the burst.

We find that this method works much better for bursts with redshifts less than about 1. For bursts with higher redshifts, a much larger range of redshifts result in values that are consistent with equation 2.8, so the uncertainty in a given estimated redshift is larger.

7.4 The Kolmogorov-Smirnov Test

There is a statistical test known as the Kolmogorov-Smirnov (or K-S) test, which allows one to determine the likelihood that two distributions are drawn from the same parent distribution.

This test gives a probability that the two distributions in question are consistent. This test is used in Chapter 9 to compare distributions of burst properties observed by Swift with those of other missions, as well as to compare properties of XRFs with those of GRBs. For our purposes, we will consider a probability below 0.1 as an indication that the two distributions are inconsistent, a probability between 0.1 and 0.3 as an indication of marginal consistency, and a probability greater than 0.3 as an indication that the two distributions are consistent.

7.5 Definition of GRBs, XRRs, and XRFs

There hasn't been a universally agreed upon definition of an "x-ray flash", other than the quantitatively imprecise definition that it emits most of its energy in x-rays and has a short duration. The definitions adopted by those whose work we reviewed in chapter 3 tended (understandably) to be based on the characteristics and energy ranges of the instruments that collected the data, and none of those definitions are quite suitable for BAT. And yet, we desire a definition that will be close enough to the others that we may reliably compare the characteristics of the BAT-detected XRF population with those from other missions.

As we discussed in section 3.4, Sakamoto et al. defined x-ray flashes in terms of the fluence ratio S_X(2-30 keV)/S_γ(30-400 keV) [70]. GRBs, XRRs, and XRFs were classified according to their value of this fluence ratio. They also found a strong correlation between $E_{\rm peak}^{\rm obs}$ and fluence ratio (see Figure 7.1). The borderline $E_{\rm peak}^{\rm obs}$ between XRFs and XRRs is $\approx$ 30 keV, and the borderline $E_{\rm peak}^{\rm obs}$ between XRRs and GRBs is $\approx$ 100 keV.

In the BAT energy range, a fluence ratio of $S(25-50\ {\rm keV})/S(50-100\ {\rm keV})$ is more natural and easier to measure with confidence. I therefore chose my working definition in terms of this ratio. In order to ensure that my definition was close to that adopted by Sakamoto et al., I calculated the fluence ratio for a burst for which the parameters of the Band model were $\alpha = -1$, $\beta = -2.5$, and $E_{\rm peak}^{\rm obs} = 30$ keV. These values of α and of β are typical of the distributions found by BATSE. The ratio thus found was 1.3217. I likewise calculated the fluence ratio for a burst for which $\alpha = -1$, $\beta = -2.5$, and $E_{\rm peak}^{\rm obs} = 100$ keV, which I found to be 0.7218. My working definition

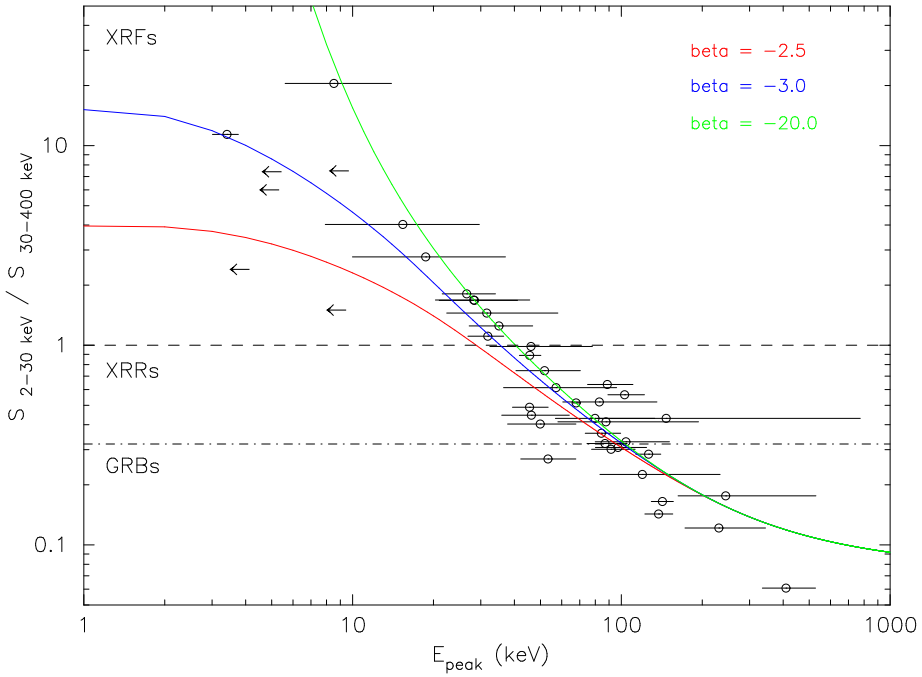

Figure 7.1: Distribution of bursts in the $E_{\rm peak}^{\rm obs}$–S(2–30 keV)/S(30–400 keV) plane. Overlaid are curves corresponding to the X-ray to γ-ray fluence ratio as a function of $E_{\rm peak}^{\rm obs}$, assuming the Band function with $\alpha = -1$ and $\beta = -2.5$ (red), -3.0 (blue), and -20.0 (green) [70]

.

for XRFs, XRRs, and GRBs thus became:

$$\begin{aligned} S(25-50\ \text{keV})/S(50-100\ \text{keV}) &\leq 0.7218 && \text{GRB} \\ 0.7218 < S(25-50\ \text{keV})/S(50-100\ \text{keV}) &\leq 1.3217 && \text{XRR} \\ S(25-50\ \text{keV})/S(50-100\ \text{keV}) &> 1.3217 && \text{XRF} \end{aligned} \tag{7.7}$$

The BAT spectrum for each burst detected through 31 July 2005 was extracted and a corresponding response matrix was generated. The "xspec" spectral fitting tool (version 11.3.1) was used to fit each spectrum to a Band model, a power law model, and a cut-off power law model. The latter two models were chosen so that good fits would be possible when $E_{\rm peak}^{\rm obs}$ extended to energies below or above the BAT energy range, so that only one branch of the Band model was visible. From the best fit model in each case, a fluence ratio was calculated. The fluence ratios found for each burst are shown in Table 7.1. A histogram of these fluence ratios is shown in Figure 7.2. Of the 49 bursts for which BAT obtained spectra between December 2004 when

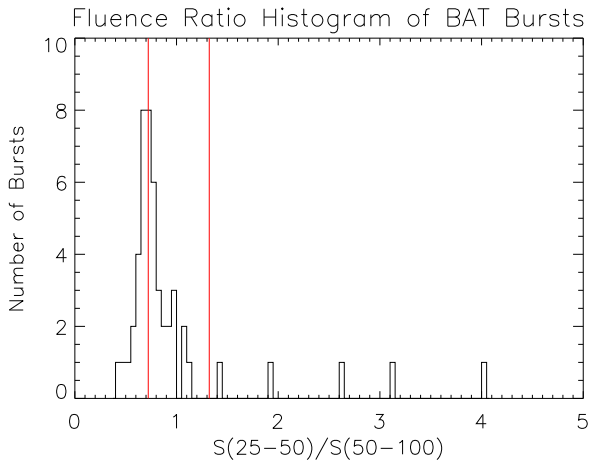

Figure 7.2: Histogram of the fluence ratios of BAT bursts observed between launch and 31 July 2005. The fluence ratios defining the boundaries between XRFs, XRRs, and GRBs are also shown.

the instrument went on line and 31 July 2005, 5 are classified as x-ray flashes, 24 as x-ray rich gamma-ray bursts, and 20 as "regular" gamma-ray bursts.

In some cases, the spacecraft began to slew while the burst was still in progress. This complicates the data analysis because, while some geometric corrections are applied to the data as the slew occurs to help normalize the count rates, the response matrix strictly only applies to a particular position in the BAT's field of view, and while the spacecraft is slewing, this position changes. A response matrix generated for the pre-slew source position should only be used to analyze spectra accumulated before the spacecraft began to slew. In determining the fluence ratios given in Table 7.1, the spectrum from the entire duration of the burst was fit using the response matrix for the pre-slew position of the burst. Therefore, we expect that for those bursts in which the slew began during the burst, the fluence ratios we calculated would not be accurate. An extreme example is GRB 050128, for which the spacecraft slewed 51 degrees. Fitting the pre-slew data with the pre-slew response matrix, we obtain a hardness ratio of 1.6205. When we use the post-slew response matrix, we obtain a hardness ratio of 1.9949, which is 23% larger. This is the largest error we might possibly see in any of the values in the table. Swift did not slew during any of the XRFs detected by BAT, so none of the values for those bursts are affected by this problem.

Table 7.1: The fluence ratio $S(25-50\text{ keV})/S(50-100\text{ keV})$ for all bursts detected by BAT through 31 July 2005, in descending order of fluence ratio. Those in the first group qualify as XRFs, those in the second as XRRs, and those in the third as GRBs.

XRFs		XRRs		GRBs	
Name	Ratio	Name	Ratio	Name	Ratio
050416A	4.0351	050315	1.1429	050509B	0.7204
050406	3.1217	050318	1.0742	050506	0.7143
050714B	2.6441	050509A	1.0693	050117	0.7139
050726B	1.9190	050507	0.9750	050401	0.6962
050215B	1.4115	050319	0.9551	050416B	0.6944
		050607	0.9541	041226	0.6828
		050421	0.9434	050422	0.6781
		050223	0.9254	050215A	0.6775
		041224	0.8942	050717	0.6653
		050721A	0.8825	050716	0.6640
		050724	0.8231	050124	0.6624
		050410	0.8121	050128	0.6497
		041228	0.8033	050126	0.6353
		050418	0.7947	050202	0.6235
		050525A	0.7930	050219A	0.6000
		041220	0.7874	050326	0.5953
		050505	0.7695	050603	0.5920
		050502B	0.7665	041223	0.5428
		050715	0.7653	050726A	0.4894
		050713A	0.7500	050412	0.4388
		050219B	0.7444		
		050713B	0.7391		
		050730	0.7323		
		050712	0.7320		

7.6 Selection Criteria

I conducted a detailed analysis of the five x-ray flashes listed in Table 7.1. An additional x-ray flash that was observed on 24 August 2005, for which a redshift was obtained, was added to the set, making a total of 6 XRFs.

The properties of these x-ray flashes were compared to those of a set of XRRs and GRBs that were detected by BAT. For extensive analysis, I selected two XRRs and 4 GRBs that were also observed by Konus. Using Konus data in addition to BAT data made possible better constraints on the model parameters and permitted the measurement of $E_{\rm peak}^{\rm obs}$ above the range in which BAT is sensitive. Two additional XRRs were selected for which redshifts had been measured, bringing the total number of XRRs studied to 4.

Chapter 8

BAT XRFs, XRRs, and GRBs

8.1 XRFs

This section describes the prompt emission and x-ray afterglow properties of the 5 XRFs observed by BAT prior to 31 July 2005, as well as the XRF observed on 24 August 2005.

8.1.1 XRF 050416A

This was the softest of the x-ray flashes observed by Swift as of 31 July 2005, with a $S(25-50\text{ keV})/S(50-100\text{ keV})$ fluence ratio of only 4.0355. BAT triggered on this burst at 11:04:44.5 UT (MET=135342283.968), and the spacecraft slewed immediately so that the XRT was able to begin accumulating data within 92.5 s (GCN 3264). The position determined by BAT was RA=12h 33m 57.6s and Dec=+21d 03' 10.8" with an estimated uncertainty radius of about 3 arcmin (95% confidence) (GCN 3273). The XRT-determined position was found to be RA=12h 33m 54.8s, Dec=+21d 03' 25.1", with a 5 arcsec uncertainty (90% confidence) (GCN 3275). Afterglow emission in the optical, infrared, and radio wavelengths was also detected (GCN 3265, 3269, 3318). The optical observations made possible a redshift determination of $z = 0.6535 \pm 0.0002$ (GCN 3542).

Prompt Emission

The duration of the burst was about 2.4 seconds ($\pm$0.2 seconds). The light curve shows a single prominent peak with a slightly longer rise time than fall time, followed by two smaller peaks. The emission comes entirely from 15-50 keV photons (see Figure 8.1).

The Band model failed to constrain $E_{\rm peak}^{\rm obs}$, so the constrained Band model was used instead. $E_{\rm peak}^{\rm obs}$ was found to be $16.7^{+5.3}_{-9.5}$ keV (90% confidence). The time interval from which the spectrum was extracted spans from 0.5 s before the trigger to 3 s after the trigger. Figure 8.2 shows the

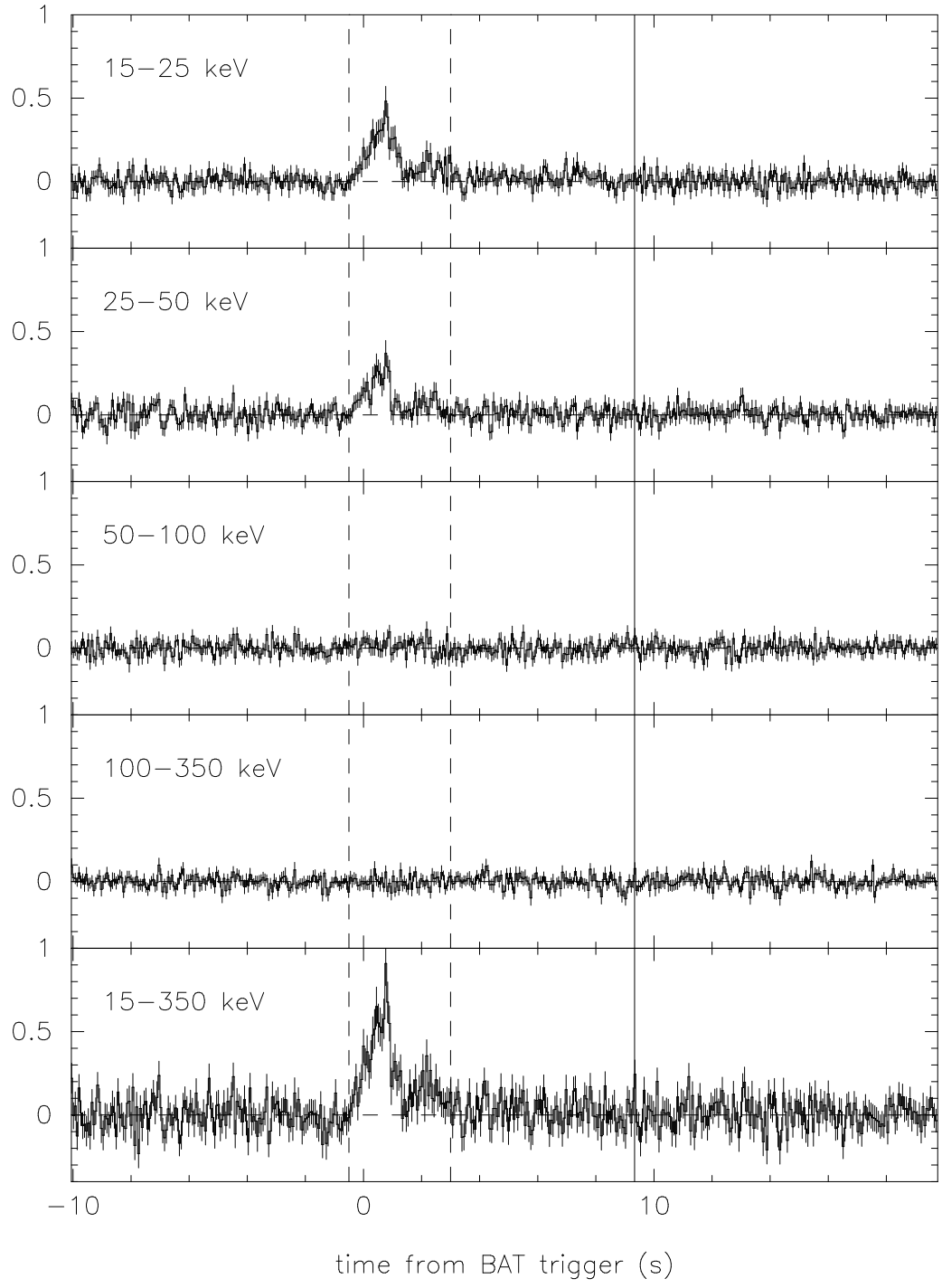

Figure 8.1: The light curve of the XRF 050416a prompt gamma-ray emission. The dashed lines mark the time interval used for the spectral analysis. The solid line marks the beginning of the spacecraft slew.

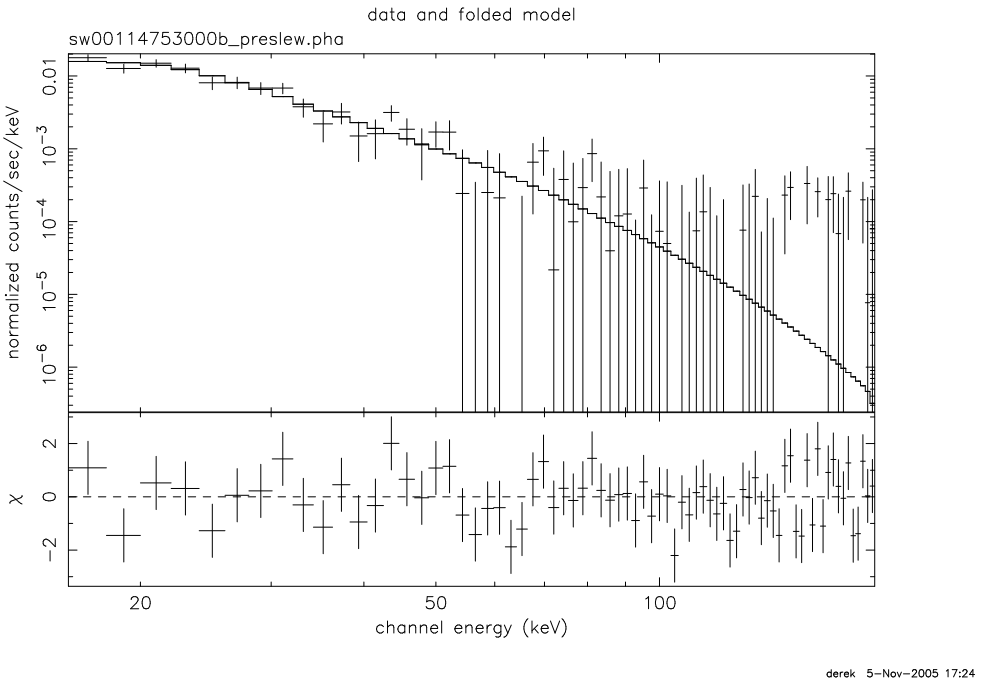

Figure 8.2: The count spectrum of the XRF 050416a prompt gamma-ray emission, along with the best fit model. See Table 8.1 for the best fit parameter values.

count spectrum and the best-fit model for this spectrum. The probability density distribution for $E_{\rm peak}^{\rm obs}$ is shown in Figure 8.3.

X-ray Afterglow

The x-ray afterglow, as measured by the XRT, is shown in Figure 8.4. The best fit to the data prior to 10^6 s results from a broken power law, which gives an early decay index of -0.672 ± 0.026, a late decay index of -0.905 ± 0.034, and a break at 8400 ± 3500 s. There is also evidence of some late time flaring about 6×10^6 seconds (68 days) after the trigger.

The count spectra measured by the XRT is shown in Figure 8.5. Two different time intervals were chosen, one before the break in the light curve and one after it. The best fit spectral indices in both cases are consistent with each other (2.2 ± 0.3 and 2.2 ± 0.2). The best fit hydrogen column density is $(2.8 \pm 1.2) \times 10^{21}$ atoms/cm^2, which is considerably higher than the hydrogen column density due to our galaxy alone in the direction of the burst, which is only 2.06×10^{20} atoms/cm^2.

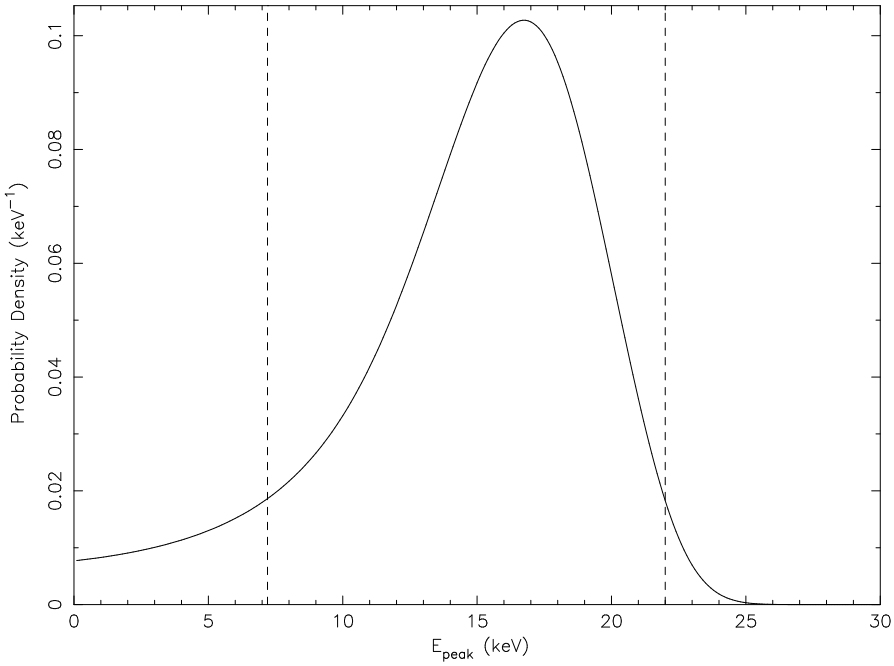

Figure 8.3: The $E^{\rm obs}_{\rm peak}$ probability density distribution for XRF 050416a. The y-axis gives the differential probability $\frac{dP}{dE}$, such that the probability that $E^{\rm obs}_{\rm peak}$ lies between two values E_1 and E_2 is given by the area under the curve between E_1 and E_2. There is a 90% probability that $E^{\rm obs}_{\rm peak}$ lies within the region bounded by the two vertical lines.

Table 8.1: The best fit spectral parameters for the XRF 050416a prompt emission, using a power law model, a cutoff power law model, and the constrained Band model. $E^{\rm obs}_{\rm peak}$ is measured in keV, A in ergs/cm^2/s/keV, and average flux is given in ergs/cm^2/s for 15 – 150 keV photons. The exposure was 2.728 s.

power law		cutoff power law		Band	
Parameter	Value	Parameter	Value	Parameter	Value
α	$-3.09^{+0.21}_{-0.22}$	α	$-1.31^{+1.43}_{-1.24}$	β	$-3.86^{+0.67}_{-1.88}$
A	$(9.0 \pm 1.6) \times 10^{-3}$	$E^{\rm obs}_{\rm peak}$	< 20.4	$E^{\rm obs}_{\rm peak}$	$16.7^{+5.3}_{-9.5}$
		A	$0.128^{+1.105}_{-0.080}$	E_{pivot}	20
				A	< 3.19
				flux	3.78×10^{-8}
χ^2_ν/ν	1.046/73	χ^2_ν/ν	0.966/72	χ^2_ν/ν	0.983/72

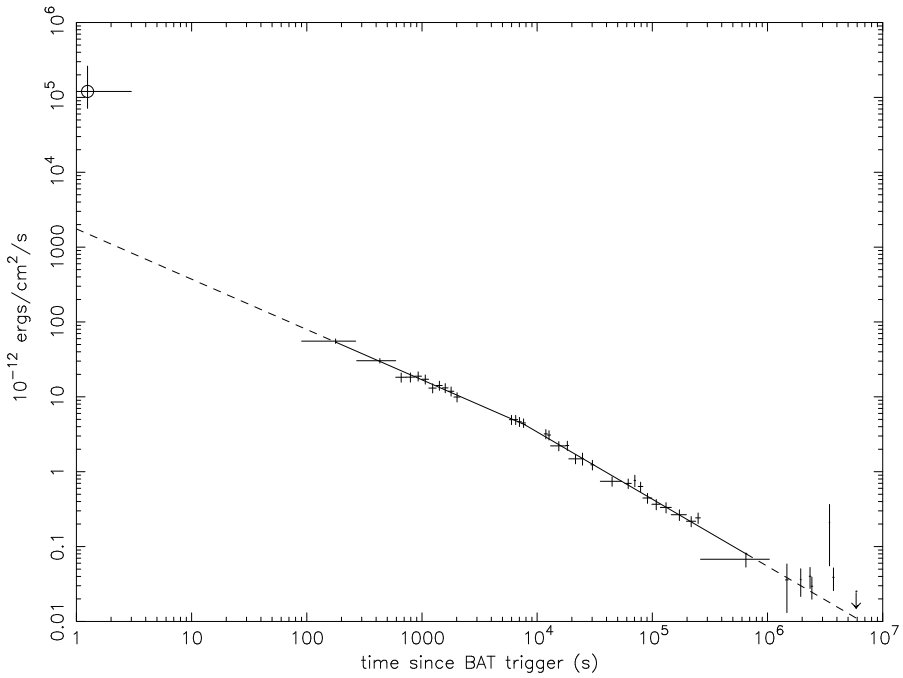

Figure 8.4: The light curve of the XRF 050416A x-ray afterglow, along with the best-fit broken power law model. Also shown with a circle is the average flux of the prompt emission extrapolated into the 0.6 – 10 keV energy range. Note that at very late times, the light curve flares up for a short period of time.

Table 8.2: The best fit spectral parameters for the XRF 050416a x-ray afterglow, before and after the break in the light curve. n_H is measured in atoms/cm^2, A in units of 10^{-3} ergs/cm^2/s/keV, and flux in units of ergs/cm^2/s. Start and stop times are in seconds since the BAT trigger.

Parameter	Before Break	After Break
I	2.2 ± 0.3	2.2 ± 0.2
n_H	$(2.8 \pm 1.2) \times 10^{21}$	$(3.1 \pm 0.8) \times 10^{21}$
A	$5.0^{1.9}_{-1.3}$	$0.27^{+0.06}_{-0.05}$
flux	$2.54^{0.77}_{0.45} \times 10^{-11}$	$1.38^{+0.26}_{-0.18} \times 10^{-12}$
start time	600 s	11510.6576 s
stop time	2158.6576 s	156961.70812 s
exposure	1543.5576 s	45292.556 s
χ^2_ν/ν	0.775/17	0.530/70

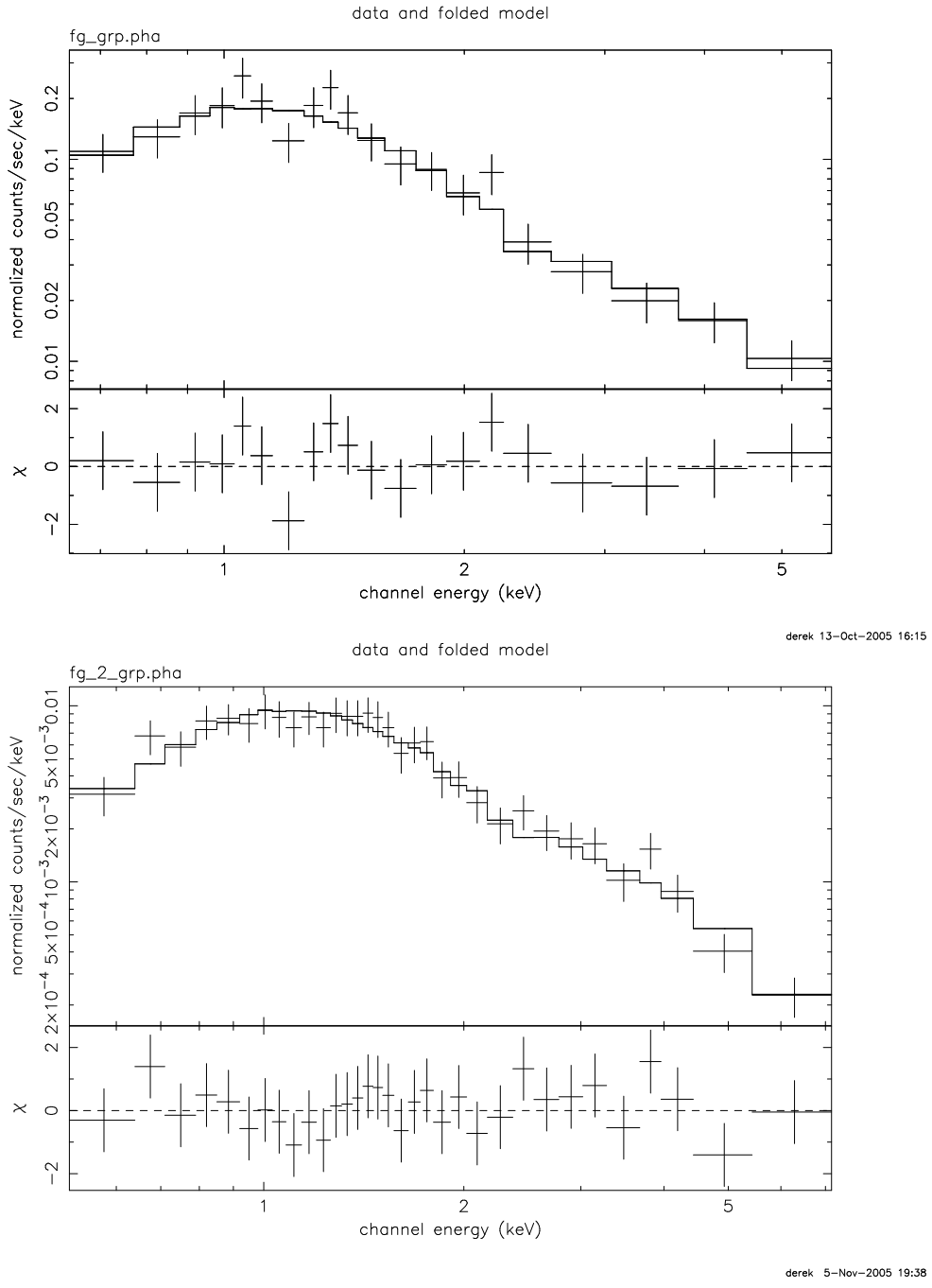

Figure 8.5: The count spectrum of the XRF 050416a x-ray afterglow, before (top) and after (bottom) the break in the light curve. Count bins corresponding to photon energies of 0.3 – 10 keV were included. See Table 8.2 for the spectral parameters.

8.1.2 XRF 050406

BAT triggered on this burst at 15:58:48.4 UT (MET=134495927.872), and the spacecraft slewed immediately so that the XRT was able to begin accumulating data within 87 s (GCN 3180, 3181). The position determined by BAT was RA=2:17:53.04 and Dec=-50:10:51.6 with an estimated uncertainty radius of about 3 arcmin (95% confidence) (GCN 3183). The XRT-determined position was found to be RA=2h 17m 52.64s, Dec=-50d 11' 18.8", with a 5 arcsec uncertainty (90% confidence) (GCN 3184). Optical afterglow emission was also detected (GCN 3185), but a redshift was not measured. Using the technique described in Section 7.3 we are able to constrain the redshift to $z > 3$.

Prompt Emission

The T90 duration of the burst was 5.78 ± 0.23 seconds. The light curve shows a single peak, but the burst was not bright enough to enable us to discern finer structure. Like XRF 050416a, the emission comes entirely from 15-50 keV photons (see Figure 8.6).

The Band model failed to adequately constrain $E_{\rm peak}^{\rm obs}$, so the constrained Band model was used instead. $E_{\rm peak}^{\rm obs}$ was found to be $27.9^{+7.9}_{-18.1}$ keV (90% confidence). The time interval from which the spectrum was extracted spans from 2.504 s before the trigger to 3.884 s after the trigger. Figure 8.7 shows the count spectrum and the best-fit model for this spectrum. The probability density distribution for $E_{\rm peak}^{\rm obs}$ is shown in Figure 8.8.

X-ray Afterglow

The x-ray afterglow, as measured by the XRT, is shown in Figure 8.9. The afterglow is rather faint, even though it was observed immediately. While the light curve is poorly fit with a single power law it is consistent with an offset power law or with a broken power law. The offset power law results in a t_0 of 138 ± 21 s, which is long after the prompt emission. The broken power law, on the other hand, results in a best fit early index of -2.01 ± 0.22, a late index of -0.50 ± 0.29, and a break time of 3900 ± 2800 s. There is a hint of a possible second break in the afterglow at

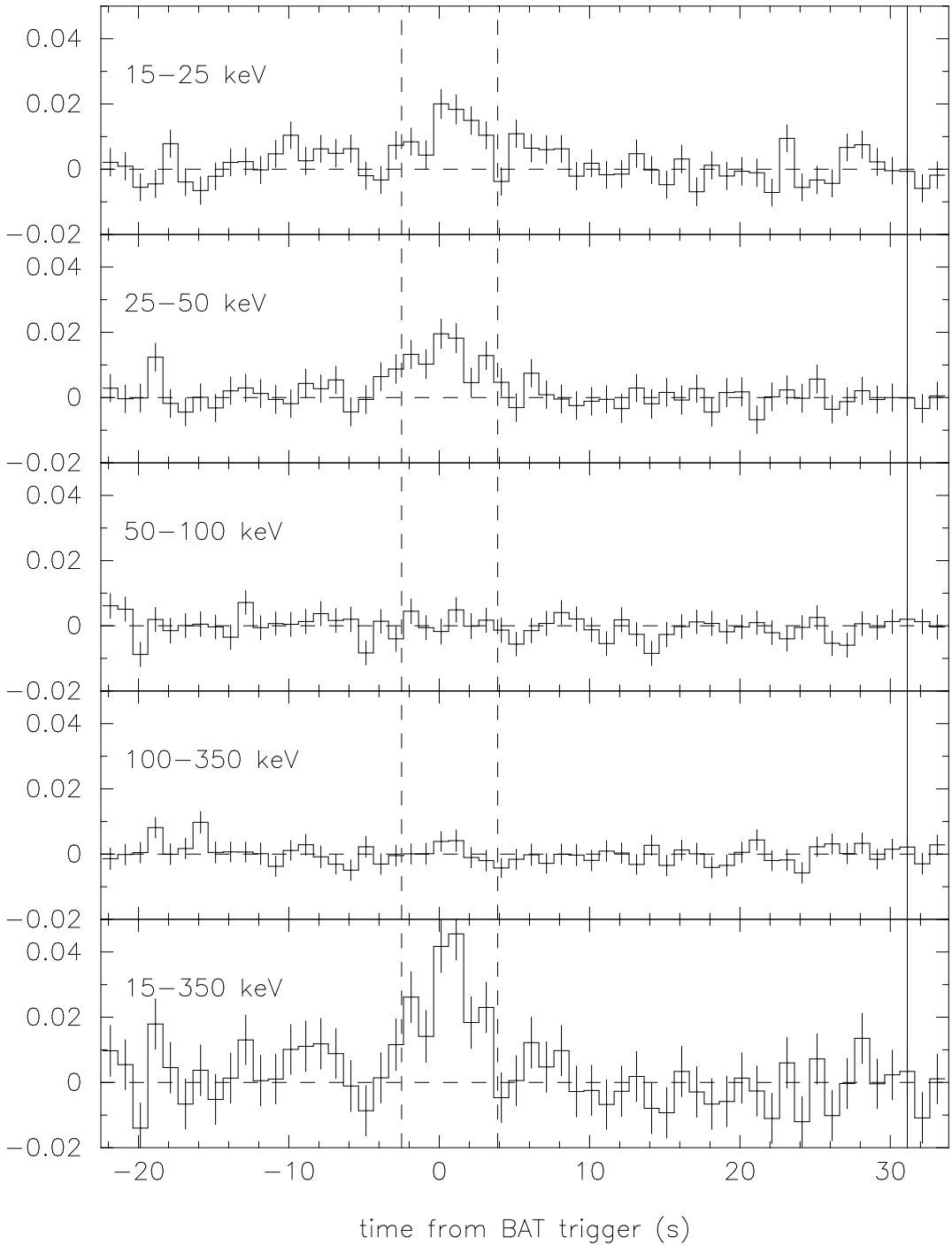

Figure 8.6: The light curve of the XRF 050406 prompt gamma-ray emission. The two dashed lines indicate the time interval used to measure the spectrum. The solid line indicates the time at which Swift began to slew.

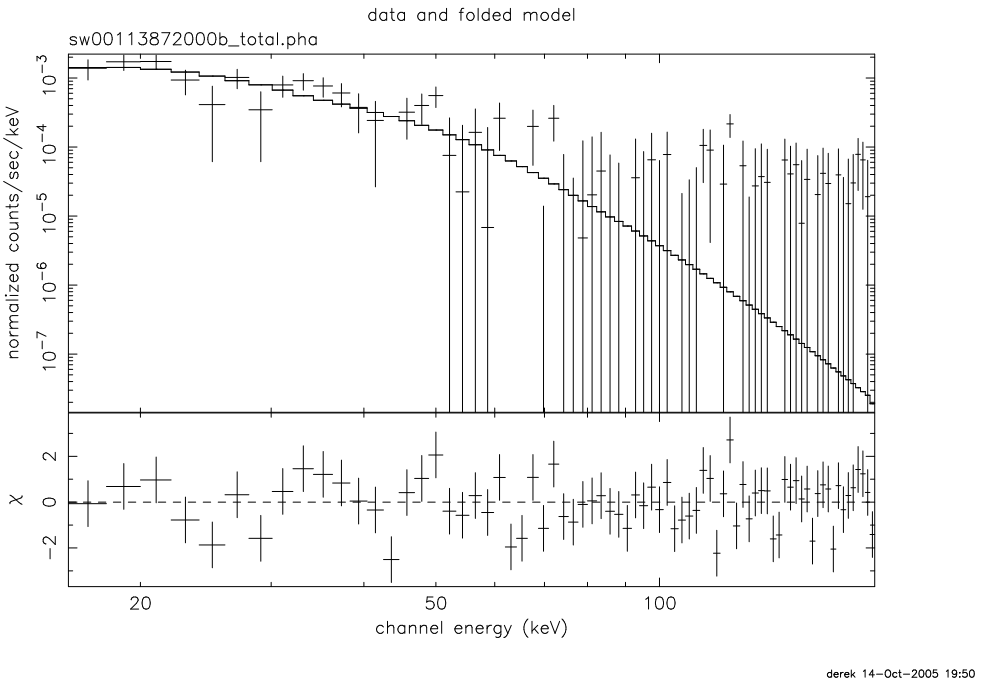

Figure 8.7: The count spectrum of the XRF 050406 prompt gamma-ray emission, along with the best fit model See Table 8.3 for the spectral parameters.

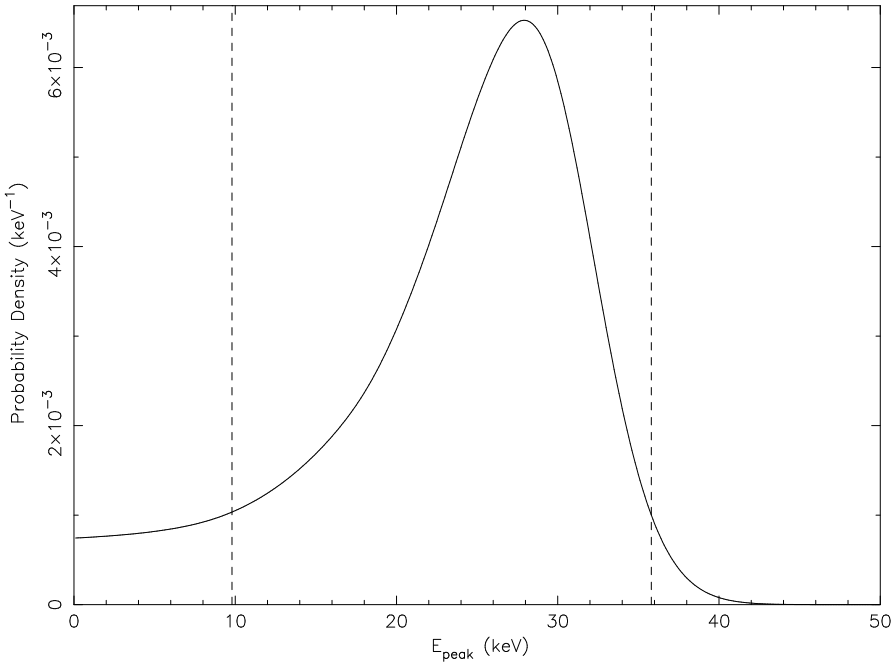

Figure 8.8: The $E^{\rm obs}_{\rm peak}$ probability density distribution for XRF 050406. The y-axis gives the differential probability $\frac{dP}{dE}$, such that the probability that $E^{\rm obs}_{\rm peak}$ lies between two values E_1 and E_2 is given by the area under the curve between E_1 and E_2. There is a 90% probability that $E^{\rm obs}_{\rm peak}$ lies within the region bounded by the two vertical lines.

Table 8.3: The best fit spectral parameters for the XRF 050406 prompt emission, using a power law model, a cutoff power law model, and the constrained Band model. $E^{\rm obs}_{\rm peak}$ is measured in keV, A in ergs/cm^2/s/keV, and average flux in ergs/cm^2/s for 15 – 150 keV photons. The exposure was 6.388 s.

power law		cutoff power law		Band	
Parameter	Value	Parameter	Value	Parameter	Value
α	$-2.59^{+0.44}_{-0.37}$	α	$-0.541^{+3.54}_{-1.70}$	β	< -2.78
A	$1.23^{+0.38}_{-0.37} \times 10^{-3}$	$E^{\rm obs}_{\rm peak}$	$25.4^{+9.1}_{-23.5}$	$E^{\rm obs}_{\rm peak}$	$27.9^{7.9}_{-18.1}$
		A	$< 6.23 \times 10^{-2}$	E_{pivot}	20
				A	< 0.32
				flux	1.11×10^{-8}
χ^2_ν/ν	1.046/73	χ^2_ν/ν	1.196/72	χ^2_ν/ν	1.186/72

around 300 ks, but the data isn't really sufficient to draw any conclusions.

An upper limit on the average 0.6 – 10 keV flux of the prompt emission is also shown, as extrapolated from the BAT data. The trend of the early afterglow power law overshoots the prompt emission data.

The count spectrum measured by the XRT is shown in Figure 8.10. Due to the faintness of the afterglow, it was not possible to produce a spectrum after the light curve break, and the location of the break itself is poorly constrained. The hydrogen column density was not well constrained, but was consistent with the hydrogen column density due to our galaxy alone in the direction of the burst (which is 2.77×10^{20} atoms/cm^2), so we set this parameter to 2.77×10^{20} atoms/cm^2 in the model and froze it at that value. With n_H thus fixed, the best fit spectral index was 1.69 ± 0.32.

8.1.3 XRF 050714B

On 14 July 2005, BAT detected two bursts the second was labeled 050714B. This burst triggered BAT at 22:40:32 UT (MET=143073632s), and the spacecraft slewed immediately so that the XRT was able to begin accumulating data within 151 s (GCN 3613). The position determined

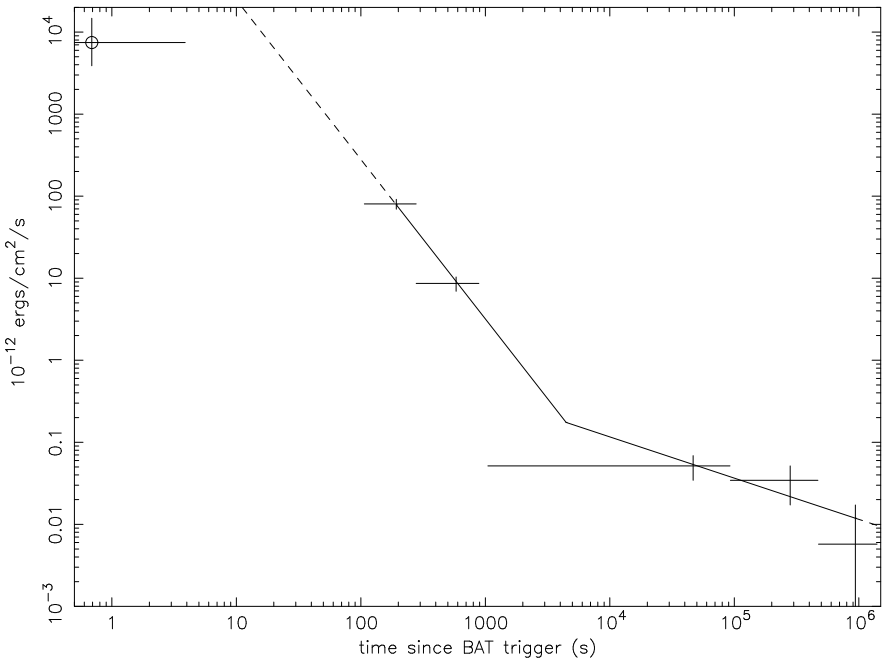

Figure 8.9: The light curve of the XRF 050406 x-ray afterglow, along with the best-fit broken power law model. The two power laws intersect at about 4 ks. Also shown with a circle is the 90% upper limit of the average flux of the prompt emission, as extrapolated from the BAT data.

Table 8.4: The best fit spectral parameters for the XRF 050604 x-ray afterglow. A is measured in units of photons/cm^2/s/keV and flux in units of ergs/cm^2/s. Start and stop times are in seconds since the BAT trigger.

Parameter	Value
I	1.69 ± 0.32
A	$1.51^{+0.66}_{-0.23} \times 10^{-5}$
0.6 – 10 keV flux	$1.37^{+0.42}_{-0.34} \times 10^{-13}$
start time	98.769023 s
stop time	150615.92636 s
exposure	49343.6 s
χ^2_ν/ν	0.775/17

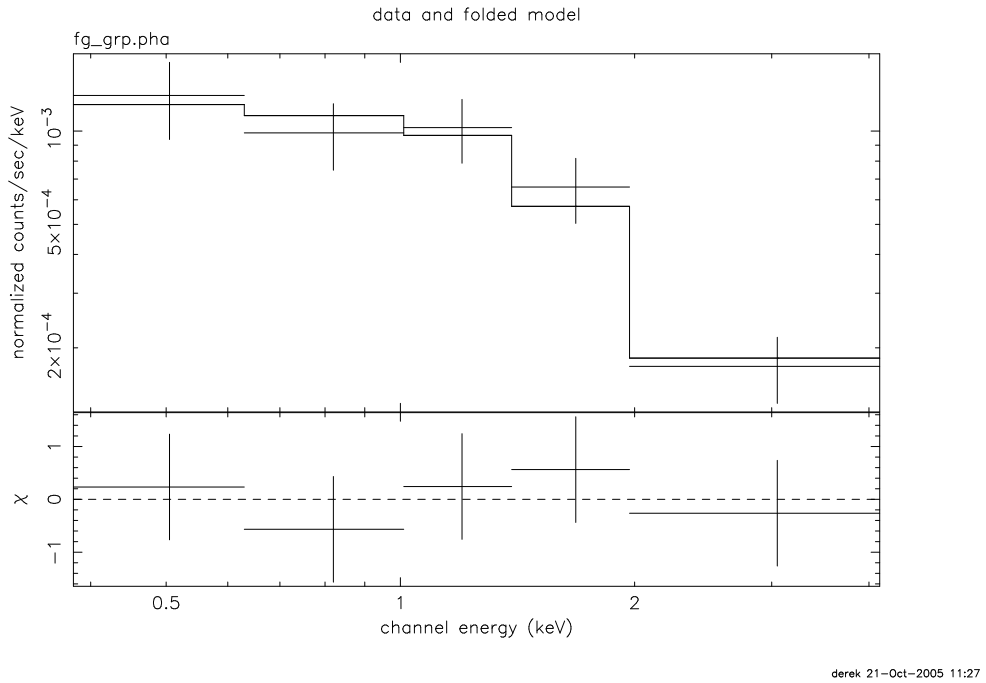

Figure 8.10: The count spectrum of the XRF 050406 x-ray afterglow. Counts bins corresponding to photon energies of 0.3 – 10 keV are shown. See Table 8.4 for the spectral parameters.

by BAT was RA=11h 18m 47.3s, Dec=-15d 32m 6s, with an estimated uncertainty radius of about 3 arcmin (95% confidence) (GCN 3615). The XRT-determined position was found to be RA=11h 18m 48.0s, Dec=-15d 32m 49.9s, with a 6 arcsec uncertainty (90% confidence) (GCN 3184). No afterglow was detected in any other waveband, and a redshift measurement could not be made. Using the technique described in Section 7.3, we constrain the redshift to $z > 1.8$. A serious limitation in our ability to constrain z better than this comes from the uncertainty in the spectral parameters.

Prompt Emission

The T90 duration of the burst was 45.9 ± 0.7 seconds. The light curve may show three separate peaks, but the burst was too dim to enable us to discern structure with much confidence. The emission comes mostly, if not entirely, from 15-50 keV photons (see Figure 8.11).

The Band model failed to adequately constrain $E_{\rm peak}^{\rm obs}$, so the constrained Band model was

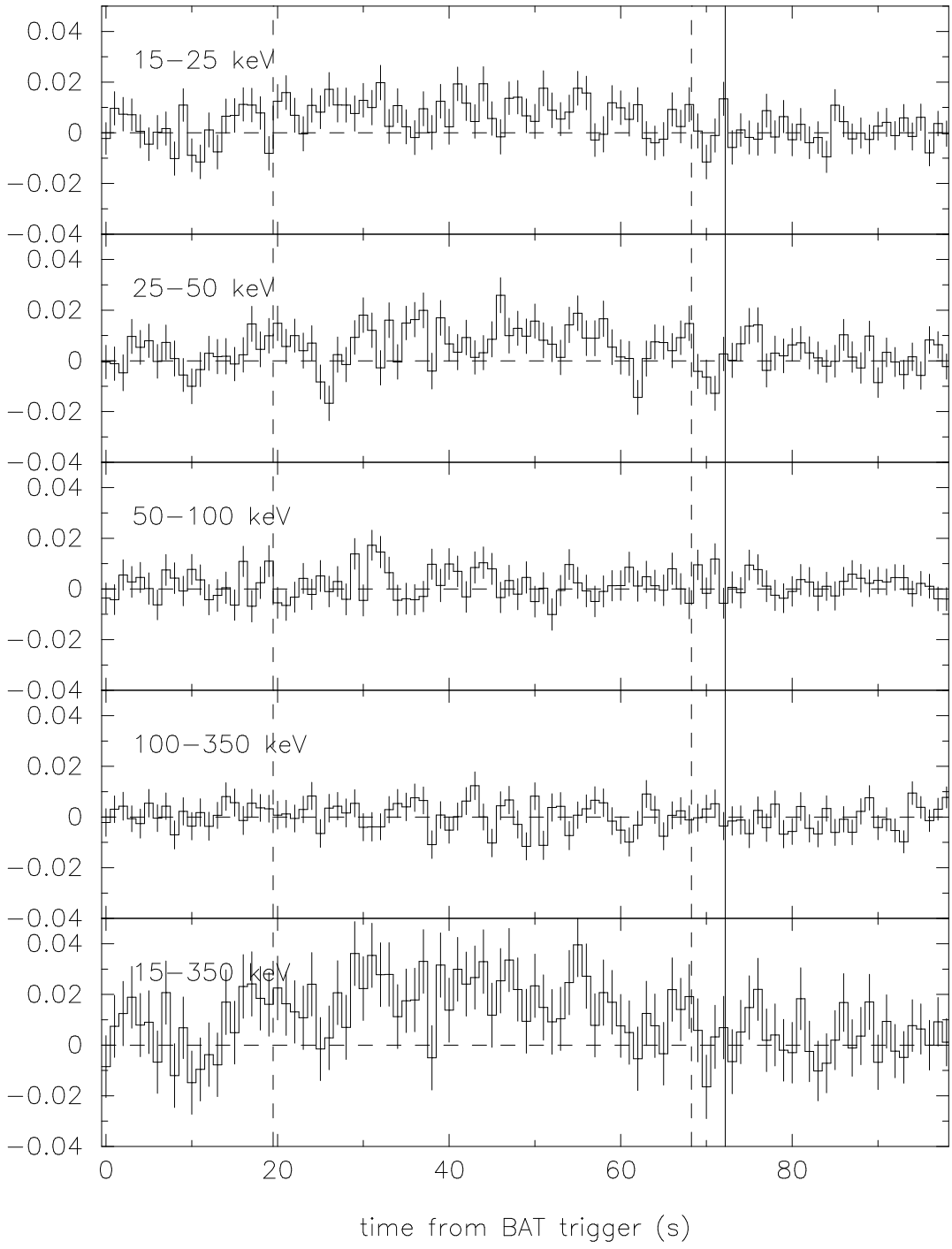

Figure 8.11: The light curve of the XRF 050714b prompt gamma-ray emission. The two dashed lines indicate the time interval used to measure the spectrum. The solid line indicates the time at which Swift began to slew.

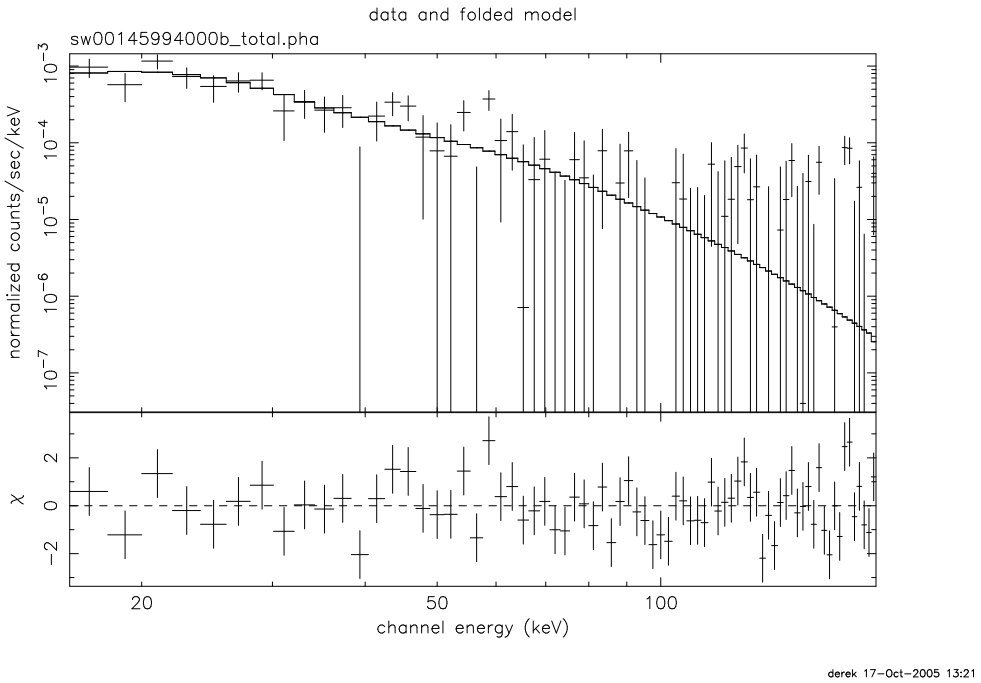

Figure 8.12: The count spectrum of the XRF 050714b prompt gamma-ray emission, along with the best fit model. See Table 8.5 for the spectral parameters.

used instead. $E_{\rm peak}^{\rm obs}$ was found to be $23.1^{+6.4}_{-20.5}$ keV (90% confidence). The time interval from which the spectrum was extracted spans from 19.492 s after the trigger to 68.248 s after the trigger. Figure 8.12 shows the counts spectrum and its best-fit model. The probability density distribution for $E_{\rm peak}^{\rm obs}$ is shown in Figure 8.13.

X-ray Afterglow

The x-ray afterglow light curve, as measured by the XRT, is shown in Figure 8.14. The best fit is a broken power law with an early decay index of -6.605 ± 0.006, a late decay index of -0.89 ± 0.06, and a break time of 225 ± 11 s. The early decay index is considerably steeper than the decay observed in most bursts, even when very early afterglow data is available.

The average 0.6 – 10 keV flux of the prompt emission is also shown, as extrapolated from the BAT data. The trend of the early afterglow overshoots the prompt emission data.

The count spectra for intervals before and after the break in the light curve are shown in Figure 8.15. Before the break, the spectrum fits a power law and a black body model equally well,

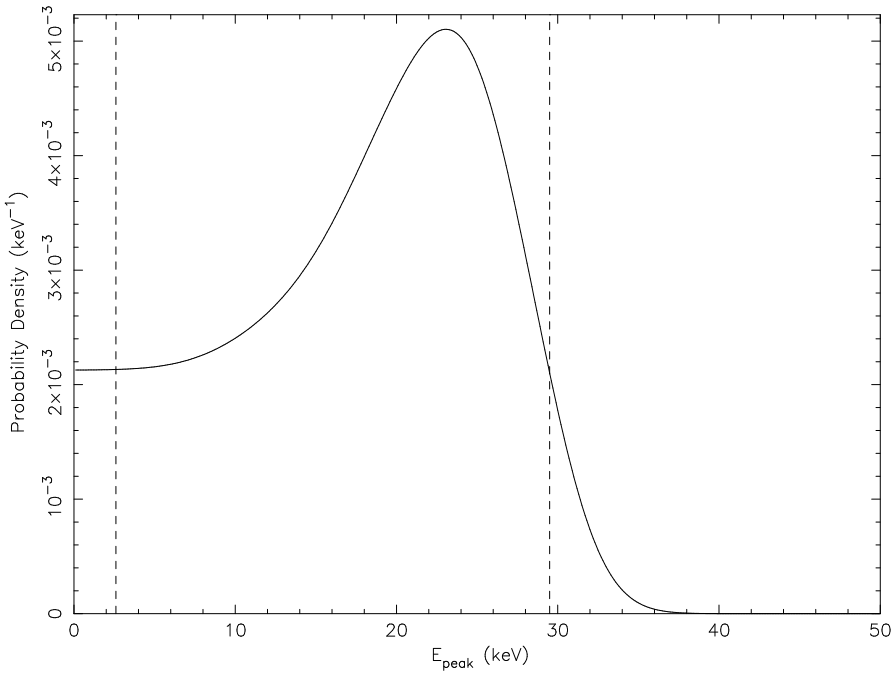

Figure 8.13: The $E^{\rm obs}_{\rm peak}$ probability density distribution for XRF 050714b. The y-axis gives the differential probability $\frac{dP}{dE}$, such that the probability that $E^{\rm obs}_{\rm peak}$ lies between two values E_1 and E_2 is given by the area under the curve between E_1 and E_2. There is a 90% probability that $E^{\rm obs}_{\rm peak}$ lies within the region bounded by the two vertical lines.

Table 8.5: The best fit spectral parameters for the XRF 050714B prompt emission, using a power law model, a cutoff power law model, and the constrained Band model. $E^{\rm obs}_{\rm peak}$ is measured in keV, A in ergs/cm^2/s/keV, and average flux in ergs/cm^2/s for 15 – 150 keV photons. The exposure was 48.756 s.

power law		cutoff power law		Band	
Parameter	Value	Parameter	Value	Parameter	Value
α	$-2.66^{+0.32}_{-0.37}$	α	$-1.04^{+0.65}_{-1.56}$	β	$-3.1^{+0.7}_{-2.1}$
A	$(1.14 \pm 0.28) \times 10^{-}3$	$E^{\rm obs}_{\rm peak}$	< 33.2	$E^{\rm obs}_{\rm peak}$	$23.1^{+6.4}_{-20.5}$
		A	$< 5.51 \times 10^{-2}$	E_{pivot}	20
				A	< 0.68
				flux	1.12×10^{-8}
χ^2_ν/ν	1.218/73	χ^2_ν/ν	1.192/72	χ^2_ν/ν	1.210/72

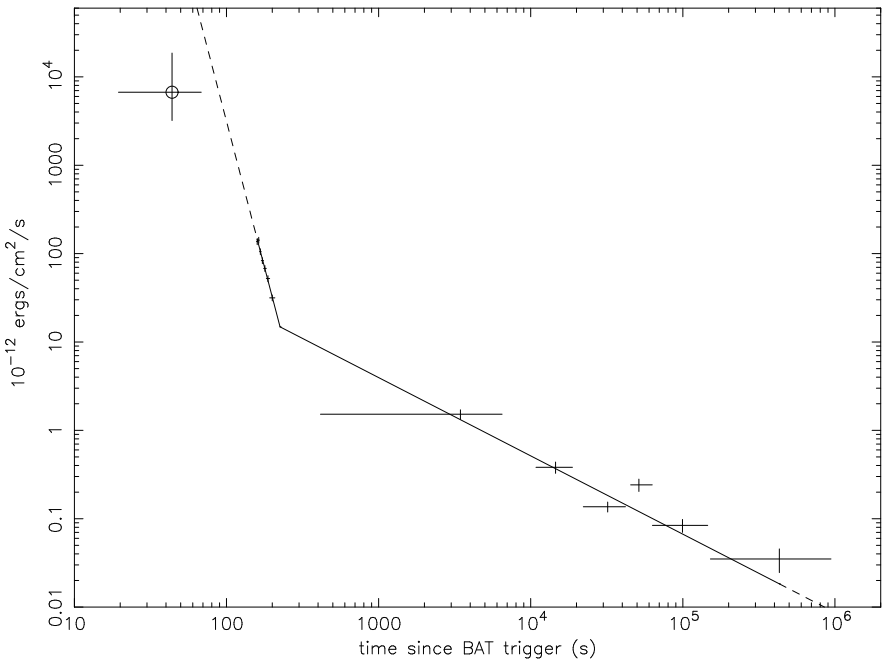

Figure 8.14: The light curve of the XRF 050714B x-ray afterglow, along with the best-fit model of two intersecting power laws. The circled data point is the average flux of the prompt emission, extrapolated into the 0.6 – 10 keV energy range. When extrapolated backward, the early power law overshoots the average 0.6 – 10 keV flux of the prompt emission.

Table 8.6: The best fit spectral parameters for the XRF 050714B x-ray afterglow. n_H is measured in 10^{21} atoms/cm^2, A in units of ergs/cm^2/s/keV, kT in units of keV, and 0.6 – 10 keV flux in units of 10^{-8} ergs/cm^2/s. Start and stop times are in seconds since the BAT trigger.

Before Break (Power Law)		Before Break (Black Body)		After Break	
n_H	$8.2^{+1.6}_{-1.0}$	n_H	$2.5^{+0.9}_{-0.8}$	n_H	$1.4^{+0.9}_{-0.8}$
I	$6.09^{+0.71}_{-0.61}$	kT	0.23 ± 0.02	I	$2.53^{+0.45}_{-0.38}$
A	$1.11^{+0.55}_{-0.34}$	A	$6.6^{+2.6}_{-1.6} \times 10^{-3}$	A	$2.36^{+0.85}_{-0.60} \times 10^{-4}$
flux	$6.39^{+11.47}_{-4.01}$	flux	214.8	flux	$1.15^{+0.50}_{-0.25}$
start time	157.4917 s	start time	157.4917 s	start time	414.47 s
stop time	207.8529 s	stop time	207.8529 s	stop time	58268.59464 s
exposure	50.299 s	exposure	50.299 s	exposure	22542.0 s
χ^2_ν/ν	0.998/24	χ^2_ν/ν	1.059/24	χ^2_ν/ν	1.500/14

but the best fit n_H is not consistent with the spectrum after the break when a power law model is used. The best fit hydrogen column density for the spectrum after the break is $1.4^{+0.9}_{-0.8} \times 10^{21}$ atoms/cm^2, which is slightly higher than the hydrogen column density due to our galaxy alone in the direction of the burst, which is 5.3×10^{20} atoms/cm^2.

8.1.4 XRF 050824

This burst triggered BAT at 23:12:16 UT (MET=146617936s) (GCN 3866). The proximity of the moon prevented Swift from slewing immediately, but the XRT was able to begin accumulating data beginning 6089 s after the trigger (GCN 3872). The position determined by BAT was RA=0h 49m 1.44s, Dec=+22d 37m 4.8s, with an estimated uncertainty radius of about 3 arcmin (90% confidence) (GCN 3871). The XRT-determined position was found to be RA=0h 48m 56.0s, Dec=+22d 36m 28.5s, with a 6.8 arcsec uncertainty (90% confidence) (GCN 3872). An optical afterglow was also detected (GCN 3865), and a redshift of 0.83 was measured (GCN 3874).

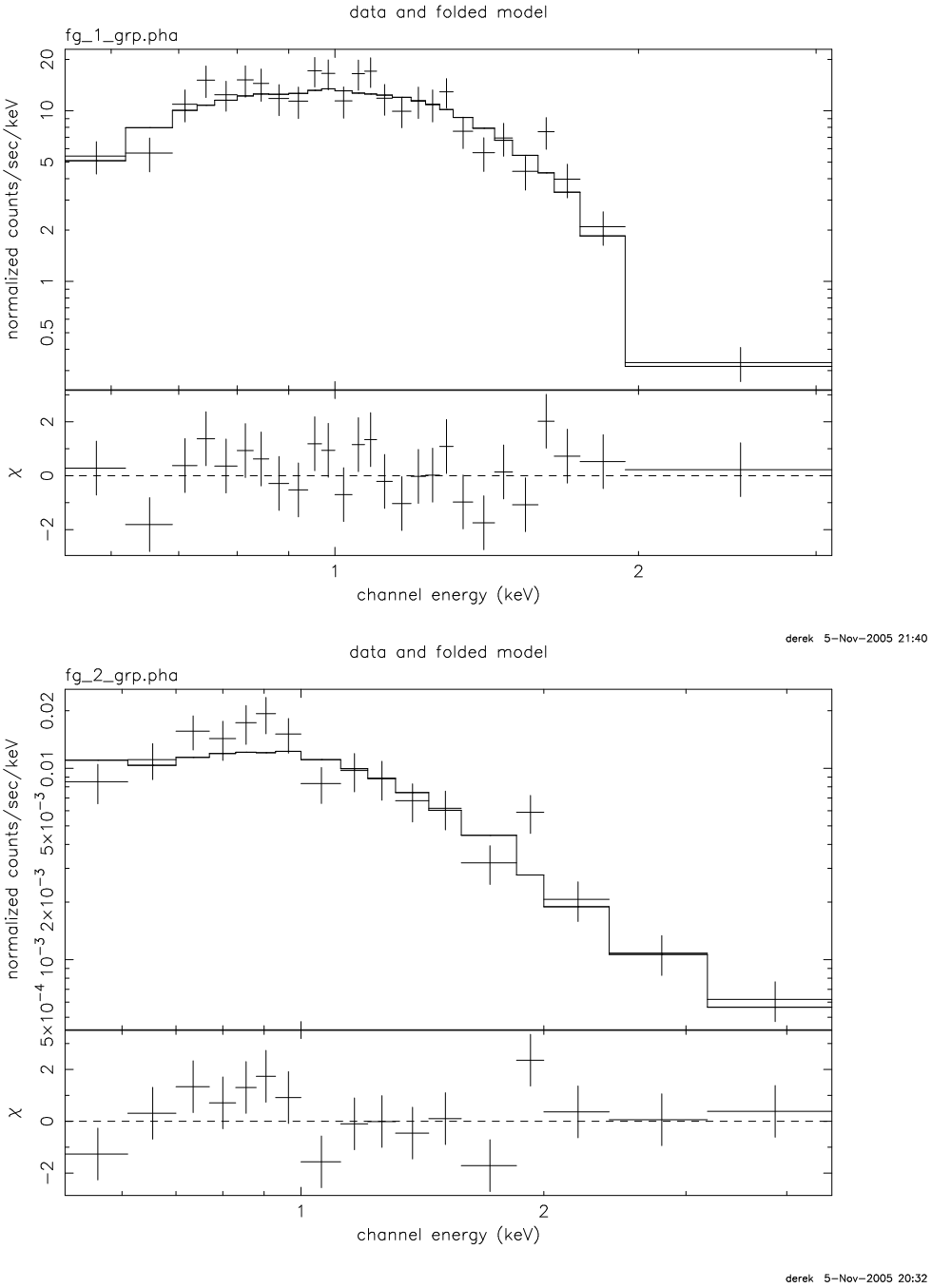

Figure 8.15: The count spectrum of the XRF 050714B x-ray afterglow before (top) and after (bottom) the break in the light curve. The count spectrum before the break is fit with a black body model, while the count spectrum after the break is fit with a power law model. Counts bins corresponding to photon energies of 0.3 – 10 keV are shown. See Table 8.6 for the spectral parameters.

Table 8.7: The best fit spectral parameters for the XRF 050824 prompt emission, using a power law model, a cutoff power law model, and the constrained Band model. $E^{\rm obs}_{\rm peak}$ is measured in keV, A is in ergs/cm^2/s/keV, and average flux is in ergs/cm^2/s for 15 – 150 keV photons. The exposure was 29.092 s.

power law		cutoff power law		constrained Band	
Parameter	Value	Parameter	Value	Parameter	Value
α	$-2.78^{+0.37}_{-0.44}$	α	$-2.61^{+2107}_{-0.47}$	β	$-2.86^{+0.42}_{-0.68}$
A	$9.1^{+2.8}_{-2.7} \times 10^{-4}$	$E^{\rm obs}_{\rm peak}$	$0.41^{+23.17}_{-0.18}$	$E^{\rm obs}_{\rm peak}$	< 19.5
		A	$8.8^{+3.1}_{-4.3} \times 10^{-4}$	E_{pivot}	10
				A	102.2
				flux	9.81×10^{-9}
χ^2_ν/ν	0.935/73	χ^2_ν/ν	0.950/72	χ^2_ν/ν	0.944/72

Prompt Emission

The T90 duration of the burst was 25.5 ± 0.1 seconds. A single broad peak can be distinguished in the light curve, although the signal is weak. The emission comes mostly from 15-50 keV photons, although there may be a hint of emission in the 50-100 keV band (see Figure 8.16).

Using the constrained Band model, we were able to constrain $E^{\rm obs}_{\rm peak}$ to < 19.5 keV. The time interval from which the spectrum was extracted spans from 32.2206 s after the trigger to 61.3126 s after the trigger. Figure 8.17 shows the count spectrum from BAT and the best-fit constrained Band model. The probability density distribution for $E^{\rm obs}_{\rm peak}$ is shown in Figure 8.18.

X-ray Afterglow

The x-ray afterglow, as measured by the XRT, is shown in Figure 8.19. The data is best fit (with a $\chi^2_{/nu}$ of 1.37) by a broken power law with an early index of -0.49 ± 0.05, a late index of -1.1 ± 0.3, and a break time of 300000 ± 150000 s. A single power law fit results in an index of -0.60 ± 0.27 and a χ^2_ν of 1.85.

The average 0.6 – 10 keV flux extrapolated from the fit to the prompt emission is also shown in Figure 8.19. When extrapolated backward, the early power law undershoots the average 0.6 –

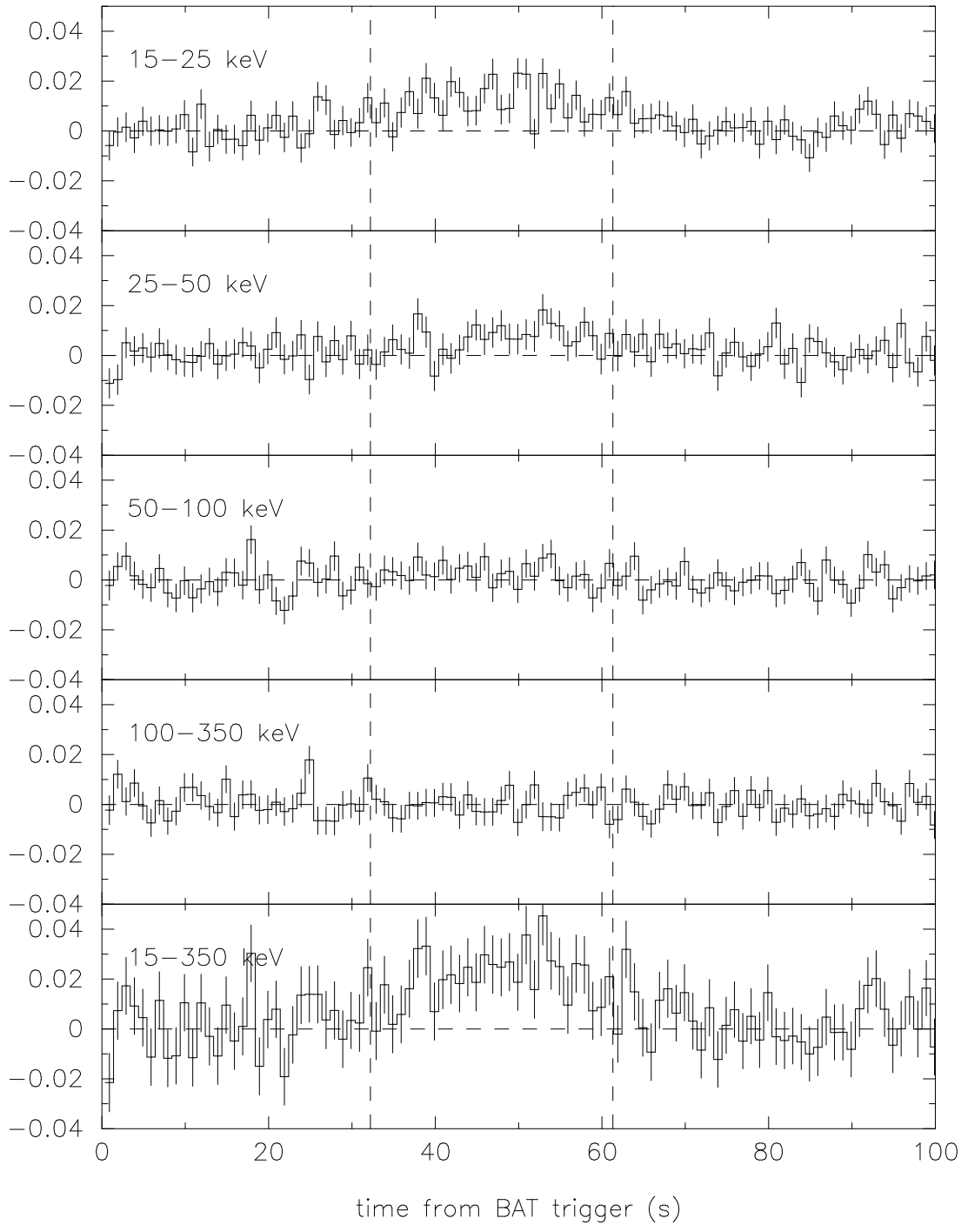

Figure 8.16: The light curve of the XRF 050824 prompt gamma-ray emission. The two dashed lines indicate the time interval used to measure the spectrum. Due to Viewing constraints posed by the Moon, Swift did not slew to this burst until long after this time interval (To+6089s).

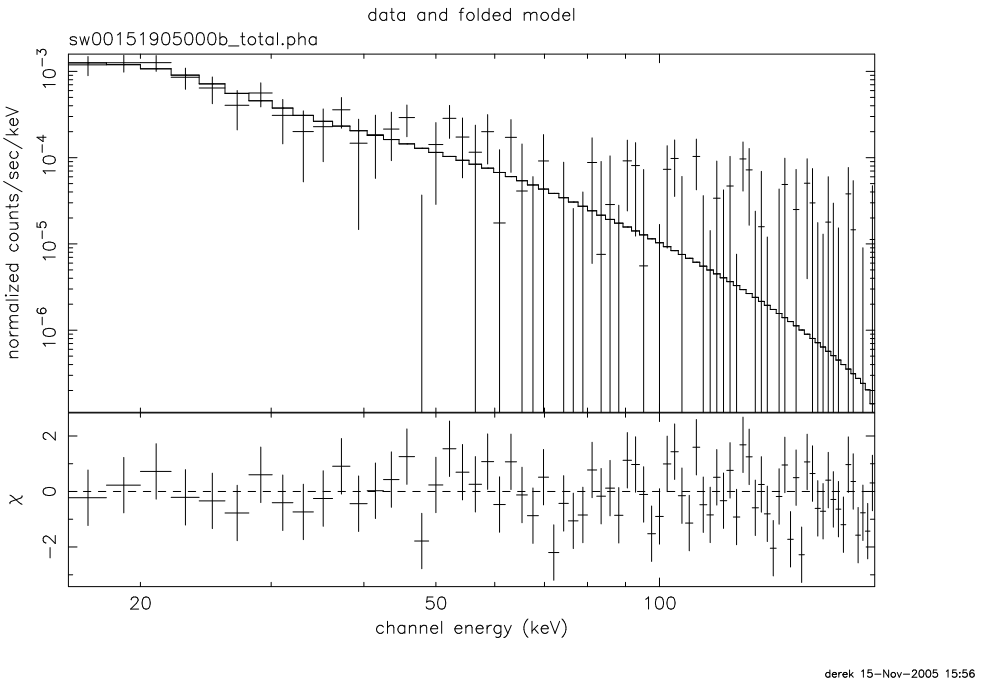

Figure 8.17: The count spectrum from BAT of the XRF 050824 prompt gamma-ray emission, along with the best fit constrained Band model. See Table 8.7 for the spectral parameters.

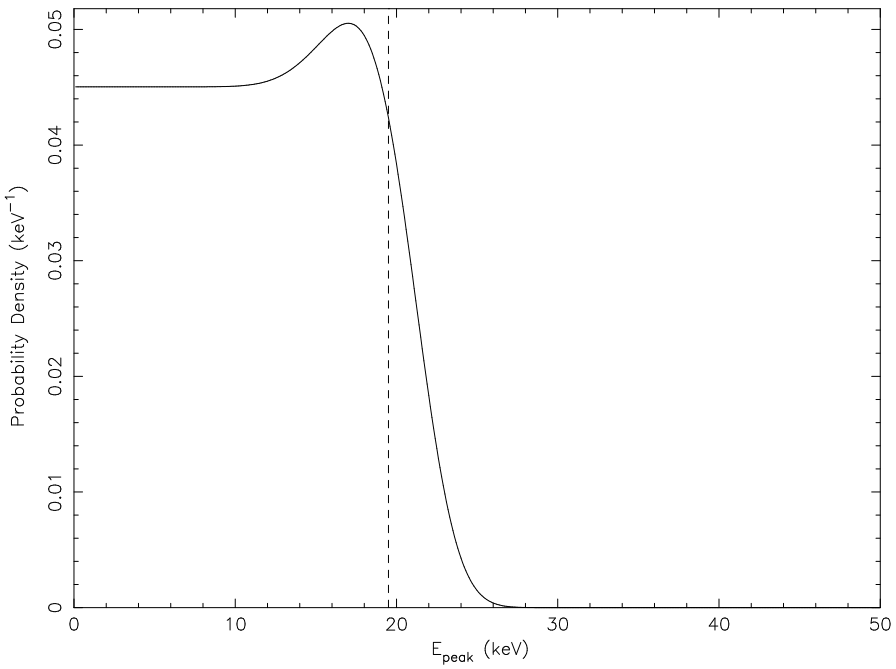

Figure 8.18: The $E^{\rm obs}_{\rm peak}$ probability density distribution for XRF 050824. The y-axis gives the differential probability $\frac{dP}{dE}$, so that the probability that $E^{\rm obs}_{\rm peak}$ lies between two values E_1 and E_2 is given by the area under the curve between E_1 and E_2. There is a 90% probability that $E^{\rm obs}_{\rm peak}$ lies below 19.5 keV.

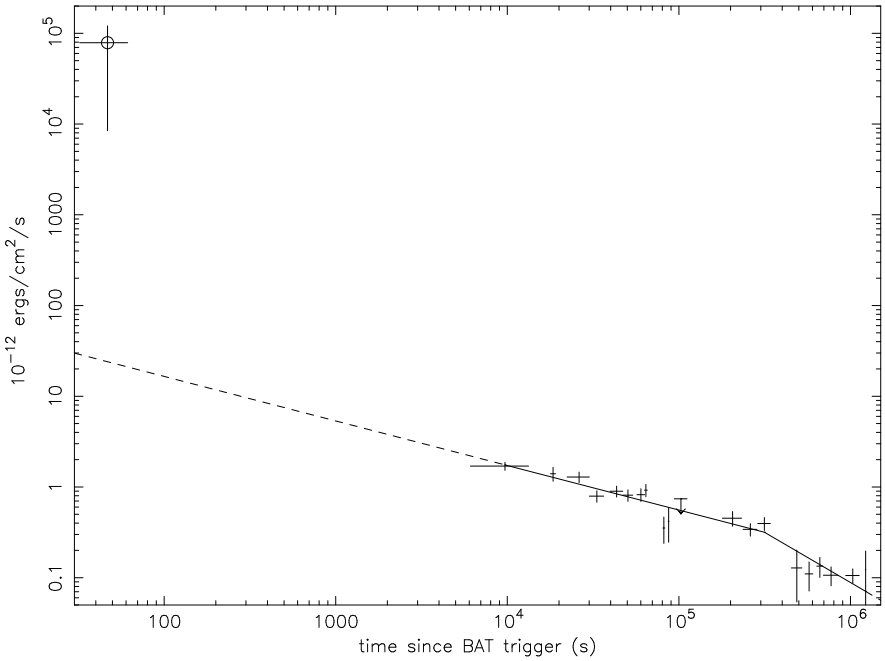

Figure 8.19: The light curve of the XRF 050824 x-ray afterglow, along with the best-fit broken power law fits to the light curve. The circled data point is the average flux of the prompt emission, extrapolated into the 0.6 – 10 keV energy range. When extrapolated backward, the early power law undershoots the average 0.6 – 10 keV flux of the prompt emission.

10 keV flux of the prompt emission.

The counts spectrum measured by the XRT is shown in Figure 8.20. The best fit spectral index is 1.9 ± 0.2. The best fit hydrogen column density is $8.1^{+6.6}_{-6.0} \times 10^{20}$ atoms/cm^2, which is consistent with the hydrogen column density due to our galaxy alone in the direction of the burst, which is 3.6×10^{20} atoms/cm^2. The spectrum used here consists of counts that were accumulated between 6092s after the trigger and 87622 s after the trigger. The afterglow had become too faint after the break for spectral analysis.

8.1.5 XRF 050528

This burst triggered BAT at 04:06:45 UT (MET=138946004.672s) (GCN 3496). While Swift immediately slewed, afterglow measurements had to be delayed because XRT was in an engineering mode at the time of the burst. XRT began collecting data 14.15 hours after the BAT trigger (GCN 3505). The position determined by BAT was RA=23h 34m 8.8s, Dec=+45d 56m 37.2s, with an

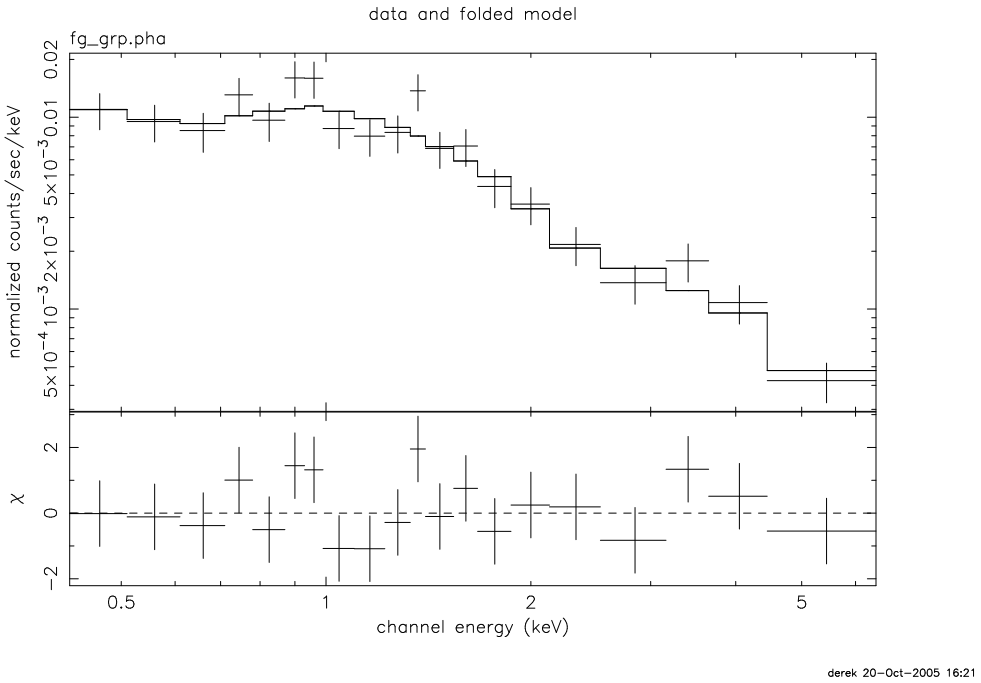

Figure 8.20: The count spectrum of the XRF 050824 x-ray afterglow. Count bins corresponding to photon energies of 0.3 – 10 keV were included. See Table 8.8 for the spectral parameters.

Table 8.8: The best fit spectral parameters for the XRF 050824 x-ray afterglow. n_H is measured in atoms/cm^2, A in units of photons/cm^2/s/keV, and flux in units of ergs/cm^2/s. Start and stop times are in seconds since the BAT trigger.

Parameter	Value
I	1.9 ± 0.2
n_H	$8.1^{+6.6}_{-6.0} \times 10^{20}$
A	$8.2^{1.6}_{-1.3} \times 10^{-5}$
0.6 – 10 keV flux	$1.24^{+0.16}_{-0.14} \times 10^{-12}$
start time	6091.773543 s
stop time	87622.19248 s
exposure	22773.8 s
χ^2_ν/ν	0.992/17

Table 8.9: The best fit spectral parameters for the XRF 050528 prompt emission, using a power law model, a cutoff power law model, and the constrained Band model. $E^{\rm obs}_{\rm peak}$ is measured in keV, A is in ergs/cm^2/s/keV, and average flux is in ergs/cm^2/s for 15 – 150 keV photons. The exposure was 12.248 s.

power law		cutoff power law		constrained Band	
Parameter	Value	Parameter	Value	Parameter	Value
α	$-2.34^{+0.26}_{-0.29}$	α	$-0.78^{+1.85}_{-1.32}$	α	$-0.96^{+1.75}_{-1.73}$
A	$3.73^{+0.69}_{-7.21} \times 10^{-3}$	$E^{\rm obs}_{\rm peak}$	$30.1^{+10.6}_{-30.1}$	β	< -2.45
		A	$< 9.86 \times 10^{-2}$	$E^{\rm obs}_{\rm peak}$	$30.5^{+9.9}_{-9.9}$
				A	$2.42^{+38.36}_{-1.73} \times 10^{-2}$
				flux	9.78×10^{-9}
χ^2_ν/ν	0.905/73	χ^2_ν/ν	0.861/72	χ^2_ν/ν	0.873/71

estimated uncertainty radius of about 3 arcmin (90% confidence). Three sources were detected inside the BAT error circle (GCN 3505) but they were too faint for my analysis to determine which, if any, was the afterglow. No other afterglow emission was detected, and no redshift was measured. The inferred redshift, using the technique described in Section 7.3, is $0.3^{+1.7}_{-0.2}$.

Prompt Emission

The T90 duration of the burst was 11.168 ± 0.036 seconds. There are possibly two peaks, one beginning at about 5 seconds before the trigger, and a second larger one centered about 3.5 seconds after the trigger. The most prominent emission results in counts in channels corresponding to photon energies of 15 - 50 keV, with a hint of counts in the 50 - 100 keV band. No counts are seen in the 100 - 350 keV band (see Figure 8.21).

For this burst, the Band model provided a good fit to the spectrum, and was able to constrain $E^{\rm obs}_{\rm peak}$ reasonably well to $30.5^{+9.9}_{-9.9}$ keV. The time interval from which the spectrum was extracted spans from 7.264 s before the trigger to 4.984 s after it. Figure 8.22 shows the counts spectra and the best-fit model.

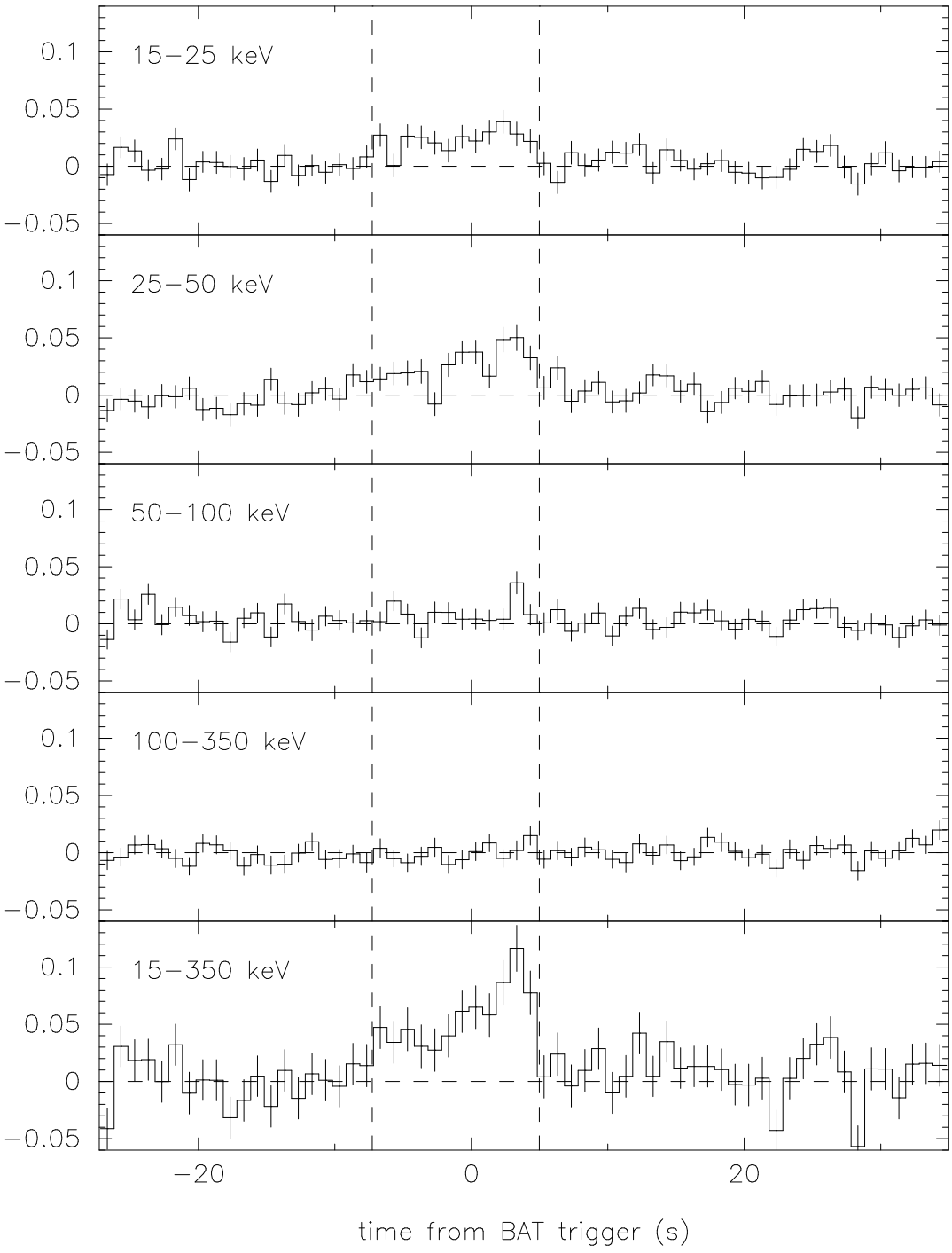

Figure 8.21: The light curve of the XRF 050528 prompt gamma-ray emission. The two dashed lines indicate the time interval used to measure the spectrum. Swift slewed after the time interval shown on this plot.

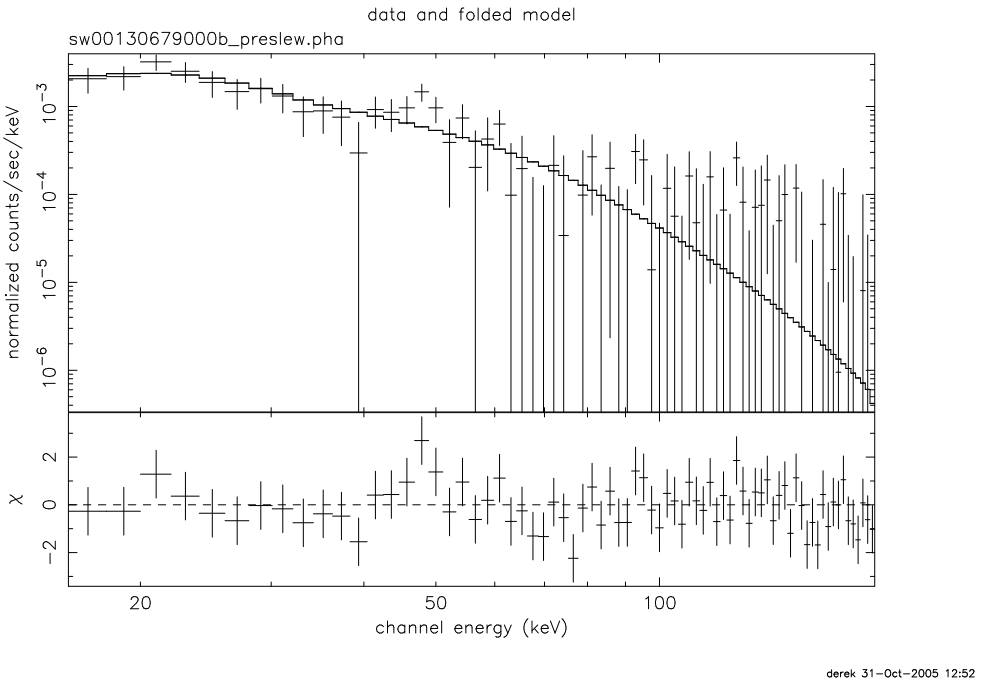

Figure 8.22: The count spectra of the XRF 050528 prompt gamma-ray emission, along with the best fit model. See Table 8.9 for the spectral parameters.

8.1.6 XRF 050215B

This burst triggered BAT at 02:35:00 UT (MET=130127622.592s) (GCN 3027). While Swift immediately slewed, afterglow measurements had to be delayed because XRT was in a manual state collecting calibration data, and Swift entered the SAA shortly after the slew. XRT began collecting data about 96 minutes after the BAT trigger. The position determined by BAT was RA=11h 37m 48s, Dec=+40d 48m 16s, with an estimated uncertainty radius of about 4 arcmin (90% confidence) (GCN 3024). The XRT-determined position was found to be RA=11h 37m 47.7s, Dec=+40d 47m 44.0s, with a 6 arcsec uncertainty (90% confidence) (GCN 3872). In addition to the x-ray afterglow, optical and infrared afterglow emission was detected (GCN 3031, 3037). No redshift was measured for this burst, but the inferred redshift, based on the Yonetoku relation, is $0.8^{+1.4}_{-0.3}$.

Table 8.10: The best fit spectral parameters for the XRF 050215B prompt emission, using a power law model, a cutoff power law model, and the Band model. $E^{\rm obs}_{\rm peak}$ is measured in keV, A in ergs/cm^2/s/keV, and average flux in 10^{-8} ergs/cm^2/s for 15 – 150 keV photons. The exposure was 11.776 s.

power law		cutoff power law		Band	
Parameter	Value	Parameter	Value	Parameter	Value
α	$-2.22^{+0.19}_{-0.21}$	α	$-1.39^{+0.74}_{-0.71}$	α	$-1.48^{+0.68}_{-0.40}$
A	$2.28^{+0.30}_{-0.32} \times 10^{-3}$	$E^{\rm obs}_{\rm peak}$	> 38.5	β	< 2.22
		A	$< 2.10 \times 10^{-2}$	$E^{\rm obs}_{\rm peak}$	$26.7^{+10.7}_{-12.5}$
				A	$< 8.60 \times 10^{-3}$
				flux	2.04 ± 0.30
χ^2_ν/ν	0.790/192	χ^2_ν/ν	0.771/191	χ^2_ν/ν	0.775/190

Prompt Emission

The T90 duration of the burst was 10.43 ± 0.06 seconds. There is a strong peak at the time of the trigger, followed by two smaller peaks at 5 s and 9 s after the trigger. The most prominent emission results in channels corresponding to photon energies of 15-50 keV, but this time we also see significant emission in the 50-100 keV band. No emission is apparent in the 100-350 keV band (see Figure 8.23).

HETE-2 also observed this burst, and we were able to use both BAT and HETE-2 data to find the photon spectrum. The Band model provided a good fit to the data and constrained $E^{\rm obs}_{\rm peak}$ to $26.7^{+10.7}_{-12.5}$ keV. The time interval from which the spectrum was extracted spans from 1.776 s before the trigger to 10 s after it. Figure 8.24 shows the counts spectra and the best-fit model.

X-ray Afterglow

The x-ray afterglow, as measured by the XRT, is shown in Figure 8.25. As we noted before, afterglow data was recorded beginning about 96 minutes after the burst. A power law with an index of -1.00 ± 0.08 fits the data quite well. An offset power law provides a better fit, but the offset time is very poorly constrained. There are too few data points to provide well-constrained

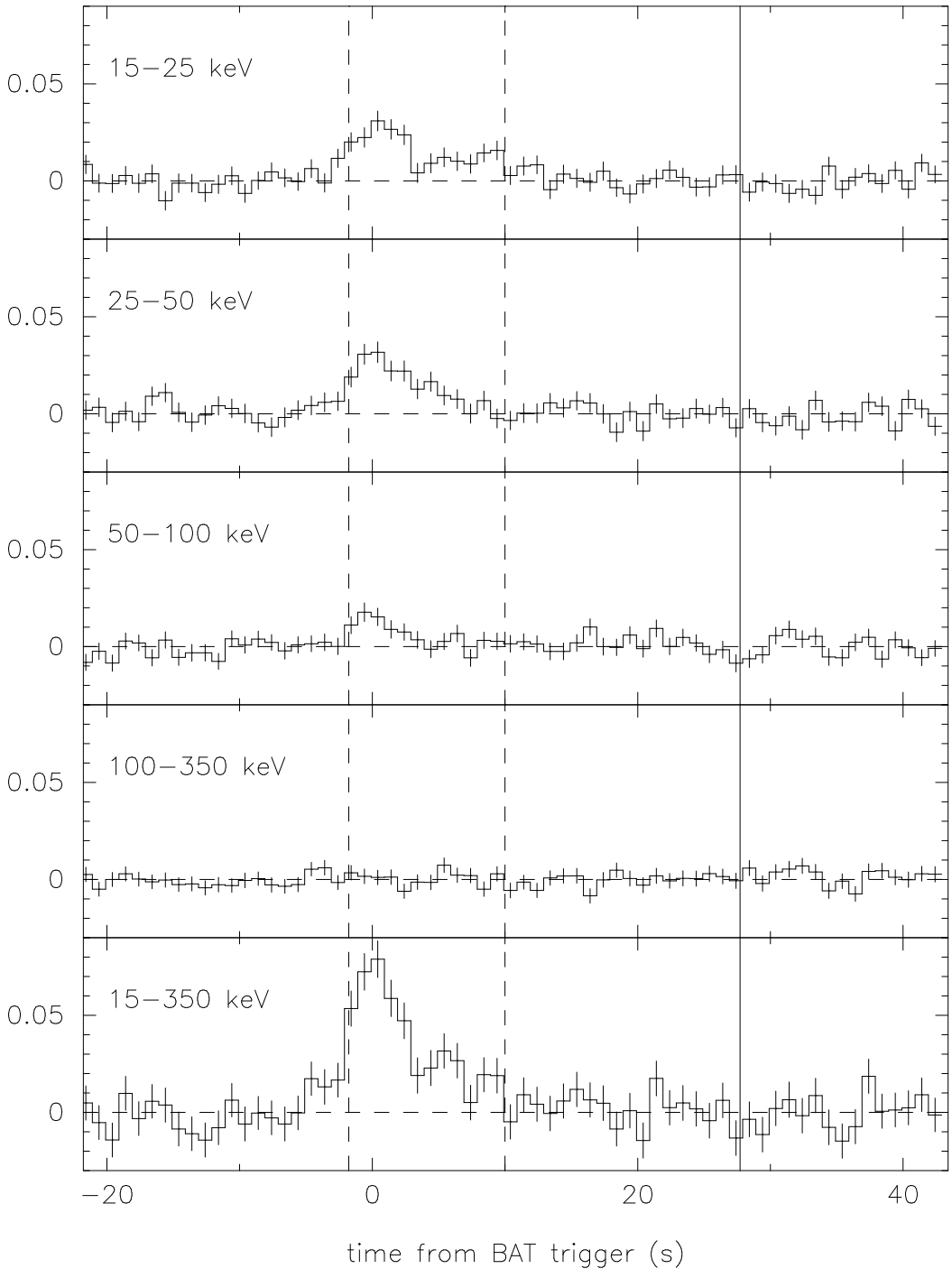

Figure 8.23: The light curve of the XRF 050215B prompt gamma-ray emission. The two dashed lines indicate the time interval used to measure the spectrum. The solid line indicates the time at which Swift began to slew.

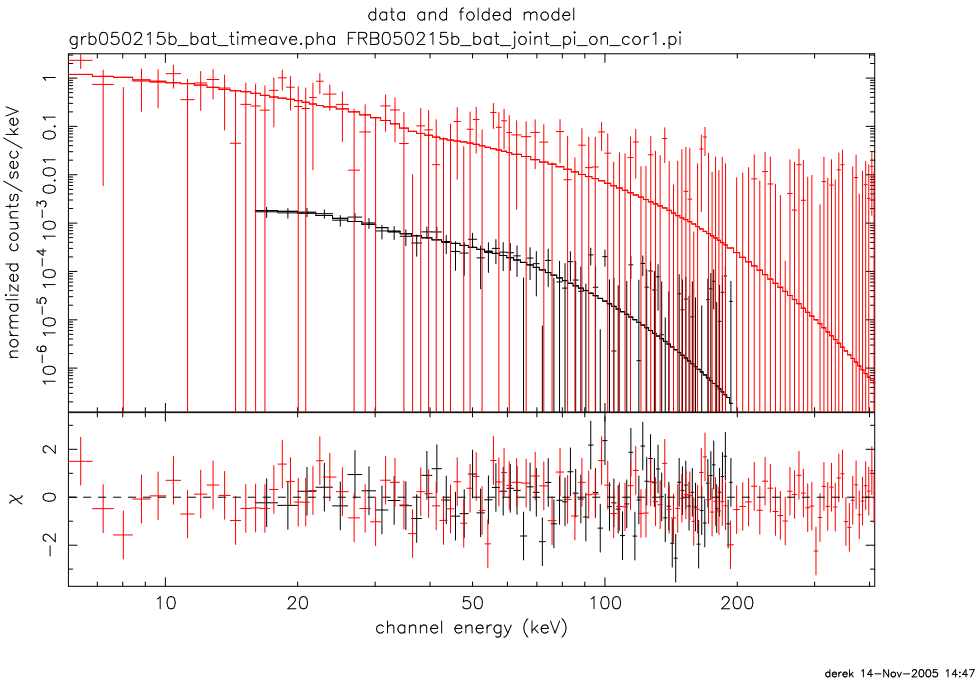

Figure 8.24: The count spectra of the XRF 050215B prompt gamma-ray emission, as recorded by BAT and HETE-2, along with the best fit Band model. The BAT spectrum is shown in black and the HETE-2 spectrum is shown in red. See Table 8.10 for the spectral parameters.

parameters from a broken power law fit. The power law is consistent with the upper limit of the extrapolated 0.6 – 10 keV flux from the prompt emission.

The count spectrum measured by the XRT is shown in Figure 8.26. The hydrogen column density was constrained to $< 3.3 \times 10^{21}$ atoms/cm^2. Since this was consistent with the hydrogen column density due to our galaxy alone in the direction of the burst (which is 2.07×10^{20} atoms/cm^2) and was not very well constrained, we set this parameter to 2.07×10^{20} atoms/cm^2 in the model and froze it at that value. With n_H thus fixed, the best fit spectral index was $1.10^{+0.55}_{-0.58}$. The spectrum used here consists of counts accumulated between 5770 s after the trigger and 35999.7 s after the trigger.

8.2 XRRs

For our sample of X-ray rich gamma-ray bursts (XRRs), which are defined as those with a fluence ratio $S(50-100 \text{ keV})/S(25-50 \text{ keV})$ between 0.7566 and 1.3855, we selected 4 bursts. Two

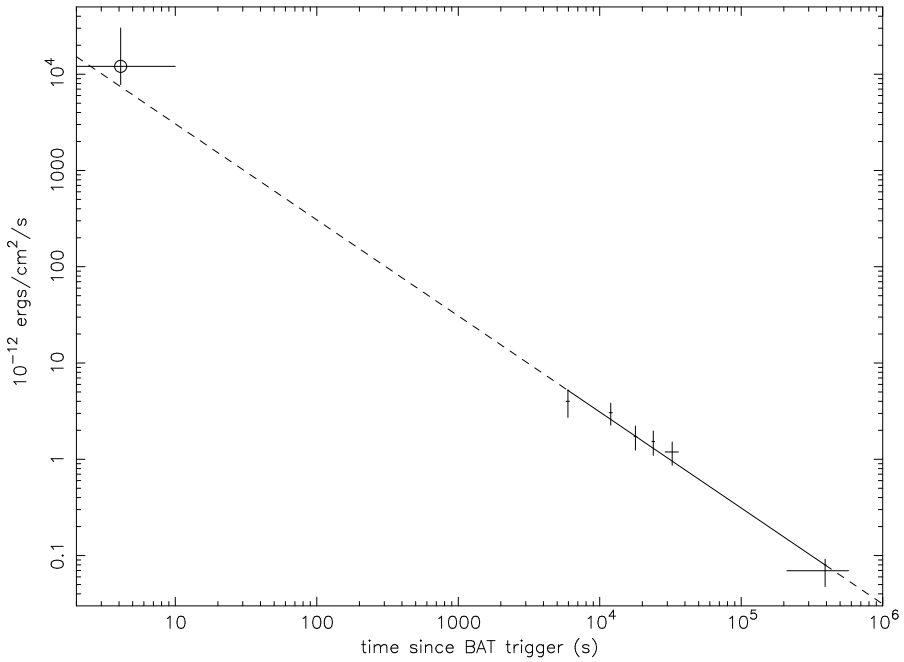

Figure 8.25: The light curve of the XRF 050215B x-ray afterglow, along with the best-fit power law model. Also shown, with a circle, is the upper limit of the average flux of the prompt emission extrapolated into the 0.6 – 10 keV energy range.

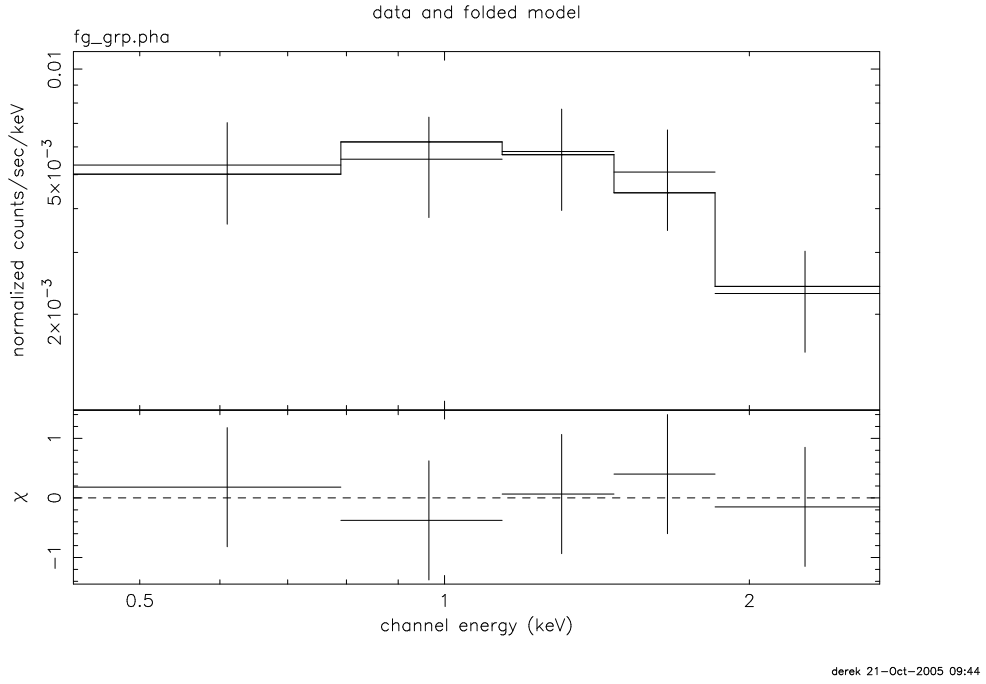

Figure 8.26: The count spectrum of the XRF 050215B x-ray afterglow. Count bins corresponding to photon energies of 0.3 – 10 keV were included. See Table 8.11 for the spectral parameters.

Table 8.11: The best fit spectral parameters for the XRF 050215B x-ray afterglow. A is measured in units of photons/cm^2/s/keV and flux in units of ergs/cm^2/s. Start and stop times are in seconds since the BAT trigger.

Parameter	Value
I	$1.10^{+0.55}_{-0.58}$
A	$1.09^{+0.32}_{-0.28} \times 10^{-4}$
0.6 – 10 keV flux	$1.52^{+1.51}_{-0.72} \times 10^{-12}$
start time	5770.0086 s
stop time	35999.67288 s
exposure	5131.1 s
χ^2_ν/ν	0.120/3

of these have a fairly low fluence ratio, making them "borderline XRRs" and were selected because we have measured redshifts for them. The other two were selected because they were simultaneously observed by Konus, enabling us to determine their spectral parameters with greater precision.

8.2.1 XRR 050315

This burst triggered BAT at 20:59:42 UT (MET=132613181.952) (GCN 3094). Swift slewed immediately and the XRT began accumulating data at 21:01:05.5 UT, 83.5 s after the trigger (GCN 3097). The position determined by BAT was RA=20h 25m 57.2s, Dec=-42d 35m 30.6s, with an estimated uncertainty radius of about 3 arcmin (90% confidence). The XRT-determined position was found to be RA=20h 25m 53.9s, Dec=-42d 36m 01.4s, with a 6 arcsec uncertainty (90% confidence) (GCN 3133). Afterglow emission in optical (GCN 3100) and radio (GCN 3102) wavebands was detected, and a redshift of 1.949 was measured (GCN 3101).

Prompt Emission

XRR 050315 was rather long, with a T90 duration of 95.46 ± 0.14 seconds. There is a small peak beginning about 56 seconds before the trigger, followed by three other small peaks centered at about 35, 25, and 15 seconds before the trigger. A large broad peak extends from 10 seconds before

the trigger to about 20 seconds after the trigger, followed by another large peak that begins about 25 seconds after the trigger and gradually decays to zero at about 8 seconds after the trigger. Most of the flux comes from channels corresponding to photon energies of 15 - 50 keV, with significant emission also coming from 50 - 100 keV channels. There is a hint of possible emission in the 100 - 350 keV band, too (see Figure 8.27).

A power law fit to this count spectra indicated that the power law index was -1.89 ± 0.10 which is less than -2, so the constrained Band model cannot be used. The Band model, with all of the parameters free to vary, was not able to constrain any of the parameters, and a confidence contour plot of α verses $E_{\rm peak}^{\rm obs}$ shows $E_{\rm peak}^{\rm obs}$ to be smaller than 100 keV if α is greater than -1.5, which is admittedly a very weak constraint (see Figure 8.28).

The time interval from which the spectrum was extracted spans from 56.18 s before the trigger to 14.14859 s after it. Figure 8.29 shows the count spectra and the best-fit power law model.

X-ray Afterglow

The x-ray afterglow, as measured by the XRT, is shown in Figure 8.30. The best fit power law index for the early phase of the afterglow (between about 90 s and about 500 s after the BAT trigger) is -3.21 ± 0.04. The data was heavily piled up over much of this range, and the difficulty in correcting for pile up may have contributed to the poor fit. The late phase of the afterglow (from 5 ks to the end of the observation) is well fit by a broken power law with an early decay index of -0.65 ± 0.02, a late decay index of -1.31 ± 0.07, and a break time of 125000 ± 13000 s. Vaughan et al. have published a paper describing this burst [79], and the x-ray light curve they derived is essentially the same as the one presented here. Their light curve does show some evidence of the early phase and the late phase smoothly joining each other.

The 0.6 – 10 keV flux of the prompt emission is also shown in Figure 8.30, as extrapolated from the BAT data.

The XRT count spectra during the early phase of the light curve, and during the late phase

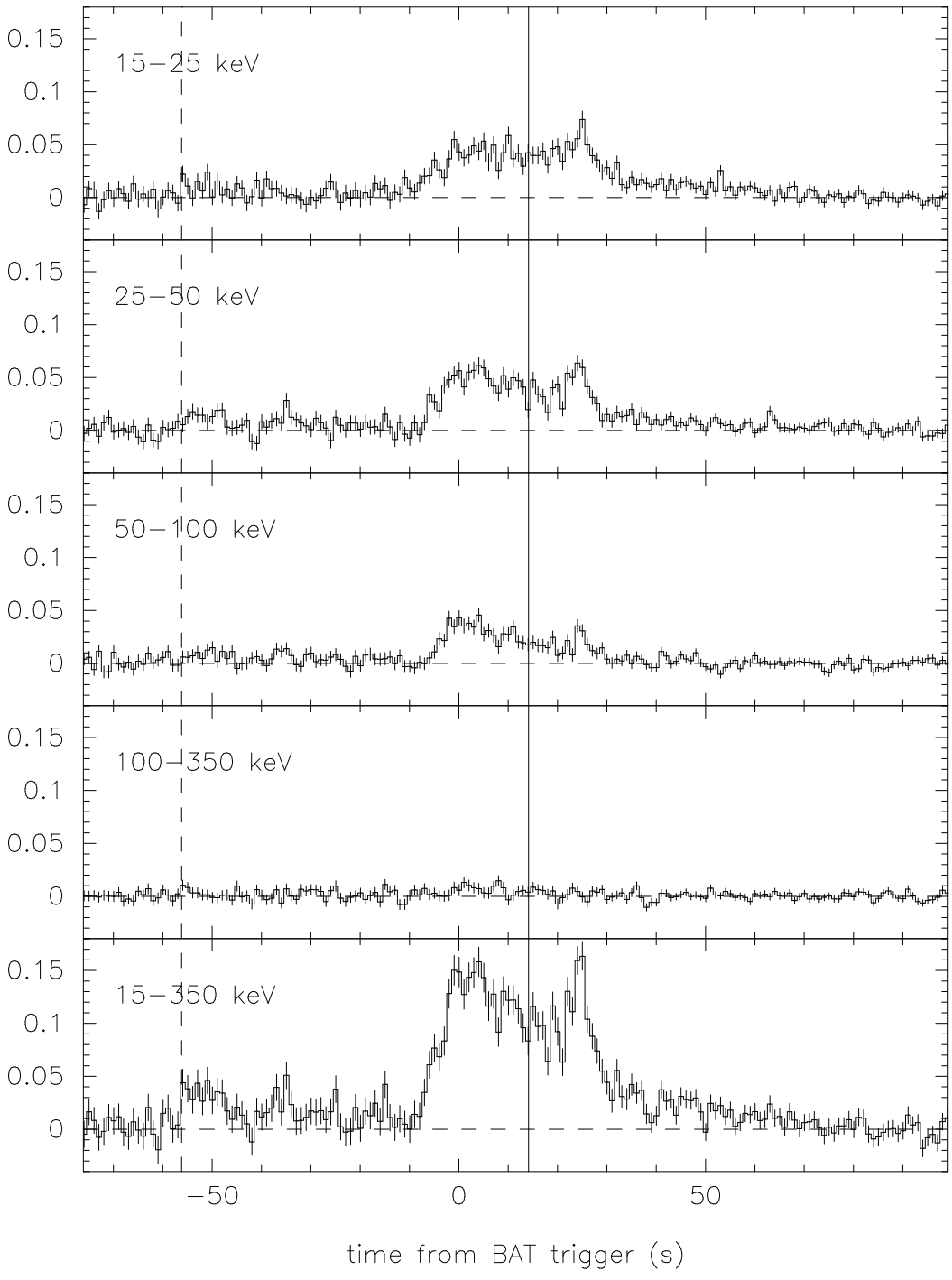

Figure 8.27: The light curve of the XRR 050315 prompt gamma-ray emission. The dashed vertical line indicates the beginning of the time interval used to measure the spectrum. Swift began to slew at the time indicated by the solid vertical line. Because of difficulties associated with fitting data that has been taken during a slew, the spectrum was extracted from a time interval ending at the slew.

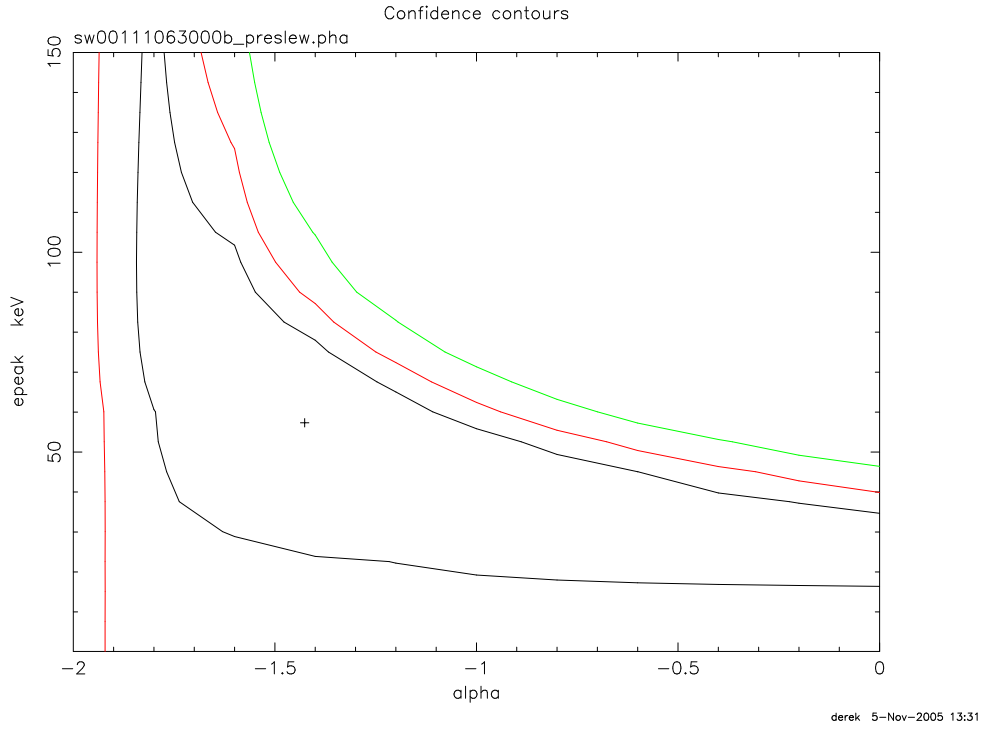

Figure 8.28: The confidence contour between α and $E_{\rm peak}^{\rm obs}$ for the XRF 050315 prompt gamma-ray emission. The probability that α and $E_{\rm peak}^{\rm obs}$ have values between the black lines is 68%. The probability that their values lie between the red lines is 90%. The probability that their values lie below the green line is 99%. Based on this plot, there is a 90% probability that $E_{\rm peak}^{\rm obs}$ is less than 100 keV if α is greater than -1.5.

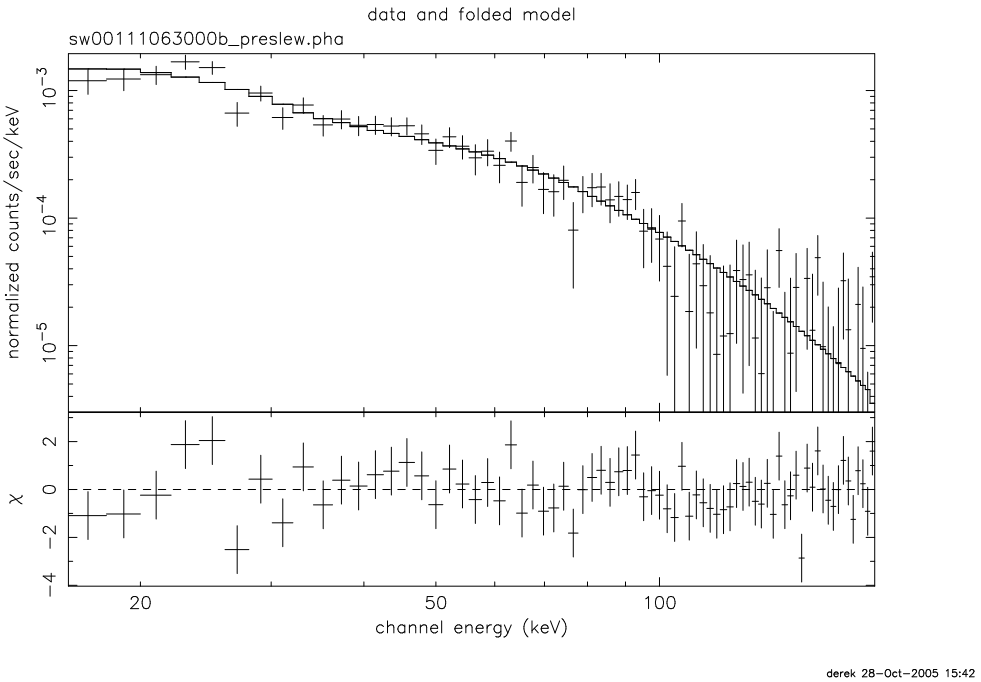

Figure 8.29: The count spectrum of the XRR 050315 prompt gamma-ray emission, along with the best fit power law model. See Table 8.12 for the spectral parameters.

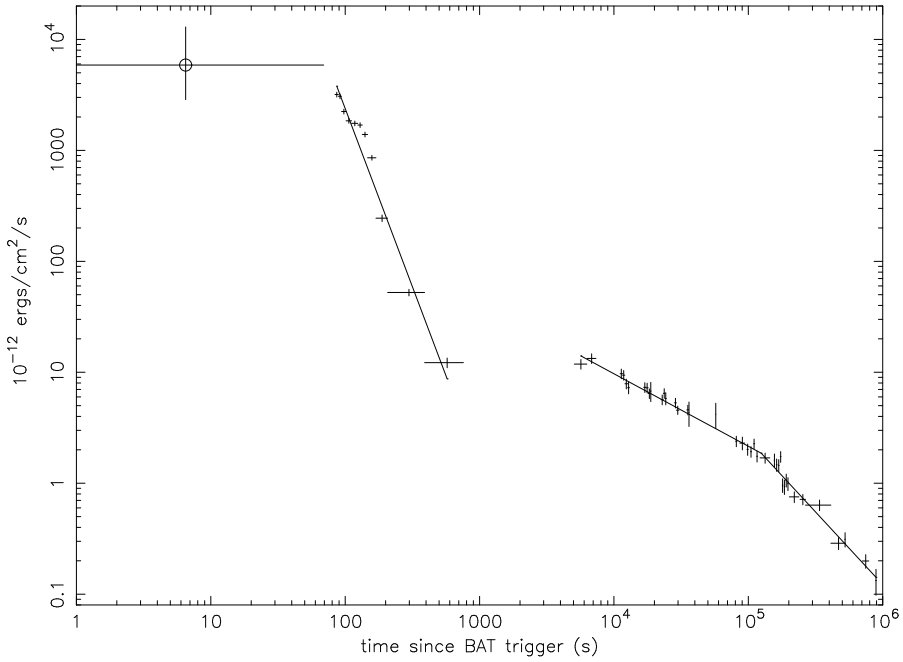

Figure 8.30: The light curve of the XRR 050315 x-ray afterglow. The early phase of the afterglow (between 90 s and 500 s) is fit with a power law, and the late phase (after 5000 s) is fit with a broken power law. The circled data point is the average flux of the prompt emission, extrapolated into the 0.6 – 10 keV energy range.

Table 8.12: The best fit spectral parameters for the XRR 050315 prompt emission, using the Band model with α frozen at -1.5, -1 and at -0.5 as well as a simple power law model. $E_{\rm peak}^{\rm obs}$ is measured in keV, A in photons/cm^2/s/keV, and average 15 – 150 keV flux in ergs/cm^2/s. It is important to note that since only the interval prior to the slew was used to extract the spectrum, the average flux given below multiplied by the exposure gives the total fluence only of that portion of the burst, not for the full burst.

Model	Parameter	Value
Band ($\alpha = -1.5$)	β	< -1.84
	$E_{\rm peak}^{\rm obs}$	< 90.9
	A	$5.01^{+37.66}_{-0.57} \times 10^{-3}$
	χ^2_ν/ν	0.930/72
Band ($\alpha = -1$)	β	$-2.07^{+0.24}_{-0.54}$
	$E_{\rm peak}^{\rm obs}$	< 59.2
	A	$1.02^{+23.91}_{-0.21} \times 10^{-2}$
	χ^2_ν/ν	0.936/72
Band ($\alpha = -0.5$)	β	$-1.95^{+0.14}_{-0.16}$
	$E_{\rm peak}^{\rm obs}$	< 46.4
	A	$2.62^{+149.88}_{-0.95} \times 10^{-2}$
	χ^2_ν/ν	0.942/72
Cutoff Power Law	α	$-1.54^{+0.44}_{-0.40}$
	$E_{\rm peak}^{\rm obs}$	> 50.5
	A	$4.8^{+3.0}_{-1.7} \times 10^{-3}$
	χ^2_ν/ν	0.932/72
Power Law	α	-1.89 ± 0.1
	A	$3.20^{+0.19}_{-0.18} \times 10^{-3}$
	χ^2_ν/ν	0.951/73
	flux	2.94×10^{-8}
	exposure	70.32859 s

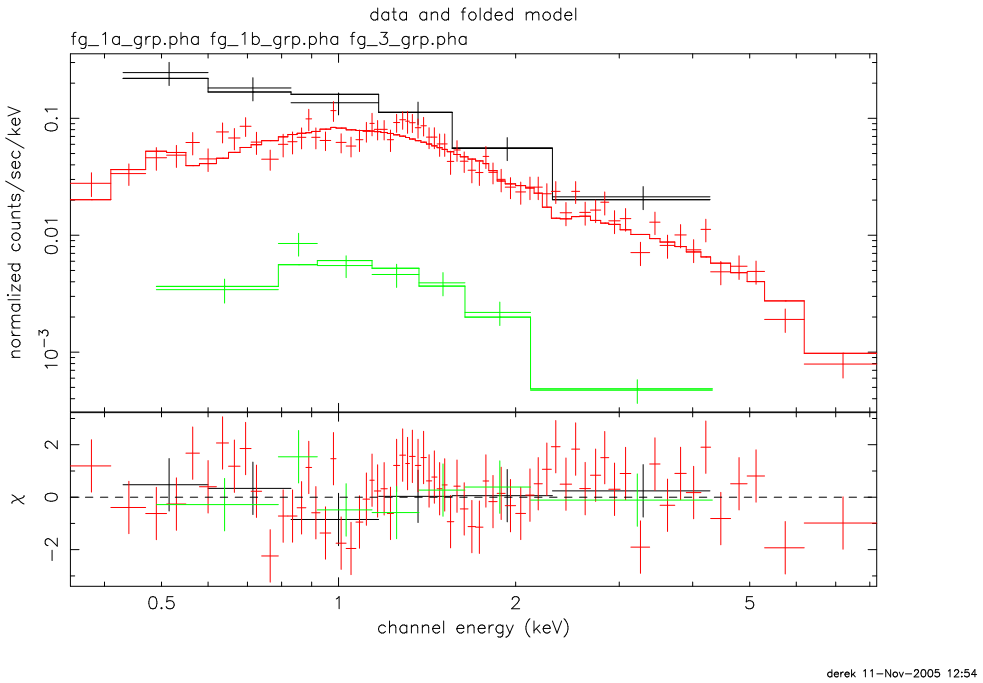

Figure 8.31: The count spectra of the XRR 050315 x-ray afterglow. The black line shows the spectrum and best fit during the early phase of the afterglow, the red line is the late phase before the break in the light curve, and the green line represents the late phase after the break in the light curve. Count bins corresponding to photon energies of 0.3 – 10 keV were included. See Table 8.13 for the spectral parameters.

before and after the break in the light curve are shown in Figure 8.31. The best fit hydrogen column density from the spectrum with the highest statistics (the portion of the late phase of the afterglow before the break in the light curve) was $2.0^{+0.4}_{-0.3} \times 10^{21}$ atoms/cm^2. This is a bit higher than the hydrogen column density due to our galaxy alone in the direction of the burst (which is 4.34×10^{20} atoms/cm^2). The spectral index after the break is a bit higher than the index before the break, indicating some spectral softening.

8.2.2 XRR 050318

This burst triggered BAT at 15:44:37 UT (MET=132853476.608) (GCN 3111). Swift did not slew immediately due to an observing constraint. The XRT began accumulating data at 16:39:14.5 UT, about 55 minutes after the trigger (GCN 3113). The position determined by BAT was RA=3h 18m 45.4s, Dec=-46d 23' 14.8", with an estimated uncertainty radius of about 3 arcmin

Table 8.13: The best fit spectral parameters for the XRR 050315 x-ray afterglow during the early phase and before and after the break in the light curve during the late phase. n_H is measured in 10^{21} atoms/cm^2, A in units of 10^{-3} ergs/cm^2/s/keV, and 0.6 – 10 keV flux in units of 10^{-12} ergs/cm^2/s. Start and stop times are in seconds since the BAT trigger.

Parameter	Early Phase	Late Phase Before Break	Late Phase After Break
n_H	< 0.88	$2.0^{+0.4}_{-0.3}$	$3.2^{+1.9}_{-1.6}$
I	$1.75^{+0.46}_{-0.27}$	$2.12^{+0.12}_{-0.11}$	$2.89^{+0.78}_{0.65}$
A	$3.33^{+0.87}_{-0.36}$	$1.87^{+0.23}_{-0.20}$	$0.21^{+0.15}_{-0.09}$
flux	$13.4^{+2.1}_{-3.6}$	$7.59^{+0.45}_{-0.43}$	$0.55^{+0.27}_{-0.13}$
start time	300 s	5057.663403 s	271409.262923 s
stop time	778.062 s	57387.17494 s	528072.4431 s
exposure	476.3 s	11587.1 s	18724.7 s
χ^2_ν/ν	0.374/3	1.253/65	0.818/4

(90% confidence). The XRT-determined position was found to be RA=3h 18m 51.1s, Dec=-46d 23' 44.7", with a 6 arcsec uncertainty (90% confidence) (GCN 3133). Optical afterglow emission was also detected (GCN 3114), and a redshift of 1.44 was measured (GCN 3122).

Prompt Emission

The T90 duration of XRR 050318 was 31.260 ± 0.004 seconds. There were two distinct episodes of emission: one lasting from about the time of the trigger until about 3 seconds later, and the second lasting from about 23 seconds after the trigger until about 35 seconds after the trigger. The first episode has a single discernible peak centered at about 1 second. The second episode has three distinct peaks: one at about 26 s, a larger peak at about 29 s, and a smaller peak at about 32 s. Most of the counts are detected in the band corresponding to photon energies of 25 - 50 keV, with significant counts also appearing in the 15 - 25 and 50 - 100 keV band. No discernible counts above background are present in the 100 - 350 keV band (see Figure 8.32).

For this burst, the Band model provided a good fit to the spectrum, and it was able to con-

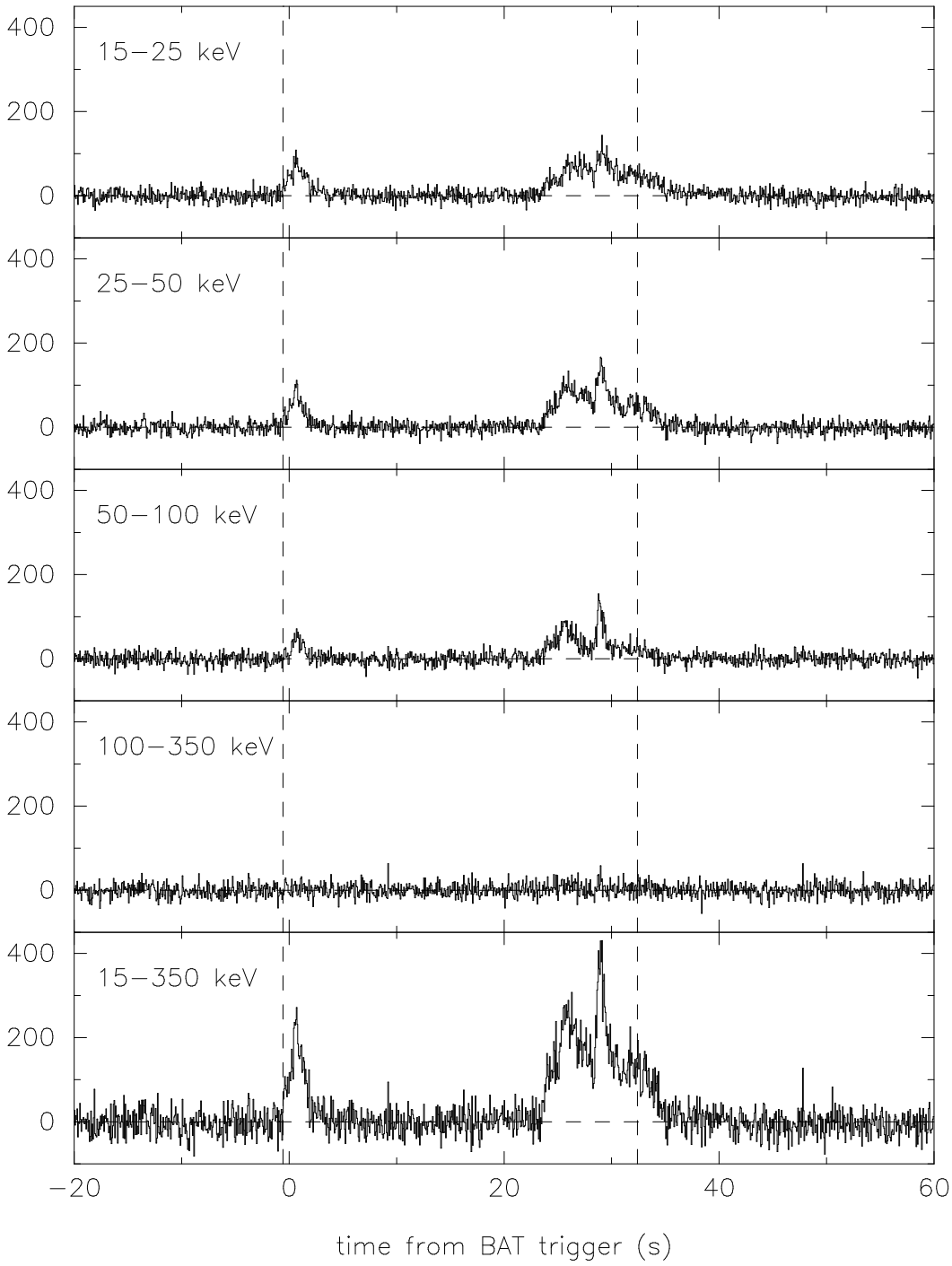

Figure 8.32: The light curve of the XRR 050318 prompt gamma-ray emission. The dashed vertical line indicates the beginning of the time interval used to measure the spectrum. Individual detector count rates were not available for this burst after 32.4 s, so the light curve shown here is the total number of counts above background in each 64 ms time interval. Also for this reason, the interval used to measure the spectrum extends only to 32.4 s. The spacecraft slewed at a time later than the time interval shown here.

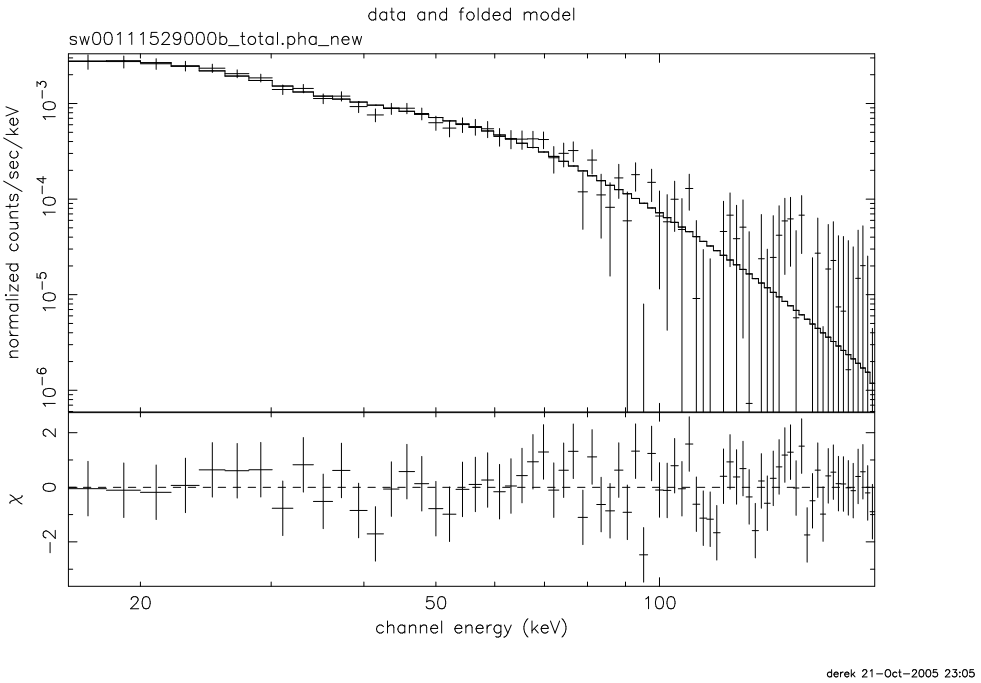

Figure 8.33: The count spectrum of the XRR 050318 prompt gamma-ray emission, along with the best fit power law model. See Table 8.14 for the spectral parameters.

strain $E_{\rm peak}^{\rm obs}$ quite well to $44.8^{+7.0}_{-10.6}$ keV. The time interval from which the spectrum was extracted spans from 0.576 s before the trigger to 32.404 s after it. Figure 8.33 shows the count spectra and the best-fit model.

X-ray Afterglow

The x-ray afterglow, as measured by the XRT, is shown in Figure 8.34. As we mentioned before, Swift was unable to slew immediately due to an observing constraint, so XRT data is not available earlier than about 3 ks after the initial trigger. The light curve is well fit by a broken power law with an early decay index of -1.17 ± 0.05, a late decay index of -2.08 ± 0.15, and a break time of 17700 ± 2200 s.

The 0.6 – 10 keV flux of the prompt emission is also shown, as extrapolated from the BAT data. The value is consistent with the decay of the x-ray afterglow emission.

The XRT count spectrum before and after the break in the light curve is shown in Figure 8.35. The hydrogen column density was constrained to $5.9^{+2.9}_{-2.5} \times 10^{20}$ atoms/cm^2. This is a

Table 8.14: The best fit spectral parameters for the XRR 050318 prompt emission, using a power law model, a cutoff power law model, and the Band model. $E_{\rm peak}^{\rm obs}$ is measured in keV, A in ergs/cm^2/s/keV, and average flux in 10^{-8} ergs/cm^2/s for 15 – 150 keV photons. The exposure was 32.980 s.

power law		cutoff power law		Band	
Parameter	Value	Parameter	Value	Parameter	Value
α	-2.03 ± 0.09	α	$-1.23^{+0.44}_{-0.40}$	α	$-1.08^{+1.65}_{0.58}$
A	$4.79^{+0.23}_{-0.24} \times 10^{-3}$	$E_{\rm peak}^{\rm obs}$	$44.8^{+6.9}_{-6.3}$	β	< 2.19
		A	$1.24^{+0.87}_{-0.47} \times 10^{-2}$	$E_{\rm peak}^{\rm obs}$	$26.7^{+10.7}_{-12.5}$
				A	$1.44^{+19.94}_{-0.67} \times 10^{-2}$
				flux	2.04 ± 0.30
χ^2_ν/ν	0.909/73	χ^2_ν/ν	0.748/72	χ^2_ν/ν	0.762/71

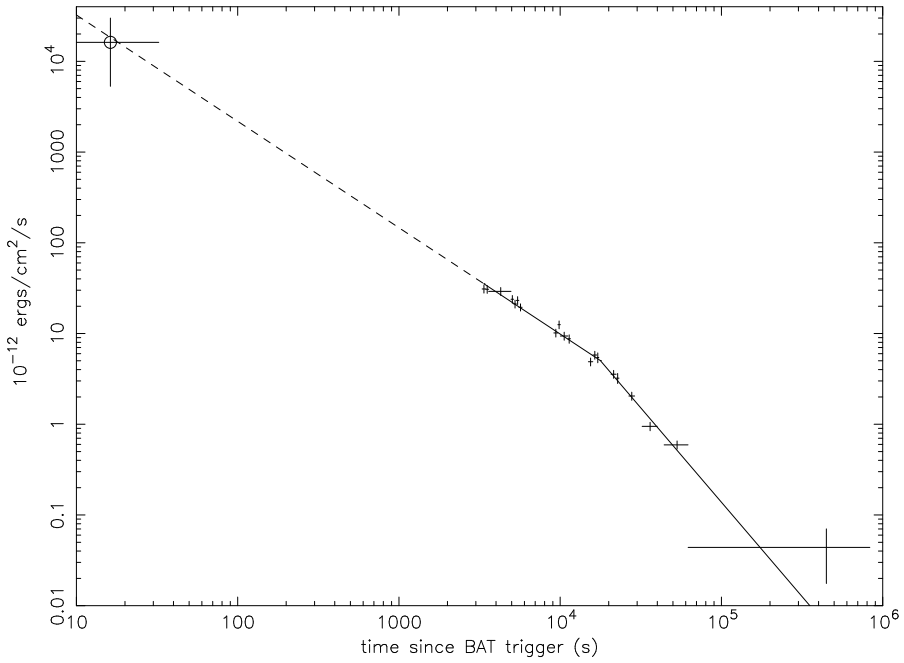

Figure 8.34: The light curve of the XRR 050318 x-ray afterglow, along with the best-fit power law model. The circled data point is the average flux of the prompt emission, extrapolated into the 0.6 – 10 keV energy range. The data is well fit by a broken power law. When extrapolated backward, the early power law is consistent with the 0.6 – 10 keV flux of the prompt emission.

Table 8.15: The best fit spectral parameters for the XRF 050318 x-ray afterglow. n_H is measured in 10^{20} atoms/cm^2, A in units of 10^{-3} ergs/cm^2/s/keV, and 0.6 – 10 keV flux in units of 10^{-12} ergs/cm^2/s. Start and stop times are in seconds since the BAT trigger.

Parameter	Interval 1	Interval 2
n_H	$5.9^{+2.9}_{-2.5}$	< 10.5
I	$1.98^{+0.14}_{-0.13}$	$1.97^{+0.29}_{-0.25}$
A	$2.27^{+0.30}_{-0.25}$	$0.226^{+0.058}_{-0.045}$
flux	$10.4^{+0.8}_{-0.7}$	$1.05^{+0.14}_{-0.13}$
start time	3284.760163 s	20654.933463 s
stop time	17387.4133 s	63671.4133 s
exposure	5225.0 s	18206.5 s
χ^2_ν/ν	0.980/48	0.800/16

little higher than the hydrogen column density due to our galaxy alone in the direction of the burst (which is 2.77×10^{20} atoms/cm^2). The spectral indices in both spectra are consistent with each other, indicating little spectral evolution.

8.2.3 XRR 050525A

On 25 May 2005, a fairly bright burst triggered BAT at 00:02:53 UT (MET=138672172.8) (GCN 3466). Swift immediately slewed, and the XRT began accumulating data at 00:04:58 UT, 125 s after the trigger. The position determined by BAT was RA=18h 32m 34s, Dec=+26d 20' 38", with an estimated uncertainty radius of about 5 arcmin (90% confidence). The XRT-determined position was found to be RA=18h 32m 32.3s, Dec=+26d 20' 17.5", with a 6 arcsec uncertainty (90% confidence) (GCN 3466). Afterglow emission in the optical, infrared, and radio bands was also detected (GCN 3465, 3471, 3495), and a redshift of 0.606 was measured (GCN 3483).

Prompt Emission

This burst has a T90 duration of 8.848 ± 0.004 seconds, but emission is detected out to about 12 seconds following the trigger. It consists of several peaks, with the highest centered at

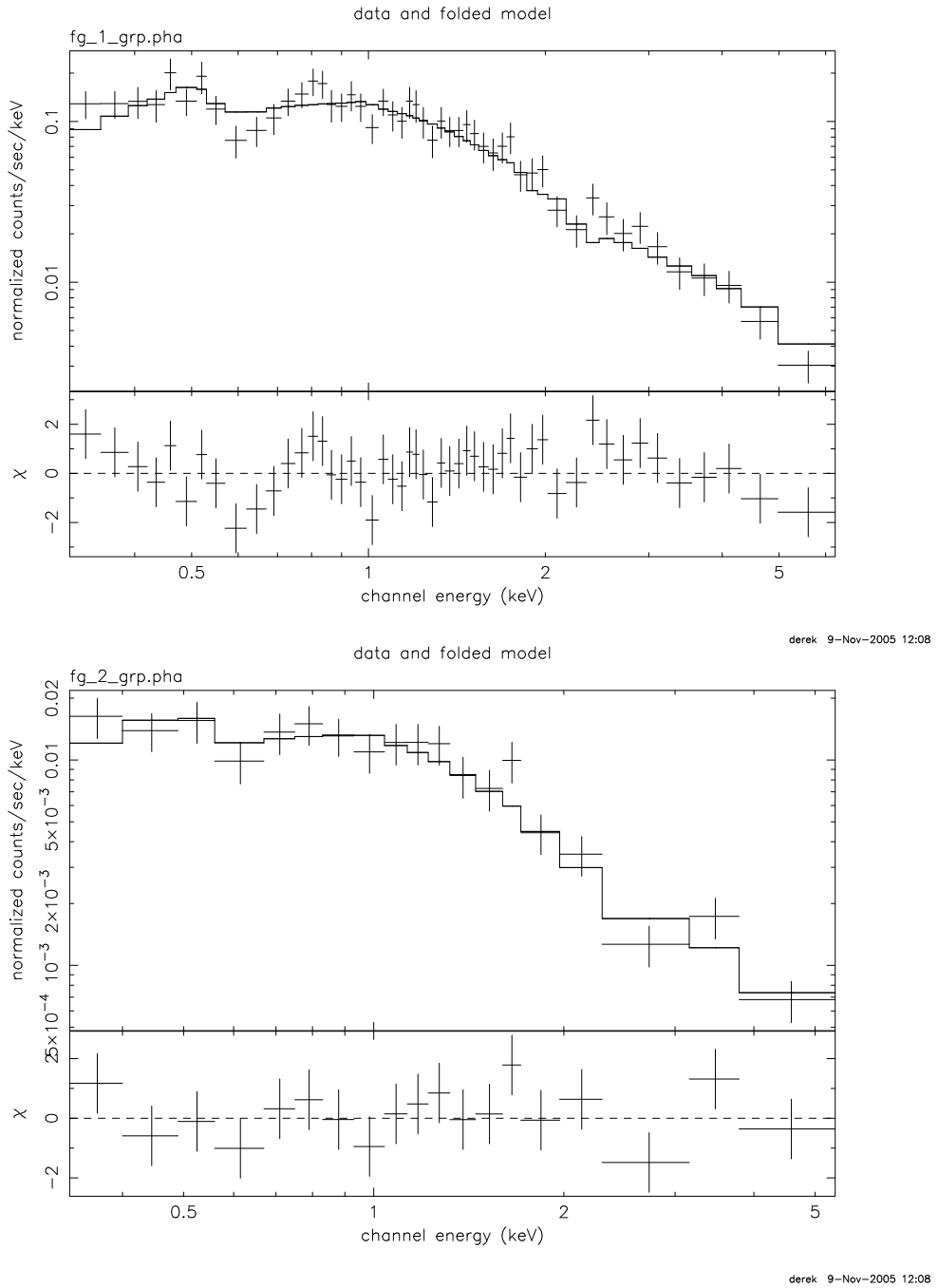

Figure 8.35: The count spectrum of the XRF 050318 x-ray afterglow before (top) and after (bottom) the break in the light curve. Both count spectra are fit with a power law model, with intervening absorption. Count bins corresponding to photon energies of 0.3 – 10 keV were included. See Table 8.15 for the spectral parameters.

Table 8.16: The best fit spectral parameters for the XRR 050525A prompt emission, using a power law model, a cutoff power law model, and the Band model. $E_{\rm peak}^{\rm obs}$ is measured in keV, A in ergs/cm^2/s/keV, and average flux in 10^{-8} ergs/cm^2/s for 15 – 150 keV photons. The exposure was 12.8463 s.

power law		cutoff power law		Band	
Parameter	Value	Parameter	Value	Parameter	Value
α	-2.06 ± 0.02	α	-1.14 ± 0.07	α	$-1.057^{+0.099}_{-0.092}$
A	0.112 ± 0.002	$E_{\rm peak}^{\rm obs}$	$84.0^{+2.7}_{-2.6}$	$-3.29^{+0.26}_{-0.50}$	
		A	$0.233^{+0.015}_{-0.013}$	$E_{\rm peak}^{\rm obs}$	$81.00^{+3.32}_{-3.26}$
				A	$0.253^{+0.026}_{-0.021}$
				flux	115.4 ± 1.8
χ^2_ν/ν	10.036/99	χ^2_ν/ν	1.399/98	χ^2_ν/ν	1.325/97

about 1.5 s after the trigger, preceded by a slightly lower peak at about 0.3 s after the trigger. Two more peaks follow at about 5.5 s and about 7 s. The largest count rates appear in channels corresponding to photon energies of 25 - 50 keV, with slightly smaller rates appearing in the 15 - 25 and 50 - 100 keV bands. Some emission is also evident in the 100 - 350 keV band (see Figure 8.36).

As with most of the other XRRs we selected for study, this burst was also observed by Konus. Since Swift began to slew during the burst, and due to the difficulty in fitting data taken during a slew, it was only practical to use BAT data from before the slew. Because of the time intervals into which the Konus data was divided, doing a joint fit with BAT and Konus data would have eliminated a large portion of the burst, so instead Konus data alone was used for the spectral analysis. We were able to constrain $E_{\rm peak}^{\rm obs}$ to $81.00^{+3.32}_{-3.26}$ keV, using the Band model. The time interval from which the spectrum was extracted spans from 0.26502 s after the BAT trigger to 14.85702 s after it. Figure 8.37 shows the count spectrum from Konus as well as the best-fit spectral model.

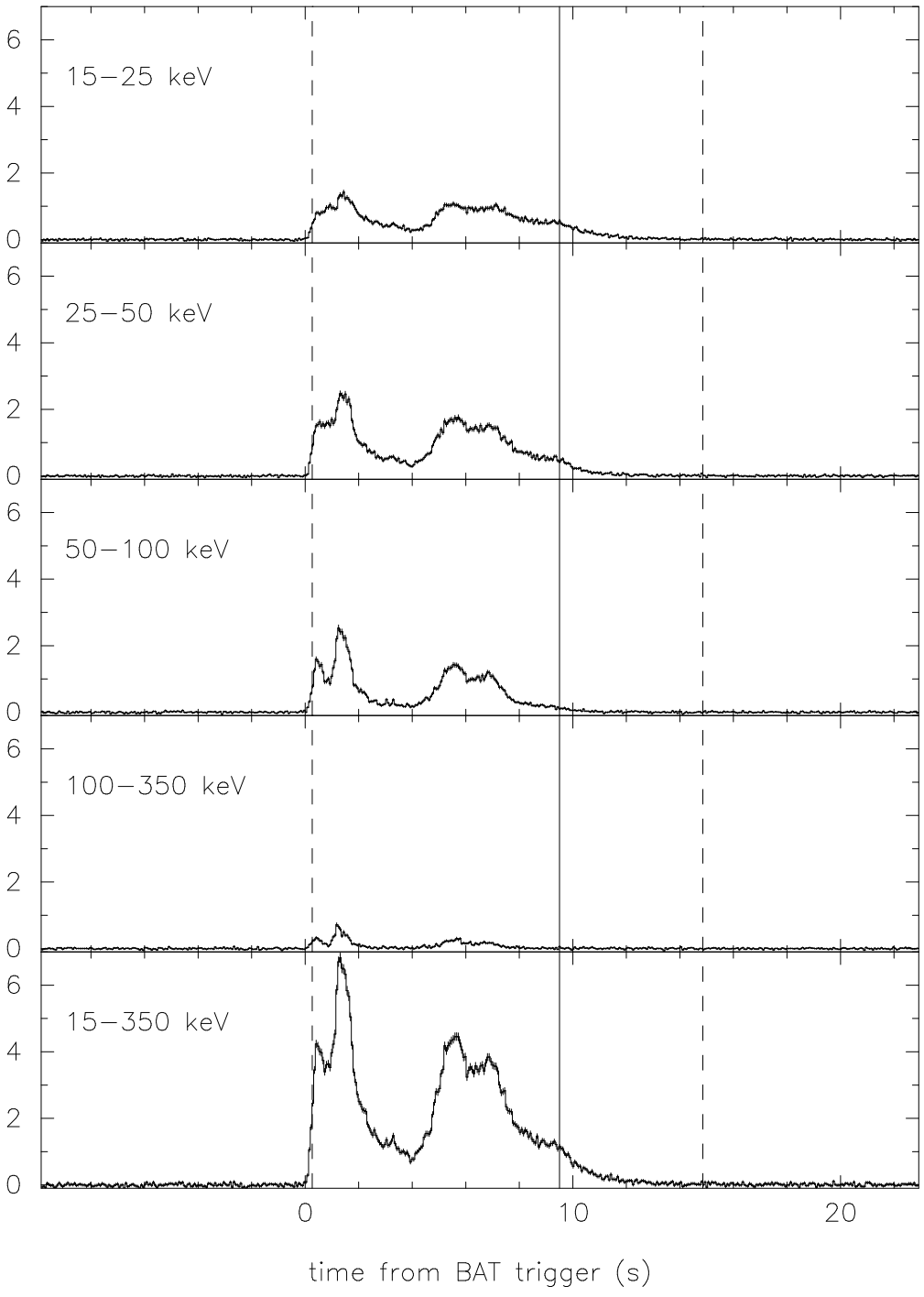

Figure 8.36: The light curve of the XRR 050525A prompt gamma-ray emission. The dashed vertical lines bound the time interval used to measure the spectrum. Swift began to slew at the time indicated by the solid vertical line. Since the slew began during the burst, only Konus data were used for the spectral fitting.

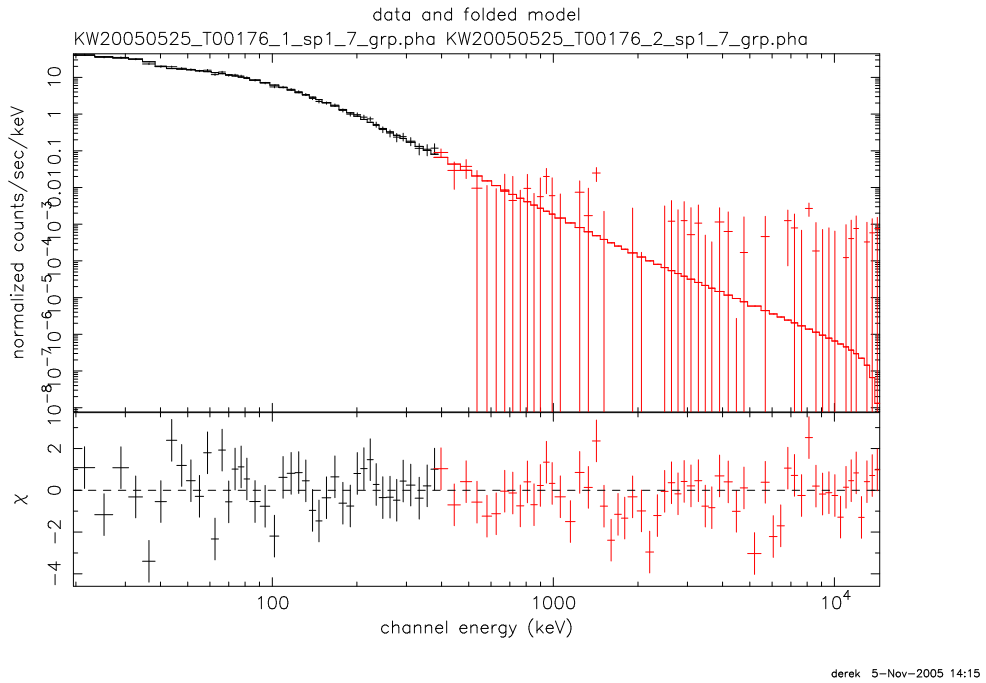

Figure 8.37: The count spectra recorded by Konus for the XRR 050525A prompt gamma-ray emission, along with the best fit Band model. See Table 8.16 for the spectral parameters.

X-ray Afterglow

The x-ray afterglow, as measured by the XRT, is shown in Figure 8.38. Although Swift slewed immediately, photon counting and window timing data were only available beginning about 6 ks after the burst. The light curve is best fit by a broken power law, with an early decay index of -1.21 ± 0.14, a late decay index of -1.68 ± 0.10, and a break time of 14700 ± 5000 s.

The 0.6 – 10 keV flux of the prompt emission is also shown, as extrapolated from the BAT data. The value is consistent with the decay of the x-ray afterglow emission.

The XRT count spectra before and after the break are shown in Figure 8.39. The hydrogen column density was constrained to $(2.2 \pm 0.8) \times 10^{21}$ atoms/cm^2. This is slightly higher than the hydrogen column density due to our galaxy alone in the direction of the burst (9.1×10^{20} atoms/cm^2). The spectral index in the second spectrum, though not well constrained, is consistent with that of the first spectrum.

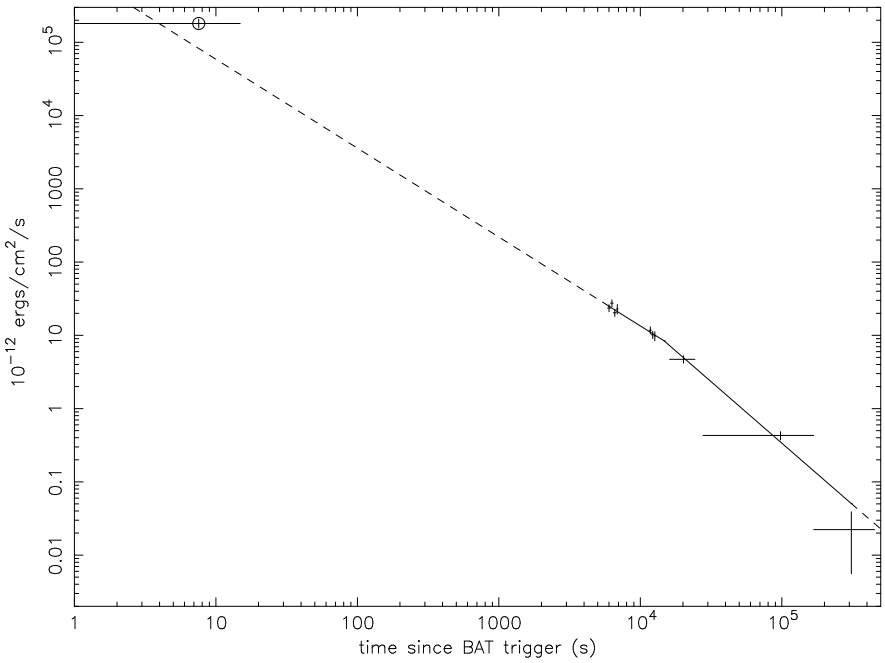

Figure 8.38: The light curve of the XRR 050525A x-ray afterglow, along with the best-fit broken power law model. The circled data point is the average flux of the prompt emission, extrapolated into the 0.6 – 10 keV energy range. When extrapolated backward, the early power law is consistent with the 0.6 – 10 keV flux of the prompt emission, as measured by BAT.

Table 8.17: The best fit spectral parameters for the XRR 050525a x-ray afterglow. n_H is measured in 10^{21} atoms/cm^2, A in units of 10^{-3} ergs/cm^2/s/keV, and 0.6 – 10 keV flux in units of 10^{-12} ergs/cm^2/s. Start and stop times are in seconds since the BAT trigger.

Parameter	Interval 1	Interval 2
n_H	$2.2^{+0.9}_{-0.8}$	< 6.7
I	$2.11^{+0.26}_{-0.23}$	$1.96^{+2.08}_{-0.80}$
A	$4.00^{+1.15}_{-0.89}$	$0.226^{+0.058}_{-0.045}$
flux	$16.3^{+1.9}_{-1.8}$	$1.82^{+0.59}_{-0.60}$
start time	5858.924463 s	16087.577083 s
stop time	12842.995612 s	87212.735492 s
exposure	1835.0 s	3915.3 s
χ^2_ν/ν	0.585/17	0.770/1

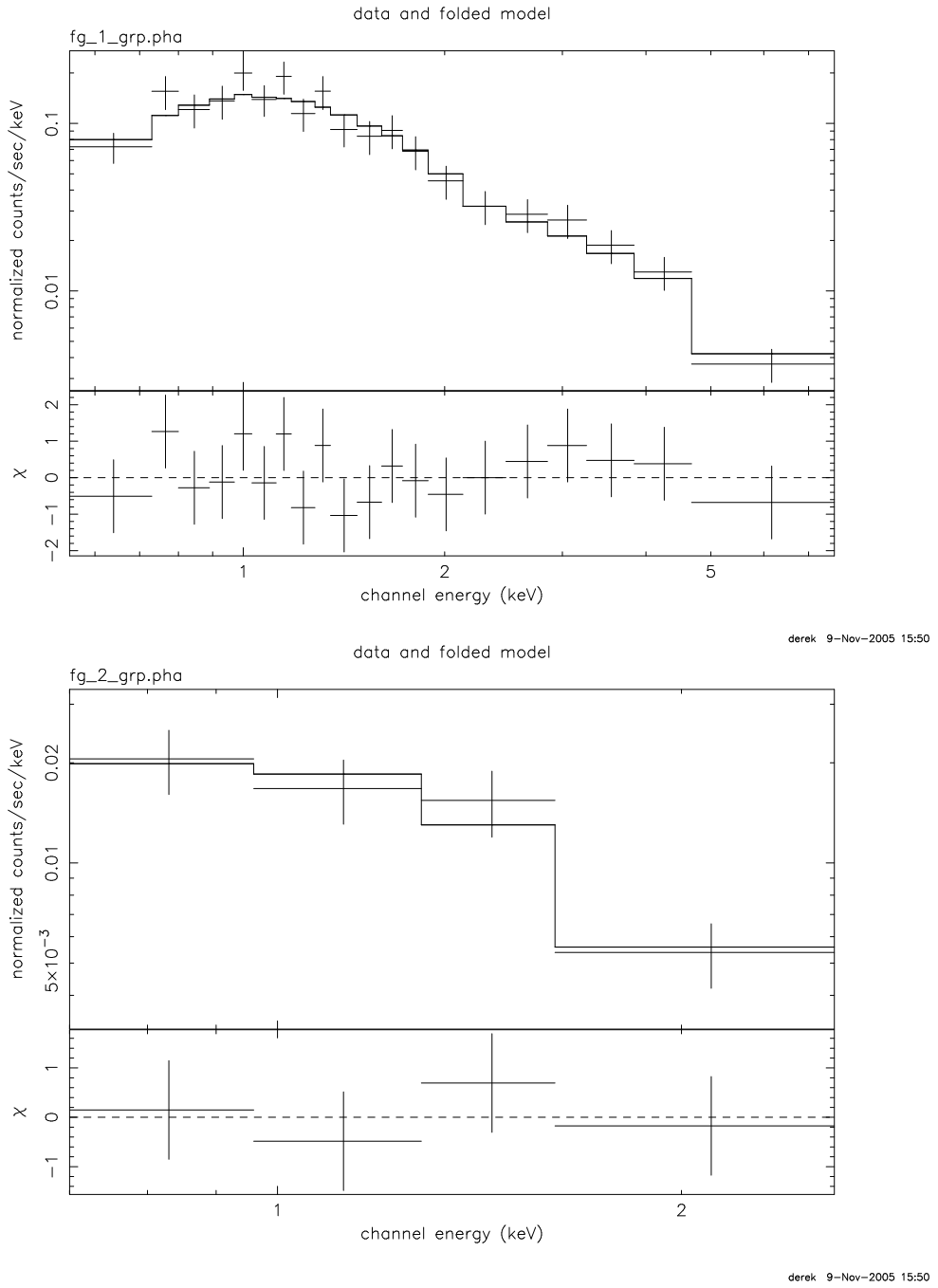

Figure 8.39: The count spectrum of the XRR 050525a x-ray afterglow before (top) and after (bottom) the break in the light curve. Both count spectra are fit with a power law model, with intervening absorption. Count bins corresponding to photon energies of 0.3 – 10 keV were included. See Table 8.17 for the spectral parameters.

8.2.4 XRR 050219B

On 19 Feb 2005, two bursts triggered BAT. The second of these (050219B) was detected at 21:05:51 UT (MET=130539950.656) (GCN 3043). Swift wasn't able to slew immediately due to an Earth limb observing constraint, but a slew took place about 50 minutes later, and 52 minutes later, the XRT began accumulating data. The position determined by BAT was RA=5h 25m 9.8s, Dec=-57d 45' 48.5", with an estimated uncertainty radius of about 3 arcmin (90% confidence). The XRT-determined position was found to be RA=5h 25m 16.31, Dec=-57d 45' 27.31", with a 6.3 arcsec uncertainty (90% confidence) (GCN 3049). In addition to the x ray, afterglow emission was detected in the infrared band, but not in any other bands (GCN 3064). A redshift was not directly measured, but the technique discussed in section 7.3 gives an inferred redshift of $1.0^{+0.5}_{-0.2}$.

Prompt Emission

This burst has a T90 duration of 30.592 ± 0.064 seconds. It consists of at least three discernible peaks, with the highest centered at about 3 s after the trigger, followed by a slightly lower peak at about 8 s after the trigger. Another much smaller peak is visible at about 38 s after the trigger. The largest count rates appear in channels corresponding to photon energies of 25 - 100 keV, with slightly smaller rates appearing in the 15 - 25 keV band. Some emission is also evident in the 100 - 350 keV band (see Figure 8.40).

This burst was also observed by Konus, and we were able to use both data sets together to find the best spectral model. We were able to constrain $E^{\rm obs}_{\rm peak}$ to $161.5^{+13.1}_{-11.1}$ keV, using the Band model. The time interval from which the spectrum was extracted spans from 1.4515 s before the trigger to 53.0765 s after the trigger. Figure 8.41 shows the count spectra from both BAT and Konus as well as the best-fit model for these spectra.

X-ray Afterglow

The x-ray afterglow, as measured by the XRT, is shown in Figure 8.42. The light curve is consistent with a power law with a decay index of -1.03 ± 0.09. The average 0.6 – 10 keV flux of

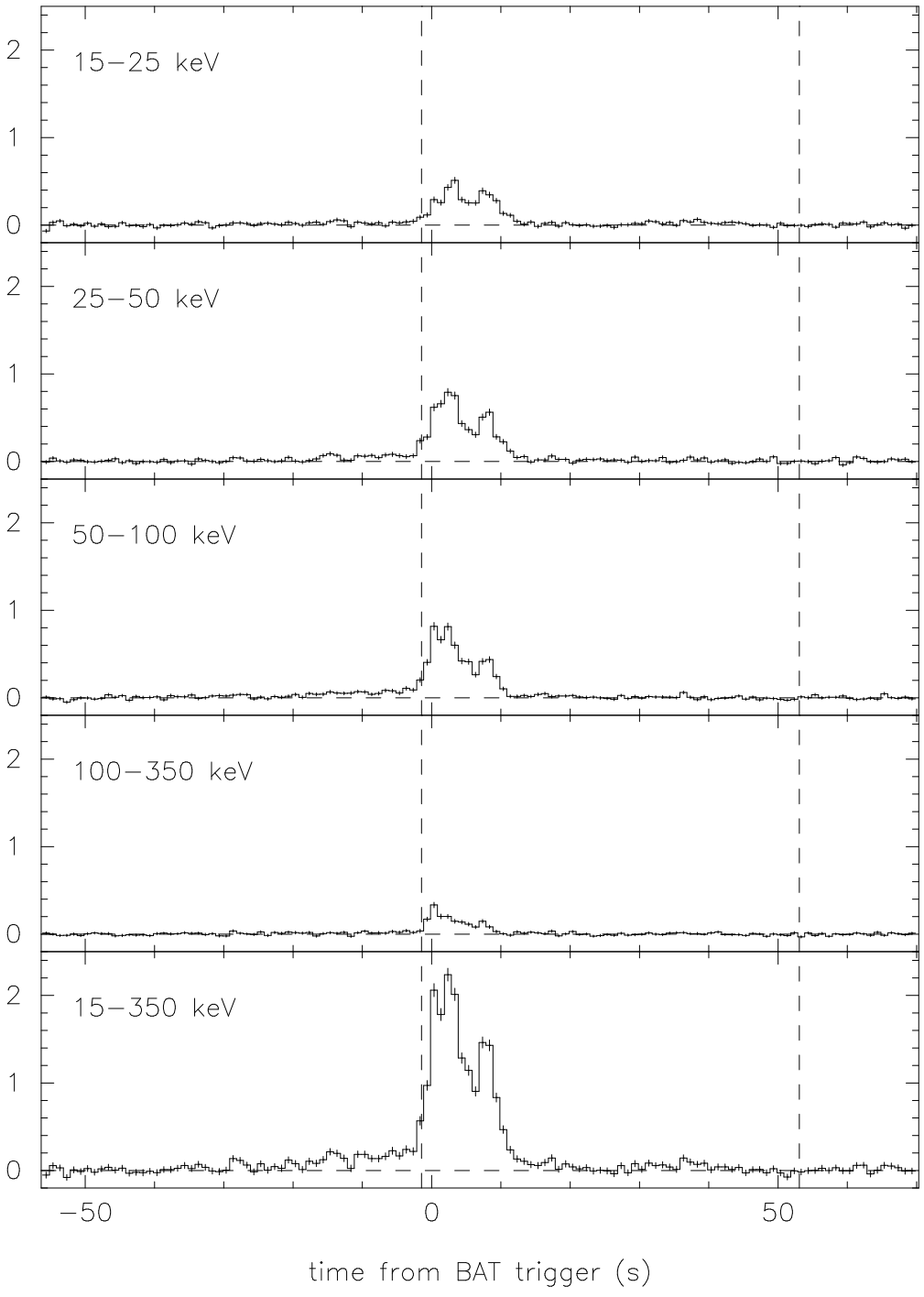

Figure 8.40: The light curve of the XRR 050219B prompt gamma-ray emission. The dashed vertical lines bound the time interval used to measure the count spectrum. Swift slewed long after the interval shown in this plot.

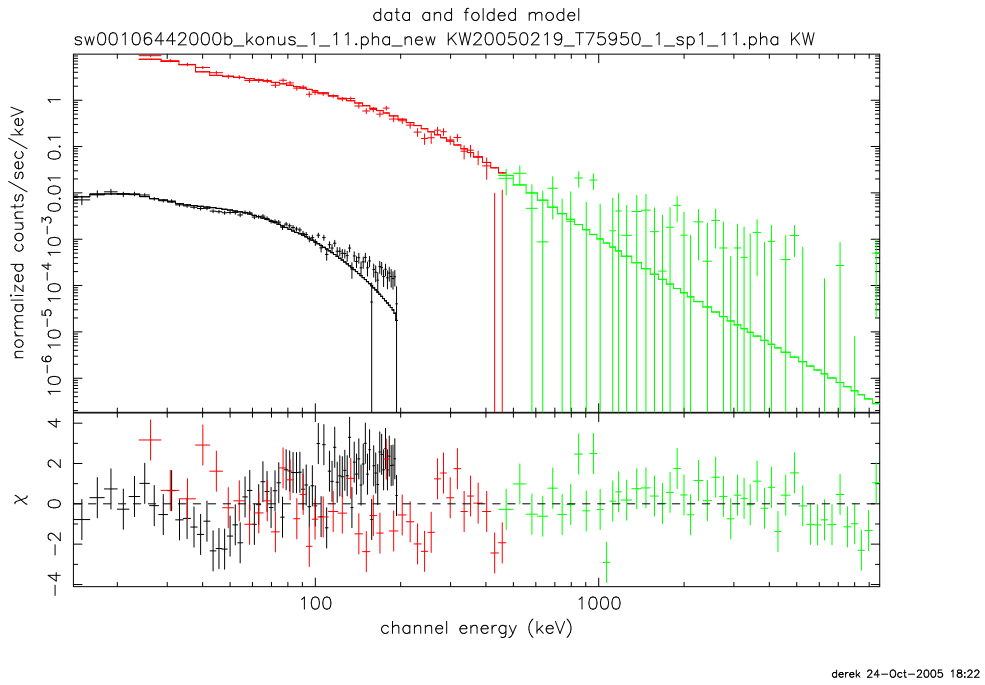

Figure 8.41: The count spectra recorded by BAT and Konus for the XRR 050219B prompt gamma-ray emission, along with the best fit power law model. Konus spectra are shown in red and green, and the BAT spectrum in black. See Table 8.18 for the spectral parameters.

Table 8.18: The best fit spectral parameters for the XRR 050219B prompt emission, using a power law model, a cutoff power law model, and the Band model. $E^{\rm obs}_{\rm peak}$ is measured in keV, A in ergs/cm^2/s/keV, and average flux in 10^{-8} ergs/cm^2/s for 15 – 150 keV photons. The exposure was 54.528 s.

power law		cutoff power law		Band	
Parameter	Value	Parameter	Value	Parameter	Value
α	-1.68 ± 0.02	α	-1.05 ± 0.07	α	-1.05 ± 0.07
A	$(2.41 \pm 0.06) \times 10^{-2}$	$E^{\rm obs}_{\rm peak}$	$162.8^{+13.1}_{-11.3}$	β	< -2.86
		A	$3.46^{+0.18}_{-0.16} \times 10^{-2}$	$E^{\rm obs}_{\rm peak}$	$161.5^{+13.1}_{-11.1}$
				A	$3.46^{+0.19}_{-0.16} \times 10^{-2}$
				flux	23.3 ± 0.6
χ^2_ν/ν	3.860/175	χ^2_ν/ν	1.633/174	χ^2_ν/ν	1.637/173

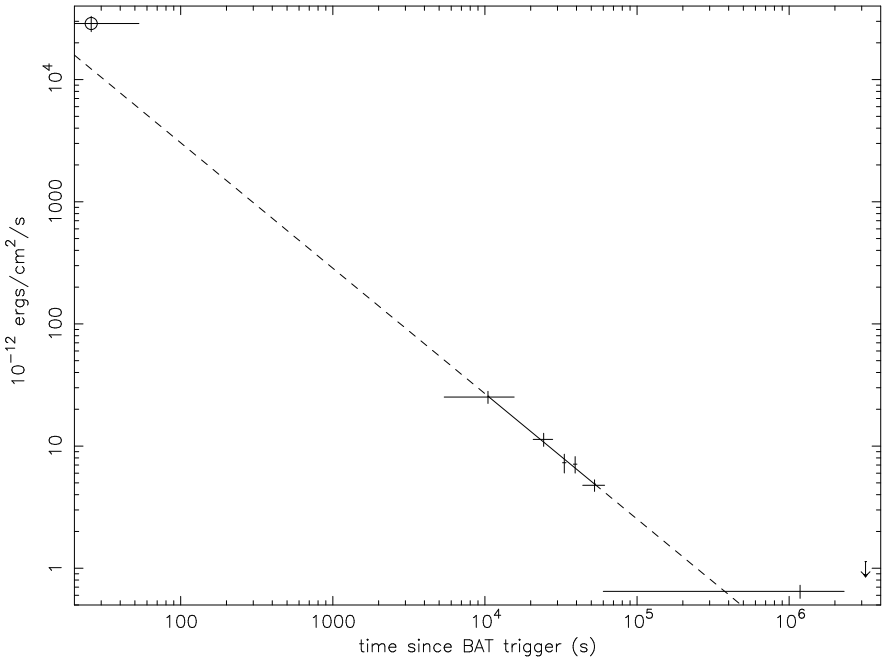

Figure 8.42: The light curve of the XRR 050219B x-ray afterglow, along with the best-fit power law model. The circled data point is the average flux of the prompt emission from BAT, extrapolated into the 0.6 – 10 keV energy range. When extrapolated backward, the power law is consistent with the average 0.6 – 10 keV flux of the prompt emission.

the prompt emission is also shown, as extrapolated from the BAT data. The trend in the afterglow is consistent with the prompt emission.

The count spectrum measured by the XRT is shown in Figure 8.43. The best fit hydrogen column density is $1.09^{+0.92}_{-0.80} \times 10^{21}$ atoms/cm^2. This value (with its rather large error bars) is consistent with the hydrogen column density due to our galaxy alone in the direction of the burst (3.83×10^{20} atoms/cm^2). The best fit spectral index is $1.80^{+0.27}_{-0.25}$. The spectrum used here consists of counts accumulated between 5394.5 s after the trigger and 120995.4 s after the trigger.

8.3 GRBs

We now move on to a collection of those bursts for which the fluence ratio $S(50-100 \text{ keV})/S(25-50 \text{ keV}) \geq 1.3855$. There are 5 bursts in our sample, selected because they were also observed by Konus.

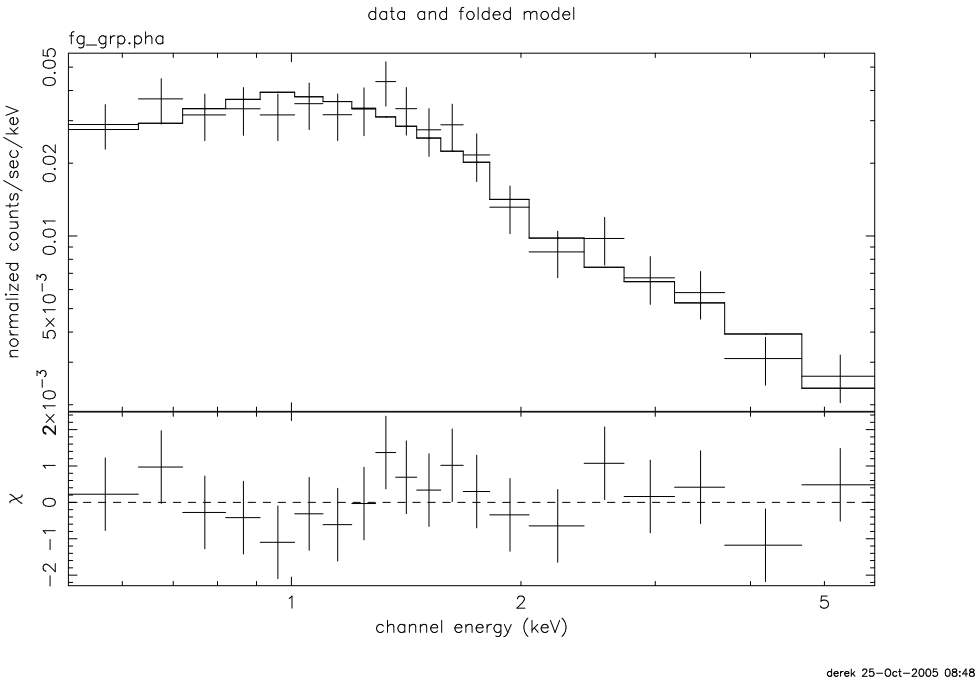

Figure 8.43: The count spectrum of the XRR 050219B x-ray afterglow. Count bins corresponding to photon energies of 0.3 – 10 keV were included. See Table 8.19 for the spectral parameters.

Table 8.19: The best fit spectral parameters for the XRR 050219B x-ray afterglow. n_H is measured in atoms/cm^2, A in units of photons/cm^2/s/keV, and flux in units of ergs/cm^2/s. Start and stop times are in seconds since the BAT trigger.

Parameter	Value
n_H	$1.09^{+0.92}_{-0.80} \times 10^{21}$
I	$1.80^{+0.27}_{-0.25}$
A	$8.14^{+2.52}_{-1.87} \times 10^{-4}$
0.6 – 10 keV flux	$5.52^{+0.71}_{-0.59} \times 10^{-12}$
start time	5395.353623 s
stop time	120995.399052 s
exposure	6603.8 s
χ^2_ν/ν	0.589/17

8.3.1 GRB 050401

With a fluence ratio of 1.4363, this is the softest in our sample of bursts with a fluence ratio large enough to be designated actual "gamma-ray bursts". This burst triggered BAT at 14:20:15 UT (MET=134058014.784) (GCN 3161). There was a 9 second delay in the slew due to an Earth observing constraint, after which the XRT began immediately to collect data. The position determined by BAT was RA=16h 31m 32.3s, Dec=2d 11' 42.5". The XRT-determined position was found to be RA=16h 31m 29s, Dec=2d 11' 14", with a 6 arcsec uncertainty (90% confidence) (GCN 3161). Afterglow emission was also detected in the optical and radio bands, and a redshift of 2.90 was measured (GCN 3163, 3187, 3176).

Prompt Emission

This burst has a T90 duration of 33.640 ± 0.004 seconds. There are two distinct episodes of emission—one beginning about 10 s before the trigger and ending about 10 s after the trigger, and the other beginning about 20 s after the trigger and ending about 30 s after the trigger. The first episode consists of at least three distinct peaks: once centered at -6 s, one at 0 s, and one at 3 s. The second episode consists of a single peak centered at 24 s. The largest count rates appear in channels corresponding to photon energies of 50 - 100 keV, with slightly smaller rates appearing in the 25 - 50 keV band. Prominent emission is also evident in the other two bands (see Figure 8.44).

As with all of the bursts selected for this sample, this burst was also observed by Konus. Swift began to slew during the burst, and due to the difficulty in fitting data taken during a slew, it is not practical to use BAT data taken during the slew. So that emission from the full interval of the burst could be analyzed, Konus data alone was used for the spectral analysis. We were able to constrain $E_{\rm peak}^{\rm obs}$ to $117.5^{+20.1}_{-16.4}$ keV, using the Band model.

The time interval from which the spectrum was extracted spans from 5.24101 s before the BAT trigger to 35.97499 s after the trigger. Figure 8.45 shows the count spectrum from Konus as well as the best-fit model for the spectrum.

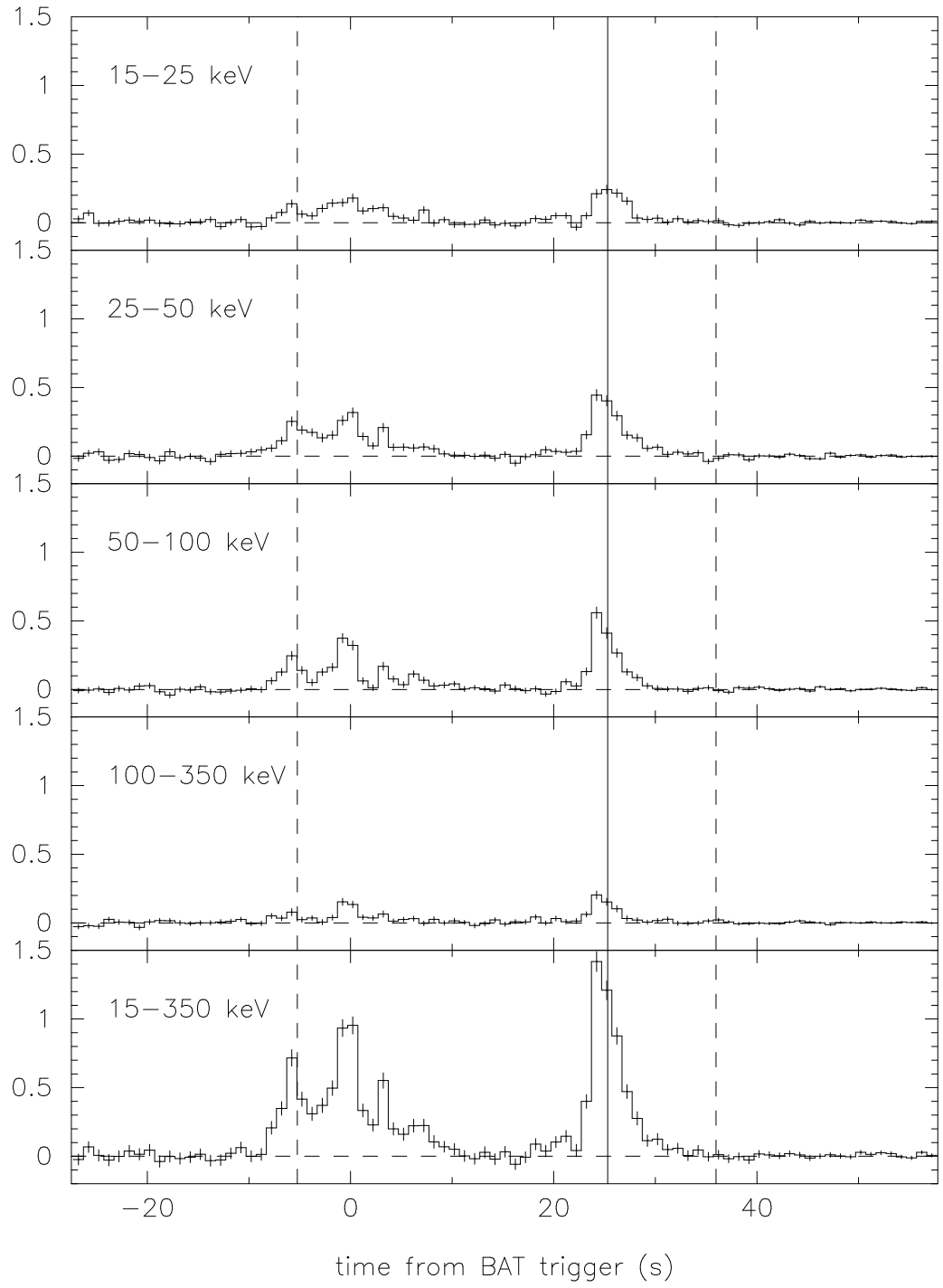

Figure 8.44: The light curve of the GRB 050401 prompt gamma-ray emission. The dashed vertical lines bound the time interval used to measure the spectrum. Swift began to slew at the time indicated by the solid vertical line. Since the slew began during the burst, only Konus data was used for the spectral fitting.

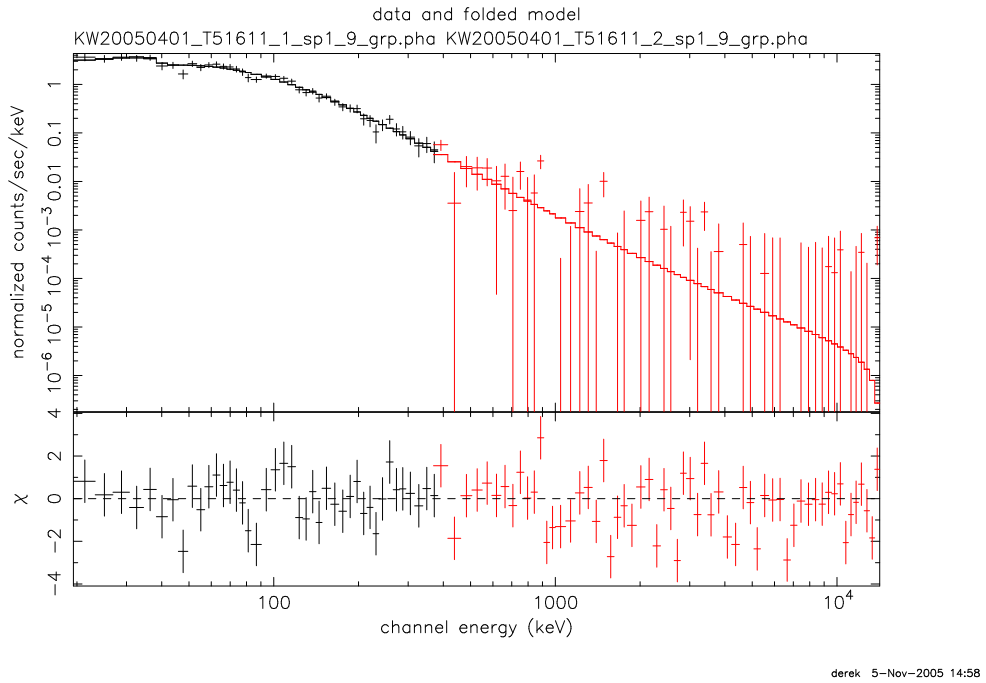

Figure 8.45: The count spectra recorded by Konus for the GRB 050401 prompt gamma-ray emission, along with the best fit Band model. See Table 8.20 for the spectral parameters.

Table 8.20: The best fit spectral parameters for the GRB 050401 prompt emission, using a power law model, a cutoff power law model, and the Band model. $E_{\rm peak}^{\rm obs}$ is measured in keV, A in ergs/cm^2/s/keV, and average flux in 10^{-8} ergs/cm^2/s for 15 – 150 keV photons. The exposure was 38.3517 s.

power law		cutoff power law		Band	
Parameter	Value	Parameter	Value	Parameter	Value
α	-1.89 ± 0.04	α	$-1.18^{+0.18}_{-0.17}$	α	$-0.90^{+0.34}_{-0.26}$
A	$(2.53 \pm 0.12) \times 10^{-2}$	$E_{\rm peak}^{\rm obs}$	$142.5^{+19.3}_{-14.6}$	β	$-2.55^{+0.22}_{-0.44}$
		A	$3.50^{+0.41}_{-0.33} \times 10^{-2}$	$E_{\rm peak}^{\rm obs}$	$117.5^{+20.1}_{-16.4}$
				A	$4.30^{+1.25}_{-0.71} \times 10^{-2}$
				flux	23.3 ± 1.1
χ^2_ν/ν	2.360/100	χ^2_ν/ν	1.402/99	χ^2_ν/ν	1.358/98

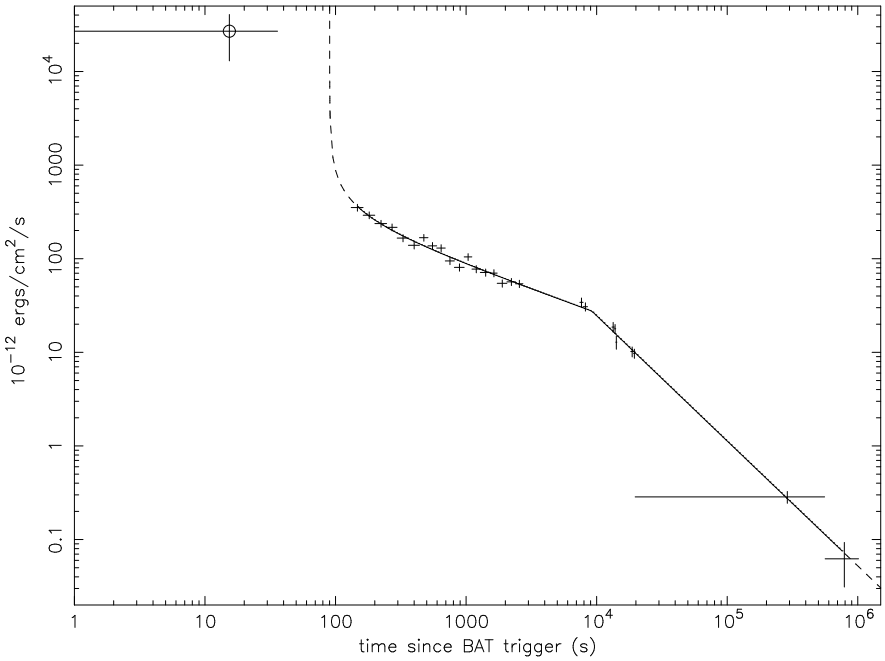

Figure 8.46: The light curve of the GRB 050401 x-ray afterglow, along with the best-fit broken power law model. The offset of the early power law has a best fit value of 90 ± 16 s. The existence of this offset causes the early power law to be plotted as a curved line with an asymptote at 90 s. The circled data point is the average flux of the prompt emission, extrapolated into the 0.6 – 10 keV energy range.

X-ray Afterglow

The x-ray afterglow, as measured by the XRT, is shown in Figure 8.46. The light curve can be fit with a broken power law, with a χ^2_ν of 1.689 (23 degrees of freedom). However, a better fit is obtained if we allow the offset of the early power law to be different from the trigger time, in which case we obtain a χ^2_ν of 1.226 (with 22 degrees of freedom). An F-test reveals that the latter model fits the data better to a confidence of 99.5%. Allowing the late power law offset to be different from the trigger time doesn't improve the fit, and requiring the two offsets vary together results in the same χ^2_ν as allowing only the early power law offset to vary. The best fit early power law index is -0.51 ± 0.30 with a best fit offset of 90 ± 16 s after the trigger. The best fit late power law index is -1.33 ± 0.05. The break time is 9200 ± 1000 s.

The XRT count rate before and after the break in the light curve is shown in Figure 8.47. The best fit hydrogen column density is $2.17^{+0.98}_{-0.83} \times 10^{21}$ atoms/cm^2. This is higher than the hydrogen

Table 8.21: The best fit spectral parameters for the GRB 050401 x-ray afterglow. n_H is measured in 10^{21} atoms/cm^2, A in units of 10^{-3} ergs/cm^2/s/keV, and 0.6 – 10 keV flux in units of 10^{-12} ergs/cm^2/s. Start and stop times are in seconds since the BAT trigger.

Parameter	Interval 1	Interval 2
n_H	$2.17^{+0.98}_{-0.83}$	$2.6^{+1.2}_{-0.9}$
I	$1.96^{+0.25}_{-0.23}$	$2.15^{+0.30}_{-0.27}$
A	$13.3^{+4.0}_{-3.0}$	$3.66^{+1.31}_{-0.90}$
flux	$62.3^{+7.2}_{-6.8}$	$14.5^{+2.1}_{-1.7}$
start time	1735.207623 s	13089.957232 s
stop time	8526.682692 s	20104.5328 s
exposure	458.3 s	1786.9 s
χ^2_ν/ν	0.902/18	1.144/18

column density due to our galaxy alone in the direction of the burst (4.84×10^{20} atoms/cm^2). The spectral indices are consistent with each other.

8.3.2 GRB 050326

This burst triggered BAT at 09:53:55 UT (MET=133523635.584) (GCN 3143). The spacecraft did not slew immediately due to an Earth observing constraint. After the slew, the XRT began to collect data, beginning at about 10:48:13 UT, about 55 minutes after the burst (GCN 3143). The position determined by BAT was RA=0h 27m 30.2s, Dec=-71d 22' 40.0". The XRT-determined position was found to be RA=0h 27m 48.7s, Dec=-71d 22' 17.2", with a 6 arcsec uncertainty (90% confidence) (GCN 3147). No afterglow emission in any other wave band was detected, and no redshift was measured. In this case, the Yonetoku relation doesn't provide an extremely good constraint on z. It predicts a redshift of $2.4^{+3.4}_{-0.9}$.

Prompt Emission

This is a very complex burst with many peaks. There are two distinct episodes of emission: one extending from 5 seconds before the trigger until 12 seconds after the trigger, and the other

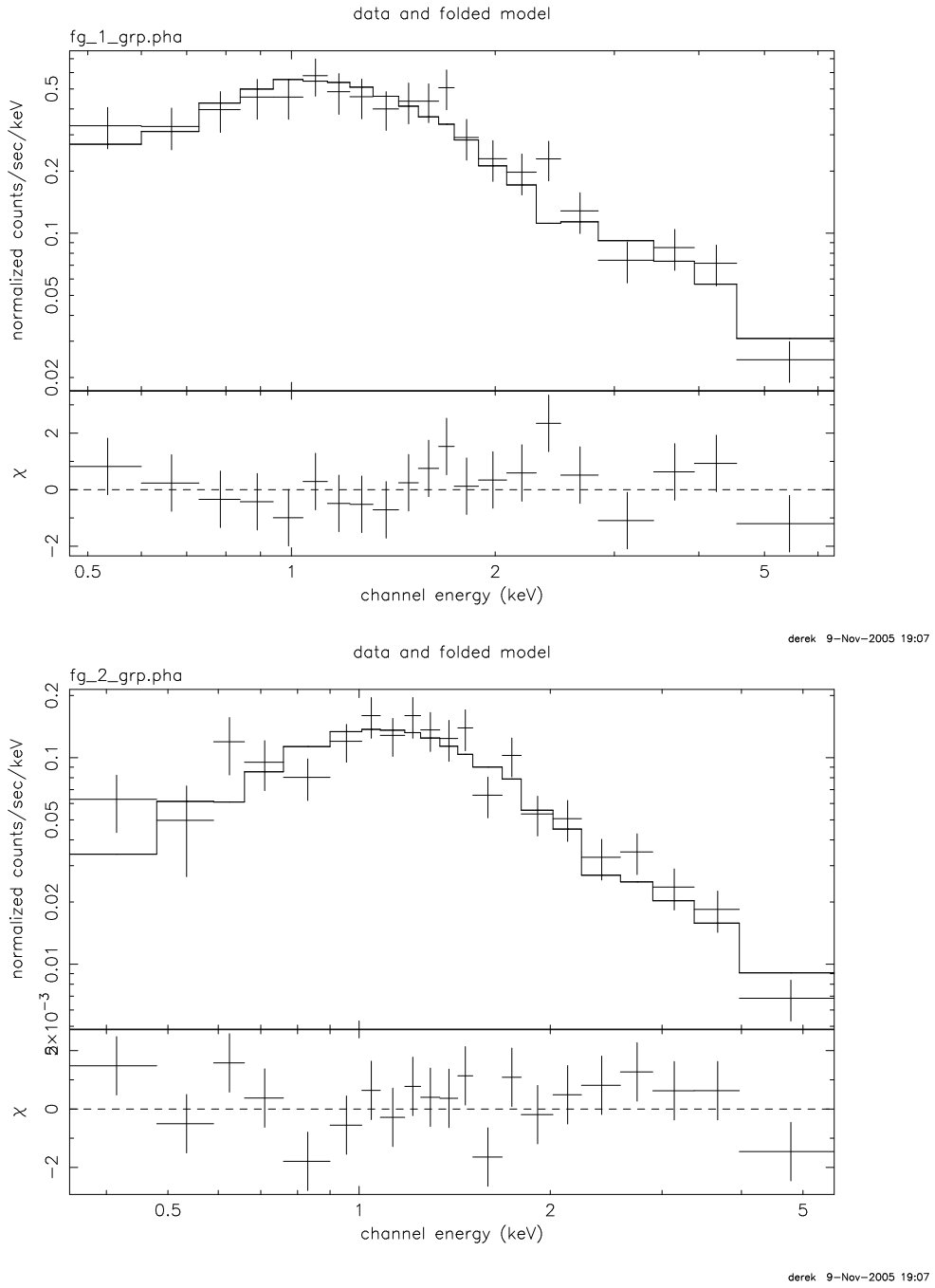

Figure 8.47: The count spectrum of the GRB 050401 x-ray afterglow before (top) and after (bottom) the break in the light curve. Both count spectra are fit with a power law model, with intervening absorption. Count bins corresponding to photon energies of 0.3 – 10 keV were included. See Table 8.21 for the spectral parameters.

Table 8.22: The best fit spectral parameters for the GRB 050326 prompt emission, using a power law model, a cutoff power law model, and the Band model. $E_{\rm peak}^{\rm obs}$ is measured in keV, A in ergs/cm^2/s/keV, and average flux in 10^{-8} ergs/cm^2/s for 15 – 150 keV photons. The exposure was 30.6496 s.

power law		cutoff power law		Band	
Parameter	Value	Parameter	Value	Parameter	Value
α	-1.63 ± 0.02	α	-0.910 ± 0.11	α	$-0.78^{+0.17}_{-0.15}$
A	$(2.99 \pm 0.09) \times 10^{-2}$	$E_{\rm peak}^{\rm obs}$	$240.8^{+2.4}_{-2.3}$	β	$-2.48^{+0.24}_{-0.63}$
		A	$3.71^{+0.22}_{-0.21} \times 10^{-2}$	$E_{\rm peak}^{\rm obs}$	$206.4^{+32.8}_{-27.1}$
				A	$4.44^{+0.42}_{-0.32} \times 10^{-2}$
				flux	$28.9^{+1.0}_{-0.8}$
χ^2_ν/ν	4.052/100	χ^2_ν/ν	1.070/99	χ^2_ν/ν	1.028/98

extending from 16 to 26 seconds after the trigger. The first episode has at least five distinct peaks, with the largest centered at roughly the time of the trigger. The second episode has consists of three or four peaks with the most prominent centered at 20 and 22 seconds. The largest count rates appear in bands corresponding to photon energies of 25 - 100 keV. Prominent rates also appear in the other two bands (see Figure 8.48). The T90 duration for this burst is 29.328 ± 0.036 s.

As with all of the other bursts selected for this sample, this burst was also observed by Konus. Swift began to slew early in the burst and due to the difficulty in fitting data taken during a slew, it is not practical to use BAT data taken during the slew. Therefore, Konus data alone was used for the spectral analysis. With the Band model, $E_{\rm peak}^{\rm obs}$ is found to be $206.4^{+32.8}_{-27.1}$. Figure 8.49 shows the count spectra from Konus and the best-fit model for these spectra.

X-ray Afterglow

The x-ray afterglow, as measured by the XRT, is shown in Figure 8.50. The light curve is consistent with a single power law with a decay index of -1.75 ± 0.04, with a reduced χ^2 of 1.047. However, a broken power law gives a slightly better fit, with $\chi^2_{/nu}$ of 0.989, giving an early decay index of -1.55 ± 0.21, a late decay index of -1.92 ± 0.11, and a break time of 14000 ± 10000 s.

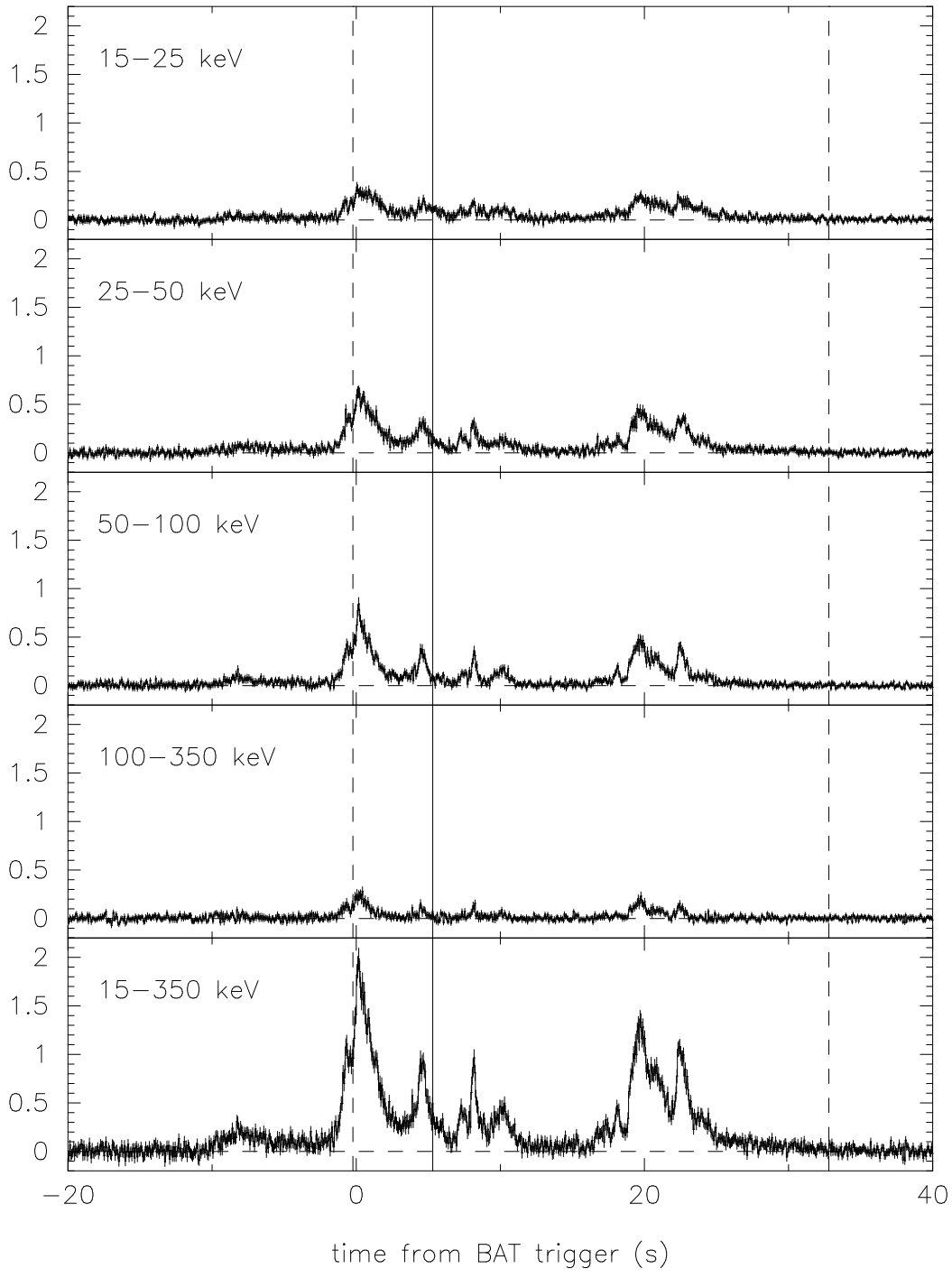

Figure 8.48: The light curve of the GRB 050326 prompt gamma-ray emission. The dashed vertical lines bound the time interval used to measure the spectrum. Swift began to slew at the time indicated by the solid vertical line. Since the slew began during the burst, only Konus data was used for the spectral fitting.

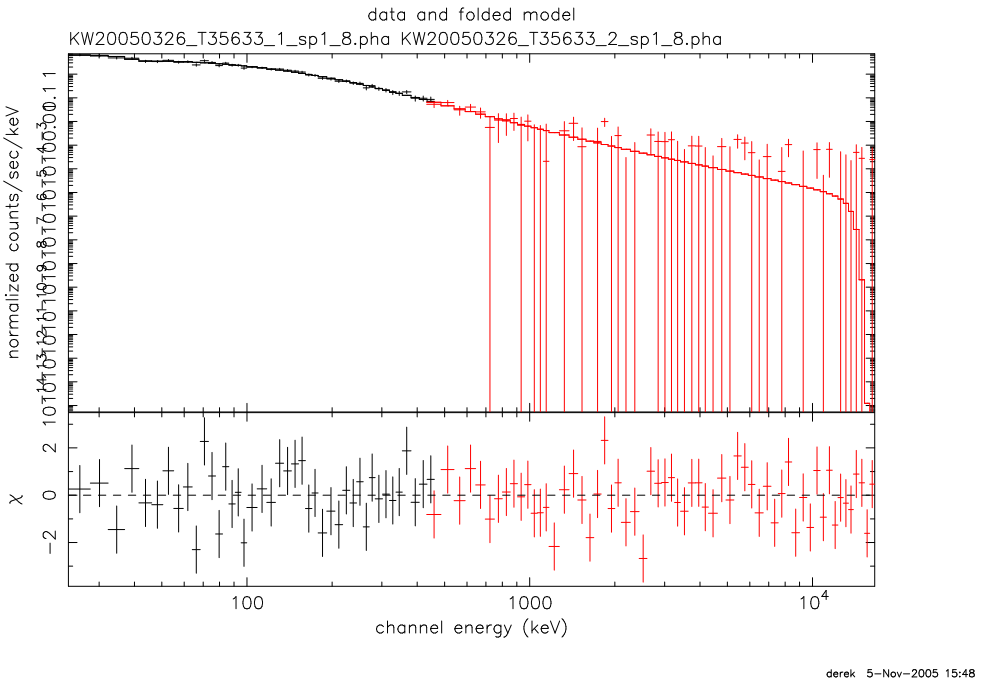

Figure 8.49: The count spectra recorded by Konus for the GRB 050326 prompt gamma-ray emission, along with the best fit Band model. See Table 8.22 for the spectral parameters.

An F-test favors the broken power law model at a 76% confidence level over that of a single power law, which is somewhat marginal. The average 0.6 – 10 keV flux for of the prompt emission is also shown, as extrapolated from the BAT data. The value is a bit lower than the extrapolated light curve of the afterglow.

The XRT count spectra both before and after the break in the light curve is shown in Figure 8.51. The best fit hydrogen column density is $4.2^{+2.8}_{-2.4} \times 10^{21}$ atoms/cm^2. This is higher than the hydrogen column density due to our galaxy alone in the direction of the burst (4.55×10^{20} atoms/cm^2). The best fit spectral indices of the two spectra are consistent with each other.

8.3.3 GRB 050603

This burst triggered BAT at 06:29:05 UT (MET=139472944.768) (GCN 3509). Swift did not slew automatically because slewing had been disabled for some engineering tests. XRT began to collect data beginning at 17:19:27 UT, about 11 hours after the burst (GCN 3514). The

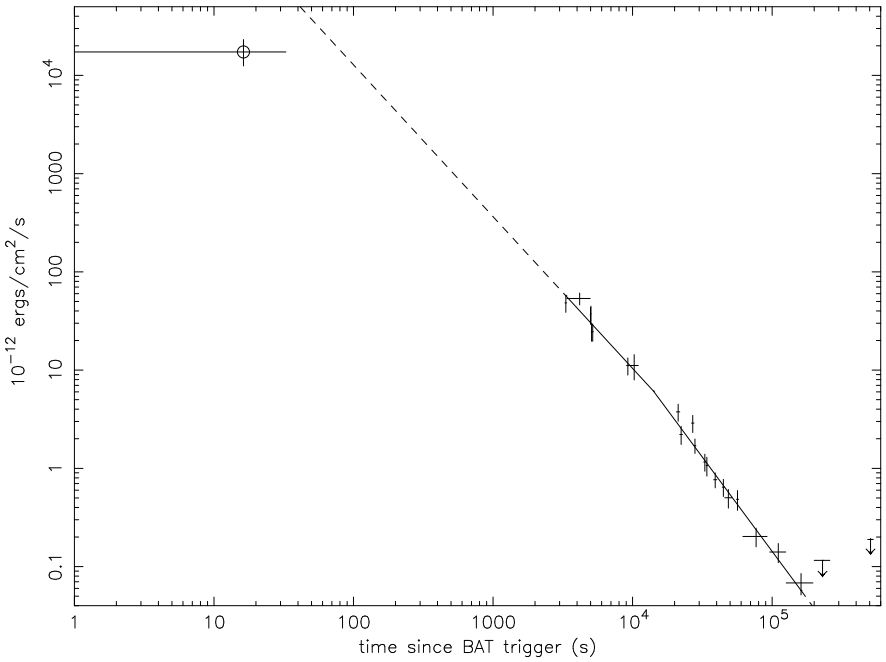

Figure 8.50: The light curve of the XRR 050326 x-ray afterglow, along with the best-fit broken power law model. The circled data point is the average flux of the prompt emission, extrapolated into the 0.6 – 10 keV energy range. When extrapolated backward, the early power law overshoots the 0.6 – 10 keV flux of the prompt emission.

Table 8.23: The best fit spectral parameters for the GRB 050326 x-ray afterglow. n_H is measured in 10^{21} atoms/cm^2, A in units of 10^{-3} ergs/cm^2/s/keV, and 0.6 – 10 keV flux in units of 10^{-12} ergs/cm^2/s. Start and stop times are in seconds since the BAT trigger.

Parameter	Interval 1	Interval 2
n_H	$4.6^{+2.8}_{-2.4}$	< 2.1
I	$2.23^{+0.56}_{-0.51}$	$2.05^{+0.60}_{-0.34}$
A	$8.25^{+6.23}_{-3.52}$	$0.053^{+0.034}_{-0.014}$
flux	$41.9^{+28.9}_{-11.4}$	$0.229^{+0.047}_{-0.045}$
start time	3272.194983 s	37954.304543 s
stop time	11002.095892 s	196277.282632 s
exposure	589.4 s	35534.9 s
χ^2_ν/ν	0.866/6	1.201/5

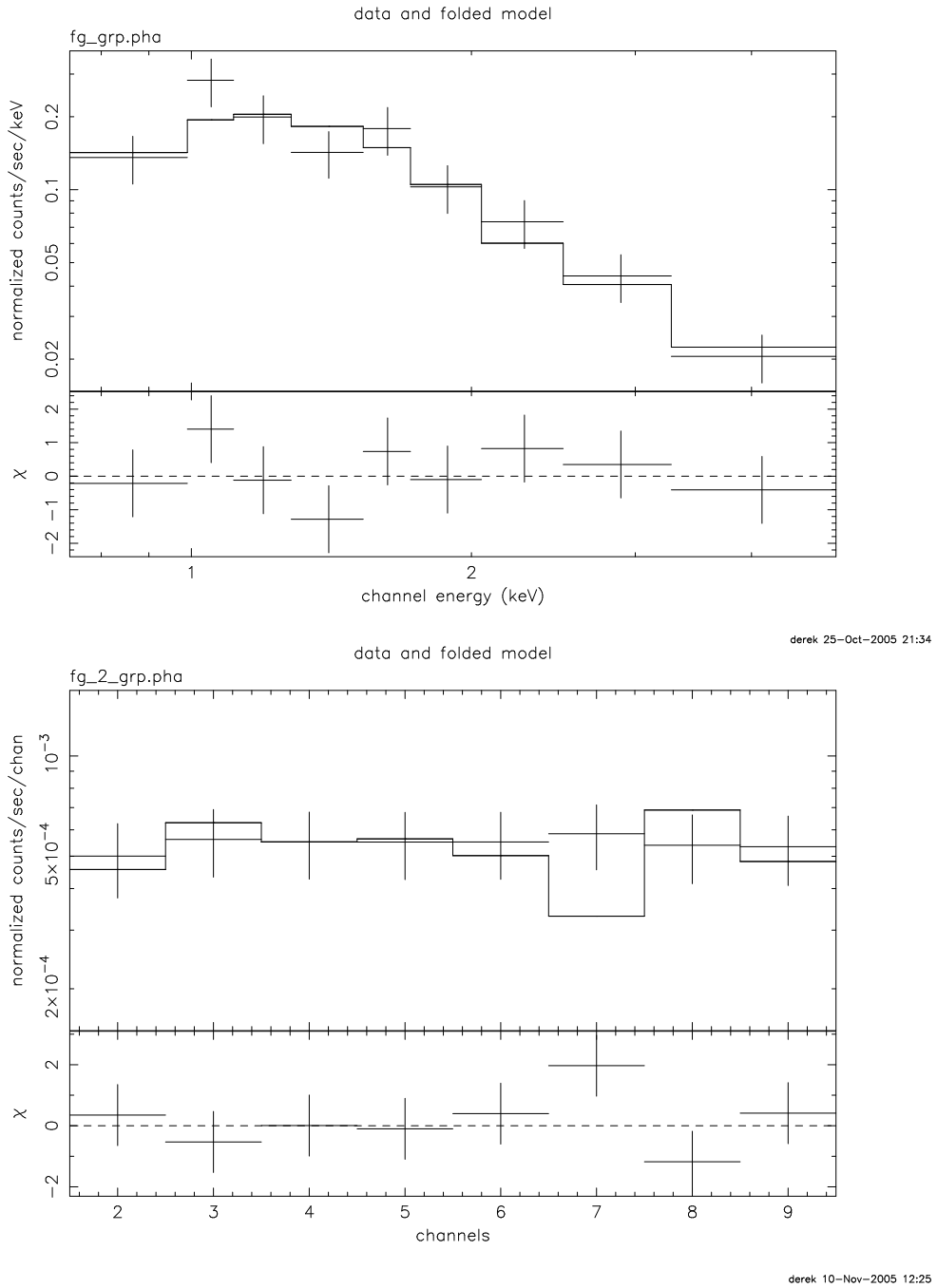

Figure 8.51: The count spectrum of the GRB 050326 x-ray afterglow before (top) and after (bottom) the break in the light curve. Both count spectra are fit with a power law model, with intervening absorption. Count bins corresponding to photon energies of 0.3 – 10 keV were included. See Table 8.23 for the spectral parameters.

position determined by BAT was RA=2h 39m 54.8s, Dec=-25d 10' 57.8". The XRT-determined position was found to be RA=2h 39m 56.8s, Dec=-25d 10' 59.8", with a 6 arcsec uncertainty (90% confidence) (GCN 3519). Afterglow emission was also detected in optical, submillimeter, and radio bands (GCN 3511, 3515, 3513). A redshift of 2.821 was measured.

Prompt Emission

This burst has a T90 duration of 12.608 ± 0.064 seconds. There are three distinct peaks. The first peak, which is shorter and broader than the others, reaches its maximum about 3 seconds before the trigger. The next peak begins about 1 s before the trigger, and the final peak, which is the highest, reaches its maximum 0.2 s after the trigger. The largest count rates appear in channels corresponding to photon energies of 50 - 100 keV, with slightly smaller rates appearing in the 25 - 50 keV band. Prominent emission is also evident in the other two bands (see Figure 8.52).

As with all of the other bursts selected for this sample, this burst was also observed by Konus. Because the Swift slew occurred long after the burst, we were able to use both data sets together to find the best spectral model. $E_{\rm peak}^{\rm obs}$ was found to be $324.4^{+46.5}_{-43.9}$ keV, using the Band model. The time interval from which the spectrum was extracted spans from 3.05323 s before the trigger to 0.78677 s after the trigger. Figure 8.53 shows the count spectra from both BAT and Konus and the best-fit model for these spectra.

X-ray Afterglow

The x-ray afterglow, as measured by the XRT, is shown in Figure 8.54. The light curve is consistent with a power law with a decay index of -1.60 ± 0.08. The 0.6 – 10 keV flux of the prompt emission is also shown, as extrapolated from the BAT data. The trend of the afterglow overshoots the prompt emission data. We have often seen breaks in the afterglow light curves at times earlier than 11 hours, however, and it is distinctly possible that one exists here.

The count spectrum measured by the XRT is shown in Figure 8.55. The fit provides an upper limit for the hydrogen column density of 7.8×10^{20} atoms/cm^2. This is consistent with the hydrogen column density due to our galaxy alone in the direction of the burst (1.92×10^{20}

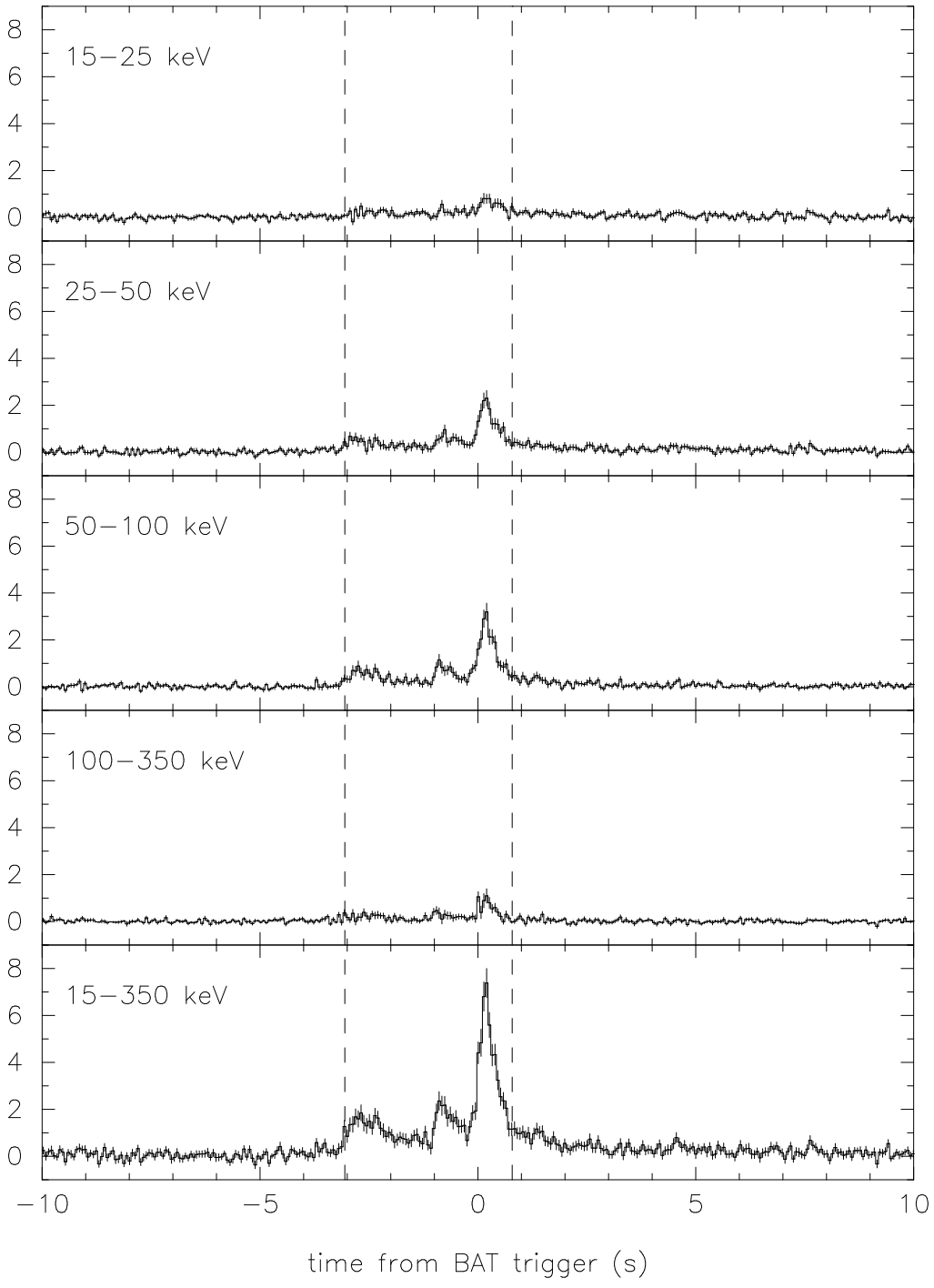

Figure 8.52: The light curve of the GRB 050603 prompt gamma-ray emission. The dashed vertical lines bound the time interval used to measure the spectrum. Swift slewed long after the time interval shown here.

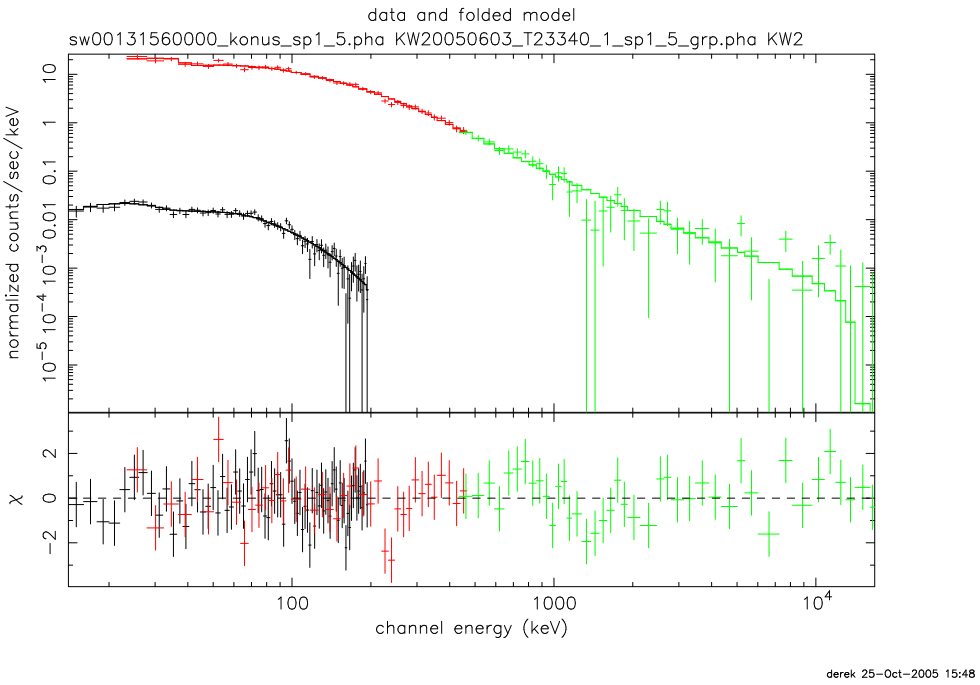

Figure 8.53: The count spectra recorded by BAT and Konus for the GRB 050603 prompt gamma-ray emission, along with the best fit Band model. The Konus data is shown in red and green and the BAT data in black. See Table 8.24 for the spectral parameters.

Table 8.24: The best fit spectral parameters for the GRB 050603 prompt emission, using a power law model, a cutoff power law model, and the Band model. $E_{\rm peak}^{\rm obs}$ is measured in keV, A in ergs/cm^2/s/keV, and average flux in 10^{-8} ergs/cm^2/s for 15 – 150 keV photons. The exposure was 3.84 s.

power law		cutoff power law		Band	
Parameter	Value	Parameter	Value	Parameter	Value
α	-2.03 ± 0.01	α	$-0.902^{+0.052}_{-0.054}$	α	$-0.74^{+0.10}_{-0.08}$
A	$(7.21 \pm 0.32) \times 10^{-2}$	$E_{\rm peak}^{\rm obs}$	$462.6^{+41.8}_{-36.7}$	β	$-2.09^{+0.11}_{-0.14}$
		A	0.1201 ± 0.0047	$E_{\rm peak}^{\rm obs}$	$324.4^{+46.5}_{-43.9}$
				A	$0.130^{+0.008}_{-0.007}$
				flux	114.3 ± 6.5
χ^2_ν/ν	18.569/156	χ^2_ν/ν	1.188/155	χ^2_ν/ν	0.915/154

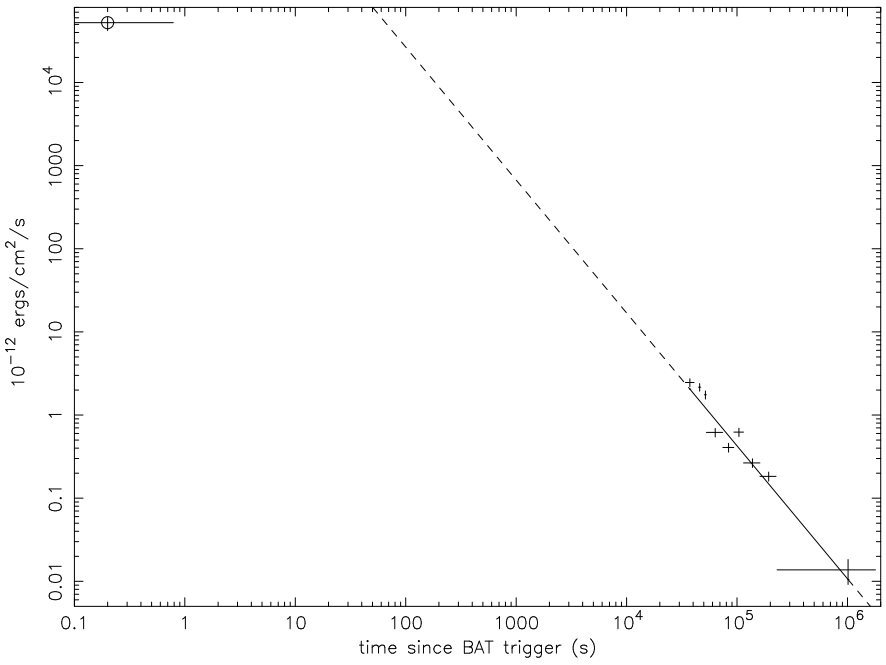

Figure 8.54: The light curve of the GRB 050603 x-ray afterglow, along with the best-fit power law model. The circled data point is the average flux of the prompt emission, extrapolated from the BAT data into the 0.6 – 10 keV energy range. When extrapolated backward, the power law overshoots the 0.6 – 10 keV flux of the prompt emission. It is distinctly possible that a break occurs before 11 hours.

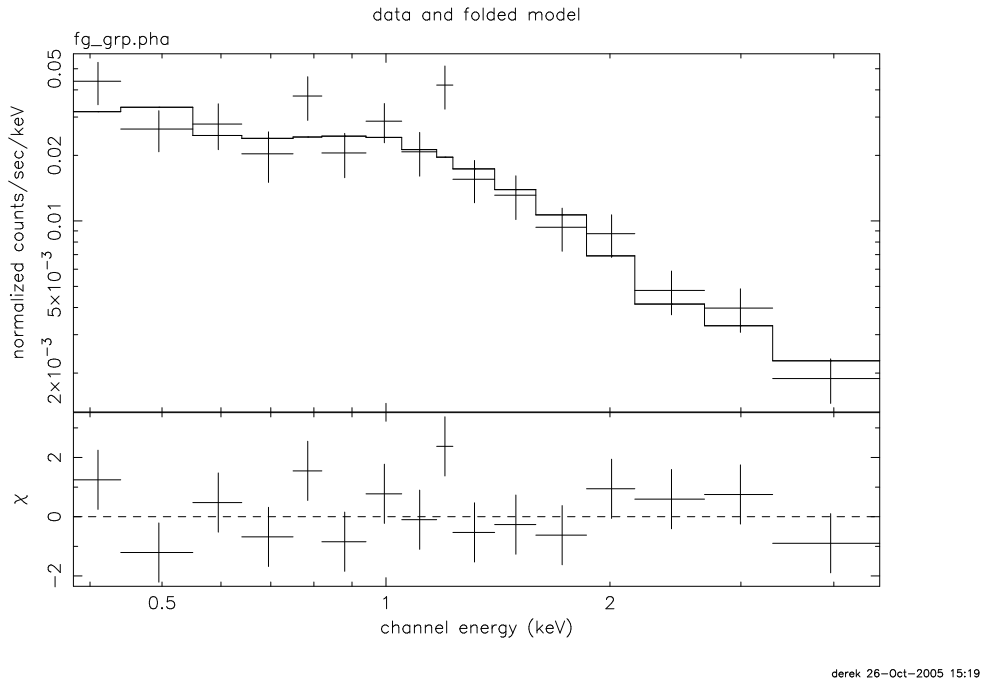

Figure 8.55: The count spectrum of the GRB 050603 x-ray afterglow. Count bins corresponding to photon energies of 0.3 – 10 keV were included. See Table 8.25 for the spectral parameters.

atoms/cm^2). The best fit spectral index is $1.75^{+0.35}_{-0.17}$. The spectrum used here consists of counts accumulated between 34046.8 s after the trigger and 57789.9 s after the trigger.

8.3.4 GRB 041223

This was one of the first bursts detected by BAT. It triggered the BAT at 14:06:18 UT (MET=125503577.28) (GCN 2898). Swift did not slew automatically because autonomous slewing had not yet been enabled at this early stage in the mission. XRT began to collect data beginning at 18:43:59 UT, about 4.6 hours after the burst (GCN 2901). The position determined by BAT was RA=6h 40m 48.8s, Dec=-37d 4' 3.0". The XRT-determined position was found to be RA=6h 40m 47.4s, Dec=-37d 4' 22.3", with an estimated uncertainty of 15 arcsec (90% confidence) (GCN 2910). Optical afterglow emission was also detected (GCN 2902), but a redshift was not measured. Any redshift higher than 3.2 would permit this burst to be consistent with the Yonetoku relation.

Table 8.25: The best fit spectral parameters for the GRB 050603 x-ray afterglow. n_H is measured in atoms/cm^2, A in units of photons/cm^2/s/keV, and flux in units of ergs/cm^2/s. Start and stop times are in seconds since the BAT trigger.

Parameter	Value
n_H	$< 7.78 \times 10^{21}$
I	$1.75^{+0.35}_{-0.17}$
A	$3.47^{+1.11}_{-0.39} \times 10^{-4}$
0.6 – 10 keV flux	$2.31^{+0.32}_{-0.30} \times 10^{-12}$
start time	34046.753303 s
stop time	57789.9225 s
exposure	7889.3 s
χ^2_ν/ν	1.263/13

Prompt Emission

This was a rather long burst with a T90 duration of 108.932 ± 0.018 seconds. It has a very complex structure with 15 or more peaks, the highest of which is centered about 35 seconds after the trigger. The largest count rates appear in channels corresponding to photon energies of 50 - 100 keV, with significant rates also appearing in the other two bands (see Figure 8.56).

As with the other bursts selected for this sample, this burst was also observed by Konus, and we were able to use both data sets together to find the best spectral model. $E^{\rm obs}_{\rm peak}$ was found to be $344.7^{+32.8}_{-28.7}$ keV, using the Band model. The time interval from which the spectrum was extracted spans from 1.182 s before the trigger to 137.058 s after the trigger. Figure 8.57 shows the count spectra from both BAT and Konus as well as the best-fit model for these spectra.

X-ray Afterglow

The x-ray afterglow, as measured by the XRT, is shown in Figure 8.58. The light curve is consistent with a power law with a decay index of -1.92 ± 0.27. The average 0.6 – 10 keV flux of the prompt emission is also shown, as extrapolated from the BAT data. The trend of the afterglow overshoots the prompt emission data. It is possible that a break in the afterglow takes place prior

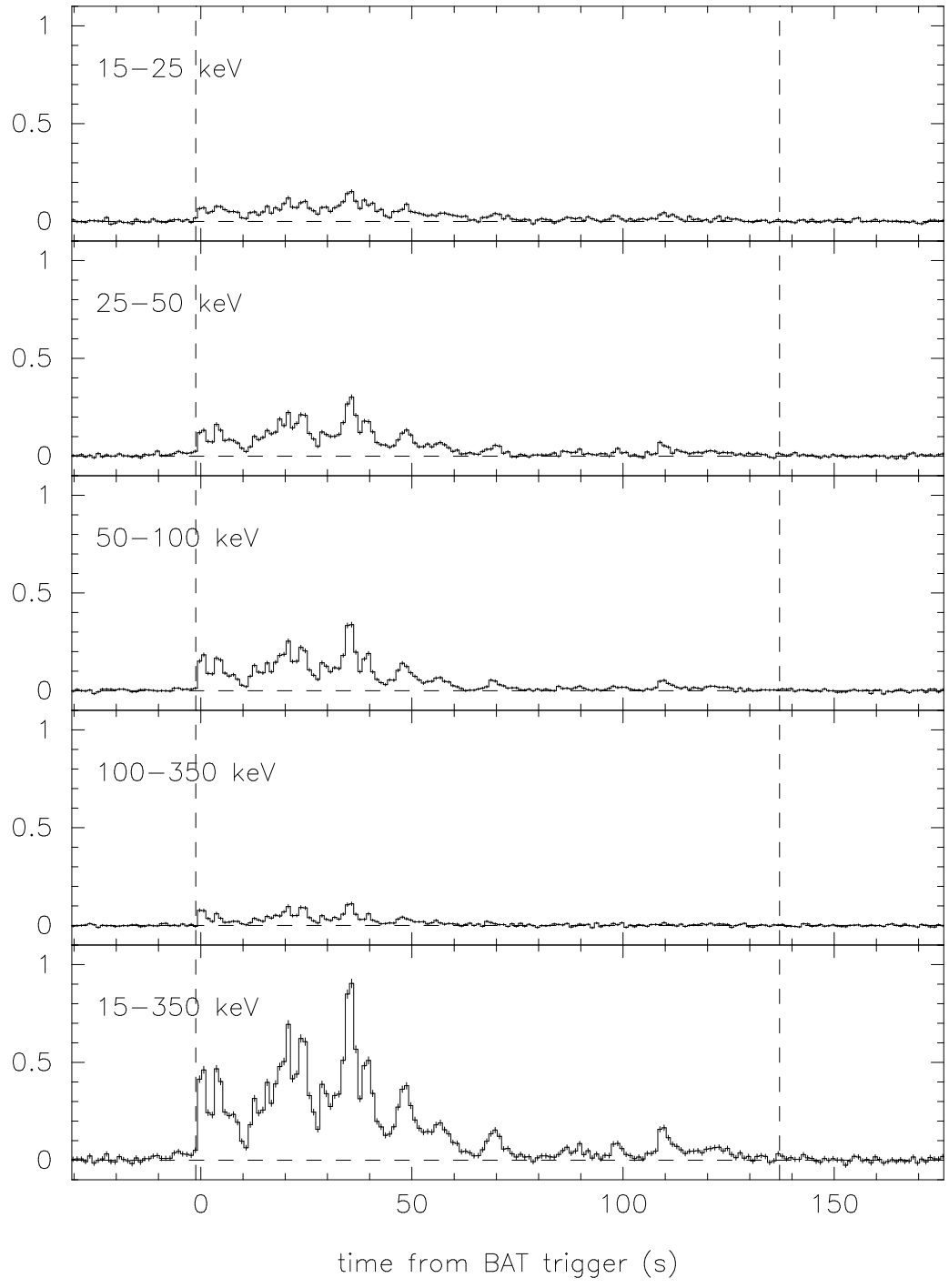

Figure 8.56: The light curve of the GRB 041223 prompt gamma-ray emission. The dashed vertical lines bound the time interval used to measure the spectrum. Swift slewed long after the time interval shown here.

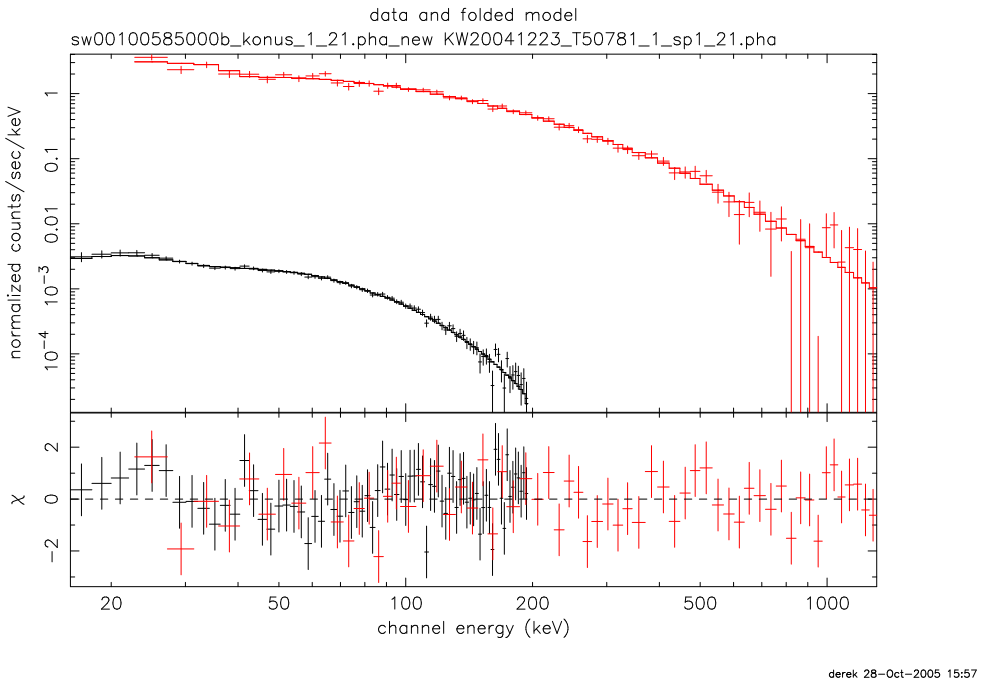

Figure 8.57: The count spectra recorded by BAT and Konus for the GRB 041223 prompt gamma-ray emission, along with the best fit Band model. The BAT data is shown in black and the Konus data in red. See Table 8.26 for the spectral parameters.

Table 8.26: The best fit spectral parameters for the GRB 041223 prompt emission, using a power law model, a cutoff power law model, and the Band model. $E_{\rm peak}^{\rm obs}$ is measured in keV, A in ergs/cm^2/s/keV, and average flux in 10^{-8} ergs/cm^2/s for 15 – 150 keV photons. The exposure was 138.24 s.

power law		cutoff power law		Band	
Parameter	Value	Parameter	Value	Parameter	Value
α	-1.34 ± 0.02	α	$-0.831^{+0.048}_{-0.046}$	α	-0.83 ± 0.05
A	$(1.19 \pm 0.02) \times 10^{-2}$	$E_{\rm peak}^{\rm obs}$	$337.6^{+27.7}_{-24.2}$	β	< 2.63
		A	$1.383^{+0.034}_{-0.032} \times 10^{-2}$	$E_{\rm peak}^{\rm obs}$	$335.9^{+28.8}_{-26.5}$
				A	$1.385^{+0.036}_{-0.033} \times 10^{-2}$
				flux	11.9 ± 0.2
χ^2_ν/ν	5.425/135	χ^2_ν/ν	0.826/134	χ^2_ν/ν	0.832/133

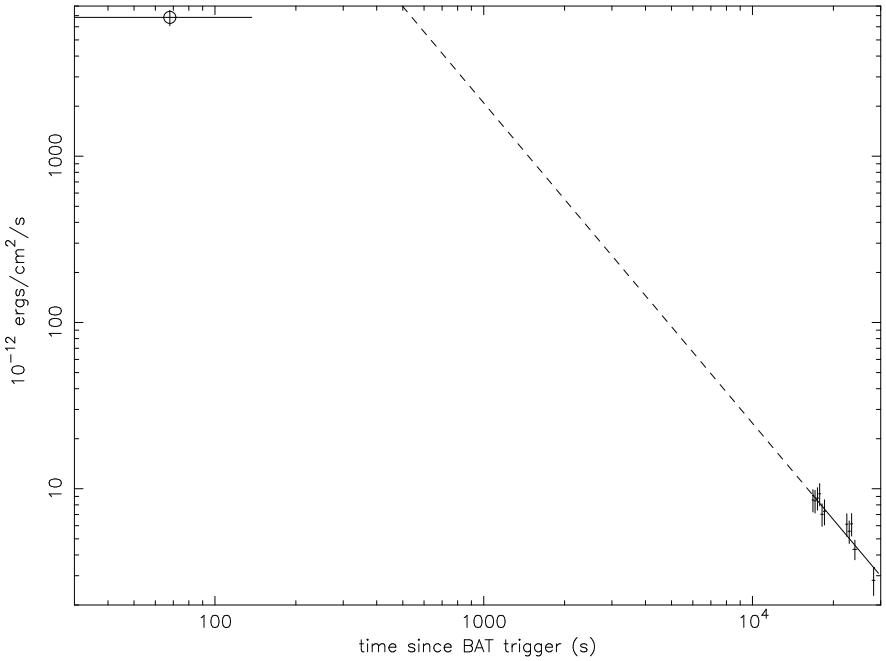

Figure 8.58: The light curve of the GRB 041223 x-ray afterglow, along with the best-fit power law model. The circled data point is the average flux of the prompt emission, extrapolated into the 0.6 – 10 keV energy range. When extrapolated backward, the power law overshoots the 0.6 – 10 keV flux of the prompt emission.

to XRT's observations.

The count spectrum measured by the XRT is shown in Figure 8.59. The best fit hydrogen column density is $1.71^{+0.71}_{-0.64} \times 10^{21}$ atoms/cm^2. This is consistent with the hydrogen column density due to our galaxy alone in the direction of the burst (1.09×10^{21} atoms/cm^2). The best fit spectral index is $2.17^{+0.25}_{-0.23}$. The spectrum used here consists of counts accumulated throughout the entire XRT observation, beginning 16658.4 s after the trigger and ending 28854.3 s after the trigger.

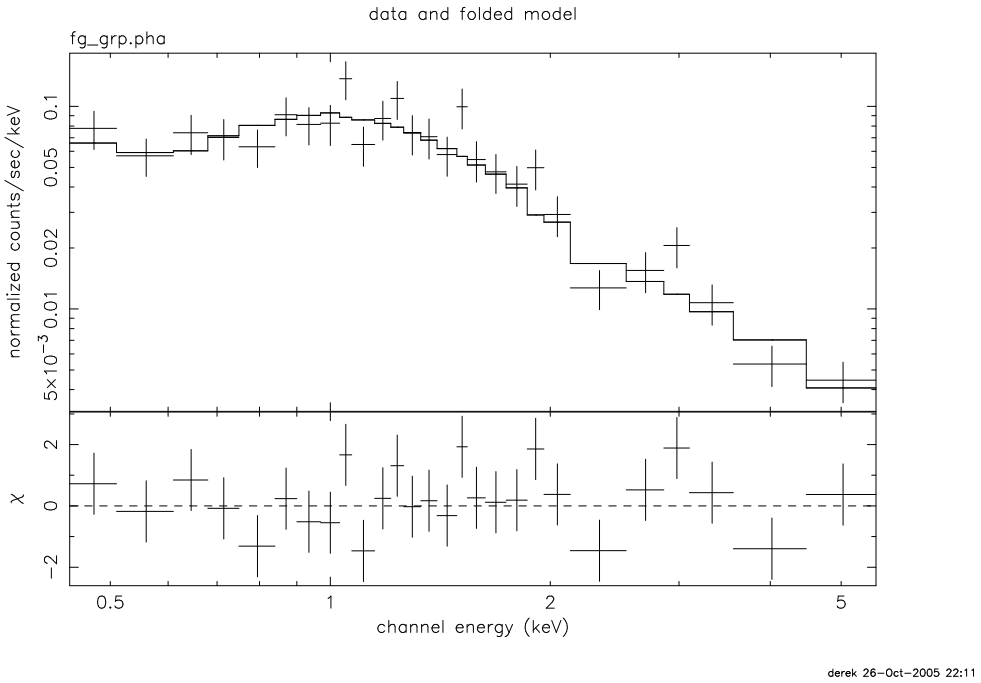

Figure 8.59: The count spectrum of the GRB 041223 x-ray afterglow. Count bins corresponding to photon energies of 0.3 – 10 keV were included. See Table 8.27 for the spectral parameters.

Table 8.27: The best fit spectral parameters for the GRB 041223 x-ray afterglow. n_H is measured in atoms/cm^2, A in units of photons/cm^2/s/keV, and flux in units of ergs/cm^2/s. Start and stop times are in seconds since the BAT trigger.

Parameter	Value
n_H	$1.71^{+0.71}_{-0.64} \times 10^{21}$
I	$2.17^{+0.25}_{-0.23}$
A	$1.96^{+0.49}_{-0.39} \times 10^{-3}$
0.6 – 10 keV flux	$1.02^{+0.18}_{-0.13} \times 10^{-11}$
start time	16658.405592 s
stop time	28854.3362 s
exposure	4016.5 s
χ^2_ν/ν	1.088/24

Chapter 9

Global Characteristics of BAT XRFs, XRRs, and GRBs

In this chapter, we will compare the prompt gamma-ray characteristics of bursts detected by BAT with those detected by other instruments. We will also compare the x-ray afterglow emission of the sample of bursts described in Chapter 8 with bursts observed by other missions. Along the way, we will also note differences and similarities between the XRFs, XRRs, and GRBs observed by Swift.

9.1 Prompt Emission

9.1.1 Fluence

Figure 9.1 shows the distribution of 15 – 150 keV fluences of all BAT bursts detected prior to 31 July 2005. XRF 050826 is also included. Aside from two GRBs with very low fluences (which, incidentally, both have durations less than 200 ms, placing them in the class of short GRBs), the XRFs detected by BAT tend to have smaller fluences than the XRRs or GRBs detected by BAT. Sakamoto et al. also noted this general trend in bursts detected by HETE-2 [70].

9.1.2 Spectral Peak Energy $E_{\rm peak}^{\rm obs}$

Figure 9.2 shows the spectral peak energies $E_{\rm peak}^{\rm obs}$ for all BAT bursts detected prior to 31 July 2005 for which $E_{\rm peak}^{\rm obs}$ was reasonably constrained. XRF 050826 is also included in the XRF histogram. X-ray flashes tend to have lower values of $E_{\rm peak}^{\rm obs}$ than x-ray rich GRBs, which in turn have lower $E_{\rm peak}^{\rm obs}$ values than GRBs. This is the same general trend observed in BeppoSAX [50] and HETE-2 bursts [70].

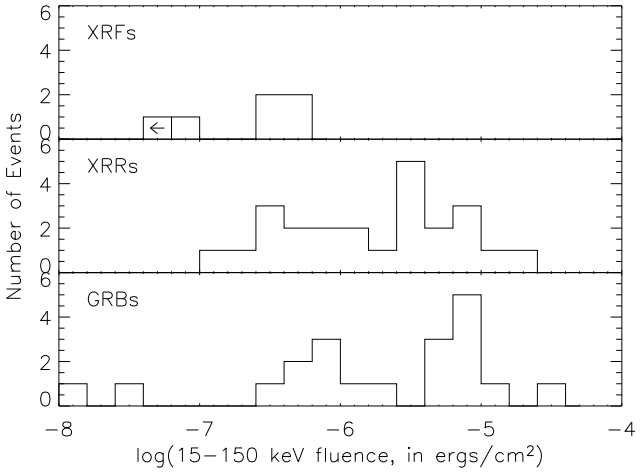

Figure 9.1: Fluence histograms of XRFs, XRRs, and GRBs detected by BAT. The x-axis shows the base-10 logarithm of the 15 – 150 keV fluence, in units of ergs/cm^2. The arrow in one of the boxes in the XRF histogram denotes that only an upper limit on the fluence was obtained for that burst.

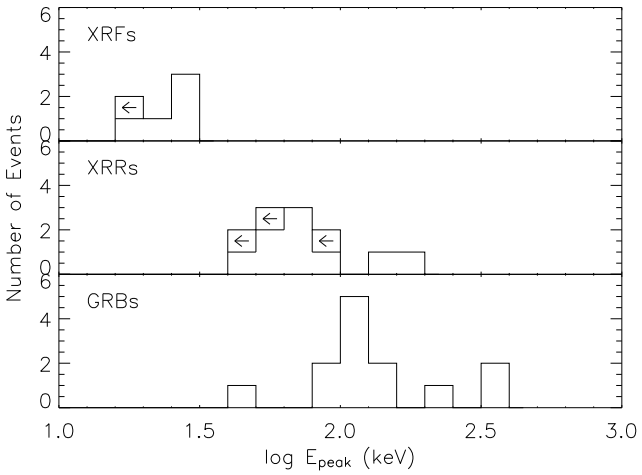

Figure 9.2: $E_{\rm peak}^{\rm obs}$ histograms of XRFs, XRRs, and GRBs detected by BAT. The x-axis shows the logarithm of $E_{\rm peak}^{\rm obs}$, in units of keV.

Table 9.1: K-S test results for Swift GRBs, XRRs, and XRFs

Distributions	Probability
Swift XRFs and Swift GRBs	0.17
Swift XRFs and Swift XRRs	0.053
Swift XRRs and Swift GRBs	0.61
Swift (all) and BATSE (all)	0.001
Swift ($>$ 3 s) and BATSE ($>$ 3 s)	0.38

9.1.3 Duration

Figure 9.3 shows the T_{90} durations for all BAT bursts detected prior to 31 July 2005, as well as for XRF 050826. Also shown are the durations of GRBs detected by BATSE. The KS-test gives a probability of 0.001 that there is no difference between the distribution of Swift burst durations and that of the BATSE burst durations. If we only include bursts for which T_{90} is greater than 3 seconds, the probability is 0.379. We can conclude that the distribution of bursts with a T_{90} greater than 3 seconds detected by BAT is consistent with those detected by BATSE, but that if we include bursts with T_{90} durations less than 3 seconds (of which BAT has detected 2 as of 31 July 2005), the two distributions are not consistent. We note that the two short-duration bursts detected by BAT fall in the "GRB" category.

Using the K-S test to compare the duration distribution of BAT-detected XRFs, XRRs, and GRBs, we obtain the values noted in Table 9.1. The T_{90} durations of the XRFs in our sample are not consistent with those of the BAT-detected XRRs and are only marginally consistent with the BAT-detected GRBs. Sakamoto et al. [70] found that the T_{90} durations of XRFs, XRRs, and GRBs detected by HETE-2 were consistent with one another. We note that both XRF samples are small, with only 6 in our sample and 16 in the sample analyzed by Sakamoto et al., so that the results may be influenced by the small statistics of the samples.

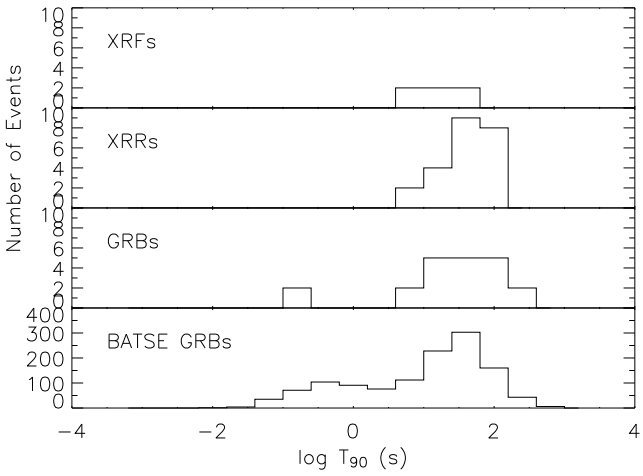

Figure 9.3: Duration histograms of XRFs, XRRs, and GRBs detected by BAT. The x-axis shows the base-10 logarithm of T_{90}, in units of seconds.

9.1.4 Correlation of $E_{\rm peak}^{\rm obs}$ with Other Quantities

Several studies examining potential correlations of $E_{\rm peak}^{\rm obs}$ with other quantities have been conducted using observations from other missions. In this section, we compare the results of some of these studies with similar results from BAT.

$E_{\rm peak}^{\rm obs}$ and Duration

Figure 9.4 shows the distribution of burst durations and $E_{\rm peak}^{\rm obs}$. In this case, the duration shown is T_{50}, the interval between the time at which the fluence reaches 25% of its full final amount and the time at which the fluence reaches 75% of its full final amount. Also shown are values taken from analysis done by Kaneko et al. on a sample of bursts detected by BATSE [47]. This plot illustrates the differences in the sensitivity of the two instruments to bursts of different durations and peak energies. While the durations of the BAT bursts are consistent with those of the BATSE bursts, as we have already noted, BAT is less sensitive to the short-duration class of bursts. Furthermore, the peak energies $E_{\rm peak}^{\rm obs}$ determined from BAT data alone tend to be lower than those determined from BATSE data. A similar study was done by Kippen et al. using XRF data from BeppoSAX [50]. We note that the sample of XRFs presented here have a similar $E_{\rm peak}^{\rm obs}$

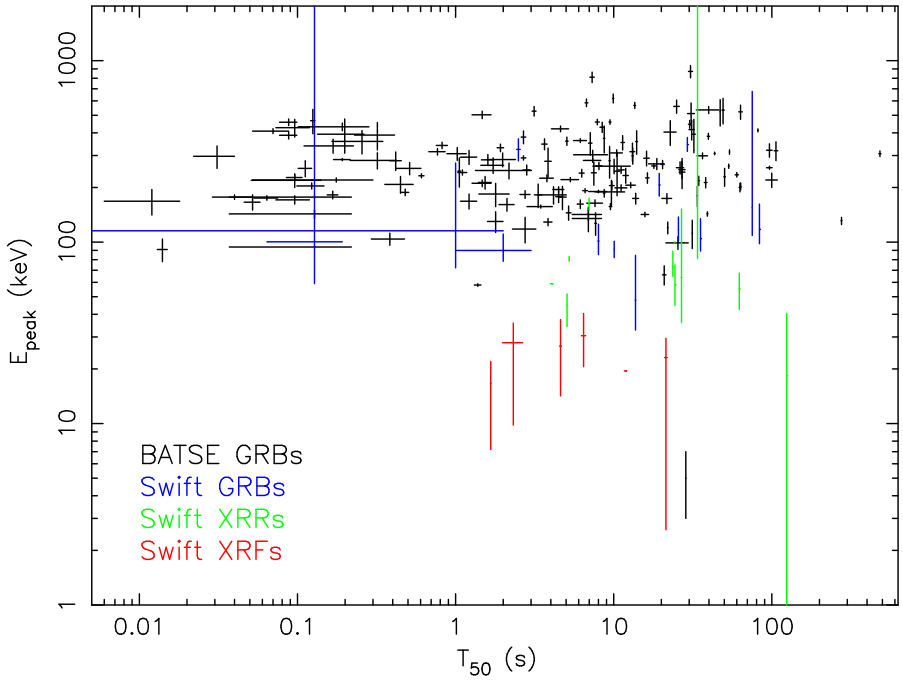

Figure 9.4: A plot of T_{50} duration and peak spectral energy $E^{\rm obs}_{\rm peak}$ of XRFs, XRRs, and GRBs detected by BAT. Also shown are the T_{50} durations and $E^{\rm obs}_{\rm peak}$ values for a sample of bursts detected by BATSE.

and T_{50} distribution as those presented by Kippen et al.

$E^{\rm obs}_{\rm peak}$ and Fluence

Figure 9.5 is a scatter plot showing $E^{\rm obs}_{\rm peak}$ verses 15 – 150 keV fluence. As before, all bursts detected prior to 31 July 2005 for which $E^{\rm obs}_{\rm peak}$ was reasonably constrained, as well as XRF 050826, are included. We note a mild correlation between fluence and $E^{\rm obs}_{\rm peak}$. The linear correlation coefficient for this sample is 0.70903. The probability of such a correlation occurring by chance in a sample of this size (27 bursts) is 1.2×10^{-4}. Sakamoto et al. [70] observed a similar though somewhat smaller correlation between $E^{\rm obs}_{\rm peak}$ and the 2 – 400 keV fluence for bursts detected by HETE-2.

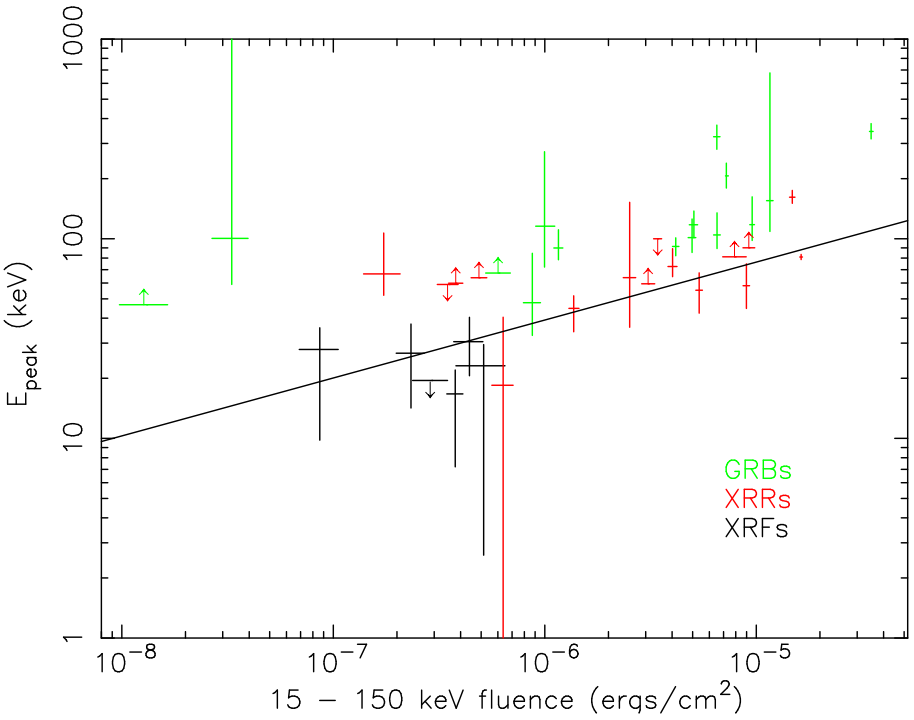

Figure 9.5: A plot of the 15 – 150 keV fluence and peak spectral energy $E^{\rm obs}_{\rm peak}$ of XRFs, XRRs, and GRBs detected by BAT. The solid line is the best linear fit to the data and is given by $E^{\rm obs}_{\rm peak} = 2158^{+1449}_{-801} \times [S_E(15\text{–}150\ {\rm keV})]^{0.29\pm0.04}$, with $S_E(15\text{–}150\ {\rm keV})$ in ergs/cm^2.

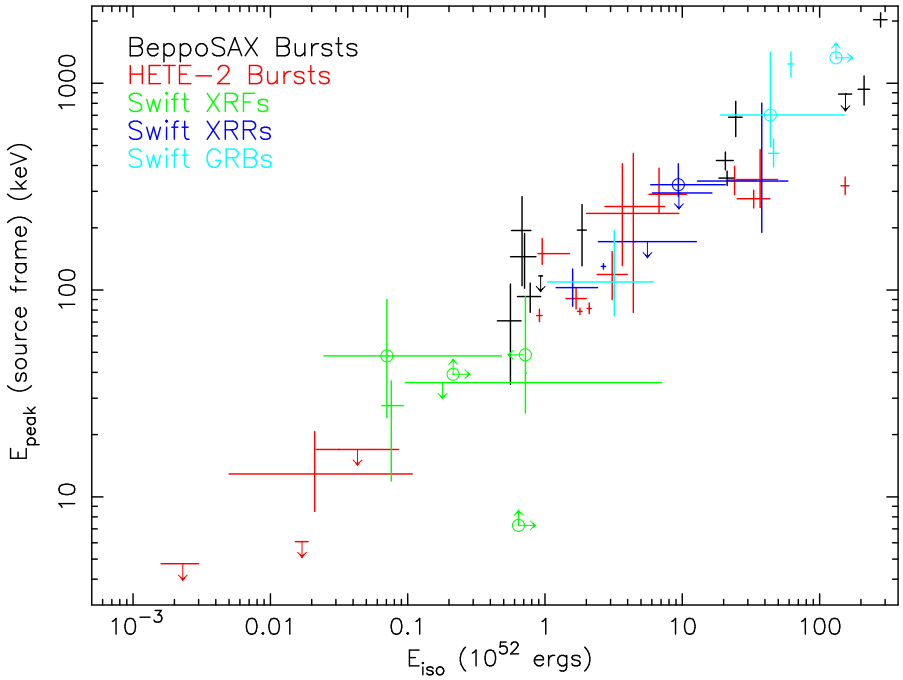

Figure 9.6: A plot of peak spectral energy in the source frame $E^{\rm src}_{\rm peak}$ verses the isotropic-equivalent energy $E_{\rm iso}$ of bursts detected by BeppoSAX, HETE-2, and Swift. The circled data points are bursts for which a redshift was not measured and consequently the Yonetoku relation was used to derive an estimated redshift, using the technique described in Section 7.3. Since the Yonetoku relation is itself very similar to the Amati relation, it is not surprising that these points lie along the correlation.

$E^{\rm obs}_{\rm peak}$ and $E_{\rm iso}$

In section 2.4.5, we described a correlation between $E^{\rm src}_{\rm peak}$ (the peak spectral energy in the source frame) and $E_{\rm iso}$ (the total isotropic-equivalent gamma-ray energy emitted). Figure 9.6 shows the data presented in Figure 2.7 along with data from bursts observed by BAT. The BAT data points lie right along this correlation and fill in a region of the $E^{\rm src}_{\rm peak}$ – $E_{\rm iso}$ plane not observed before. Table 9.2 gives the redshift, $E^{\rm src}_{\rm peak}$, and $E_{\rm iso}$ values for Swift bursts.

9.2 Afterglow Emission

9.2.1 Light Curves

Figure 9.7 is a composite plot of all of the x-ray afterglow light curves presented in Chapter 8. Figures 9.8, 9.9, and 9.10 show the light curves in each class. The 0.6 – 10 keV average flux

Table 9.2: Redshifts, $E_{\rm peak}^{\rm src}$ values and $E_{\rm iso}$ values for Swift bursts. *Bursts in italics result from inferred redshifts derived using the technique described in Section 7.3.*

Burst	z	$E_{\rm peak}^{\rm src}$ (keV)	$E_{\rm iso}$ (10^{52} ergs)
XRF 050416A	0.6535	$27.6^{+8.8}_{-16.7}$	$0.076^{+0.017}_{-0.011}$
XRF 050406	> 3	> 39.2	> 0.214
XRF 050714B	> 1.8	> 7.28	> 0.641
XRF 050824	0.83	< 35.7	$0.179^{+6.877}_{-0.083}$
XRF 050528	$0.3^{+1.7}_{-0.2}$	$39.7^{+53.4}_{-14.2}$	< 0.72
XRF 050215B	$0.8^{+1.4}_{-0.3}$	$48.1^{+42.1}_{-23.9}$	$0.070^{+0.411}_{-0.046}$
XRR 050315	1.949	< 294.9	$9.5^{+7.0}_{-3.4}$
XRR 050318	1.44	$109.3^{+17.1}_{-25.9}$	$1.59^{+0.82}_{-0.39}$
XRR 050319	3.24	$78.3^{+93.2}_{-77.9}$	$4.5^{+8.2}_{-2.0}$
XRR 050525A	0.606	$130.1^{+4.0}_{-3.8}$	$2.663^{+0.100}_{-0.094}$
XRR 050505	4.27	336^{+466}_{-147}	38^{+21}_{-25}
XRR 050219B	$1^{+0.5}_{-0.2}$	323^{+85}_{-39}	$9.4^{+11.2}_{-3.5}$
GRB 050401	2.9	458^{+78}_{-64}	$46.2^{+4.2}_{-3.9}$
GRB 050126	1.29	109^{+84}_{-34}	$3.2^{+2.9}_{-2.2}$
GRB 050326	$2.4^{+3.4}_{-0.9}$	702^{+711}_{-207}	44^{+108}_{-25}
GRB 050603	2.821	1240^{+178}_{-168}	$61.8^{+3.1}_{-3.1}$
GRB 041223	> 3.2	> 1327.2	> 131.5

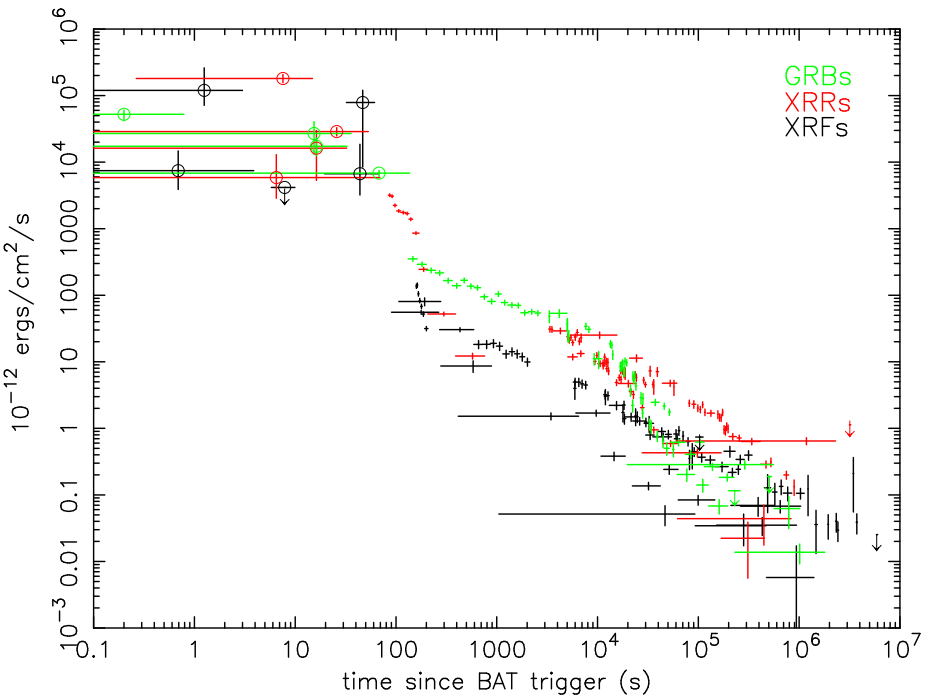

Figure 9.7: A composite plot of the GRB, XRR, and XRF x-ray afterglow light curves presented in Chapter 8. The 0.6 – 10 keV average fluxes extrapolated from the prompt emission spectra are designated by circles.

extrapolated from the prompt emission varies over three orders of magnitude. There is a hint that XRFs have a smaller extrapolated prompt emission on average than XRRs and GRBs. The afterglow fluxes of all three classes are spread throughout a wide range of intensities at various times along their evolution.

9.2.2 Photon Index and n_H

Figure 9.11 shows the distribution of best-fit neutral hydrogen column densities n_H and photon indices I for the sample of bursts described in Chapter 8. Also shown are values gathered and cited by Frontera [27]. No apparent correlation exists between these quantities. Using the K-S test to compare n_H values from Frontera's sample with the n_H values from our sample, we obtain a probability of 0.064 that the two samples are drawn from the same distribution. Thus, the two sets differ significantly. The probability for the photon indices of the two samples is 0.89. Thus, the photon indices of the two samples are consistent with one another. There is a hint that the

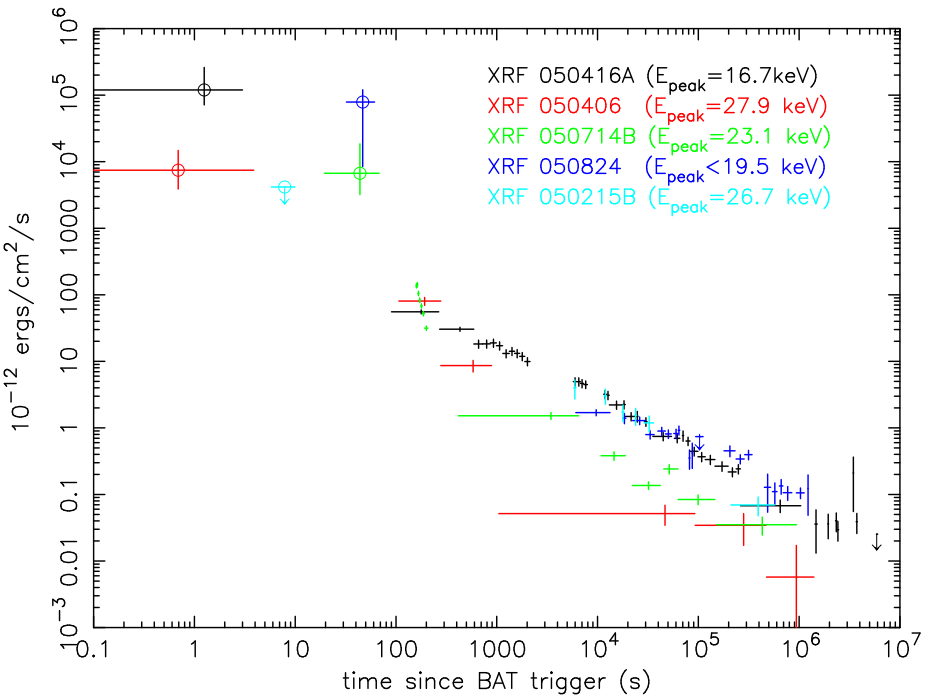

Figure 9.8: A composite plot of the afterglow light curves of x-ray flashes presented in Chapter 8. The 0.6 – 10 keV average fluxes extrapolated from the prompt emission spectra are designated by circles. $E_{\rm peak}^{\rm obs}$ is also given for each burst.

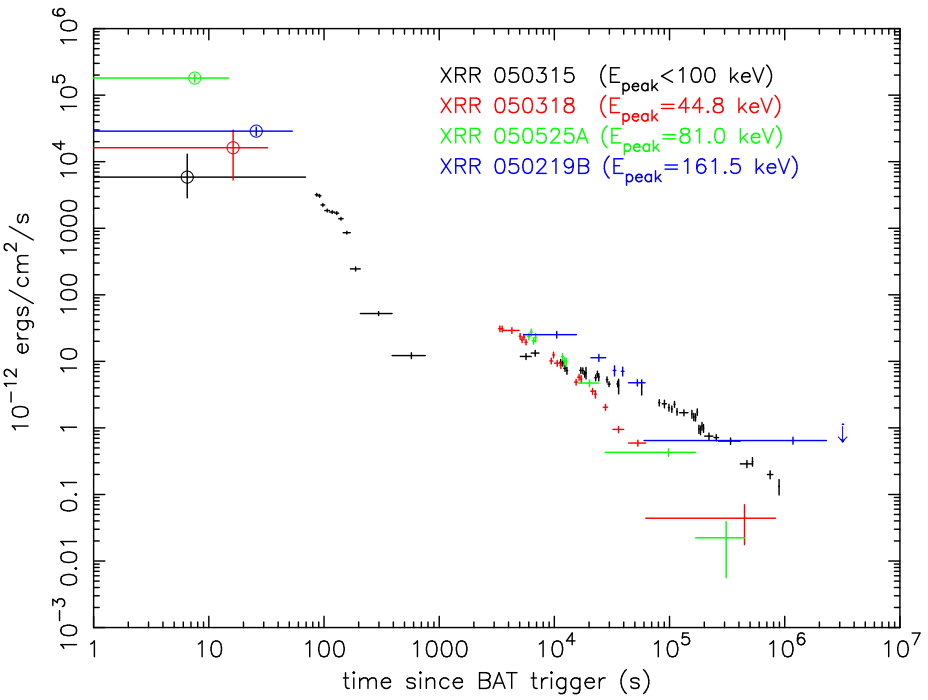

Figure 9.9: A composite plot of the afterglow light curves of x-ray-rich gamma-ray bursts presented in Chapter 8. The 0.6 – 10 keV average fluxes extrapolated from the prompt emission spectra are designated by circles. $E_{\rm peak}^{\rm obs}$ is also given for each burst.

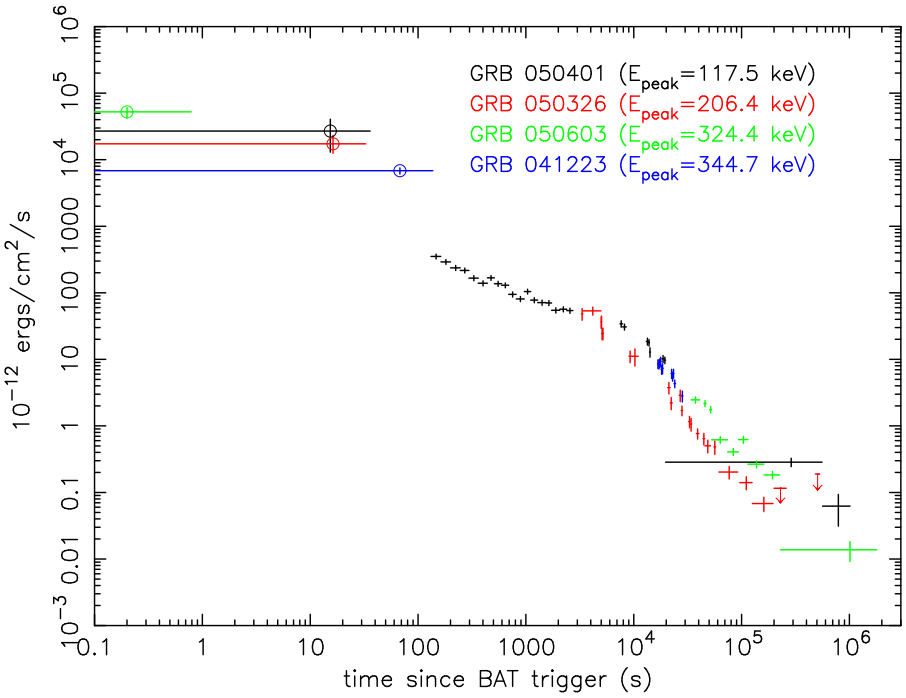

Figure 9.10: A composite plot of the afterglow light curves of gamma-ray bursts presented in Chapter 8. The 0.6 – 10 keV average fluxes extrapolated from the prompt emission spectra are designated by circles. $E_{\rm peak}^{\rm obs}$ is also given for each burst.

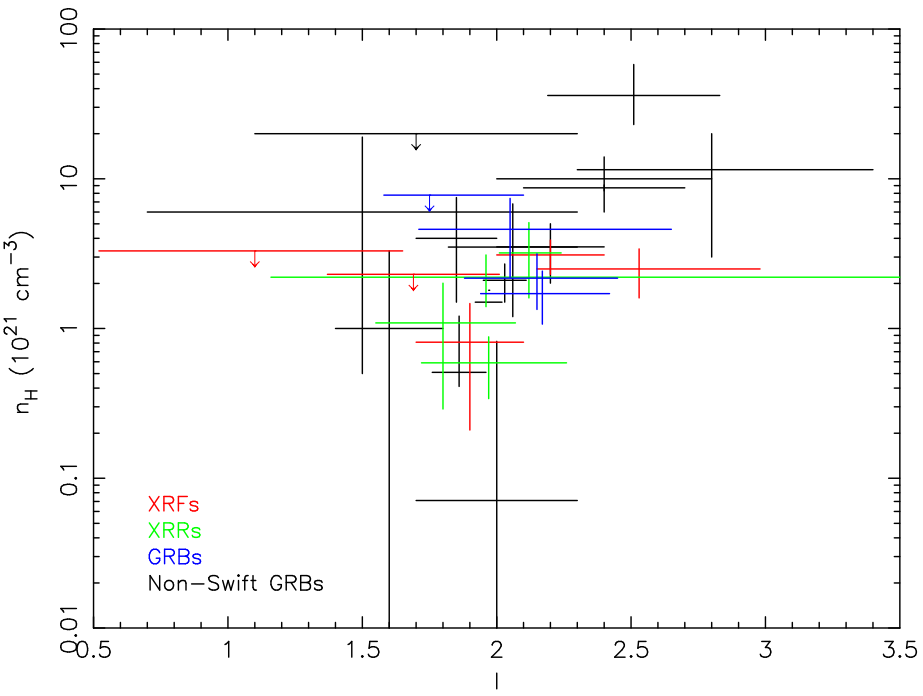

Figure 9.11: A plot of the best-fit neutral hydrogen column densities n_H and photon indices I of afterglows described in Chapter 8, along with values taken from Frontera [27]. The values plotted here are taken from spectra measured 10 hours after the burst trigger.

GRBs in the sample tend to manifest systematically higher column densities and photon indices than XRFs or XRRs.

9.2.3 Photon Index and Temporal Index

Figure 9.12 shows the distribution of best-fit temporal decay indices β and photon indices I for the sample of bursts described in Chapter 8. Also shown are values gathered and cited by Frontera [27]. The values plotted are those measured 10 hours after the burst. We have already seen that the photon indices from the two samples are consistent. The probability that the two distributions of decay indices are drawn from the same parent distribution is 0.31. Thus, the decay indices of the two samples are also consistent. We note that the GRBs in our sample tend to have higher (that is, steeper) temporal indices than XRRs, which in turn have higher indices than XRFs.

Figure 9.13 shows the temporal decay indices β and photon indices I for the Swift bursts

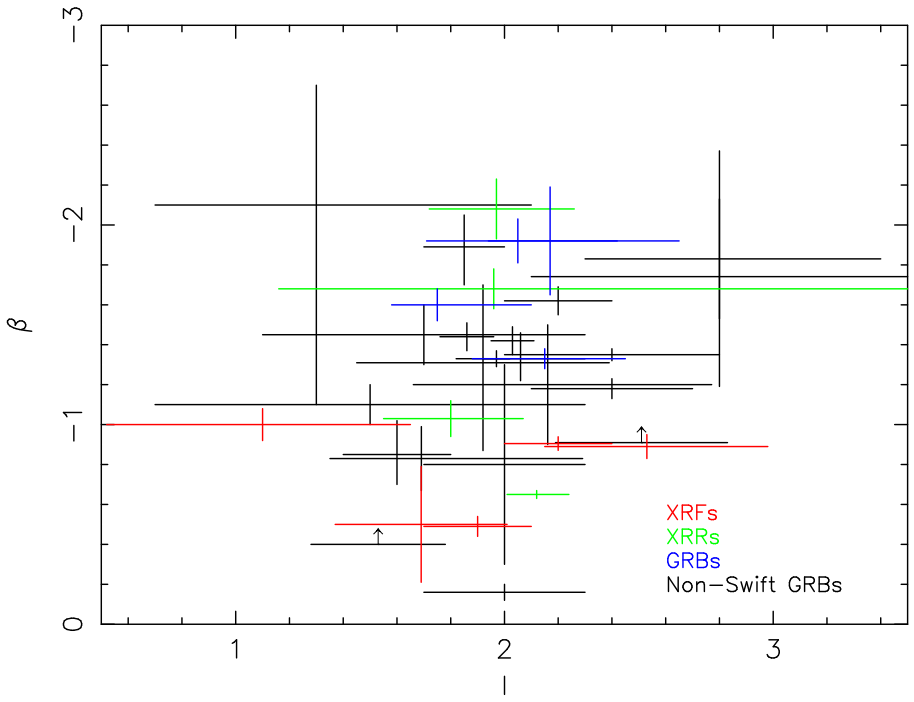

Figure 9.12: A plot of the best-fit temporal decay indices β and photon indices I of afterglows described in Chapter 8, along with values taken from Frontera [27]. The values plotted here are taken from spectra measured 10 hours after the burst trigger.

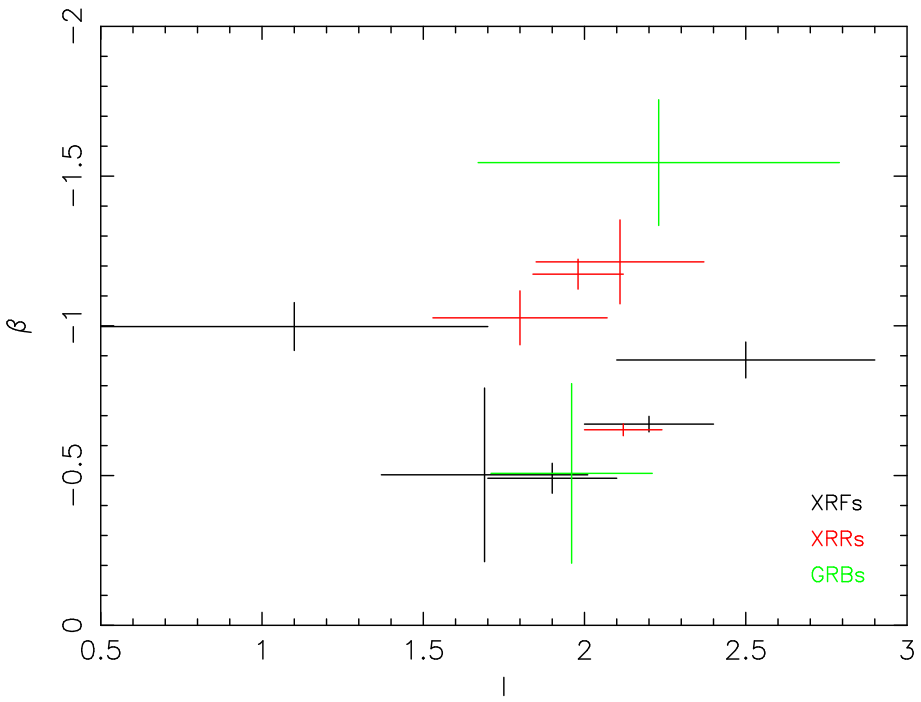

Figure 9.13: A plot of the best-fit temporal decay indices β and photon indices I of afterglows described in Chapter 8, as measured 8000 seconds after the burst trigger. Two of the four GRB afterglows in our sample were not observed until a later time, so they are not included.

8000 seconds (2.2 hours) after the burst. We note that at 8000 s, as at 10 hours, the XRF afterglows tend to have smaller decay indices than XRRs and GRBs.

9.2.4 2 – 10 keV Flux

Figure 9.14 shows the distribution of 2 – 10 keV x-ray afterglow flux values measured 10^5 seconds (a little over a day) after the burst for GRBs, XRRs, and XRFs. Also shown are values from BeppoSAX presented by Frontera [27]. The K-S test gives a probability of 0.30 that the Swift values and the BeppoSAX values are drawn from the same distribution. There is a hint that the XRFs in our sample may tend to have slightly lower fluxes than the GRBs and XRRs.

9.2.5 2 – 10 keV Isotropic Luminosity

Figure 9.15 shows the distribution of 2 – 10 keV isotropic-equivalent luminosity $L_{\rm iso}$ at a time 10 hours after the burst trigger for GRBs, XRRs, and XRFs. Also shown are values calculated

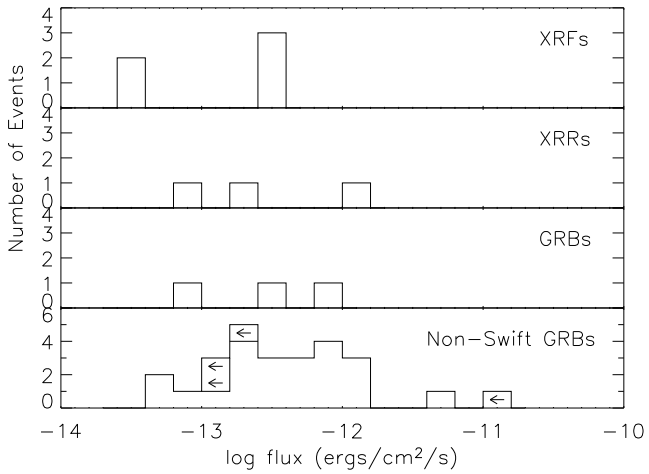

Figure 9.14: The distribution of 2 – 10 keV flux values from Swift GRB, XRR, and XRF afterglows measured 10^5 seconds after the burst, along with corresponding values from BeppoSAX bursts [27]. In two cases (namely, XRR 050219B and GRB 041223), the XRT observations did not extend out to 10^5 seconds, so those bursts were excluded from the plot.

and presented by Berger and Kulkarni [10]. Using the K-S test to compare values from Berger's paper with the those from our sample we obtain a probability of 0.058 that the two are consistent. Thus, the two distributions differ significantly. There is a very definite trend evident in this plot, with XRFs tending to have distinctly lower $L_{\rm iso}$ values than XRRs, which in turn have lower values than GRBs.

Figure 9.16 shows a similar distribution to that of Figure 9.15. In this case, the luminosity is calculated for a time of 5 hours $\times\,(z+1)$ after the trigger for each burst. These luminosities are therefore all measured at the same time in the source frame—namely, 5 hours. This may be a more valid comparison of isotropic luminosities. The distinct trend of lower luminosities for XRFs and higher luminosities for GRBs seen in Figure 9.15 is less prominent here, but it is still somewhat evident.

9.2.6 Jet Breaks and Opening Angles

In Section 2.5.3, we described a type of light curve break that is caused when the relativistic outflow of the burst slows down enough that the edge of the jet becomes visible. Although distinguishing between these so-called "jet breaks" and other breaks that result from spectral evolution

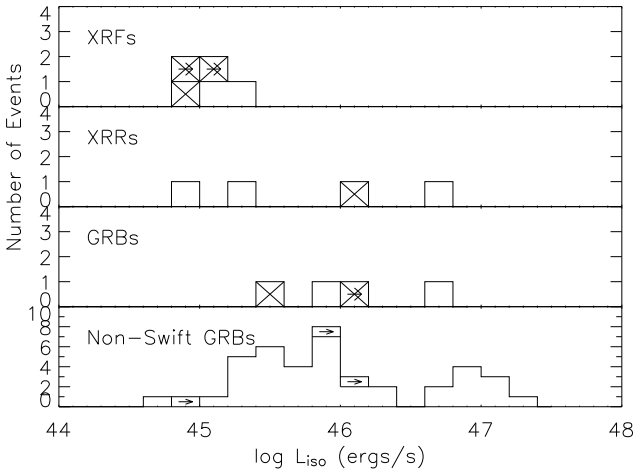

Figure 9.15: The distribution of 2 – 10 keV isotropic luminosities $L_{\rm iso}$ from Swift GRB, XRR, and XRF afterglows at a time of 10 hours after the burst, along with corresponding values from bursts cited by Berger and Kulkarni [10]. In some cases, redshifts were not measured for the burst. In these instances, the Yonetoku relation was used to derive an approximate redshift. Such values are designated in the plot with a cross through the box. In some cases, only a lower limit for the redshift could be obtained, in which cases an arrow is placed in the corresponding box.

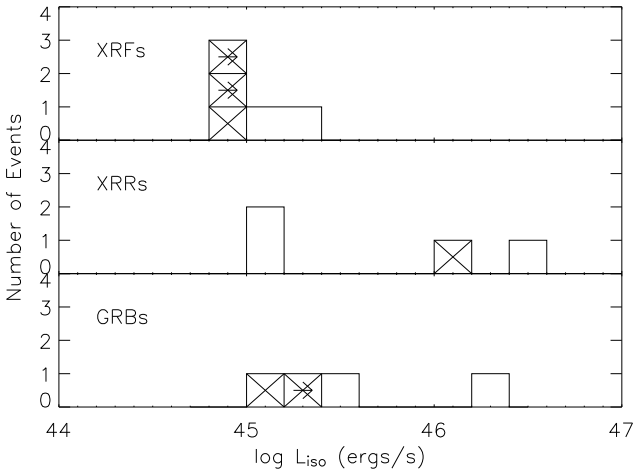

Figure 9.16: The distribution of 2 – 10 keV isotropic luminosities $L_{\rm iso}$ from Swift GRB, XRR, and XRF afterglows at a time of 5 hours $\times$ $(z + 1)$ after the burst. In some cases, redshifts were not measured for the burst. In these instances, the Yonetoku relation was used to derive an approximate redshift. Such values are designated in the plot with a cross through the box. Also, in some cases, only a lower limit could be obtained, in which cases an arrow is placed in the corresponding box.

Table 9.3: Constraints on jet break times and opening angles for the XRFs in our sample. In finding the opening angles, we have followed the example of Ghirlanda et al. [34] and assumed $n = 1$ cm^{-3} and η_γ is 0.2. *We note that for those bursts in italics, the redshifts used are the inferred redshifts, based on the Yonetoku relation, as described in Section 7.3.* Jet breaks seen in past afterglows typically occur at or after about 1 day (10^5 s), and the decay index typically changes from about -1 to about -2 at the break.

Burst	z	Jet Break	Opening angle $\Delta\Theta$	Comments
050416A	0.6536	$> 3.73 \times 10^6$ s	$> 40.6°$	
050406	> 3	$> 2.81 \times 10^5$ s	$> 8.7°$	later data shows signs of a break, but the error bar is too large to be sure
050714B	> 1.8	$> 4.3 \times 10^5$ s	$> 10.0°$	
050824	0.83	3×10^5 s	$13.6°$	if this break is a jet break—the decay index after the break (-1.1) is shallower than is typically observed after a jet break, which argues against this being the jet break
		$> 1.22 \times 10^6$ s	$> 23.1°$	otherwise
050215B	0.8	$> 3.92 \times 10^5$ s	$> 16.7°$	

is difficult without multi-wavelength measurements, we can place some constraints on the jet break times of the bursts in our sample. We can also calculate the corresponding jet opening angle using Equation 2.6, if we assume that the bursts are viewed from within the jet. Tables 9.3, 9.4, and 9.5 list the constraints we have on the jet break times and corresponding jet angles.

9.3 Prompt Emission and Afterglow Emission

9.3.1 Ratio of Prompt Emission Fluence and Afterglow Emission Fluence

The ratio of energy emitted during the afterglow to energy emitted during the prompt emission is of interest with reference to many burst models. It has typically been presumed that the energy of the afterglow is orders of magnitude smaller than the energy of the burst. Swift's early afterglow observations enable us to test whether this is the case. Table 9.6 gives the ratio of afterglow fluence from 0.6 – 10 keV photons for the interval over which XRT measurements were made to prompt emission fluence from photons of all energies. Because we are only able to include photons in a limited energy band and because the measurements cover a finite time interval, the ratios we obtain are only lower limits—the actual ratio could be much higher. Prompt emission

Table 9.4: Constraints on jet break times and opening angles for the XRRs in our sample. For more details, See the description in Table 9.3.

Burst	z	Jet Break	Opening angle $\Delta\Theta$	Comments
050315	1.949	1.25×10^5 s	5.0°	if this is a jet break—the decay index after the break (-1.3) is shallower than is typically observed after a jet break, which argues against this being the jet break
		$> 8.92 \times 10^5$ s	$> 10.5°$	otherwise
050318	1.44	17700 s	3.2°	if this is a jet break—the decay index changes from -1.2 to -2.1 at the break, which is consistent with most jet breaks, but it occurs at an earlier time than is typical
		$> 4.47 \times 10^5$ s	$> 10.8°$	otherwise
050525A	0.606	14700 s	3.3°	if this is the jet break—the decay index changes from -1.2 to -1.7 at the break, which is a smaller change than occurs in most jet breaks, and the break occurs much earlier than is typical, both of which argue against this being the jet break
		> 97800 s	$> 6.7°$	otherwise
050219B	1.0	< 10500 s	$< 2.3°$	if the jet break is earlier than the observation—the decay index is -1.0, so this is not likely
		> 52600 s	$> 4.2°$	if the jet break is later than the observation

Table 9.5: Constraints on jet break times and opening angles for the GRBs in our sample. For more details, See the description in Table 9.3.

Burst	z	Jet Break	Opening angle $\Delta\Theta$	Comments
050401	2.9	9200 s	1.4°	if this is the jet break—the decay after the break is -1.3, which is shallower than typical, and the break occurs much earlier than is typical, both of which argue against this being the jet break
		$> 7.89 \times 10^5$ s	$> 7.4°$	otherwise
050603	2.821	< 37400 s	$< 2.3°$	if the jet break is earlier than the observation—the break would be earlier than is typical for jet breaks, so this is not likely. The decay index is -1.6, which doesn't tell us much.
		$> 1.01 \times 10^6$ s	$> 7.9°$	otherwise
050326	2.4	14000 s	1.7°	if this is the jet break—the decay index changes from -1.5 to -1.9 at the break, which is a smaller change than occurs in most jet breaks, and the break occurs much earlier than is typical, both of which argue against this being the jet break
		$> 5.08 \times 10^5$ s	$> 6.6°$	otherwise
041223	4	< 16800 s	$< 1.3°$	if the jet break is earlier than the observation—the decay index is -1.9, which argues for this, but it would mean a jet break that is earlier than is typical
		> 28200 s	$> 1.6°$	if the jet break is later than the observation

Table 9.6: Ratio of 0.6 – 10 keV afterglow fluence to prompt emission fluence. The beginning and end of the time interval over which the fluence was calculated are given in seconds after the BAT trigger. Since only a limited energy range and time interval is available, the ratios presented here are lower limits—the actual afterglow-to-prompt-emission fluence ratio may be much larger

Burst	Start of Interval (s)	End of Interval (s)	Ratio lower limit
XRF 050416A	90	3.73×10^6	0.445
XRF 050406	107	1.4×10^6	0.479
XRF 050715B	158	9.42×10^5	0.0336
XRF 050824	6092	1.23×10^6	0.349
XRF 050215B	5796	5.74×10^5	0.200
XRR 050315	87	8.92×10^5	0.0659
XRR 050318	3367	4.47×10^5	0.100
XRR 050525A	6011	3.10×10^5	0.0115
XRR 050219A	10479	1.18×10^6	0.0417
GRB 050401	147	7.89×10^5	0.0481
GRB 050326	3323	1.61×10^5	0.00882
GRB 050603	37430	1.01×10^6	0.00432
GRB 041223	16770	28223	0.000241

fluence covering all photon energies is calculated using the best fit Band parameters and assuming the lower and upper spectral indices continue without breaks beyond the measured energy range.

It is interesting to note that in the cases of the five bursts for which very early observations were possible, two of them (XRF 050416A and XRF 050406) had very high afterglow-to-prompt-emission ratios ($\approx 50\%$), while the other three (XRF 050715B, XRR 050315, and GRB 050401) had considerably lower ratios (3% – 7%). It appears that some physical process must be at work that sometimes enhances the energy of the afterglow relative to the prompt emission and at other times suppresses it.

9.3.2 Prompt Emission $E_{\rm iso}$ and Afterglow Emission $L_{\rm iso}$

We observed in the last section that XRFs tend to have lower isotropic luminosities than XRRs and GRBs. Since this is also true of the prompt emission's isotropic energy, we examine here whether a correlation exists between $E_{\rm iso}$ and $L_{\rm iso}$. Figure 9.17 shows a scatter plot of the isotropic energy of the prompt emission $E_{\rm iso}$ and the isotropic luminosity $L_{\rm iso}$ 10 hours after the

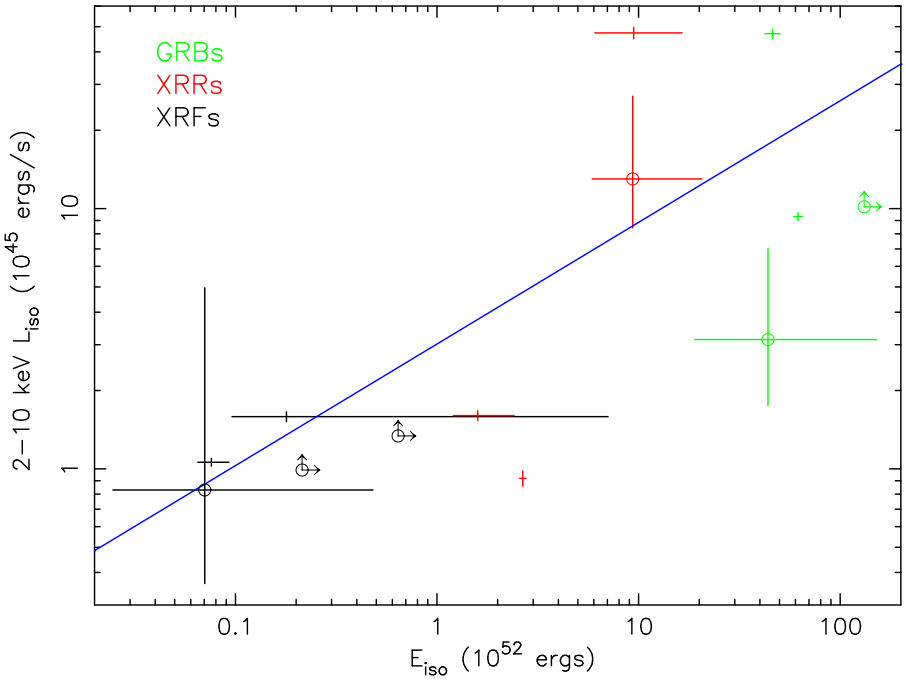

Figure 9.17: A scatter plot showing the correlation of the isotropic energy of the prompt emission $E_{\rm iso}$ and the isotropic luminosity of the afterglow emission 10 hours after the burst trigger. Bursts for which approximate redshifts were derived using the Yonetoku relation are marked with circles. A definite correlation is evident in the plot. The solid line is the best linear fit to the distribution and is given by $E_{\rm iso}/(10^{52}\ {\rm ergs}) = (3.019 \pm 0.017) \times [L_{\rm iso}/(10^{45}\ {\rm ergs/s})]^p$, where $p = 0.4672 \pm 0.0061$.

trigger for the 13 bursts described in Chapter 8 for which afterglow measurements were made. A correlation is evident, with a linear correlation coefficient between $\log(E_{\rm iso})$ and $\log(L_{\rm iso})$ of 0.722. The probability of such a correlation occurring by chance for this sample size (10 bursts) is 3.3%. If we exclude the three bursts for which an estimated redshift was used, the correlation coefficient becomes 0.756, with a 6.5% probability of a chance occurrence.

Figure 9.18 shows a similar scatter plot, but this time $E_{\rm iso}$ is plotted against the isotropic luminosity $L_{\rm iso}$ at 5 hours $\times\ (z+1)$ after the burst. The correlation is much weaker with a linear correlation coefficient between $\log(E_{\rm iso})$ and $\log(L_{\rm iso})$ of 0.533. The probability of such a correlation occurring by chance for this sample size (10 bursts) is 20.4%—relatively high. If we exclude the three bursts for which an estimated redshift was used, the correlation actually improves slightly, with a coefficient of 0.627 and a probability of chance coincidence of 17.5%.

As we noted in section 2.5.3, $E_{\rm iso}$ (and $L_{\rm iso}$) are functions of the jet angle, with the actual

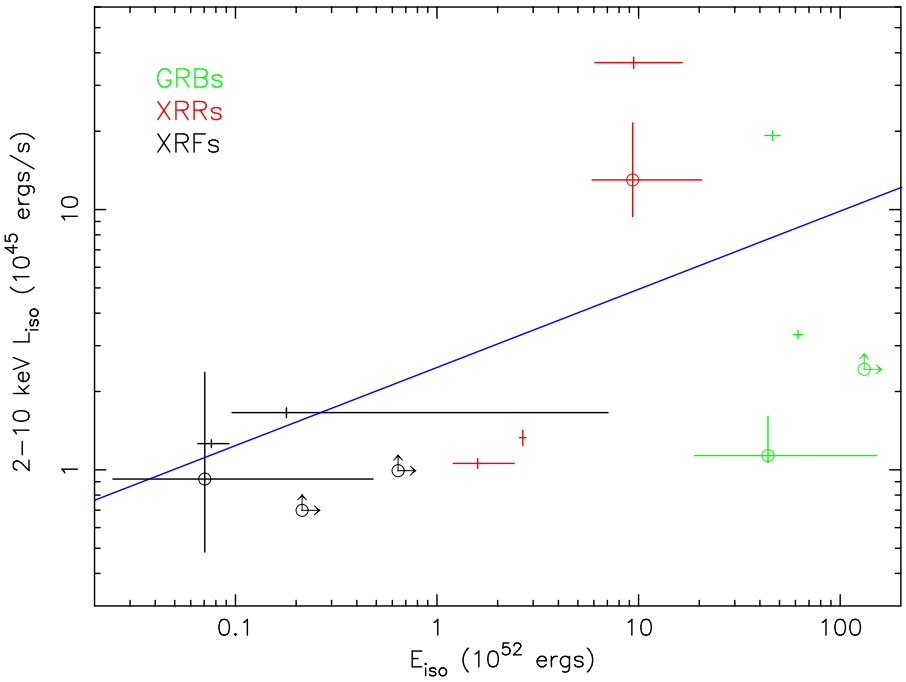

Figure 9.18: A scatter plot showing the correlation of the isotropic energy of the prompt emission $E_{\rm iso}$ and the isotropic luminosity of the afterglow emission 5 hours after the burst trigger in the source frame (5 hours $\times\,(z+1)$ in the observer frame). Bursts for which approximate redshifts were derived using the Yonetoku relation are marked with circles. A weaker correlation is evident in this plot than is seen in Figure 9.17. The solid line is the best linear fit to the distribution and is given by $E_{\rm iso}/(10^{52}\ {\rm ergs}) = (2.473 \pm 0.017) \times [L_{\rm iso}/(10^{45}\ {\rm ergs/s})]^p$, where $p = 0.2993 \pm 0.0061$.

energy and luminosity given by

$$E_\gamma = (1 - \cos(\theta))E_{\rm iso} \tag{9.1}$$

$$L_x = (1 - \cos(\theta))L_{\rm iso}. \tag{9.2}$$

Nardini et al. [59] noted a correlation similar to that shown in Figure 9.17 by studying a set of bursts detected by other missions. He found that when $E_{\rm iso}$ and $L_{\rm iso}$ were corrected for jet angle, the correlation disappeared. This indicates that the correlation is due entirely to the dependence of the two quantities on jet angle.

Chapter 10

Discussion

10.1 The Continuity of XRFs, XRRs, and GRBs

The results of the analysis described in the last chapter strengthen the case that x-ray flashes and long-duration gamma-ray bursts are not separate and distinct phenomena, but instead are simply ranges along a single continuum describing some sort of broader phenomenon. As Figure 9.2 illustrates, XRFs, XRRs and GRBs form a continuum in peak energies $E_{\rm peak}^{\rm obs}$, with XRF $E_{\rm peak}^{\rm obs}$ values tending to be lower than those of XRRs, which in turn are lower than those of GRBs. We have also seen that this same spread is evident in the peak energy in the frame of the burst progenitor $E_{\rm peak}^{\rm src}$ and that XRFs, XRRs, and GRBs all obey the same $E_{\rm peak}^{\rm src} - E_{\rm iso}$ correlation (see Figure 9.6). Further evidence of the continuous nature of these phenomena comes from the continuity in the fluences of XRFs, XRRs, and GRBs, with XRFs tending to manifest lower fluences than XRRs, which tend to have lower fluences than GRBs. This is illustrated by the correlation between fluences and $E_{\rm peak}^{\rm obs}$ shown in Figure 9.5. Sakamoto et al. noted a similar trend in XRFs and GRBs detected by HETE-2 [70].

10.2 Differences and similarities between the afterglows of XRFs and GRBs

As we examined the x-ray afterglow properties of XRFs, XRRs and GRBs in the last chapter, we noted that their spectral indices showed no strong correlation to indicate that the spectra of XRF afterglows are distinctly different from those of XRRs or GRBs. We did, however, note a definite distinction in the shape of the afterglow light curves. Table 10.1 gives a summary of the break times and decay indices of the light curves we have analyzed.

We found that the gamma-ray bursts in our sample tend to have afterglows with shallow decay indices (ranging in our sample from -0.5 to -1.6) at early times followed by steeper indices

Table 10.1: The decay indices and break times of the x-ray afterglows described in Chapter 8, as well as the times of the earliest and latest observations by the XRT. Values for the 5 XRFs in our sample are included first, followed by those of the XRRs in our sample. Lastly, we list the values for the 4 GRBs in our sample.

	Earliest Observation	1st Decay Index	1st Break	2nd Decay Index
050416A	90 s	-0.672 ± 0.026	8400 ± 3500 s	-0.905 ± 0.034
050406	107 s	-2.01 ± 0.22	3900 ± 2800 s	-0.50 ± 0.29
050714B	158 s	-6.6064 ± 0.0056	225 ± 11 s	-0.886 ± 0.060
050824	6092 s	-0.491 ± 0.046	$(3.1 \pm 1.6) \times 10^5$ s	-1.11 ± 0.32
050215B	5796 s	-0.998 ± 0.084	-	-
050315	84 s	-3.210 ± 0.039	(758 – 5064 s)	-0.653 ± 0.024
050318	3281 s	-1.172 ± 0.048	$(1.77 \pm 0.22) \times 10^4$ s	-2.08 ± 0.15
050525A	5858 s	-1.21 ± 0.14	$(1.47 \pm 0.50) \times 10^4$ s	-1.678 ± 0.096
050219B	5394 s	-1.027 ± 0.092	-	-
050401	132 s	-0.507 ± 0.030	$(9.1 \pm 1.0) \times 10^3$ s	-1.336 ± 0.050
050326	3276 s	-1.55 ± 0.21	$(1.41 \pm 0.99) \times 10^4$ s	-1.92 ± 0.11
050603	34048 s	-1.599 ± 0.082	-	-
041223	16665 s	-1.93 ± 0.28	-	-

	2nd Break	3rd Decay Index	Latest Observation
050416A	-	-	3.73×10^6 s
050406	-	-	1.4×10^6 s
050714B	-	-	9.42×10^5 s
050824	-	-	1.23×10^6 s
050215B	-	-	5.74×10^5 s
050315	$1.25 \pm 0.13 \times 10^5$ s	-1.309 ± 0.067	8.98×10^5 s
050318	-	-	8.32×10^5 s
050525A	-	-	4.52×10^5 s
050219B	-	-	2.30×10^6 s
050401	-	-	1.01×10^6 s
050326	-	-	5.31×10^5 s
050603	-	-	1.79×10^6 s
041223	-	-	28582 s

(ranging in our sample from -1.3 to -1.9) at later times, and that the breaks between these two indices occur at about 10^4 seconds (see Figure 10.1). This pattern is evident in the composite light curve plot in Figure 9.10. For example, the afterglow of GRB 050401 had a decay index of -0.5 until about 9000 s after the burst, after which its decay index changed to about -1.3, which continued until it faded below the XRT's detection threshold. The GRB 050326 x-ray afterglow had an early index of -1.5, which steepened to -1.9 about 14 ks after the burst. The other two GRBs in our sample (GRB 050603 and GRB 041223) likewise showed steep decay indices at late times. No breaks were observed for 050603 or 041223, but observations began rather late, so it is very plausible that the early shallow decay index was missed.

X-ray flash afterglows, on the other hand, seem to follow a different pattern. They often have a very steep index early on, followed by a fairly early break, after which the index becomes much more shallow for the duration of the observation (see Figure 10.1). For two of the bursts in our sample (XRF 050824 and XRF 050215B), the early steep index was not observed, but in both cases, the observation began relatively late, so the early steep indices may have been missed. In one case (XRF 050824), the late shallow index is followed by a later steeper decay index, as was observed in the GRBs in our sample. However, the break preceding this steeper index occurred much later than the breaks observed in the GRB sample— 3.1×10^5 s after the burst. It is possible that such late breaks occurred in the other XRFs in our sample as well, but that the light curve had faded below the sensitivity threshold of the XRT by that time. The XRF 050416A afterglow light curve is the notable exception to this pattern. No steep index was observed at an early time, the break between shallow index and steep index was very early (at 8500 s), and the later index was relatively shallow (-0.9).

The afterglows of the X-ray-rich gamma-ray bursts (XRRs) in our sample were split between these two behaviors, with some manifesting a pattern like the XRF sample and others a pattern like the GRB sample. The afterglow of XRR 050315 looks like an x-ray flash afterglow, with a steep decay of index -3.2 followed by a shallow index of -0.6, followed by a steep index of -1.3. The break between the latter two indices occurred at 1.2×10^5 s, much later than the breaks in the

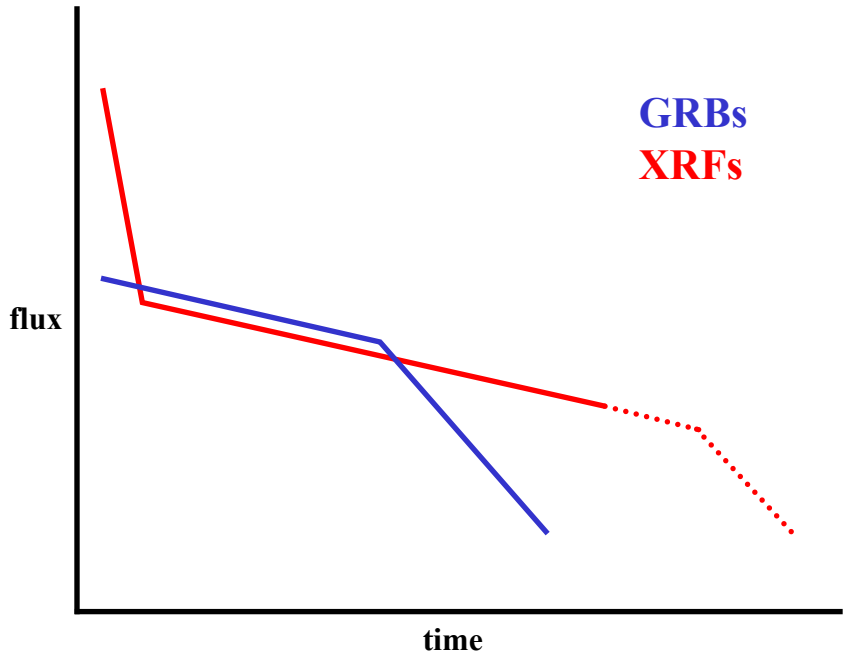

Figure 10.1: The pattern of XRF and GRB afterglow light curves. GRB afterglow light curves tend to have a shallow index followed by a steep index, with a break between the two occurring at about 10^4 to 2×10^4 seconds after the burst. XRF afterglows, on the other hand, tend to have a very steep early index followed by a shallower index. The shallow index, in the case of one burst in our sample, is followed by another steeper index at a very late time (3×10^5 seconds). It may be that this steepening is present in all XRF afterglows at late times, but that the afterglows in our sample had become too dim by that point to allow us to detect the steepening.

GRB sample. The XRR 050219B afterglow was a single power law with an index of -1.0 extending from the beginning of the observation at 5394 s to the end of the observation at 2.3×10^6 s. This appears to fit the pattern of the XRF afterglows, with the observation beginning after the early steep index. The other two bursts in our sample (XRR 050318 and XRR 050525A) have afterglows resembling those of GRBs, with an early shallow index (-1.2 in both cases) followed by a steeper index (-2.1 and -1.7 respectively). The breaks occur at 1.8×10^4 s and 1.5×10^4 s, respectively.

It is possible that these two patterns form a continuum, with the break between shallow index and steep index occurring at later times for XRFs (sometimes after the afterglow has faded

below our detection threshold) and at earlier times for GRBs. The very early steep index observed in two of the XRFs and one of the XRRs in our sample may be a special phenomenon that is unique to some bursts and which may be preferential to x-ray flashes.

Another distinction we observe is that XRF afterglows have systematically lower fluxes than GRB afterglows, particularly from about 100 seconds to about 3×10^4 seconds after the burst. This can be seen in the composite plot of the GRB, XRR, and XRF afterglow light curves in Figure 9.7. The plot of 2 – 10 keV flux at 10^5 seconds after the burst shown in Figure 9.14 also shows a slightly systematic tendency toward lower fluxes for XRFs.

10.3 Implications for the off-jet model

In Section 4.4.1, we described a model that suggests that x-ray flashes are intrinsically the same as gamma-ray bursts, except that they are viewed from outside the relativistic outflow jet (see Figure 4.4). This model predicts an afterglow light curve that rises until it reaches a peak before diminishing again. Swift is the first mission capable of observing afterglows quickly enough to fully test this prediction. The XRF afterglows described in Chapter 8 show a diminishing light curve throughout the observation, which in some cases began as early as 90 seconds after the burst and in all cases began by 6100 seconds after the burst. This means that if a peak occurred, it must have appeared before the beginning of the observation.

Equation 4.21 gives a relationship between the peak in the light curve t_p, the time $t_{j,0}$ of the jet break that would have been observed if the afterglow were viewed from within the jet, the viewing angle θ_v, and the half-opening angle of the jet $\Delta\theta$:

$$t_p = \left[5 + 2\ln\left(\frac{\theta_v}{\Delta\theta} - 1\right)\right]\left(\frac{\theta_v}{\Delta\theta} - 1\right)^2 t_{j,0}. \tag{10.1}$$

This equation is valid when $\theta_v \gtrsim 2\Delta\theta$. If we divide both sides of Equation 10.1 by $t_{j,0}$, it takes the form:

$$\frac{t_p}{t_{j,0}} = \left[5 + 2\ln\left(\frac{\theta_v}{\Delta\theta} - 1\right)\right]\left(\frac{\theta_v}{\Delta\theta} - 1\right)^2. \tag{10.2}$$

The GRB and XRF afterglow observations described in Chapter 8 allow us to place constraints on

the quantities in this equation. We note that breaks were observed in two of the GRB afterglows in our sample: at 9000 seconds in the case of GRB 050401 and at 14000 seconds in the case of GRB 050326. These may be jet breaks resulting from the relativistic outflow slowing to a point that the edge of the jet becomes observable, or they may be breaks due to spectral evolution as the afterglow progresses. If they are not jet breaks, then the jet breaks must occur at some time later, after the light curve faded below the XRT sensitivity threshold. In either case, we have an upper limit on typical GRB jet breaks: $t_j > 9000$ seconds. Jet breaks noted by others (for instance, Frail et al. [26]) are typically on the order of a day (10^5 s) or later after the burst. We also have a lower limit on t_p from our XRF afterglow observations. In all cases, observations began earlier than 6100 seconds after the burst, so we may say that $t_p < 6100$ seconds for all of the XRFs in our sample (in some cases, much less). Consequently, the quantity $t_p/t_{j,0}$ in Equation 10.2 must be less than $6100/9000 = 0.68$. Now,

$$\left[5 + 2\ln\left(\frac{\theta_v}{\Delta\theta} - 1\right)\right]\left(\frac{\theta_v}{\Delta\theta} - 1\right)^2 \geq 5 \tag{10.3}$$

for all possible choices of $\theta_v \gtrsim 2\Delta\theta$. Thus, based on the x-ray flash afterglow observations presented here, Equation 10.1 cannot be satisfied.

There are indications that Equation 10.1 may not be valid in cases of moderately low Lorentz factors ($\Gamma \lesssim 100$) and relative viewing angles ($\theta_v - \Delta\theta \lesssim 0.1$ rad (6°)). Yamazaki et al. [82] investigated a situation in which $\Gamma = 100$ and $\theta_v - \Delta\theta = 0.05$ rad and noted that the off-jet model predicts a peak **before** the jet break time—at around 40000 seconds—in the UV photon energy range (see Figure 10.2). The position of the peak in the light curve should be independent of photon energy, so we would expect the same peak position at x-ray energies. We note that these conditions (moderately low Γ and low $\theta_v - \Delta\theta$) may hold for at least some of the x-ray flashes we observed. Equation 4.19 gives us a constraint on Γ and $\theta_v - \Delta\theta$:

$$E^{\rm src}_{\rm peak} \approx \frac{E^{\rm src}_{\rm peak,in\ jet}}{1 + \Gamma^2(\theta_v - \Delta\theta)^2}. \tag{10.4}$$

In the case of XRF 050416A for which $E^{\rm src}_{\rm peak} = 27.6$ keV, if we assume $E^{\rm src}_{\rm peak,in\ jet} = 300$ keV and $\Gamma = 100$, then $\theta_v - \Delta\theta = 0.03$ rad (1.8°), in which case we might expect a peak for XRF 050416A

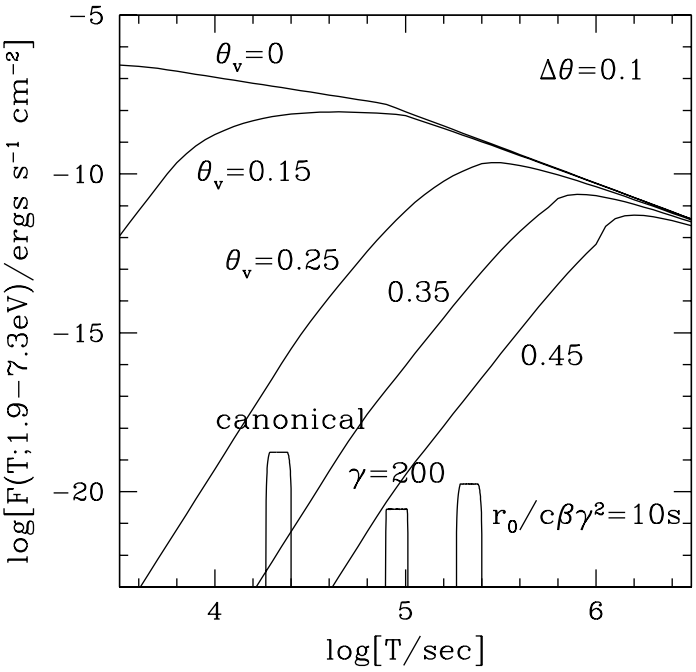

Figure 10.2: The light curves of an x-ray flash afterglow in the UV band are shown at various viewing angles, as predicted by the off-jet model. For these plots, the parameters are fixed as $\Delta\theta = 0.1$ rad, $\Gamma = 100$, $n = 1$ cm$^{-}3$, $p = 2.25$, $E = 2 \times 10^{54}$ ergs, $\epsilon_e = 0.1$, $\epsilon_B = 0.01$, and $D = 1$ Gpc [82].

at a relatively early time—perhaps at around 10^4 seconds. Such a peak is not observed in any of our measurements.

Another indication of the prominence of the early afterglow emission is the afterglow-to-prompt-emission fluence ratios given in Table 9.6. These ratios are at least on the order of 50% in some instances. This is hard to account for in the off-jet model. This, along with the lack of observation of a peak in the afterglow, suggests that the off-jet model may need to be re-examined or re-evaluated.

10.4 Conclusion

We have seen that the XRFs observed by Swift form a continuum with the GRBs observed by Swift and by other missions, having systematically lower fluences and lower $E^{\rm obs}_{\rm peak}$ and $E^{\rm src}_{\rm peak}$

values than GRBs. The bursts observed by Swift also confirm the $E_{\rm iso}$ – $E^{\rm src}_{\rm peak}$ correlation first noted by Amati et al. [1]

We have also noted that the light curves of x-ray flashes follow a different "template" than those of gamma-ray bursts, with a steep decay index early in the afterglow, followed by a shallow index that extends to very late times. Gamma-ray burst afterglows, on the other hand, do not show this early steep decay and show a break to steeper indices at much earlier times than do XRF afterglows. XRF afterglows also have significantly lower fluxes than GRB afterglows.

Perhaps the most significant finding in these studies is the lack any observed peak in the afterglow light curves of x-ray flashes. This contradicts predictions made by the off-jet and structured jet models of x-ray flashes, indicating that the differences between gamma-ray bursts and x-ray flashes may be the result of intrinsic properties rather than solely the result of viewing geometry. The sample of x-ray flashes observed to date is still very small, and as Swift continues its mission, this data set will grow, enabling us to confirm and study these aspects more fully.

Appendix A

Mask-Weighted Count Rates

This appendix describes a procedure that is somewhat analogous to the one used to find bright sources in the sky. It is a technique called "mask-weighting" that enables us to find the count rate resulting from photons from a given source, with counts from all other sources removed.

Consider a stream of monochromatic photons incident on the array. Imagine that there are S of these photons passing through each cm^2 of area each second. Whenever a stream of gamma-ray photons passes through some material, some of them are absorbed or scattered in other directions. Typically, the less energy the photon has, the bigger the chance it will be absorbed or scattered. This means that of these S photons/cm^2/s, a certain fraction f_{trans} will be transmitted through the structure that holds the lead tiles in place, the grid of wire that maintains the high voltage in the detectors, and the epoxy holding the grid to the detectors. The number of photons/cm^2/s arriving at a detector that is fully illuminated through the mask is then

$$S \cdot f_{trans}. \tag{A.1}$$

Now, suppose a lead tile is partially obstructing the source, so that a fraction f_{illum} of the detector is illuminated and a fraction $1 - f_{illum}$ is obstructed by the lead tile. The number of photons/cm^2/s arriving at the detector is then

$$S \cdot f_{trans} \cdot \{f_{illum} + [1 - f_{illum}] \cdot f_{Pb}\}, \tag{A.2}$$

where f_{Pb} is the fraction of photons transmitted through lead ($f_{Pb} = 0$ for low energy photons and $f_{Pb} \to 1$ for high energy photons.

We will not introduce a new quantity called the "mask-weighting factor", w, defined as

$$w \equiv \frac{2f_{illum} - C}{K}, \tag{A.3}$$

where C is chosen so that w satisfies the equation:

$$\begin{aligned} \sum_{detectors} w &= \sum_{detectors} \left(\frac{2 f_{illum} - C}{K} \right) \\ \Rightarrow 2 \sum_{detectors} &-C \cdot N_{detectors} = 0 \\ \Rightarrow C &= \frac{2}{N_{detectors}} \sum_{detectors} f_{illum} \end{aligned} \tag{A.4}$$

It turns out that for a situation like ours, in which equal numbers of detectors are masked and illuminated, $C \approx 1$. K is a normalization factor that may be chosen in a number of different ways, depending on how we desire the end result to be normalized. For now, we'll hold off on choosing what value to give it. Note that, if K were chosen to be 1, w would equal $2\, f_{illum} - 1$, so that detectors that are fully-illuminated would receive a mask weight of +1 and detectors that are fully-masked would receive a mask weight of -1. All other detectors would receive a mask weight somewhere between -1 and +1, depending on the degree of illumination through the mask (see Figure 5.3).

Substituting equation A.3 into equation A.2 gives

$$S \cdot f_{trans} \cdot \left\{ \frac{Kw + C}{2} + \left[1 - \frac{Kw + C}{2} \right] \cdot f_{Pb} \right\}. \tag{A.5}$$

It is common practice to define the "effective area" of a detector as the ratio of the detected counts/s to the number of incident photons/cm^2/s. This ratio has units of area (commonly cm^2), and another way to think of it is that it is the area of the detector multiplied by the "quantum efficiency" of the detector (or the probability that a photon will be detected by the detector) for that particular incident photon direction. Now, photons with more energy have a greater chance of passing through the detector undetected Likewise, a flux of photons coming at the detector "straight on" will "see" a larger cross-sectional area of the detector than a flux of photons coming in at an angle. For these reasons, the effective area is a function of energy and also of angle. In the case we are considering, then, the counts/s that the detector would record would be equal to the flux of photons incident on it multiplied by its effective area:

$$S \cdot f_{trans} \cdot \left\{ \frac{Kw + C}{2} + \left[1 - \frac{Kw + C}{2} \right] \cdot f_{Pb} \right\} \cdot A_{eff} \tag{A.6}$$

(where A_{eff} is the effective area of the detector). Now, in addition to those photons that happen to be coming from the source we are interested in, the detector is also recording "background" counts. These are counts that result from photons from other sources, from photons scattered into the detector from the shield or other nearby material or that simply manage to pass through the shield, and from stray cosmic protons, electrons, or other particles that deposit energy in the detectors. We will call the count rate from these sources B. Adding this to the total count rate measured by the detector, we obtain

$$R_d = S \cdot f_{trans} \cdot \left\{ \frac{Kw + C}{2} + \left[1 - \frac{Kw + C}{2} \right] \cdot f_{Pb} \right\} \cdot A_{eff} + B. \tag{A.7}$$

Now, to generate a "mask-weighted" count rate for the entire array, we add the count rates of all the individual detectors together, weighted by their mask-weighting factors:

$$\begin{aligned} R &= \sum_{detectors} R_d \cdot w_d \\ &= \sum_{detectors} \left[S \cdot f_{trans} \cdot \left\{ \frac{Kw_d + C}{2} + \left[1 - \frac{Kw_d + C}{2} \right] \cdot f_{Pb} \right\} \cdot A_{eff,d} + B_d \right] \cdot w_d, \end{aligned} \tag{A.8}$$

where the subscript d indicates that the variable applies to a particular detector.

If we assume that both A_{eff} and B are the same for every detector, then this equation

simplifies quite nicely:

$$
\begin{aligned}
R \approx\ & S \cdot f_{trans} \cdot A_{eff} \cdot \frac{1}{2} \sum_{detectors} \left(K w_d^2 + C w_d + 2 f_{Pb} w_d - f_{Pb} K w_d^2 - C f_{Pb} w_d \right) \\
& + B \cdot \sum_{detectors} w_d \\
=\ & S \cdot f_{trans} \cdot A_{eff} \cdot \frac{1}{2} K \left(\sum_{detectors} w_d^2 \right) \\
& + S \cdot f_{trans} \cdot A_{eff} \cdot \frac{1}{2} C \left(\sum_{detectors} w_d \right) \\
& + S \cdot f_{trans} \cdot A_{eff} \cdot \frac{1}{2} 2 f_{Pb} \left(\sum_{detectors} w_d \right) \\
& - S \cdot f_{trans} \cdot A_{eff} \cdot \frac{1}{2} f_{Pb} K \left(\sum_{detectors} w_d^2 \right) \\
& - S \cdot f_{trans} \cdot A_{eff} \cdot \frac{1}{2} C f_{Pb} \left(\sum_{detectors} w_d \right) \\
& + B \cdot \left(\sum_{detectors} w_d \right) \\
=\ & S \cdot f_{trans} \cdot (1 - f_{Pb}) \cdot A_{eff} \cdot \frac{1}{2} K \left(\sum_{detectors} w_d^2 \right)
\end{aligned}
\tag{A.9}
$$

since by definition $\sum w_d = 0$ (because of how the constant C was chosen). Note that all of the terms that include the background counts B have cancelled out.

Parenthetically, $\sum w_d^2$ is approximately equal to a constant multiplied by the number of detectors in the sum. This constant, which depends only upon the distance between the source and the array, is approximately 0.54 for a source at infinity.

By default, K is chosen so that

$$
\frac{1}{2} K \sum_{detectors} w_d^2 = \frac{1}{C_{angle}}, \tag{A.10}
$$

where C_{angle} is a geometric correction factor. It is intended to account for effect of photons being incident on the edge of the detectors and on the different cross sectional area of the detector that is illuminated when the photons are incident at different angles, so that

$$
A_{eff} \approx A_{eff,on-axis} \cdot C_{angle}. \tag{A.11}
$$

In practical terms,

$$\begin{aligned} C_{angle} = & \cos\theta_z \\ & + \min\left[0.15, 0.05 \cdot \left|\frac{z_s}{x_s}\right|\right] \cdot \cos\theta_x \\ & + \min\left[0.15, 0.05 \cdot \left|\frac{z_s}{y_s}\right|\right] \cdot \cos\theta_y, \end{aligned} \tag{A.12}$$

where θ_x, θ_y, and θ_z are the angles between the line joining the source and the detector, and the x, y, and z axes, respectively, and x_s, y_s, and z_s are the coordinates (relative to the center of the array) of the source. This factor has been defined in such a way that it may be applied to calibration sources near the detector and to astrophysical sources at infinity, in which case the ratios in the equation are still finite.

With K chosen according to Equation A.10, the mask-weighted count rate becomes

$$S \cdot f_{trans} \cdot (1 - f_{Pb}) \cdot A_{eff,on-axis} \tag{A.13}$$

Note that at low photon energies, $f_{Pb} \approx 0$, so the mask-weighted count rate is just the expected count rate for a single detector that is illuminated from directly above and is not shadowed by the mask. At higher photon energies, f_{Pb} approaches 1, so that as the mask becomes more and more transparent, the mask-weighted count rate decreases to 0.

By defining K in this way (in terms of C_{angle}), the mask-weighted count rate is approximately the same regardless of the incident angle of the photons, so that as the spacecraft slews, the count rate will not be affected by it (much).

B does not actually have to be the same for every detector for it to cancel out of the expression. It just needs to satisfy $\sum B \cdot w = 0$ this is true if there is an equal probability that some detector will have a value of $B \cdot w$ as there is that one will have a value of $-B \cdot w$ (that is, B and w are "uncorrelated"), and if there are a large number of detectors. Both of these conditions hold for our situation.

Appendix B

Glossary of Terms

Afterglow The light that comes from the position of a gamma-ray burst long after the gamma-ray burst itself ends. The gamma-ray burst only lasts for a matter of seconds, whereas the afterglow can last for days or even weeks. The afterglow can be seen in x-rays, optical light, and radio wavelengths, all of which have longer wavelengths than gamma rays.

Amati relation A relationship between $E_{\rm peak}^{\rm src}$ (the energy of peak power in the source frame) and $E_{\rm iso}$ (the total amount of gamma-ray energy emitted by the burst if it emitted the same amount in all directions) that was discovered by Amati and others. [1] They found that gamma-ray bursts exhibiting a large $E_{\rm peak}^{\rm src}$ also tend to exhibit a large $E_{\rm iso}$. In particular, they found that $E_{\rm peak}^{\rm src} \sim E_{\rm iso}^{0.52\pm0.06}$.

BAT ("Burst Alert Telescope") One of the three telescopes aboard the Swift spacecraft. The BAT, which is sensitive to gamma rays, detects the gamma-ray bursts and x-ray flashes and records their spectra and light curves. It also determines their position in the sky and sends that position to the spacecraft so that Swift can slew the other two telescopes to point at the afterglow.

BATSE ("Burst and Transient Source Experiment") An instrument aboard the Compton Gamma-Ray Observatory spacecraft launched in 1991. BATSE's primary purpose was to determine the distribution of gamma-ray bursts in the sky by determining the locations of a large number of bursts to within a few degrees. During the course of its nine-year mission, BATSE made measurements and found positions of over 2700 gamma-ray bursts.

BeppoSAX An Italian-Dutch satellite launched in 1996. It contained instruments that could detect and localize gamma-ray bursts to 2-3 arcmin as well as instruments that could measure the afterglow emission. BeppoSAX was the first satellite to detect an afterglow, which was

a major breakthrough in GRB astronomy. It continued to observe and make contributions until it re-entered the earth's atmosphere in April 2003.

Break A time (or energy) at which the light curve (or spectrum) abruptly changes from one power law index to a different power law index. In a plot where the axes are logarithmic, this looks like two straight lines with different slopes that meet. The place where they meet is the "break".

Chandra An x-ray telescope launched into orbit in 1999. It is the most sophisticated and sensitive x-ray telescope built to date. As such, it is well-suited to observing x-ray afterglows of gamma-ray bursts. As of this writing, Chandra is still in operation.

E_γ Pronounced "Ee-gamma". The total energy emitted by a gamma-ray burst.

$E_{\rm iso}$ Pronounced "Ee-eye-so". The "isotropic equivalent" energy emitted by a gamma-ray burst—that is, the total energy emitted if the amount radiated toward the Earth were radiated in all directions. If the radiation all comes from jets in which the radiation is uniform, then $E_\gamma = E_{\rm iso}(1 - \cos(\Delta\theta))$, where $\Delta\theta$ is the half-angle of the jet.

$E_{\rm peak}^{\rm obs}$ Pronounced "Ee-peak-observed" or just "Ee-peak". The photon energy at which the greatest amount of energy is radiated, as measured in the reference frame of the telescope (see Figure 2.6).

$E_{\rm peak}^{\rm src}$ Pronounced "Ee-peak-source" or "Ee-peak in the source frame". The photon energy at which the greatest amount of energy is radiated, as measured in the reference frame of the burst. $E_{\rm peak}^{\rm src} = E_{\rm peak}^{\rm obs}(1+z)$.

Gaussian Distribution A function of the form

$$\frac{1}{\sigma\sqrt{2\pi}} e^{-\frac{(x-\mu)^2}{2\sigma^2}}. \tag{B.1}$$

This function describes a bell-shaped curve that peaks at $x = \mu$ and has a width of $\approx \sigma$.

Ginga A Japanese x-ray astronomy mission that orbited the Earth from 1987 through 1991. Gamma-ray bursts detected by Ginga resembled those detected by BATSE, except that the peak energies of the bursts extended to lower photon energies.

Gamma Ray Photons that have more than about 10 keV of energy each. These are the highest energy photons in the electromagnetic spectrum.

GCN ("Gamma-ray burst Coordinates Network") A system used to transmit information about a newly-detected gamma-ray burst to scientists and instruments all over the world in seconds. This enables others to quickly begin observing the burst and the afterglow. GCN circulars provide information about specific observations. Throughout this work, sources that are cited as "GCN" followed by a number refer to these circulars, and can be found at http://gcn.gsfc.nasa.gov/gcn3_archive.html.

GRB ("Gamma-Ray Burst") A burst of gamma-rays originating from a distant galaxy that lasts anywhere from a few milliseconds to a few minutes and then disappears, never to reappear in the same place again.

HETE-2 ("High Energy and Transient Explorer") The first satellite dedicated to observing GRBs. It was launched in October 2000 and, as of this writing, is still in operation.

keV ("kiloelectron-volt") An electron-volt (eV) is the amount of energy an electron gains by traveling through a potential difference of 1 volt. It is often used to describe very small quantities of energy, like the energy levels within atoms. X-ray and gamma-ray photon energies are often given in units of keV (thousands of electron-volts). Sometimes, gamma-ray photon energies are even expressed in MeV (millions of electron-volts) or larger units.

Lorentz Factor Γ ("Gamma") A quantity related to the speed of an object:

$$\Gamma = \frac{1}{\sqrt{1 - \frac{v^2}{c^2}}}, \tag{B.2}$$

where v is the velocity of the object, and c is the speed of light. For an object at rest ($v = 0$), $\Gamma = 1$. As v approaches c, Γ gets larger and larger, approaching infinity when $v = c$. This

quantity comes up often in special relativity.

Order of Magnitude This is just a fancy way of saying "a factor of 10". If A is "an order of magnitude" smaller than B, that means that A is about a factor of 10 smaller than B. If it is "many orders of magnitude" smaller, that means it is many factors of 10 (like, for instance, 1000 or 10000) times smaller.

Photon A "bundle" (or "quantum") of light. A photon can be thought of as a tiny, massless particle that carries a certain amount of energy.

Power law A function of the form $y = ax^k$, where k is called the "power law index". Spectra and light curves often follow a power law.

Redshift Light originating from a star that is moving away from us has a longer wavelength when measured on Earth than it had in the star's own reference frame. This is known as a "redshift". The redshift (z) of an object is defined as

$$z = \frac{\Delta\lambda}{\lambda} \tag{B.3}$$

where λ is the wavelength of light measured at the source, and $\Delta\lambda$ is the difference between the wavelength measured on earth and the wavelength measured at the source. By this definition, $z = 0$ would correspond to a source that is neither moving away from nor toward the earth. Galaxies farther from us tend to move away from us at a faster speed than galaxies closer to us. For that reason, redshift is often used as a surrogate measure for distance—objects farther from us have a higher redshift.

Spectrum The number of photons emitted (or detected) as a function of energy. "Photon" spectra (the number of photons emitted as a function of energy) are often given in units of photons/cm^2/s. "Count" spectra (the number of detected photons as a function of energy) are often given in units of counts/s.

Trigger The moment when a gamma-ray burst is first detected. It gets its name from the fact that when a telescope first detects a burst, it often initiates a specific set of procedures or

measurements (for instance, when BAT detects a burst, it calculates its position and initiates a slew). The detection of the burst "triggers" this set of procedures. The time of the afterglow is usually measured relative to the trigger time.

UVOT ("Ultra-Violet and Optical Telescope") One of the three telescopes aboard the Swift spacecraft. The UVOT makes measurements of the ultra-violet and optical afterglows that sometimes accompany gamma-ray bursts and x-ray flashes.

Vela A series of satellites launched in 1963 to monitor the Earth and the nearby solar system for signs of violations of the 1963 nuclear test ban treaty between the United States and the Soviet Union. In 1967, these satellites were the first to detect gamma-ray bursts.

X-Ray Photons that have between about 0.1 and about 10 keV of energy each (though this energy range is sometimes defined a little bit differently).

XRF ("X-Ray Flash") An event similar to a gamma-ray burst, but in which most of the emitted energy is in x-rays (that is, in photons with energies below about 10 keV).

XRR ("X-Ray Rich Gamma-Ray Burst") A gamma-ray burst for which a substantial fraction of the emitted energy is in x-rays (that is, in photons with energies below about 10 keV).

XRT ("X-Ray Telescope") One of the three telescopes aboard the Swift spacecraft. The XRT makes measurements of the x-ray afterglows that accompany gamma-ray bursts and x-ray flashes.

BIBLIOGRAPHY

[1] L. Amati, F. Frontera, M. Tavani, J. J. M. in 't Zand, A. Antonelli, E. Costa, M. Feroci, C. Guidorzi, J. Heise, N. Masetti, E. Montanari, L. Nicastro, E. Palazzi, E. Pian, L. Piro, P. Soffitta, "Intrinsic spectra and energetics of BeppoSAX Gamma-Ray Bursts with known redshifts", A&A **390**, 81 (2002).

[2] L. Amati, F. Frontera, J. J. M. in 't Zand, M. Capalbi, R. Landi, P. Soffitta, L. Vetere, L. A. Antonelli, E. Costa, S. Del Sordo, M. Feroci, C. Guidorzi, J. Heise, N. Masetti, E. Montanari, L. Nicastro, E. Palazzi, L. Piro, "Prompt and afterglow X-ray emission from the X-Ray Flash of 2002 April 27", A&A **426**, 415 (2004).

[3] R. L. Aptekar, D. D. Frederiks, S. V. Golenetskii, V. N. Ilynskii, E. P. Mazets, V. N. Panov, Z. J. Sokolova, M. M. Terekhov, L. O. Sheshin, T. L. Cline, D. E. Stilwell, "Konus-W gamma-ray burst experiment for the GGS Wind spacecraft", SSRv **71**, 265 (1995).

[4] J. L. Atteia, "A simple empirical redshift indicator for gamma-ray bursts", A&A **407**, L1 (2003).

[5] D. Band, J. Matteson, L. Ford, B. Schaefer, D. Palmer, B. Teegarden, T. Cline, M. S. Briggs, W. Paciesas, G. Pendleton, G. Fishman, C. Kouveliotou, C. Meegan, R. Wilson, P. Lestrade, "BATSE Observations of Gamma-Ray Burst Spectra. I. Spectral Diversity", ApJ **413**, 281 (1993).

[6] C. Barraud, G. Ricker, J-L. Atteia, N. Kawai, D. Lamb, S. Woosley, T. Donaghy, E. Fenimore, M. Galassi, C. Graziani, M. Matsuoka, Y. Nakagawa, T. Sakamoto, R. Sato, Y. Shirasaki, M. Suzuki, T. Tamagawa, K. Torii, Y. Urata, T. Yamazaki, Y. Yamamoto, A. Yoshida, N. Butler, G. Crew, J. Doty, A. Dullighan, G. Prigozhin, R. Vanderspek, J. Villasenor, J. G. Jernigan, A. Levine, G. Azzibrouck, J. Braga, R. Manchanda, and G. Pizzichini, M. Boer, J-F Olive, J-P Dezalay, K. Hurley, "XRF040701 (=U11548): a bright XRF detected by HETE", GCN, 2620 (2004).

[7] C. Barraud, F. Daigne, R. Mochkovitch, J. Atteia, "On the Nature of X-ray Flashes", A&A **440**, 809 (2005).

[8] S. D. Barthelmy, T. L. Cline, P. Butterworth, R. M. Kippen, M. Briggs, V. Connaughton, G. Pendleton, "GRB Coordinates Network: A Status Report", AIP Conf. Proc. **526**, 731 (2000).

[9] S. D. Barthelmy, "The burst Alert Telescope (BAT) on the Swift MIDEX mission", Proc. SPIE **5165**, 175 (2003).

[10] E. Berger, S. R. Kulkarni, G. Pooley, D. A. Frail, V. McIntyre, R. M. Wark, R. Sari, A. M. Soderberg, D. W. Fox, S. Yost, P. A. Price, Natur. **426**, 154 (2003).

[11] J. Bloom, S. Djorgovski, S. Kulkarni, "The redshift and the ordinary host galaxy of GRB 970228," ApJ **554**, 678 (2001).

[12] J. S. Bloom, D. A. Frail, S. R. Kulkarni, "GRB Energetics and the GRB Hubble Diagram: Promises and Limitations", ApJ **594**, 674 (2003).

[13] J.S. Bloom, D. Fox, P. G. Van Dokkum, S. R. Kulkarni, E. Berger, S. G. Djorgovski, D. A. Frail, "The First Two Host Galaxies of X-ray Flashes: XRF 011030 and XRF 020427", ApJ **599**, 957 (2003).

[14] A. A. Breeveld, T. S. Poole, C. H. James, A. J. Blustin, S. R. Rosen, W. Landsman, P. Boyd, C. Gronwall, S. Holland, S. D. Hunsberger, M. Ivanushkina, K. O. Mason, K. McGowan, M. de Pasquale, P. W. A. Roming, M. Still, "On-orbit calibration of the Ultraviolet/Optical Telescope (UVOT) on swift: part 2", Proc. SPIE **5898**, 379 (2005).

[15] D. N. Burrows, J. E. Hill, J. A. Nousek, A. A. Wells, G. Chincarini, A. F. Abbey, A. P. Beardmore, J. Bosworth, H. W. Brauninger, W. Burkert, S. Campana, M. Capalbi, W. Chang, O. Citterio, M. J. Freyberg, P. Giommi, G. D. Hartner, R. Killough, B. Kittle, R. Klar, C. Mangels, M. McMeekin, B. J. Miles, A. Moretti, K. Mori, D. C. Morris, K. Mukerjee, J. P. Osborne, A. D. T. Short, G. Tagliaferri, F. Tamburelli, D. J. Watson, R. Willingale, M. E. Zugger, "The Swift X-Ray Telescope", Proc. SPIE **5165**, 201 (2003).

[16] N. Butler, A. Dullighan, P. Ford, G. Ricker, R. Vanderspek, K. Hurley, J. Jernigan, D. Lamb, C. Graziani, "Optical and X-ray Observations of the Afterglow to XRF030723", AIP Conf. Proc. **727**, 111 (2003).

[17] E. Caroli, J. B. Stephen, G. Di Cocco, L. Natalucci, A. Spizzichino, "Coded Aperture Imaging in X- and Gamma-Ray Astronomy", SSRv **45**, 349 (1987).

[18] E. Costa, F. Frontera, J. Heise, M. Feroci, J. in 't Zand, F. Fiore, M.N. Cinti, D. Dal Fiume, L. Nicastro, M. Orlandini, E. Palazzi, M. Rapisarda, G. Zavattini, R. Jager, A. Parmar, A.Owens, S.Molendi, G. Cusumano, M.C. Maccarone, S. Giarrusso, A. Coletta, L.A. Antonelli, P. Giommi, J.M. Muller, L. Piro, R.C. Butler, "Discovery of the X-Ray Afterglow of the Gamma-Ray Burst of February 28 1997", Nature, 19 June 1997.

[19] G. B. Crew, D. Q. Lamb, G. R. Ricker, J.-L. Atteia, N. Kawai, R. Vanderspek, J. Villasenor, J. Doty, G. Prigozhin, J. G. Jernigan, C. Graziani, Y. Shirasaki, T. Sakamoto, M. Suzuki, N. Butler, K. Hurley, T. Tamagawa, A. Yoshida, M. Matsuoka, E. E. Fenimore, M. Galassi, C. Barraud, M. Boer, J.-P. Dezalay, J.-F. Olive, A. Levine, G. Monnelly, F. Martel, E. Morgan, T. Q. Donaghy, K. Torii, S. E. Woosley, T. Cline, J. Braga, R. Manchanda, G. Pizzichini, K. Takagishi, M. Yamauchi, "HETE-2 Localization and Observation of the Bright, X-Ray-Rich Gamma-Ray Burst GRB021211", ApJ **599**, 387 (2003).

[20] M. De Pasquale, L. Piro, R. Perna, E. Costa, M. Feroci, G. Gandolfi, J. in 't Zand, L. Nicastro, F. Frontera, L.A. Antonelli, F. Fiore, G. Stratta, "A Comparative Study of the X-ray Afterglow Properties of Optically Bright and Dark GRBs", ApJ **592**, 1018 (2003).

[21] C. D. Dermer, J. Chiang, M. Böttcher, "Fireball Loading and the Blast-Wave Model of Gamma-Ray Bursts", ApJ **513**, 656 (1999).

[22] E. E. Fenimore, "Time-resolved and energy-resolved coded aperture images with URA tagging", ApOpt **26**, 2760 (1987).

[23] E. E. Fenimore, D. Palmer, M. Galassi, T. Tavenner, S. Barthelmy, N. Gehrels, A. Parsons, J. Tueller, "The Trigger Algorithm for the Burst Alert Telescope on Swift", AIP Conf. Proc. **662**, 491 (2003).

[24] G. Fishman, C. Meegan, T. Parnell, R. Wilson, "The Burst and Transient Source Experiment for the Gamma Ray Observatory", AIP Conf. Proc. **77**, 67 (1982).

[25] D.B. Fox, "XRF040701: First-Epoch Chandra Observations", GCN, 2626 (2004).

[26] D. A. Frail, S. R. Kulkarni, R. Sari, S. G. Djorgovski, J. S. Bloom, T. J. Galama, D. E. Reichart, E. Berger, F. A. Harrison, P. A. Price, S. A. Yost, A. Diercks, R. W. Goodrich, F. Chaffee, "Beaming in Gamma-Ray Bursts: Evidence for a Standard Energy Reservoir", ApJL **562**, 55 (2001).

[27] F. Frontera, "X-Ray Observations of Gamma-Ray Burst Afterglows", *Supernovae and Gamma Ray Bursters*, ed. K. Weiler, Lecture Notes in Physics (Springer), 598 (2003).

[28] A. Fruchter, S. Pattel, C. Kouveliotou, J. Rhoads, S. Holland, I. Burud, R. Wijers, "XRF/GRB 011030: Detection of the Probable Host Galaxy", GCN, 1268 (2001).

[29] J. P. U. Fynbo, J. Hjorth, J. Gorosabel, B. L. Jensen, M. I. Andersen, R. A. M. J. Wijers, C. Kouveliotou, "XRF 030723: Detection of a rebrightening in the optical afterglow", GCN, 2345 (2003).

[30] J. P. U. Fynbo, J. Sollerman, J. Hjorth, F. Grundahl, J. Gorosabel, M. Weidinger, P. Moller, B. L. Jensen, P. M. Vreeswijk, C. Fransson, E. Ramirez-Ruiz, P. Jakobsson, S. F. Jorgensen, C. Vinter, M. I. Andersen, J. M. Castro Cern, A. J. Castro-Tirado, A. S. Fruchter, J. Greiner, C. Kouveliotou, A. Levan, S. Klose, N. Masetti, H. Pedersen, E. Palazzi, E. Pian, J. Rhoads, E. Rol, T. Sekiguchi, N. R. Tanvir, P. Tristram, A. de Ugarte Postigo, R. A. M. J. Wijers, E. van den Heuvel, "On the Afterglow of the X-Ray Flash of July 23 2003: Photometric evidence for an off-axis Gamma-Ray Burst with an associated Supernova?", ApJ **609**, 962 (2004).

[31] G. Gandolfi, "BeppoSAX ALERT: Possible X-ray rich GRB011030", GCN, 111 (2001).

[32] N. Gehrels, G Chincarini, P. Giommi, K. O. Mason, J. A. Nousek, A. A. Wells, N. E. White, S. D. Barthelmy, D. N. Burrows, L. R. Cominsky, K. C. Hurley, F. E. Marshall, P. Meszaros, P. W. A. Roming, L. Angelini,, L. M. Barbier, T. Belloni, P. T. Boyd, S. Campana, P. A. Caraveo, M. M. Chester, O. Citterio, T. L. Cline, M. S. Cropper, J. R. Cummings, A. J. Dean, E. D. Feigelson, E. E. Fenimore, D. A. Frail, A. S. Fruchter, G. P. Garmire, K. Gendreau, G. Ghisellini, J. Greiner, J. E. Hill, S. D. Hunsberger, H. A. Krimm, S. R. Kulkarni, P. Kumar, F. Lebrun, N. M. Lloyd-Ronning, C. B. Markwardt, B. J. Mattson, R. F. Mushotzky, J. P. Norris, B. Paczynski, D. M. Palmer, H.-S. Park, A. M. Parsons, J. Paul, M. J. Rees, C. S. Reynolds, J. E. Rhoads, T. P. Sasseen, B. E. Schaefer, A. T. Short, A. P. Smale, I. A. Smith, L. Stella, M. Still, G. Tagliaferri, T. Takahashi, M. Tashiro, L. K. Townsley, J. Tueller, M. J. L. Turner, M. Vietri, W. Voges, M. J. Ward, R. Willingale, F. M. Zerbi, W. W. Zhang, "The Swift Gamma-Ray Burst Mission", ApJ **611**, 1005 (2004).

[33] G. Ghisellini, "Gamma-Ray Bursts: Some Facts and Ideas", in conference proceedings, *A Relativistic Spacetime Odyssey, Proceedings of the 25th Johns Hopkins Workshop on Current Problems in Particle Theory, Firenze, Italy, 3-5 September 2001*, ed. I. Cuifolini, D. Dominici, L. Lusana (New Jersey: World Scientific), 381 (2003).

[34] G. Ghirlanda, G. Ghisellini, D. Lazzati, "The Collimation-Corrected GRB Energies Correlate with the Peak Energy of their νF_ν Spectrum", ApJ **616**, 331 (2004).

[35] S. V. Golenetskii, E. P. Mazets, R. L. Aptekar, V. N. Ilinskii, "Correlation between luminosity and temperature in gamma-ray burst sources", Natur **306**, 451 (1983).

[36] E. V. Gotthelf, T. T. Hamilton, D. J. Helfand, "The EINSTEIN Observatory Detection of Faint X-Ray Flashes", ApJ **466**, 779 (1996).

[37] J. Granot, A. Panaitescu, P. Kumar, S. Woosley, "Off-axis Afterglow Emission from Jetted Gamma-ray Bursts", ApJL **570**, 61 (2002).

[38] J. Granot, E. Ramirez-Ruiz, R. Perna, "Afterglow Observations Shed New Light on the Nature of X-Ray Flashes", ApJ **630**, 1003 (2005).

[39] J. Granot, "Afterglow Light Curves from Impulsive Relativistic Jets with an Unconventional Structure", submitted to ApJ (astro-ph/0504254).

[40] J. Greiner, "Search for GRB Counterparts", NYASA, **759**, 429 (1995).

[41] F. A. Harrison, S. Yost, D. Fox, J. Heise, S. R. Kulkarni, P. A. Price, E. Berger, "XRF011030: Chandra Observations", GCN, 1143 (2001).

[42] K. Hecht, "Zum Mechanismus des lichtelektrischen Primärstromes in isolierenden Kristallen", ZPhy **77**, 235 (1932).

[43] J. Heise, J. J. M. in 't Zand, R. M. Kippen, P. M. Woods, "X-ray Flashes and X-ray Rich Gamma Ray Bursts", AIP Conf. Proc. **662**, 229 (2003).

[44] J. Heise, J. J. M. in 't Zand, S. R. Kulkarni, E. Costa, "The X-ray Flash 011030 ('GRB 011030')", GCN, 1138 (2001).

[45] Y. F. Huang, Z. G. Dai, T. Lu, "Failed gamma-ray bursts and orphan afterglows", MNRAS **332**, 735 (2002).

[46] Y. F. Huang, X. F. Wu, Z. G. Dai, H. T. Ma, T. Lu, "Rebrightening of XRF 030723: Further Evidence for a Two-Component Jet in a Gamma-Ray Burst", ApJ **605**, 300 (2004).

[47] Y. Kaneko et al. in preparation (2005).

[48] J. I. Katz, L. M. Canel, "The Long and the Short of Gamma-Ray Bursts", ApJ **471**, 915 (1996).

[49] D. D. Kelson, K. Koviak, E. Berger, D.B. Fox, "XRF040701: Magellan Spectroscopy of Chandra Source #2 Associated Galaxy", GCN, 2627 (2004).

[50] R. M. Kippen, P. M. Woods, J. Heise, J. J. M. in 't Zand, M. S. Briggs, R. D. Preece, "Spectral Characteristics of X-ray Flashes compared to Gamma-Ray Bursts", AIPC **662**, 244K (2003).

[51] R. Klebesadel, I. Strong, R. Olson, "Observations of Gamma-Ray Bursts of Cosmic Origin", ApJ **I82**, L85 (1973).

[52] C. Kouveliotou, C. G. Meegan, G. J. Fishman, N. P. Bhat, M. S. Briggs, T. M. Koshut, W. S. Paciesas, G. N. Pendleton, "Identification of Two Classes of Gamma-Ray Bursts", ApJ **413**, L101 (1993).

[53] D. Q. Lamb, G. R. Ricker, J-L. Atteia, C. Barraud, M. Boer, J. Braga, N. Butler, T. Cline, G. B. Crew, J.-P. Dezalay, T. Q. Donaghy, J. P. Doty, A. Dullighan, E. E. Fenimore, M. Galassi, C. Graziani, K. Hurley, J. G. Jernigan, N. Kawai, A. Levine, R. Manchanda, M. Matsuoka, F. Martel, G. Monnelly, G. Morgan, J.-F. Olive, G. Pizzichini, G. Prigozhin, T. Sakamoto, Y. Shirasaki, M. Suzuki, K. Takagishi, T. Tamagawa, K. Torii, R. Vanderspek, G. Vedrenne, J. Villasenor, S. E. Woosley, M. Yamauchi, A. Yoshida, "Scientific Highlights of the HETE-2 Mission", NewAR **48**, 423 (2004).

[54] D. Q. Lamb, T. Q. Donaghy, C. Graziani, "A Unified Jet Model of X-Ray Flashes and Gamma-Ray Bursts", NewAR **48**, 459 (2004).

[55] E. Mazets, S. Golenetskii, V. Ilinskii, V. Panov, I. Aptekar, I. Gurian, I. Sokolov, Z. Sokolov, T. Kharitonova, "Energy spectra of the cosmic gamma-ray bursts", AIPC **101**, 36 (1983).

[56] P. Mészáros and M. J. Rees, "Gamma-Ray Bursts: Multiwaveband Spectral Predictions for Blast Wave Models", ApJ, **418**, L59 (1993).

[57] P. Mészáros, E. Ramirez-Ruiz, M. J. Rees, B. Zhang "X-ray Rich GRB, Photospheres and Variability", ApJ **587**, 812 (2002).

[58] A. R. Metzger, R. H. Parker, D. Gilman, L. E. Peterson, J. I. Trombka, "Observation of a Cosmic Gamma-Ray Burst on *Apollo 16*. I. Temporal Variability and Energy Spectrum", ApJL **194**, 19 (1974).

[59] M. Nardini, G. Ghisellini, G. Ghirlanda, F. Tavecchio, C. Firmani, D. Lazzati, "The clustering of the luminosities of optical afterglows of long Gamma Ray Bursts", submitted to A&A (astro-ph/0508447).

[60] J. P. Norris, J. D. Scargle, J. T. Bonnell, "Short Gamma-Ray Bursts Are Different", HEAD **5**, 3402N (2000).

[61] Y. Ogasaka, K. Tamura, T. Okajima, Y. Tawara, K. Yamashita, A. Furuzawa, K. Haga, S. Ichimaru, S. Takahashi, S. Fukuda, H. Kito, A. Goto, S. Kato, H. Satake, K. Nomoto, N. Hamada, P. J. Serlemitsos, J. Tueller, Y. Soong, K. Chan, S. M. Owens, F. Berendse, H. Krimm, W. Baumgartner, S. D. Barthelmy, H. Kunieda, K. Misaki, R. Shibata, H. Mori, K. Itoh, Y. Namba, "Development of supermirror hard x-ray telescope and the results of first observation flight of InFOCuS flight observation", Proc. SPIE **4851**, 619 (2003).

[62] W. Paciesas, C. Meegan, G. Pendleton, M. Briggs, C. Kouveliotou, T. Koshut, J. Lestrade, M. McCollough, J. Brainerd, J. Hakkila, W. Henze, R. Preece, V. Connaughton, R. M. Kippen, R. Mallozzi, G. Fishman, G. Richardson, M. Sahi, "The Fourth BATSE Gamma-Ray Burst Catalog (Revised)", ApJS **122**, 465 (1999).

[63] T. Piran, "Gamma-Ray Bursts and the Fireball Model", PhR **314**, 575 (1999).

[64] L. Piro, "Global properties of X-ray afterglows of GRB", submitted to il nuovo cimento (astro-ph/0506020).

[65] G. Prigozhin, N. Butler, G. Crew, J. Doty, A. Dullighan, R. Vanderspek, J. Villasenor, T. Cline, J. G. Jernigan, A. Levine, F. Martel, E. Morgan, G. Monnelly, G. Azzibrouck, J. Braga, R. Manchanda, G. Pizzichini, "XRF030723 (=H2777): An X-ray Flash Localized by the HETE WXM and SXC", GCN, 2313 (2003).

[66] D. E. Reichart, D. Q. Lamb, E. E. Fenimore, E. Ramirez-Ruiz, T. L. Cline, K. Hurley, "A Possible Cepheid-like Luminosity Estimator for the Long Gamma-Ray Bursts", ApJ **552**, 57 (2001).

[67] P. W. A. Roming, S. D. Hunsberger, K. O. Mason, J. A. Nousek, P. S. Broos, M. J. Carter, B. K. Hancock, H. E. Huckle, T. E. Kennedy, R. Killough, T. S. Koch, M. K. McLelland,

M. S. Pryzby, P. J. Smith, J. C. Soto, J. Stock, P. T. Boyd, M. D. Still, "The Swift Ultra-Violet/Optical Telescope", Proc. SPIE **5165**, 262 (2003).

[68] E. Rossi, D. Lazzati, M Rees, "Afterglow lightcurves, viewing angle and the jet structure of γ-ray bursts", MNRAS **332**, 945 (2002).

[69] T. Sakamoto, D. Q. Lamb, C. Graziani, T. Q. Donaghy, M. Suzuki, G. Ricker, J-L. Atteia, N. Kawai, A. Yoshida, Y. Shirasaki, T. Tamagawa, K. Torii, M. Matsuoka, E. E. Fenimore, M. Galassi, T. Tavenner, J. Doty, R. Vanderspek, G. B. Crew, J. Villasenor, N. Butler, G. Prigozhin, J. G. Jernigan, C. Barraud, M. Boer, J-P. Dezalay, J-F. Olive, K. Hurley, A. Levine, G. Monnelly, F. Martel, E. Morgan, S. E. Woosley, T. Cline, J. Braga, R. Manchanda, G. Pizzichini, K. Takagishi, M. Yamauchi, "High Energy Transient Explorer 2 Observations of the Extremely Soft X-Ray Flash XRF 020903", ApJ **602**, 875 (2004).

[70] T. Sakamoto, D. Q. Lamb, C. Graziani, T. Q. Donaghy, M. Suzuki, G. Ricker, J-L. Atteia, N. Kawai, A. Yoshida, Y. Shirasaki, T. Tamagawa, K. Torii, M. Matsuoka, E. E. Fenimore, M. Galassi, J. Doty, R. Vanderspek, G. B. Crew, J. Villasenor, N. Butler, G. Prigozhin, J. G. Jernigan, C. Barraud, M. Boer, J-P. Dezalay, J-F. Olive, K. Hurley, A. Levine, G. Monnelly, F. Martel, E. Morgan, S. E. Woosley, T. Cline, J. Braga, R. Manchanda, G. Pizzichini, K. Takagishi, M. Yamauchi, "Global Characteristics of X-Ray Flashes and X-Ray-Rich GRBs Observed by HETE-2", ApJ **629**, 311 (2005).

[71] R. Sari, T. Piran, R. Narayan, "Spectra and Light Curves of Gamma-Ray Afterglows", ApJ **497**, L17 (1998).

[72] R. Sari, T. Piran, J. Halpern, "Jets in Gamma-Ray Bursts", ApJL **519**, 17 (1999).

[73] A. M. Soderberg, S. R. Kulkarni, E. Berger, D. B. Fox, P. A. Price, S. A. Yost, M. P. Hunt, D. A. Frail, R. C. Walker, M. Hamuy, S. A. Shectman, J. P. Halpern, N. Mirabal, "A Redshift Determination for XRF 020903: First Spectroscopic Observations of an X-Ray Flash", ApJ **606**, 994 (2004).

[74] B. Stern, J. Poutanen, R. Svensson, "Seeing the Turnover in the Brightness Distribution of Complex Gamma Ray Bursts", ApJ **510**, 312, (1999).

[75] T. E. Strohmayer, E. E. Fenimore, T. Murakami, A. Yoshida, "X-Ray Spectral Characteristics of GINGA Gamma-Ray Bursts", ApJ **500**, 873 (1998).

[76] K. Toma, R. Yamazaki, T. Nakamura, "$E_p - E_{iso}$ Correlation in a Multiple Subjet Model of Gamma-Ray Bursts", accepted by ApJ (astro-ph/0504624).

[77] T. Totani, A. Panaitescu, "Orphan Afterglows of Collimated Gamma-ray Bursts: Rate Predictions and Prospects for Detection", ApJ **576**, 120 (2002).

[78] J. I. Trombka, E. L. Eller, R. L. Schmadebeck, I. Adler, A. E. Metzger, D. Gilman, P. Gorenstein, P. Bjorkholm, "Observation of a Cosmic Gamma-Ray Burst on *Apollo 16*. II. X-ray Time Profile and Source Location", ApJL **194**, 27 (1973).

[79] S. Vaughan, M. R. Goad, A. P. Beardmore, P. T. O'Brien, J. P. Osborne, K. L. Page, S. D. Barthelmy, D. N. Burrows, S. Campana, J. K. Cannizzo, M. Capalbi, G. Chincarini, J. R. Cummings, G. Cusumano, P. Giommi, O. Godet, J. E. Hill, S. Kobayashi, P. Kumar, V. La Parola, A. Levan, V. Mangano, P. Meszaros, A. Moretti, D. C. Morris, J. A. Nousek, C. Pagani, D. M. Palmer, J. L. Racusin, P. Romano, G. Tagliaferri, B. Zhang, N. Gehrels, "Swift observations of the X-ray bright GRB 050315", Accepted by ApJ (astro-ph/0510677).

[80] W. A. Wheaton, M.P. Ulmer, W.A. Baity, D. W. Datlowe, M.J. Elcan, L. E. Peterson, R. W. Klebesadel, I. B. Strong, T. L. Cline, U. D. Desai, "The Direction and Spectral Variability of a Cosmic Gamma-Ray Burst", ApJL **185**, 57 (1973).

[81] R. Yamazaki, K. Ioka, "X-ray Flashes from Off-axis Gamma-Ray Bursts", ApJL **571**, 31 (2002).

[82] R. Yamazaki, K. Ioka, T. Nakamura, "Delayed Flashes from Counter Jets of Gamma Ray Bursts", ApJ **591**, 283 (2003).

[83] D. Yonetoku, T. Murakami, T. Nakamura, R. Yamazaki, A.K. Inoue, K. Ioka, "GRB Formation Rates inferred from the Spectral Peak Energy – Luminosity Relation", ApJ **609**, 935Y (2004).